UNIVERSITE DE NANTES **École polytechnique de l'Université de Nantes**

ÉCOLE DOCTORALE

SCIENCES POUR L'INGENIEUR, GEOSCIENCES, ARCHITECTURE

DE NANTES

2010

Thèse de **DOCTORAT**

Discipline : Sciences de l'Ingénieur
Spécialité : Thermique - Énergétique

présentée et soutenue publiquement par

HABCHI Charbel

le 15 octobre 2010

à l'École Polytechnique de l'Université de Nantes

ÉTUDE EXPERIMENTALE ET NUMERIQUE DES PHENOMENES DE MELANGE TURBULENT ET DE TRANSFERT THERMIQUE EN PRESENCE DE VORTICITE

Jury :

M. Laurent FALK	Rapporteur	D.R. CNRS, LRGP, Université de Nancy
M. Laurent LIMAT	Rapporteur	D.R. CNRS, LSMC, Université Paris 7
M. Christophe GOURDON	Examinateur	Professeur, LGC, ENSIACET Toulouse
M. Jean-Luc HARION	Examinateur	Professeur, DEI, École des Mines de Douai
M. Cédric GARNIER	Examinateur	Docteur-Ingénieur, ADEME, Angers
M. Hassan PEERHOSSAINI	Directeur de thèse	Professeur, LTN, Université de Nantes
M^{me} Dominique DELLA VALLE	Co-encadrant	Maître de Conférences, LTN, ONIRIS Nantes
M. Thierry LEMENAND	Co-encadrant	Maître de Conférences, LTN, Université d'Angers

Directeur de thèse : Professeur Hassan PEERHOSSAINI

Laboratoire : Laboratoire de Thermocinétique de Nantes
Adresse : Rue Christian Pauc - BP 50609 - 46 306 Nantes Cedex 3

N° ED 498-130

ECOLE DOCTORALE
MÉCANIQUE, THERMIQUE ET GÉNIE CIVIL
ED 0367

LISTE DES DIRECTEURS DE RECHERCHE

AMBIANCES ARCHITECTURALES ET URBAINES

Michel	BERENGIER	HDR	DR LCPC	LCPC	Division Exploitation Entretien Acoustique Routière	
Gérard	HEGRON		PR	Ecole Architecture Nantes	CERMA Nantes	UMR 1563
Jean-Pierre	PENEAU		PR émérite		CERMA Nantes	UMR 1563

DYNAMIQUE DES FLUIDES ET DES TRANSFERTS

Bertrand	ALESSANDRINI	HDR	IR	Ecole Centrale de Nantes	L. M. F.	UMR 6598
Jacques	ASTOLFI	HDR	MC	Ecole Navale de Brest	IRENAV Brest	EA 3634
Jean-Yves	BILLARD		PR	Ecole Navale de Brest	IRENAV Brest	EA 3634
Alain	CLEMENT	HDR	IR	Ecole Centrale de Nantes	L. M. F.	UMR 6598
Gérard	DELHOMMEAU	DE	IR	Ecole Centrale de Nantes	L. M. F.	UMR 6598
Henda	DJERIDI	HDR	MC	Ecole Navale de Brest	IRENAV Brest	EA 3634
Pierre	FERRANT	HDR	MC	Ecole Centrale de Nantes	L. M. F.	UMR 6598
Jean-François	HETET		PR	Ecole Centrale de Nantes	L. M. F.	UMR 6598
Dominique	MARICHAL		PR	Ecole Centrale de Nantes		
Patrice	MESTAYER		DR CNRS	Ecole Centrale de Nantes	L. M. F.	UMR 6598
Jean	PIQUET		PR	Ecole Centrale de Nantes	L. M. F.	UMR 6598
Jean-Michel	ROSANT	DE	CR CNRS	Ecole Centrale de Nantes	L. M. F.	UMR 6598
Jean-François	SINI		PR	Ecole Centrale de Nantes	L. M. F.	UMR 6598
Michel	VISONNEAU		DR CNRS	Ecole Centrale de Nantes	L. M. F.	UMR 6598

GENIE CIVIL

Alain	ALEXIS		PR	IUT Saint-Nazaire - Univ. Nantes	GeM	UMR 6183
Guy	BASTIAN		PR émérite	IUT Saint-Nazaire - Univ. Nantes	GeM	UMR 6183
Pierre	CHAMBON	HDR	MC	Fac. Sc. et Techn - Univ. Nantes	GeM	UMR 6183
Francis	DE LARRARD	HDR	Pr. Ag.	LCPC	Division Technologies du GC et de l'Environnement	
Jacques	GARNIER	HDR	DR LCPC	LCPC	Division Reconnaissance et Mécanique des Sols	
Pierre-Yves	HICHER		PR	Ecole Centrale de Nantes	GeM	UMR 6183
Agnès	JULLIEN	HDR	DR LCPC	LCPC	Division Technologies du GC et de l'Environnement	
Abdelhafid	KHELIDJ		PR	IUT Saint-Nazaire - Univ. Nantes	GeM	UMR 6183
Van Anh	LE		PR	Fac. Sc. et Techn - Univ. Nantes	GeM	UMR 6183
Ahmed	LOUKILI	HDR	MC	Ecole Centrale de Nantes	GeM	UMR 6183
Gilles	PIJAUDIER-CABOT		PR	Ecole Centrale de Nantes	GeM	UMR 6183
Abdul-Hamid	SOUBRA		PR	Fac. Sc. et Techn - Univ. Nantes	GeM	UMR 6183
Philippe	TAMAGNY	HDR	DR LCPC	LCPC	Division Mécanique et Structure des Chaussées	
Pierre	THOMAS		PR	IUT Saint-Nazaire - Univ. Nantes	GeM	UMR 6183
Christian	WIELGOSZ		PR	Fac. Sc. et Techn - Univ. Nantes	GeM	UMR 6183

GEOSCIENCES

Odile	ABRAHAM	HDR	IDTPE	LCPC	Division Reconnaissance et Mécanique des Sols	
Véronique	CARRERE	HDR	MC	Fac. Sc. et Techn - Univ. Nantes	Lab. Planét. et Géodyn.	UMR 6112
Philippe	CÔTE	DE	DR LCPC	LCPC	Division Reconnaissance et Mécanique des Sols	
Hervé	DIOT		PR	Univ. La Rochelle	Lab. Planét. et Géodyn.	UMR 6112
Patrick	GENOT		PR	Fac. Sc. et Techn - Univ. Nantes	Lab. Planét. et Géodyn.	UMR 6112
Jacques	GIRARDEAU		PR	Fac. Sc. et Techn - Univ. Nantes	Lab. Planét. et Géodyn.	UMR 6112
Olivier	GRASSET		PR	Fac. Sc. et Techn - Univ. Nantes	Lab. Planét. et Géodyn.	UMR 6112
Eric	HUMLER		PR	Fac. Sc. et Techn - Univ. Nantes	Lab. Planét. et Géodyn.	UMR 6112
Richard	LAGABRIELLE	DE	DR LCPC	Directeur Technique - LCPC		
Bernard	LASNIER		PR émérite	Fac. Sc. et Techn - Univ. Nantes	Lab. Planét. et Géodyn.	UMR 6112
Patrick	Patrick		PR	Fac. Sc. et Techn - Univ. Nantes	Lab. Planét. et Géodyn.	UMR 6112
Daniel	MEGE	HDR	MC	Fac. Sc. et Techn - Univ. Nantes	Lab. Planét. et Géodyn.	UMR 6112
Eric	MERCIER		PR	Fac. Sc. et Techn - Univ. Nantes	Lab. Planét. et Géodyn.	UMR 6112
Antoine	MOCQUET		PR	Fac. Sc. et Techn - Univ. Nantes	Lab. Planét. et Géodyn.	UMR 6112
Martin	SANCHEZ	HDR	MC	Fac. Sc. et Techn - Univ. Nantes	Lab. Planét. et Géodyn.	UMR 6112
Christophe	SOTIN		PR	Fac. Sc. et Techn - Univ. Nantes	Lab. Planét. et Géodyn.	UMR 6112

GENIE MECANIQUE

Fouad	BENNIS		PR	Ecole Centrale de Nantes	IRCCyN	UMR 6597
Alain	BERNARD		PR	Ecole Centrale de Nantes	IRCCyN	UMR 6597
Christian	BURTIN	HDR	MC	Ecole Centrale de Nantes		
Patrice	CARTRAUD		PR	Ecole Centrale de Nantes	GeM	UMR 6183
Pascal	CASARI	HDR	MC	Fac. Sc. et Techn - Univ. Nantes	GeM	UMR 6183
Patrick	CHEDMAIL		PR	Ecole Centrale de Nantes	IRCCyN	UMR 6597
Chi Yuen	CHIEM		PR	Ecole Centrale de Nantes	GeM	UMR 6183
Philippe	DEPINCE	HDR	MC	Ecole Centrale de Nantes	IRCCyN	UMR 6597
Benoît	FURET		PR	IUT Nantes - Univ. Nantes	IRCCyN	UMR 6597
Laurent	GORNET	HDR	MC	Ecole Centrale de Nantes	GeM	UMR 6183
Ronald	GUILLEN		PR	IUT Saint-Nazaire - Univ. Nantes	GeM	UMR 6183
Jean-Yves	HASCOËT		PR	Ecole Centrale de Nantes	IRCCyN	UMR 6597
Frédéric	JACQUEMIN	HDR		IUT Saint-Nazaire - Univ. Nantes	GeM	UMR 6183
Bernard	LAMY		PR	Ecole Centrale de Nantes	GeM	UMR 6183
Donatien	LE HOUËDEC		PR émérite	Ecole Centrale de Nantes	GeM	UMR 6183
Surandar	MARYA		PR	Ecole Centrale de Nantes	GeM	UMR 6183
Nicolas	MOES		PR	Ecole Centrale de Nantes	GeM	UMR 6183
Pascal	MOGNOL	HDR	MC	ENS CACHAN	IRCCyN	UMR 6597
Bernard	PESEUX		PR Emérite	Ecole Centrale de Nantes	GeM	UMR 6183
Jean-François	PETIOT		PR	Ecole Centrale de Nantes	IRCCyN	UMR 6597
Arnaud	POITOU		PR	Ecole Centrale de Nantes	GeM	UMR 6183
Guillaume	RACINEUX		PR	Ecole Centrale de Nantes	GeM	UMR 6183
Erwan	VERRON	HDR	MC	Ecole Centrale de Nantes	GeM	UMR 6183
Philippe	WENGER		DR CNRS	Ecole Centrale de Nantes	IRCCyN	UMR 6597

THERMIQUE, ÉNERGÉTIQUE ET GÉNIE DES PROCÉDÉS

Yves	ANDRES	HDR	MA	Ecole des Mines de Nantes	GEPEA	UMR 6144
Hervé	ANDRIEU	HDR	IDTPE	LCPC	Division Eau	
Marie	DELAMBALLERIE	HDR	PR	ENITIAA Nantes	GEPEA	UMR 6144
Marc	ANTON		DR	INRA Nantes	Unité BIA	
Abdellah	ARHALIASS		PR	IUT Saint-Nazaire - Univ. Nantes	GEPEA	UMR 6144
Jean-Pierre	BARDON		PR Emérite	Ecole Polytechnique - Univ. Nantes	Lab. Thermocinétique	UMR 6607
Jérôme	BELLETRE	HDR	MA	Ecole des Mines de Nantes	Dép. Syst. Energ & Environnement	UMR 6144
Lionel	BOILLEREAUX		PR	ENITIAA Nantes	GEPEA	UMR 6144
Brahim	BOUROUGA		PR	Ecole Polytechnique - Univ. Nantes	Lab. Thermocinétique	UMR 6607
Jacques	COMITI		PR	IUT Saint-Nazaire - Univ. Nantes	GEPEA	UMR 6144
Didier	DELAUNAY		DR CNRS	Ecole Polytechnique - Univ. Nantes	Lab. Thermocinétique	UMR 6607
Arnaud	DELEBARRE		PR	Ecole des Mines de Nantes	GEPEA	UMR 6144
Guy	DELLA VALLE	HDR	IR	INRA Nantes	Unité BIA	
Anne	DESRUMAUX	HDR	MC	ENITIAA Nantes	GEPEA	UMR 6144
Rémi	DETERRE		PR	IUT Nantes - Univ. Nantes	OPERP EE 0101	
Jean-Louis	DOUBLIER		DR	INRA Nantes	Unité BIA	
Louis	DOUBLIEZ		PR	Fac. Sc. et Techn - Univ. Nantes	GEPEA	UMR 6144
Francine	FAYOLLE	HDR	MC	ENITIAA Nantes	GEPEA	UMR 6144
Alain	FOUCAULT	HDR	IR CNRS	CRTT Saint-Nazaire	GEPEA	UMR 6144
Bertrand	GARNIER	HDR	CR	Ecole Polytechnique - Univ. Nantes	Lab. Thermocinétique	UMR 6607
Jean-Luc	ILARI	HDR	PR	ENITIAA Nantes	GEPEA	UMR 6144
Pascal	JAOUEN		PR	Fac. Sc. et Techn - Univ. Nantes	GEPEA	UMR 6144
Yvon	JARNY		PR	Ecole Polytechnique - Univ. Nantes	Lab. Thermocinétique	UMR 6607
Abdeljalil	LAHMAR		PR	IUT La Roche/Yon - Univ. Nantes	Lab. Thermocinétique	UMR 6607
Alain	LE BAIL	HDR	PR	ENITIAA Nantes	GEPEA	UMR 6144
Laurence	LE COQ	HDR	MA	Ecole des Mines de Nantes	Dép. Syst. Energ & Environnement	UMR 6144
Olivier	LE CORRE	HDR	MA	Ecole des Mines de Nantes	Dept Syst.Energet. et Environnement	
Yves	LECOINTE		PR	Ecole Polytechnique - Univ. Nantes	Lab. Thermocinétique	UMR 6607
Patrick	LEGENTILHOMME		PR	IUT Saint-Nazaire - Univ. Nantes	GEPEA	UMR 6144
Jack	LEGRAND		PR	IUT Saint-Nazaire - Univ. Nantes	GEPEA	UMR 6144
Michel	LEGRET	HDR	DR LCPC	LCPC	Division Eau	
Denis	LOURDIN		CR	INRA Nantes	BIA	
Agnès	MONTILLET	HDR	MC	IUT Saint-Nazaire - Univ. Nantes	GEPEA	UMR 6144
Ahmed	OULD EL MOCTAR	HDR	MC	Ecole Polytechnique - Univ. Nantes	Lab. Thermocinétique	UMR 6607
Hassan	PEERHOSSAINI		PR	Ecole Polytechnique - Univ. Nantes	Lab. Thermocinétique	UMR 6607
Denis	PONCELET		PR	ENITIAA Nantes	GEPEA	UMR 6144
Jérémy	PRUVOST	HDR	MC	Fac. Sc. et Techn - Univ. Nantes	GEPEA	UMR 6144
Francis	QUEMENEUR		PR Emérite	IUT Saint-Nazaire - Univ. Nantes	GEPEA	UMR 6144
Véronique	RUBAN	HDR	DR LCPC	LCPC	Division Eau	
Jean-Pierre	SCHLUMPF	HDR	MC	IUT Saint-Nazaire - Univ. Nantes	GEPEA	UMR 6144
Camille	SOLLIEC	HDR	MA	Ecole des Mines de Nantes	GEPEA	UMR 6144
Mohan	TAZEROUT	HDR	MA	Ecole des Mines de Nantes	Dép. Syst. Energ & Environnement	

« Je veux connaître les pensées de Dieu ; tout le reste n'est que détail »
Albert Einstein

Remerciements

Durant la thèse nous sommes souvent confrontés à des obstacles scientifiques et techniques dont les solutions sont rarement trouvées de manière intellectuellement simple. En effet, les solutions sont souvent inspirées grâce à des contacts avec des personnes passionnées dans leurs spécialités. Ainsi, j'aimerais remercier celles et ceux qui d'une manière ou d'une autre ont contribué à mes travaux de thèse réalisée au sein du Laboratoire de Thermocinétique de Nantes (LTN) dans le cadre d'une allocation de recherche ADEME-CNRS.

Je tiens dans un premier temps à remercier profondément mon directeur de thèse Prof. Hassan PEERHOSSAINI et mes encadrants Mme. Dominique DELLA VALLE et M. Thierry LEMENAND pour le temps qu'ils m'ont aimablement accordé, pour leurs nombreux conseils et surtout pour l'excellente relation professionnelle et personnelle. Je suis profondément reconnaissant à M. Cédric GARNIER (ADEME, Angers) pour son suivi et pour l'intérêt qu'il a exprimé pour mon travail de thèse.

Je souhaite également remercier les membres de mon Jury pour avoir accepté de juger mon travail de thèse ; je remercie Prof. Christophe GOURDON (LGC, ENSIACET Toulouse) le président du Jury, Messieurs Laurent LIMAT (LSMC, Université Paris 7) et Laurent FALK (LRGC, Université de Nancy) les rapporteurs de thèse, Prof. Jean-Luc HARION (DEI, École des Mines de Douai) et M. Cédric GARNIER (ADEME, Angers) les examinateurs.

Je tiens aussi à remercier le directeur du LTN, M. Didier DELAUNAY, pour m'avoir accueilli en Master 2 Recherche, sous la direction du Prof. Hassan PEERHOSSAINI, et ensuite durant ma thèse. Je remercie également le personnel du LTN ; Mesdames Brigitte ROUSSEAU, Christine TESSIER et Muriel SPANEVELLO du service Secrétariat et Gestion Financière et Mme. Nathalie ROBERT du Service Informatique pour leurs disponibilités et leurs aides dans les procédures administratives et techniques. Je remercie également les personnels du Service Etude et Fabrication ; Messieurs Nicolas LEFEVRE, Michel JEZEGOU, Gwenaël BIOTTEAU, Olivier GIBOULOT et surtout Jérôme DELMAS qui était toujours disponible pour les instrumentations et les montages des divers bancs d'essais et pour les conseils techniques et pratiques.

Je n'oublie pas de remercier le personnel de la Cellule Thèse de l'ADEME et notamment Mme. Valérie PINEAU pour sa disponibilité et son aide dans les procédures administratives.

J'adresse mes sincères remerciements à Messieurs Ahmed OULD EL MOCTAR (LTN, Polytech' Nantes), Michel GONZALEZ (CORIA, Rouen) et Philippe CARIERE (LMFA, Ecole Centrale de Lyon) pour leurs nombreux conseils respectivement sur les transferts de chaleurs convectifs, la turbulence et l'advection chaotique. Je remercie également Mme. Emilie GADOIN (LTN, Polytech' Nantes) pour ses conseils pour les simulations numériques.

Je tiens à remercier profondément Hakim MOHAND KACI (CEA, Saclay) qui m'a permis, grâce à ses conseils, d'avancer rapidement sur les mesures par la méthode de sonde chimique et par l'anémométrie laser à effet Doppler.

Les journées des thésards sont parfois très longues et peuvent être solitaires. Je suis reconnaissant pour le temps passé avec les collègues permanents et thésards du LTN et les nombreuses discussions scientifiques et aussi humaines que j'ai eu avec eux. Je pense à Prof. Jérôme BELLETTRE, M. Bertrand GARNIER, Yann FAVENNEC, Gilberto DOMINGUES, Yahia LASBET, Yanneck WIELHORSKI, Mojtaba JARRAHI, Leonardo PACHECO et finalement mon cher colocataire et aussi collègue de bureau Mahmoud KHALED pour le soutien moral et pour ses nombreux conseils scientifiques. Je souhaite également remercier mon second colocataire Mohamed JAWAD et aussi Farah HAJJ pour leur « patience » et pour le soutien moral durant les années de ma thèse.

Pour finir, je tiens à remercier ma chère famille et mes amis au Liban, particulièrement mon Père, ma Mère et ma Sœur, qui m'ont soutenu tout au long de ces trois années.

PREAMBULE

Ce mémoire est présenté sous forme d'articles, publiés ou soumis pendant la durée de la thèse. Une synthèse des travaux faisant état des résultats marquants précède l'ensemble des articles, en se référant à la liste de publications correspondante (page 49).

Deux articles (articles 1 et 2) s'articulent autour de la caractérisation du micromélange par la méthode de sonde chimique, et cinq articles (articles 3 à 7) concernent l'étude des phénomènes de mélange turbulent et de transferts thermiques dans des ERM (Echangeurs-Réacteurs Multifonctionnels). Les publications sont présentées en format « épreuve » par ordre de citation dans la partie synthèse. La liste des références bibliographiques et les annexes sont présentées à la fin du manuscrit.

TABLE DES MATIERES

LISTE DES FIGURES

LISTE DES TABLEAUX

INTRODUCTION GENERALE

L'accélération du développement économique et industriel et des besoins énergétiques associés complique le défi mondial que représente la crise écologique. Celle-ci a pour origine la pollution des eaux, des sols et de l'air causée par les déchets industriels et domestiques (ADEME, 2008). Un aspect important en est le réchauffement climatique, c'est-à-dire la hausse des températures moyennes de l'atmosphère et des océans, ce qui pourrait avoir de multiples conséquences. Les scientifiques du GIEC[1] prévoient par exemple une fonte massive des neiges et des glaces polaires, et l'élévation du niveau moyen de la mer à cause de la dilatation thermique (GIEC, 2008). Ce réchauffement, dans l'état actuel des connaissances, est imputé aux « gaz à effet de serre » qui absorbent le rayonnement infrarouge réémis par la terre, augmentant l'énergie interne de l'atmosphère et sa température (GIEC, 2008 ; Fernando *et al.*, 2010). Ces gaz sont principalement le méthane, la vapeur d'eau et le dioxyde de carbone, le fameux CO_2. Or, les émissions « anthropiques »[2] de CO_2 ont augmenté exponentiellement au cours du siècle dernier. Ces émissions sont dues essentiellement aux unités de chauffage, aux moteurs et systèmes de combustion, mais aussi à plusieurs types de procédés chimiques comme la décarbonatation (ADEME, 2008 ; GIEC, 2008).

Dans le but de réduire ou au moins stabiliser l'impact humain sur l'environnement, il faut agir sur les paramètres d'équilibre entre les éléments de ce qu'on appelle le « *triple E* » (représenté sur la Figure 1) : *Environnement-Énergie-Économie* : c'est la démarche de développement durable (IEA, 2006 ; ADEME, 2008). Ce concept consiste à maîtriser la production et l'utilisation de l'énergie pour des stratégies économiques rentables, tout en permettant l'amélioration de la qualité de vie (Brundtland, 1986).

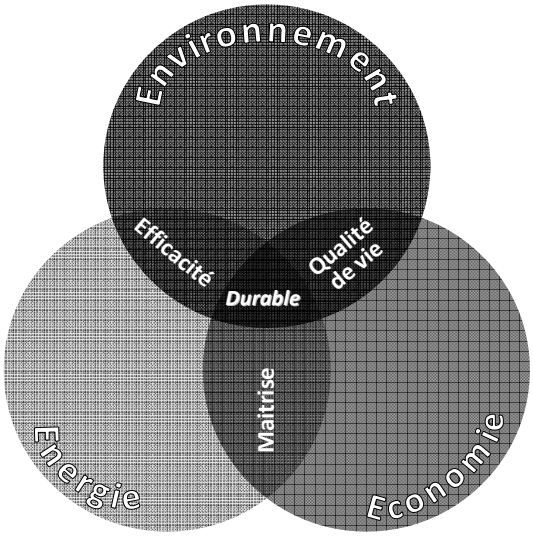

Figure 1 : Synoptique du développement durable à la conjonction des 3 E (adapté de Brundtland, 1986)

[1] Groupe d'experts Intergouvernemental sur l'Evolution du Climat
[2] Émissions « anthropiques » : liées à l'activité humaine

Dans ce contexte mondial, les préoccupations du développement durable peuvent être classées en trois catégories (Colloque Énergie CNRS, 2009 ; Saulnier, 2009) :

- la réduction de l'émission de CO_2
- l'optimisation et la promotion de l'utilisation de l'énergie, comme l'hydrogène, les piles à combustibles, l'électricité et la chaleur
- l'amélioration de l'efficacité énergétique des systèmes et des composantes productrices ou consommatrices de l'énergie.

Les objectifs de cette thèse s'inscrivent pleinement dans le cadre du troisième point, puisqu'elle vise le *développement des échangeurs/réacteurs multifonctionnels (ERM) pour un procédé énergétiquement efficace, sobre et sûr*.

La Figure 2 montre un système batch qui est constitué d'une cuve agitée par un mobile mécanique (a) et un ERM constitué de tubes parallèles munis d'inserts favorisant les transferts radiaux de masse et de chaleur dans la section de l'écoulement (b).

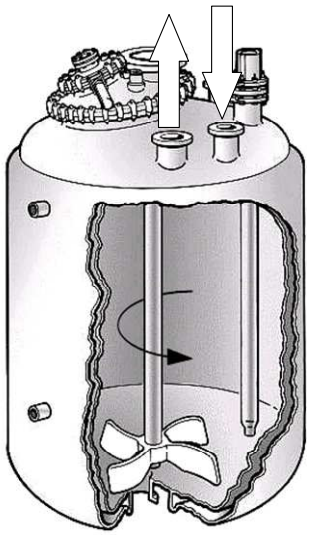

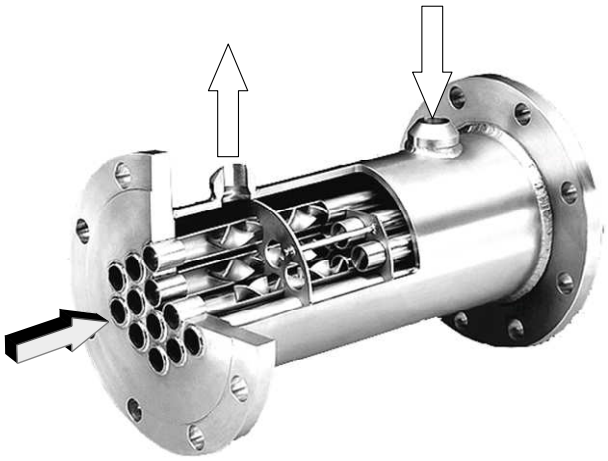

Surface spécifiques ~ 10 m^2 m^{-3} (a)

Surface spécifiques ~ 400 m^2 m^{-3} (b)

Figure 2 : (a) Réacteur en batch de type DIN-CE[3], (b) ERM de type Kenics[4] où les surface spécifiques sont adaptées de Ferrouillat et al. (2006c)

En effet, les ERM proposent une alternative à un grand nombre de procédés industriels et résidentiels dès lors que sont en jeu des transferts en milieu fluide, comme par exemple : les radiateurs domestiques, les échangeurs de chaleur dans les véhicules, le mélange de différents produits médicamenteux dans les procédés pharmaceutiques, le traitement et la désinfection de l'eau par ajout de produit chimique, …

[3] Pfaudler™
[4] Chemineer™

Le concept d'intensification en génie des procédés consiste à agir essentiellement sur les trois points fondamentaux suivants (Stankiewicz et Moulijn, 2000 ; Ferrouillat *et al.*, 2006a ; Moulijn *et al.*, 2008 ; Anxionnaz *et al.*, 2008) :

- le passage de systèmes agités ou en batch aux procédés en continu
- l'intensification des transferts de masse et de chaleur par rapport aux géométries de base en canaux rectilignes
- l'intégration de plusieurs opérations unitaires comme le mélange, la réaction chimique et le transfert de chaleur dans un seul système, rendu possible par des géométries intensifiées

Ceci constitue la définition de l'ERM : un appareil qui réalise le mélange, la réaction chimique et les transferts thermiques dans un seul passage en continu selon le schéma de la Figure 3.

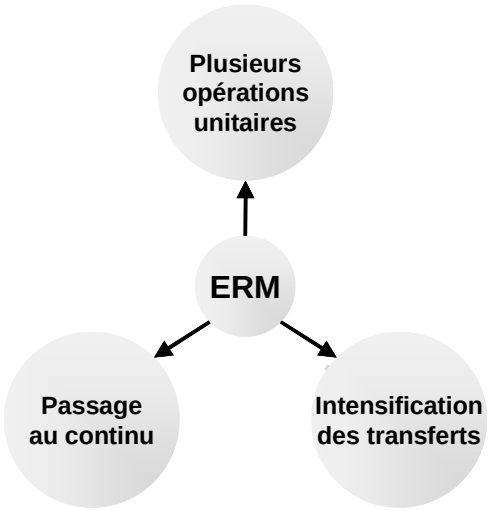

Figure 3 : Principe des ERM combinant plusieurs opérations unitaires

Par rapport aux systèmes en batch, les ERM présentent plusieurs avantages cruciaux pour un procédé rentable et efficace, en termes de compacité, homogénéité, sélectivité, et sécurité (Thakur *et al.*, 2003 ; Ferrouillat *et al.*, 2006a ; Anxionnaz *et al.*, 2008).

Compacité : Les ERM sont généralement constitués de tubes dans lesquels sont insérées des lames ou des générateurs de tourbillons facilement amovibles, contrairement aux systèmes en batch constitués généralement de pièces mécaniques complexes. Grâce à leur grande compacité, les ERM réduisent l'encombrement et le poids des dispositifs industriels, et les rend plus facile à maintenir et à nettoyer.

Efficacité énergétique : Munis d'éléments mécaniques mobiles, les systèmes en batch consomment beaucoup plus d'énergie que les ERM, dans lesquels l'énergie de mise en mouvement du fluide est en grande partie utilisée pour le mélange.

Homogénéité : Le temps de séjour dans les ERM peut être réduit de 10 à 1000 fois relativement aux systèmes agités (Trambouze et Euzen, 2002), et peut être proche du temps théorique

de la réaction. La distribution des temps de séjour (DTS) dans les ERM est proche d'un écoulement à piston, tandis que celle des systèmes en batch présente une traîne importante (Thakur *et al.*, 2003), réduisant ainsi l'homogénéité du mélange final. De plus, les ERM permettent d'effectuer un mélange à de faibles taux de cisaillement bien distribués dans le volume du mélangeur, par comparaison aux zones locales à hauts taux de cisaillement des systèmes en batch.

Sélectivité : Les ERM présentent une meilleure sélectivité grâce à leur capacité d'évacuation de la chaleur enthalpique de 100 à 1000 fois plus importante que celle des cuves agitées (Ferrouillat, 2005 ; Della Valle *et al.*, 2009). Ceci est rendu possible grâce à un meilleur contrôle thermique ce qui permet de réduire les effluents et les déchets en permettant de travailler avec des réactifs plus concentrés.

Sécurité : Cette évacuation de chaleur très efficace réduit les risques d'emballement du système et favorise ainsi la sécurité des ERM en cas de réactions chimiques exothermiques, diminuant de fait les risques humains et matériels. Quant aux batch agités, les risques d'emballement sont élevés dus aux faibles capacités d'échange thermique entre le centre de l'écoulement et la paroi.

L'idée principale d'intensification des transferts dans les ERM consiste essentiellement à générer un mélange radial par des perturbations d'écoulement. Ces perturbations peuvent être temporelles, par exemple les écoulements pulsés (Timité *et al.*, 2009 ; Mao and Xu, 2009), ou spatiales. Les perturbateurs « spatiaux » sont de plusieurs types, par exemple : les tubes ou les canaux ondulés (Habchi *et al.*, 2009a ; Anxionnaz, 2009) ; les générateurs de tourbillons (Fiebig, 1998 ; Ferrouillat *et al.*, 2006b ; Habchi *et al.*, 2009c) ; les inserts à hélices (Cazan et Aidun, 2009 ; Eiamsa-ard *et al.*, 2010) (voir Figure 2), les mousses métalliques (Boomsma *et al.*, 2003 ; Ferrouillat *et al.*, 2006c). *La géométrie d'un ERM conditionne fortement son efficacité énergétique en contrôlant la structure de l'écoulement. Ainsi, la conception de nouvelles géométries d'ERM ou l'amélioration de géométries existantes, constituent un verrou technologique important dans le chemin du développement durable.* En effet, l'amélioration de l'efficacité du mélange et/ou des transferts thermiques repose sur une utilisation optimale de la perte de charge pour générer les transferts de masse et de chaleur.

La compréhension des mécanismes du mélange turbulent et des transferts convectifs constitue un enjeu fondamental pour l'amélioration de l'efficacité énergétique des ERM, particulièrement pour des intérêts pratiques dans les industries chimiques, pharmaceutiques, et dans une moindre mesure alimentaires et cosmétiques. En effet, la sélectivité des réactions chimiques rapides dépend fortement de la manière dont les réactifs sont mélangés à l'échelle moléculaire (Baldyga et Bourne, 1999). Ce mécanisme est appelé le micromélange, ultime échelle de mélange par l'écoulement jusqu'à la diffusion moléculaire. *La cinétique du micromélange est un paramètre clé pour la sélectivité des réactions chimiques :* il faut que le micromélange soit achevé « avant » que les réactifs commencent à réagir.

Pour expliquer le mélange en régime turbulent, trois mécanismes parallèles peuvent être distingués : le macromélange, le mésomélange et le micromélange (Baldyga et Bourne, 1999) :

- **Macromélange :** c'est le mélange à l'échelle du mélangeur, responsable de la dispersion du fluide par les champs de vitesse moyenne. Un fluide dans un mélangeur se disperse sous l'effet de l'écoulement principal et se réparti finalement dans tout le volume du mélangeur. Cette étape de mélange est influencée par des tourbillons longitudinaux ou transversaux permanents qui contribuent aux transferts convectifs de masse et de chaleur. Pour quantifier le macromélange, on peut déterminer la distribution des temps de séjour (DTS) ou le nombre de Nusselt (*Nu*), pour les écoulements avec échanges thermiques.

- **Mésomélange :** ce mécanisme est lié à l'agitation turbulente de l'écoulement. Dans la région inertielle-convective du spectre turbulent se produit la désintégration des grands tourbillons par les fluctuations turbulentes, c'est-à-dire dans les nombres d'onde compris entre l'échelle intégrale κ_E et l'échelle de Kolmogorov κ_η : $\kappa_E < \kappa < \kappa_\eta$ (voir Figure 4). Le mésomélange donc est un processus d'homogénéisation par l'advection liée aux fluctuations de vitesse, et il se réfère généralement à l'échelle du jet, dans le cas de l'injection d'un fluide dans un écoulement principal (Baldyga et Bourne, 1999). Il peut être caractérisé par l'énergie cinétique turbulente k, ou par une composante dominante du tenseur de Reynolds $\overline{u_i u_j}$.

- **Micromélange :** c'est un processus se déroulant dans le sous-domaine visqueux-convectif $\kappa_\eta < \kappa < \kappa_B$ (κ_B est le nombre d'onde de l'échelle de Batchelor), échelle à laquelle le mélange s'effectue par un étirement laminaire proportionnel à $(\varepsilon/\upsilon)^{1/2}$ (Batchelor, 1953 ; Baldyga et Bourne, 1986 ; Baldyga et Pohorecki, 1995). A l'échelle de Batchelor la diffusion moléculaire et les déformations laminaires contribuent à parts égales au micromélange. La diffusion moléculaire devient dominante pour les échelles les plus petites (inférieures à l'échelle de Batchelor, $\kappa_B < \kappa$) et dissipe rapidement la variance de la concentration, entraînant ainsi l'homogénéisation des réactifs à l'échelle moléculaire. Le mécanisme limitant se situe lors de l'engouffrement dans les tourbillons de Kolmogorov, par conséquent, le micromélange dépend du taux de dissipation de l'énergie cinétique turbulente ε, ou de manière équivalente de l'échelle de Kolmogorov η.

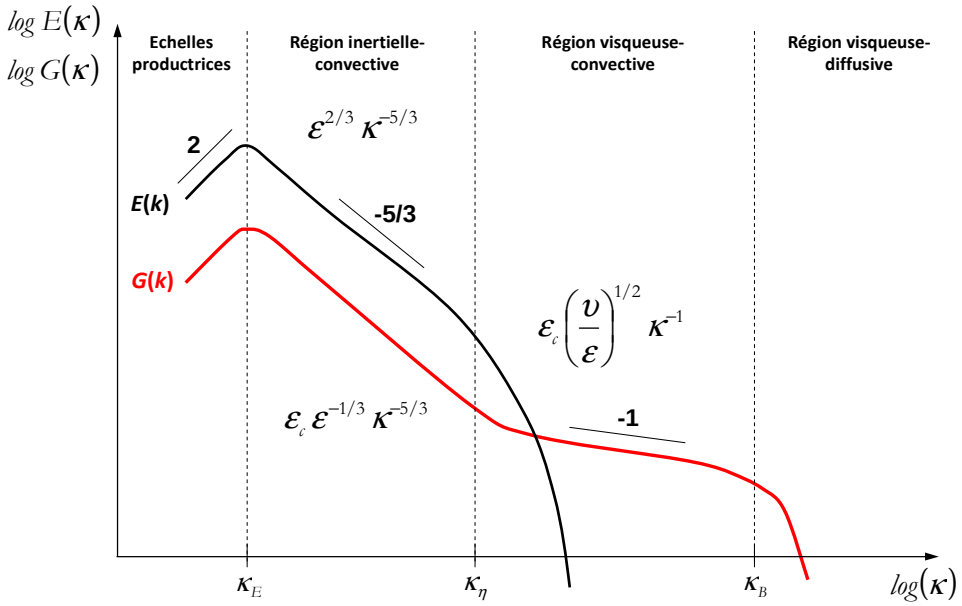

Figure 4 : Spectres classiques de l'énergie cinétique turbulente $E(\kappa)$ et de scalaire $G(\kappa)$ en fonction du nombre d'onde κ (pour des nombres de Schmidt>>1)

En écoulement laminaire le macromélange peut être amélioré par des systèmes d'advection chaotique qui rendent l'écoulement irrégulier (Aref 1984 ; Jones *et al.* 1989 ; Le Guer et Peerhossaini, 1991 ; Wiggins et Ottino, 2004 ; Carrière, 2007 ; Habchi *et al.*, 2009a). Le mélange aux échelles intermédiaires est liée aux éventuelles structures fractales "mésoscopiques" de l'écoulement (Muzzio *et*

al., 1992), tandis que le micromélange est dû à l'étirement local induit par les élongations et cisaillements associés aux plus petites structures (Baldyga *et al.*, 1998 ; Habchi *et al.*, 2009a).

Le micromélange est un processus local, il ne peut être satisfaisant sur l'ensemble du réacteur que lorsque les mécanismes de mélange aux plus grandes échelles, macro et mésomélange, ne sont pas limitants. En effet cela détermine l'environnement local qui permet ensuite l'homogénéisation moléculaire des réactifs (phase nécessaire à la mise en contact des réactifs).

Plusieurs méthodes existent pour la caractérisation du micromélange (Wallace, 2009 ; Aubin *et al.*, 2010). Parmi ces méthodes, la sonde chimique est une technique qui se base sur l'idée de la compétition entre les cinétiques de réactions chimiques et le temps de micromélange (Fournier *et al.*, 1996 ; Guichardon et Falk, 2000 ; Bourne, 2003). Elle repose sur le résultat chimique de l'injection locale d'un réactif dans l'écoulement. Des modèles physiques de micromélange permettent ensuite de relier le résultat de la réaction, *via* l'indice de ségrégation, au temps de micromélange, qui ne dépend que des conditions hydrodynamiques de l'écoulement.

Aubin *et al.* (2010) ont dressé un état de l'art sur ces différentes techniques utilisées pour la caractérisation du mélange, quatre types de méthodes chimiques sont répertoriées :

- **Réactions acide-base ou indicateur pH :** cette technique est basée sur le changement de couleur d'un indicateur pH contenu dans la solution de réactions acido-basiques. Cette méthode donne des informations qualitatives sur le mélange et nécessite un accès optique à l'écoulement. Pour des informations quantitatives, Branebjerg *et al.* (1996) ont estimé le temps de mélange en mesurant le temps pendant lequel la couleur continue à changer. Une autre estimation du temps de mélange est effectuée par Kockmann *et al.* (2006) en divisant la longueur sur laquelle il y a un changement de couleur par la vitesse débitante.

- **Réactions générant des produits colorés :** cette méthode utilise différentes réactions chimiques produisant la formation d'un produit coloré qui peut caractériser la qualité de mélange (Hessel *et al.*, 2003).

- **Suivi temporel ou spatial des concentrations :** le suivi de l'évolution temporelle et/ou spatiale de la concentration d'un ou de plusieurs réactifs peut être utilisé pour quantifier le mélange. Cette méthode est surtout utilisée pour mesurer le coefficient de variance dans des ERM ou dans des cuves agitées (Paul *et al.*, 2004). Cette technique permet d'obtenir des profils de concentration spatiale uni- ou bidimensionnels et l'évolution temporelle en un point. Le calcul des grandeurs moyennes et de la variance fournit le coefficient de ségrégation qui caractérise l'intensité du mélange (Hessel *et al.* 2003). Le principal but de cette méthode est d'obtenir l'épaisseur de striation à partir de profils de concentrations qui est ensuite liée au temps de mélange, paramètre quantitatif. La principale difficulté de cette technique est d'obtenir un accès optique à l'écoulement. L'inconvénient est qu'il n'y a pas d'informations sur le mélange dans la troisième direction de l'écoulement ce qui peut fausser l'estimation du temps de mélange en cas d'écoulements tridimensionnels.

- **Réactions compétitives-consécutives ou compétitives-parallèles :** cette méthode est basée sur le principe de la compétition entre le micromélange et les cinétiques d'un système de réactions chimiques (Fournier *et al.*, 1996 ; Guichardon et Falk, 2000 ; Bourne, 2003). Cette technique repose sur deux réactions consécutives ou parallèles ayant un réactif en commun noté *B* qui est injecté en défaut dans l'écoulement. Une des deux réactions est quasi-instantanée, et l'autre est rapide, avec un temps caractéristique proche du temps de micromélange. Cette méthode est représentée schématiquement dans la Figure 5. La qualité du mélange est mesurée avec un indice de ségrégation

X_S (ou taux de sélectivité), qui représente l'écart du mélange réel mesuré par rapport à un mélange parfait. En cas de micromélange parfait, c'est la réaction la plus rapide qui prédomine et le réactif commun *B* est totalement consommé par cette réaction, d'où $X_S = 0$. En cas de ségrégation totale, il existe des zones de surconcentration en *B* et seule la réaction la plus lente peut réagir avec *B*, ainsi $X_S = 1$. En résumé, moins le micromélange est bon, plus il y a de produits de la réaction la plus lente. Dépendant à la fois des conditions hydrodynamiques et des concentrations des réactifs mis en œuvre, ce paramètre X_S ne donne qu'une information qualitative sur le micromélange. Pour caractériser le micromélange d'une manière quantitative, un paramètre dépendant uniquement des conditions hydrodynamiques est nécessaire. Ce paramètre quantitatif est obtenu à partir de modèles physiques de micromélange comme le modèle d'engouffrement développé par Baldyga et Bourne (1989), ou le modèle d'incorporation développé par Fournier *et al.* (1996a), qui sont utilisés pour relier le taux de ségrégation X_S mesuré au temps de micromélange et ainsi au taux de dissipation de l'énergie cinétique turbulente ε.

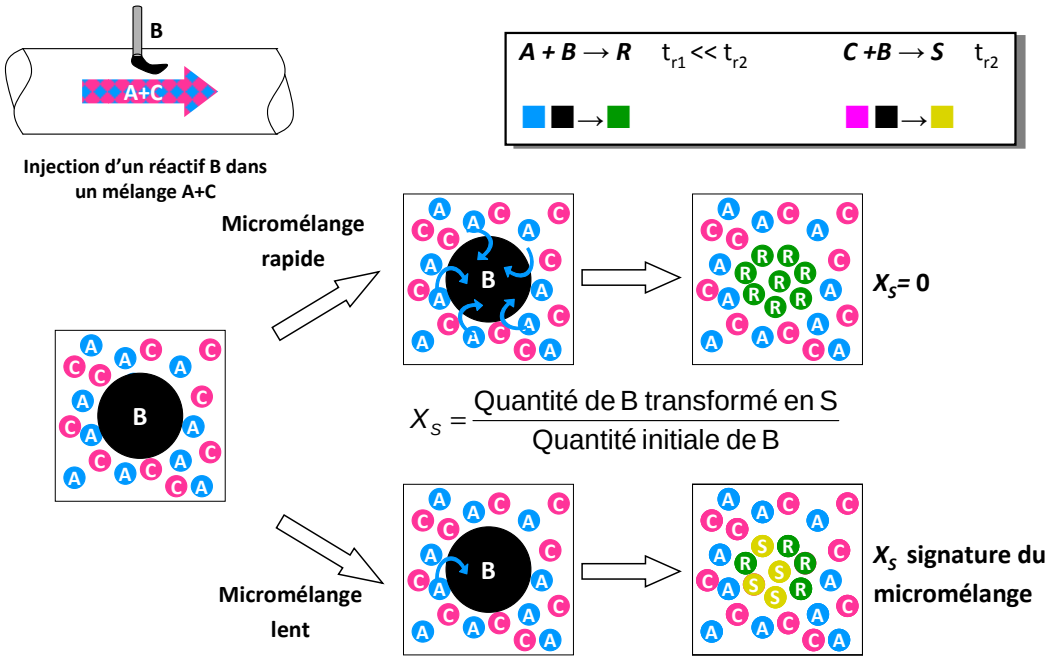

Figure 5 : Principe de la sonde chimique avec deux réactions compétitives-parallèles

Plusieurs systèmes réactionnels de sonde chimique existent dans la littérature (Bourne, 2003) dont les plus connus sont :

- le couplage du naphtol-1 et 2 avec l'acide sulfanilique diazoté, développé par Bourne *et al.* (1992),
- le système iodure-iodate dit de Villermaux-Dushman, utilisé par Fournier *et al.* (1996), et amélioré par Guichardon (Guichardon et Falk (2000)).

Dans ce travail, nous avons retenu la méthode iodure-iodate car elle est simple à utiliser, les cinétiques chimiques sont suffisamment connues, et a fait référence dans de nombreux travaux pour caractériser le mélange en batch ou dans des systèmes continus (Durandal (2007), Ferrouillat(2005) , Mohand Kaci (2007), Guichardon *et al.* (2000)).

La sonde chimique permet de déterminer un taux de ségrégation X_S qui peut être relié au temps de micromélange par un « modèle de micromélange », cette partie est détaillée dans la synthèse au paragraphe I.1.

Les objectifs et la démarche de la thèse sont articulés autour de deux axes :

- La méthodologie de sonde chimique afin de caractériser l'intensification des transferts dans les ERM

- l'étude de l'intensification et de l'efficacité énergétique d'un ERM spécifique, basé sur le principe des générateurs de vortex.

Dans une première partie de ce travail, nous nous intéressons à l'utilisation de la sonde chimique pour caractériser le micromélange dans des écoulements turbulents continus. Le choix des réactifs, de leurs concentrations, de la vitesse d'injection et d'autres paramètres détaillés dans la suite, n'est pas trivial (Mohand Kaci, 2007 ; Bourne, 2008 ; Kölbl, 2008). Ici, nous proposons une procédure expérimentale innovante pour obtenir des résultats quantitatifs absolus lorsque cela est possible. En nous appuyant sur la modélisation physique des différentes échelles du mélange, nous définissons un domaine de validité pour cette méthode, dépendant des conditions hydrodynamiques et des dimensions de l'aiguille d'injection. L'approche expérimentale développée ici et le domaine de validité peuvent être utilisés pour toute autre méthode de sonde chimique. Cette approche est appliquée au mélangeur statique HEV (high efficiency vortex), dont les résultats sont comparés à ceux obtenus à partir d'études antérieures numériques et expérimentales (Mohand Kaci, 2007). De plus, dans le cadre du projet ANR CP2D - RAPIC, la procédure expérimentale adaptative est appliquée pour caractériser le mélange dans des mini-canaux ondulés, pour une large gamme de nombre de Reynolds. Cette application nous a nettement montré l'intérêt de la procédure expérimentale adaptative par rapport aux procédures classiques.

La deuxième partie est consacrée à l'étude de l'intensification du mélange et des transferts thermiques dans un écoulement turbulent en présence de vorticité générée par des perturbateurs. Nous nous intéressons à l'intensification des transferts de masse et de chaleur dans une géométrie industrielle d'ERM. Pour cela, nous utilisons comme géométrie de base celle du mélangeur statique HEV largement étudié au sein du Laboratoire Thermocinétique de Nantes (Mokrani, 1997 ; Lemenand, 2002 ; Mohand Kaci, 2007). Dans le but d'explorer une possible intensification du mélangeur HEV, deux types de modifications géométriques sont testées : la première consiste à alterner tangentiellement les rangées de perturbateurs, l'une par rapport à l'autre, d'une manière périodique et d'un angle de 45°, et la deuxième modification consiste à inverser le sens de l'écoulement dans la géométrie de base. Les outils utilisés pour cette étude sont la LDA (laser Doppler velocimetry) et des simulations numériques utilisant le modèle de turbulence $k-\varepsilon$ standard (Launder et Spalding, 1974 ; Versteeg et Malalasekera, 1995) et le modèle RSM (Launder *et al.*, 1975 ; Gibson et Launder, 1978 ; Launder, 1989) en complément de la sonde chimique.

SYNTHESE DES TRAVAUX

I. Caractérisation du mélange par sonde chimique

I.1. Schéma réactionnel et modèle de micromélange

Cette partie porte sur le développement de la méthode de sonde chimique pour la caractérisation du micromélange dans les écoulements continus. La mesure du micromélange par la méthode chimique est basée sur la compétition entre le processus du mélange et deux ou plusieurs réactions chimiques de cinétiques différentes. Un bon micromélange favorise la réaction la plus rapide sur celle de cinétique plus lente, et inversement.

Nous utilisons la méthode iodure-iodate (Fournier *et al.* 1996 ; Guichardon et Falk 2000 ; Guichardon *et al.* 2000). Cette méthode se base sur un système réactionnel compétitif-parallèle qui est le couplage entre la réaction de neutralisation du borate (Eq. (1)) et la réaction de Dushman (1904) (Eq. (2)).

$$H_2BO_3^- + H^+ \leftrightarrow H_3BO_3 \tag{1}$$

$$5I^- + IO_3^- + 6H^+ \leftrightarrow 3I_2 + 3H_2O \tag{2}$$

La réaction (1) de temps caractéristique t_{r1}, est quasi-instantanée, quant à la réaction (2) elle est beaucoup plus lente $(t_{r2} >> t_{r1})$. Ces temps caractéristiques sont donnés dans les Eqs. (3) et (4).

$$t_{r1} = \frac{Min\left(\left[H_2BO_3^-\right], \left[H^+\right] \right)}{r_1} \tag{3}$$

$$t_{r2} = \frac{Min\left(\frac{3}{5}\left[I^-\right], 3\left[IO_3^-\right], \frac{1}{2}\left[H^+\right] \right)}{r_2} \tag{4}$$

les crochets [ ] représentent les concentrations des réactifs, r_1 et r_2 sont respectivement les cinétiques des réactions (1) et (2), données en particulier par (Guichardon *et al.* 2000) :

$$r_1 = K_1 \left[H_2BO_3^-\right] \left[H^+\right] \tag{5}$$

$$r_2 = K_2 \left[I^-\right]^2 \left[H^+\right]^2 \left[IO_3^-\right] \tag{6}$$

avec $K_1 = 10^{11}$ L/mol.s et K_2 est une fonction de la force ionique λ selon la définition de Palmer *et al.* (1984), explicitée par les Eqs. (7) et (8) (Guichardon *et al.*, 2000 ; Ferrouillat *et al.* 2006c) :

$$\lambda < 0.166\,\mathrm{M} \Rightarrow \log_{10}(K_2) = 9.28105 - 3.664\sqrt{\lambda} \tag{7}$$

$$\lambda > 0.166\,\mathrm{M} \Rightarrow \log_{10}(K_2) = 8.383 - 1.5112\sqrt{\lambda} + 0.23689\,\lambda \tag{8}$$

L'iode I_2 formé par la réaction de l'Eq. (2) peut réagir ensuite avec les ions iodure I^- pour donner les ions triiodure I_3^- suivant la réaction quasi-instantanée :

$$I_2 + I^- \rightarrow I_3^- \tag{9}$$

Pour mettre en œuvre la méthode, il faut ajouter en défaut stœchiométrique de l'acide sulfurique à un mélange initial de KI, KIO_3, H_3BO_3. Dans le cas d'un micromélange parfait, l'acide sulfurique injecté est totalement consommé par la réaction quasi-instantanée (1) et il n'y a pas formation de l'iode I_2. Quand le micromélange n'est pas parfait, des zones locales de surconcentration en H^+ sont présentes et réagissent suivant la réaction (2) pour donner de l'iode I_2, qui réagit ensuite avec les ions iodure I^- et donne des ions triiodure I_3^- suivant la réaction (9). Par conséquent, la sélectivité en I_2 est une mesure de la qualité du micromélange. En système ouvert, l'écoulement principal formant le mélange initial est caractérisé par un débit volumique Q_p, et Q_{H^+} est le débit d'acide injecté. L'indice de ségrégation est défini par le paramètre suivant (Fournier *et al.*, 1996 ; Ferrouillat *et al.* 2006c ; Mohand Kaci, 2007):

$$X_S = 2\,\frac{[I_2] + [I_3^-]}{[H^+]_0}\left(1 + \frac{Q_p}{Q_{H^+}}\right)\left(1 + \frac{[H_2BO_3^-]_0}{6\,[IO_3^-]_0}\right) \tag{10}$$

$X_S = 0$ pour un micromélange parfait, et $X_S = 1$ en cas de ségrégation totale. Les concentrations initiales et les débits étant connus, la détermination de X_S dépend des concentrations en I_3^- et I_2.

La concentration de l'ion iodate I_3^- peut être déterminée expérimentalement par spectrophotométrie dans le spectre visible car il confère une coloration orangée à la solution. En effet, d'après la loi de Beer-Lambert, l'absorption de la lumière A est proportionnelle à la concentration en I_3^- suivant l'Eq. (11).

$$[I_3^-] = \frac{A}{\xi\,\ell} \tag{11}$$

avec ℓ la longueur optique, ξ est le coefficient d'extinction molaire de I_3^- à 353 nm, égal à $\xi = 2597 \pm 148\ \mathrm{m^2/mol}$ (Mohand Kaci, 2007).

La concentration en I_2 se déduit de la conservation du nombre d'atomes d'iode :

$$[\mathrm{I}_2]^2 - \left(\frac{3}{5}[\mathrm{I}^-]_0 - \frac{8}{5}[\mathrm{I}_3^-]\right)[\mathrm{I}_2] + \frac{3}{5}\frac{[\mathrm{I}_3^-]}{K_B} = 0 \tag{12}$$

avec K_B la constante d'équilibre de la réaction (9) : elle est définie par Palmer *et al.* (1984) et dépend de la température du milieu réactionnel T (voir Mohand Kaci, 2007) :

$$\log_{10}(K_B) = \frac{555}{T} + 7.355 - 2.575\log_{10}(T) \tag{13}$$

Pour passer de la caractérisation qualitative, représentée par l'indice de ségrégation X_S, à la caractérisation quantitative, c'est-à-dire le temps de micromélange, nous utilisons le modèle d'engouffrement (modèle-E) développé par Baldyga et Bourne (1989). Le modèle-E est une simplification du modèle d'engouffrement-déformation-diffusion (modèle-EDD) (Baldyga et Bourne, 1984), puisque, pour des nombres de Schmidt faibles ($Sc < 4000$), les mécanismes d'étirement dans les échelles sub-Kolmogorov et de diffusion moléculaire sont rapides devant le mécanisme d'engouffrement dans les tourbillons de Kolmogorov. Le modèle-E se base donc sur l'hypothèse que le processus visqueux-convectif contrôle le mélange aux échelles proches de Kolmogorov η. Il a été démontré que ce modèle est le plus fiable pour la caractérisation du micromélange par rapport à d'autres approches physiques (Baldyga et Bourne, 1990 ; Durandal, 2007).

Selon ce modèle, un volume V dans le domaine de mélange augmente selon une cinétique de premier ordre avec un taux d'engouffrement E (Baldyga et Bourne, 1989) :

$$\frac{dV}{dt} = EV_0 \tag{14}$$

Le taux d'engouffrement est défini comme étant l'inverse du temps de micromélange t_m , et il est relié au taux de dissipation de l'énergie cinétique turbulente ε et à la viscosité cinématique υ selon l'équation (Baldyga et Bourne, 1989) :

$$E = \frac{1}{t_m} = 0.058\left(\frac{\varepsilon}{\upsilon}\right)^{\frac{1}{2}} \tag{15}$$

D'après l'Eq. (14), l'équation de conservation de masse pendant l'accroissement de la zone de mélange ayant une concentration c_i s'écrit :

$$\frac{dc_i}{dt} = E(< c_i > - c_i) + \mathrm{R}_i \tag{16}$$

où $< c_i >$ est la concentration de l'environnement extérieur de la zone de mélange en croissance, et R_i est le taux de formation de la substance i par la réaction chimique.

La solution du modèle-E est obtenue en résolvant l'Eq. (16) pour chaque réactif du système réactionnel, soit neuf équations non linéaires pour la méthode iodure-iodate.

Pour une valeur donnée du taux d'engouffrement, ou du temps de micromélange, ces équations sont intégrées temporellement en utilisant le schéma itératif Newton-Raphson jusqu'à ce que la concentration de l'acide sulfurique tende vers zéro. Le calcul du temps de mélange n'est donc pas direct, et pour le déterminer une courbe d'étalonnage $X_S = f(t_m)$ est établie par balayage de t_m (voir article n°1, Habchi *et al.* (2010a))[5].

Les calculs sont effectués sous MATLAB™, à l'aide du programme développé par Durandal (2007).

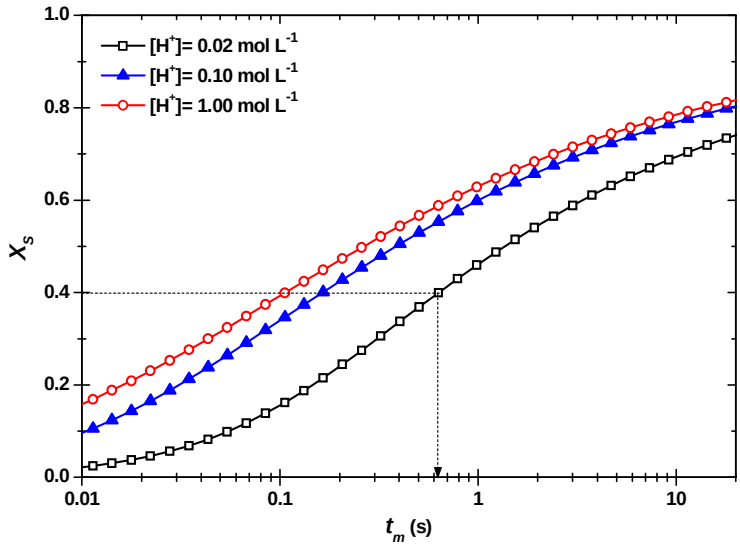

Figure 6 : Courbe d'étalonnage obtenue par le modèle d'engouffrement pour différentes concentrations initiales de l'acide sulfurique et pour les concentrations suivantes des réactifs principaux : $[KI]_0 = 0.01165$ mol L^{-1}, $[KIO_3]_0 = 0.00233$ mol L^{-1}, $[NaOH]_0 = [H_3BO_3]_0 = 0.001512$ mol L^{-1}, pour $\phi = 15$, le rapport entre la vitesse débitante et la vitesse d'injection de H^+

I.2. Boucle hydraulique et préparation des réactifs

Le milieu réactionnel initial de la sonde chimique formé de KI, KIO_3, H_3BO_3, NaOH et de l'eau désionisée dans une bombonne à résine (<5 µ Siemens), est contenu dans un réservoir de 200 litres (voir Figure 7). Ce réservoir est équipé d'une pompe immergée qui permet d'homogénéiser le mélange initial. La température dans le système est régulée à un niveau constant de 298 K par un échangeur de chaleur hélicoïdal dont la température est contrôlée par un thermostat (CRYTHERMOSTAT 71 HUBER).

Ce mélange est amené dans la section test par une pompe rotative à engrenage (LEROY-SOMER® VARMECA). Le débit principal est mesuré par une balance de précision et les données sont traitées par le logiciel Labview™.

Le système d'injection est constitué d'un pousse-seringue relié à un moteur pas à pas contrôlé par un régulateur de vitesse, qui permet l'injection locale de l'acide sulfurique dans la section test par

[5] Habchi *et al.*, Assessment of micro-mixing in turbulent flows by chemical probe, Chem. Eng. J., Submitted, 2010a.

une aiguille de diamètre intérieur 0,6 mm. Le positionnement de l'aiguille dans la section est déterminé par un système de déplacement avec une précision de 10 µm.

La section test est reliée à la boucle hydraulique par des tubes flexibles pour éliminer les fluctuations dues aux vibrations de la pompe. Elle est précédée par un pré-conditionneur qui est un tube droit de longueur 1,5 m pour assurer un profil de vitesse établi à l'entrée de l'ERM. Un post-conditionneur de 0,3 m de longueur est ajouté en sortie pour éliminer les effets de remontées de l'aval.

Les produits finaux du système réactionnel sont mesurés en continu dans un spectromètre (JENWAY 6505™) placé à la sortie du tube post-conditionneur. Ce spectromètre fonctionne pour un intervalle de longueur d'onde entre 190 nm et 1100 nm, une résolution de 0.1 nm et une bande de passage de 1.8 nm. L'intervalle de l'absorbance mesurable est entre 0 et 3 avec une précision de 0.001. La mesure de la concentration du I_3^- se fait dans le domaine UV (ultraviolet), qui traverse en continu un réservoir de recirculation en quartz avec une capacité volumique de 750 µl. La calibration du spectromètre se fait avec de l'eau distillée.

Les réactifs principaux (KI, KIO_3, H_3BO_3, $NaOH$) se présentent sous forme solide avec une pureté comprise entre 98% et 99.5%. Leurs poids sont mesurés par une balance analytique ayant une précision de 5 x 10^{-5} g. Les réactifs sont dissous dans de l'eau désionisée. Le mélange de H_3BO_3 et $NaOH$ est dissous en premier dans le réservoir initial pour que la solution tampon soit réalisée. Ensuite, KI et KIO_3 dissous sont ajoutés successivement à la solution tampon. On complète le mélange par de l'eau désionisée pour obtenir les concentrations demandées.

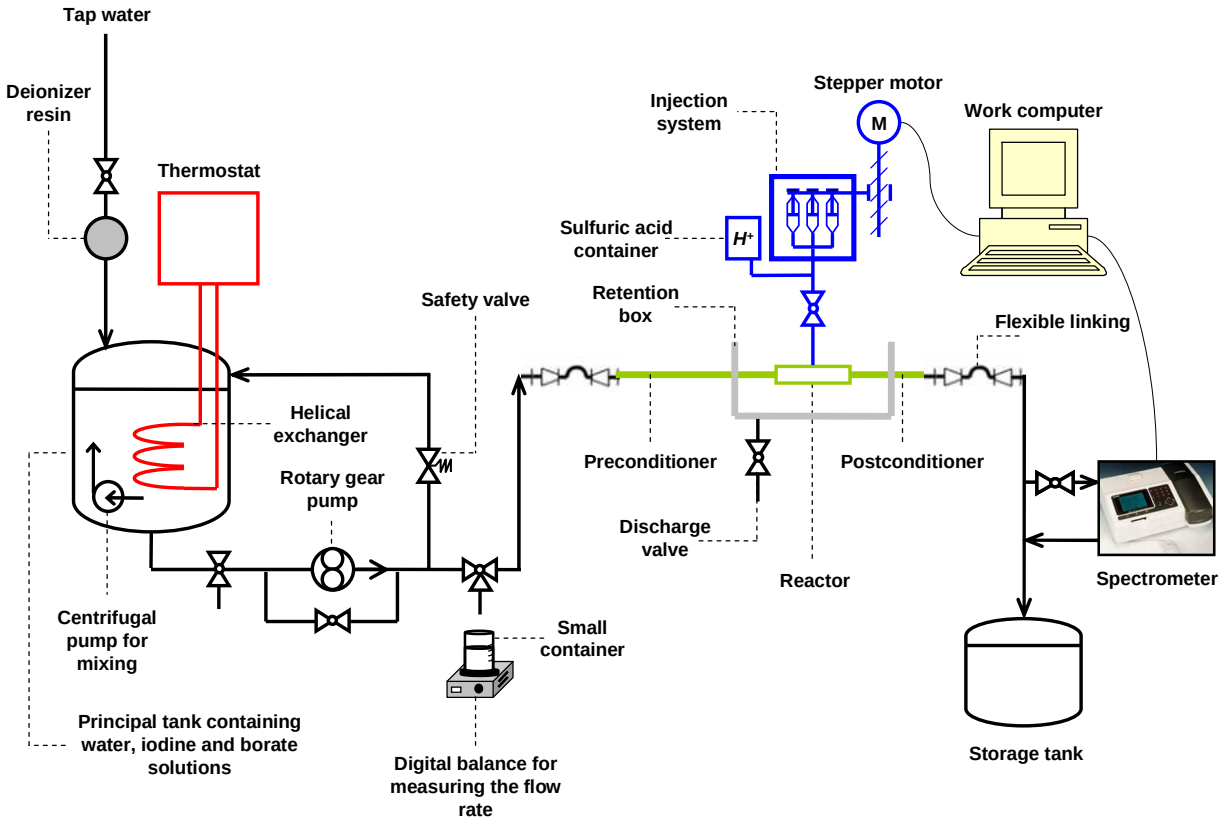

Figure 7 : Schéma de la boucle hydraulique

Il faut vérifier que le pH n'est pas inférieur au pH* (proche de 7) pour que la production de I_2 soit due seulement au micromélange suivant la réaction de l'Eq. (2), et non à la dissociation thermodynamique de l'iode. Les valeurs préconisées pour la solution initiale se situent dans l'intervalle 8.5<pH<9.5 (Guichardon *et al.*, 2000 ; Ferrouillat *et al.* 2006c ; Mohand Kaci, 2007).

Dans nos mesures le pH est mesuré à chaque fois avec un pH mètre digital.

I.3. Hydrodynamique de l'injection

La méthode de sonde chimique possède des limites d'utilisation qui sont dues essentiellement à la turbulence parasite de l'injection et au caractère local de la mesure qui dépendent des cinétiques chimiques. En effet, les réactions chimiques se déroulent dans une zone proche de l'injection : l'hydrodynamique due à l'injection du réactif secondaire peut dans certains cas affecter la sélectivité de la seconde réaction : le micromélange doit être dû uniquement à l'écoulement principal dans la zone d'injection. De plus, il faut que le micromélange soit mesuré juste au point d'injection et pour cela il faut que la seconde réaction soit achevée à une distance très courte de l'injection. Dans ce qui suit nous présentons ces deux enjeux d'une manière plus détaillée.

Deux mécanismes de mésomélange sont identifiés par Baldyga *et al.* (1997) : le premier est lié à la dispersion turbulente du filament d'injection dans le circuit principal, et le second à la réduction des agrégats injectés par la cascade turbulente.

Selon Batchelor (1953), Corrsin (1964), Baldyga et Bourne (1993), deux temps caractéristiques représentent les mécanismes de dispersion turbulente : le premier noté t_{D1} (Eq. (17)) caractérise la dispersion longitudinale du jet, et le deuxième noté t_{D2} (Eq. (18)) représente la dispersion radiale :

$$t_{D1} = \frac{Q_i}{W D_t} \tag{17}$$

$$t_{D2} = \frac{d^2}{4 D_t} \tag{18}$$

avec d le diamètre interne du tube d'injection, W la vitesse moyenne locale de l'écoulement principal au point d'injection et D_t la viscosité turbulente de l'écoulement principal, donnée par le modèle $k-\varepsilon$:

$$D_t = 0.1\frac{k^2}{\varepsilon} \tag{19}$$

où k est l'énergie cinétique turbulente.

Le débit d'injection est donné par :

$$Q_i = \frac{\pi d^2}{4} W_i \tag{20}$$

avec W_i la vitesse d'injection.

En remplaçant le rapport de vitesse W/W_i par ϕ et le coefficient de diffusion turbulente par l'Eq. (19) dans les Eqs. (17) et (18) on obtient :

$$t_{D1} = \frac{\pi}{0.4}\frac{d^2}{\phi}\frac{\varepsilon}{k^2} \tag{21}$$

$$t_{D2} = \frac{d^2}{0.4}\frac{\varepsilon}{k^2} \tag{22}$$

Les fluctuations de concentration autour de l'injection se désintègrent de l'échelle intégrale Λ vers les micro-échelles de Kolmogorov. Ce mécanisme est nommé mésomélange convectif-inertiel. D'après Batchelor (1953) et Corrsin (1964), le temps caractéristique de ce mécanisme est donné par :

$$t_C = 2\left(\frac{\Lambda^2}{\varepsilon}\right)^{1/3} \tag{23}$$

Si la quantité de mouvement de l'injection est faible par rapport à celle de l'écoulement principal, les particules injectées sont instantanément amenées à l'environnement hydrodynamique de l'écoulement principal. En nommant L_0 le rayon initial du filament injecté, le débit d'injection peut être évalué par $Q_i \approx \pi L_0^2 W$ (Baldyga *et al.*, 1997). Cette expression n'est pas tout à fait exacte, mais Baldyga *et al.* (1995) ont montré que l'hypothèse $\Lambda = L_0$ est correcte pour le « scale-up » des jets et des réacteurs agités. D'où :

$$\Lambda = \sqrt{\frac{\phi d^2}{4}} \tag{24}$$

En combinant les Eqs. (23) et (24), le temps caractéristique du mésomélange convectif-inertiel devient :

$$t_C = 1.26\left(\frac{d^2}{\phi\varepsilon}\right)^{1/3} \tag{25}$$

Ces trois temps caractéristiques doivent être plus petits que le micromélange pour ne pas être limitants. Pour les comparer avec le temps de micromélange, nous définissons trois temps adimensionnels : $\tau_1 = t_{D1}/t_m$, $\tau_2 = t_{D2}/t_m$ et $\tau_3 = t_C/t_m$. Ceux-ci fournissent un critère pour le domaine de validité dans lequel la sonde chimique peut être utilisée pour mesurer le micromélange :

$$\tau_1 = 0.145\pi\frac{d^2}{\phi\upsilon^{1/2}}\frac{\varepsilon^{3/2}}{k^2} \tag{26}$$

$$\tau_2 = 0.145 \frac{d^2}{\upsilon^{1/2}} \frac{\varepsilon^{3/2}}{k^2} \tag{27}$$

$$\tau_3 = 0.073 \frac{d^{2/3}}{\phi^{1/3} \upsilon^{1/2}} \varepsilon^{1/6} \tag{28}$$

Pour relier ces expressions aux paramètres de contrôle de l'expérience, il est possible de les exprimer en fonction de la vitesse débitante de l'écoulement principal $\overline{W}$ en utilisant l'analyse dimensionnelle :

$$k = C_k \overline{W}^2 \tag{29}$$

$$\varepsilon = C_\varepsilon \frac{\overline{W}^3}{D} \tag{30}$$

$$W = C_W \overline{W} \tag{31}$$

Les coefficients C_k et C_ε et C_W ne sont pas constants et dépendent de la position dans l'écoulement principal. Ces coefficients peuvent être déterminés expérimentalement ou à partir de simulations numériques. En substituant dans les Eqs. (26) et (28) on obtient :

$$\tau_1 = \left(0.145 \pi \frac{C_\varepsilon^{3/2}}{C_k^2 D^{3/2} \upsilon^{1/2}} \right) \frac{d^2}{\phi} \overline{W}^{1/2} \tag{32}$$

$$\tau_2 = \left(0.145 \frac{C_\varepsilon^{3/2}}{C_k^2 D^{3/2} \upsilon^{1/2}} \right) d^2 \overline{W}^{1/2} \tag{33}$$

$$\tau_3 = \left(0.074 \frac{C_\varepsilon^{1/6}}{D^{1/6} \upsilon^{1/2}} \right) \frac{d^{2/3}}{\phi^{1/3}} \overline{W}^{1/2} \tag{34}$$

Une étude paramétrique peut être menée à partir de ces trois critères pour étudier les effets de paramètres extérieurs sur la validité de la méthode chimique pour la caractérisation locale du micromélange, à savoir les trois paramètres irréductibles que sont le rapport des vitesses, la vitesse débitante et le diamètre d'aiguille, respectivement ϕ, $\overline{W}$ et d.

I.4. Ajustement de la concentration

Pour des temps de micromélange très inférieurs au temps de réaction, le micromélange est très efficace, et dans ce cas il n'y a pas d'influence du champ hydrodynamique de l'écoulement sur l'indice de ségrégation X_S . En effet les réactifs sont homogénéisés rapidement et la seconde réaction n'a pas le « temps » de former l'iode, de sorte que le X_S reste constant au niveau 0 dans tous les cas où $t_m << t_{r2}$. D'autre part, pour $t_m >> t_{r2}$, la sélectivité de la sonde chimique est régie par la cinétique de la seconde réaction, et l'effet de l'écoulement sur X_S est également faible. De ce fait, la meilleure sensibilité de la sonde chimique est obtenue quand $t_{r2} = O(t_m)$.

Une procédure expérimentale est proposée ici pour ajuster les concentrations des réactifs afin de respecter au mieux la condition $t_{r2} = t_m$. Pour cela, la solution la plus « simple » dans un premier temps consisté à modifier la concentration de l'acide sulfurique, contenu dans un réservoir séparé. Si l'écoulement qu'on souhaite caractériser est dans le domaine de validité de la sonde chimique, cette procédure consiste à effectuer des mesures de X_S pour différentes concentrations, à partir desquelles on peut obtenir les temps de micromélange correspondants. En traçant t_{r2} en fonction de la concentration de H^+ selon la définition de l'Eq. (4), il suffit alors de retenir la concentration de H^+ à l'intersection des deux courbes, qui est celle qui donne la meilleure précision de mesure de X_S .

I.5. Critère sur le volume de mesure

Le micromélange étant un mécanisme local, il est nécessaire que la seconde réaction soit achevée à une distance très proche de l'injection. Cette « longueur de réaction » peut être évaluée par $L_{r2} \approx W t_{r2}$, t_{r2} étant le temps de la deuxième réaction. Il faut alors que $L_{r2} = o(\Lambda)$, avec Λ l'échelle intégrale. Cela montre que le temps de la deuxième réaction peut ou doit être adapté pour le contrôle du volume de mesure, c'est-à-dire que t_{r2} doit être inférieur à L_{r2}/W pour respecter la condition d'une mesure locale.

Par ailleurs, il est également possible d'augmenter la valeur t_{r2} bien au-delà de cette limite, de manière à caractériser le mélange dans une région donnée, voire le mélange à l'échelle du réacteur (voir § I.8).

I.6. Procédure expérimentale adaptative

L'organigramme donné dans la Figure 8 résume l'ensemble de la procédure expérimentale adaptative à suivre lors de l'utilisation de la sonde chimique pour la caractérisation du micromélange (voir l'article n°1 : Habchi *et al.* (2010a)).

Cette procédure adaptative se déroule en trois étapes :

- vérification de l'hydrodynamique de l'injection (§ I.3)
- ajustement de la concentration du réactif H^+ (§ I.4)
- vérification du volume de mesure (§ I.5)

La première étape ne dépend que de l'hydrodynamique d'injection, quel que soit le système chimique utilisé, et les deux autres étapes sont des paramètres de la sonde chimique, qui peuvent être adaptés en modifiant les concentrations des réactifs. Dans la première étape nous avons besoin d'une

estimation de k, ε et W pour initialiser la procédure, or ε est justement la variable de sortie des mesures.

Nous proposons d'utiliser les expressions de Hinze (1975) pour une turbulence pleinement développée dans un tube droit, données par les équations suivantes :

$$k = \frac{3}{2}\left(\overline{W}\, I\right)^2 \tag{35}$$

$$\varepsilon = 2.35\frac{k^{3/2}}{D} \tag{36}$$

avec l'intensité de turbulence $I = 0.16\, Re^{-1/8}$

La vitesse locale W peut être estimée égale à la vitesse débitante $\overline{W}$ pour des points d'injection « éloignés » de la paroi, et selon la loi linéaire de sous-couche visqueuse ou de la zone logarithmique pour des points de coordonnée $y^+ < 100$.

A la fin du processus, si la valeur de ε « mesuré » est trop éloignée de la valeur initiale estimée $\hat{\varepsilon}$ on reboucle la procédure en faisant varier k, ε.

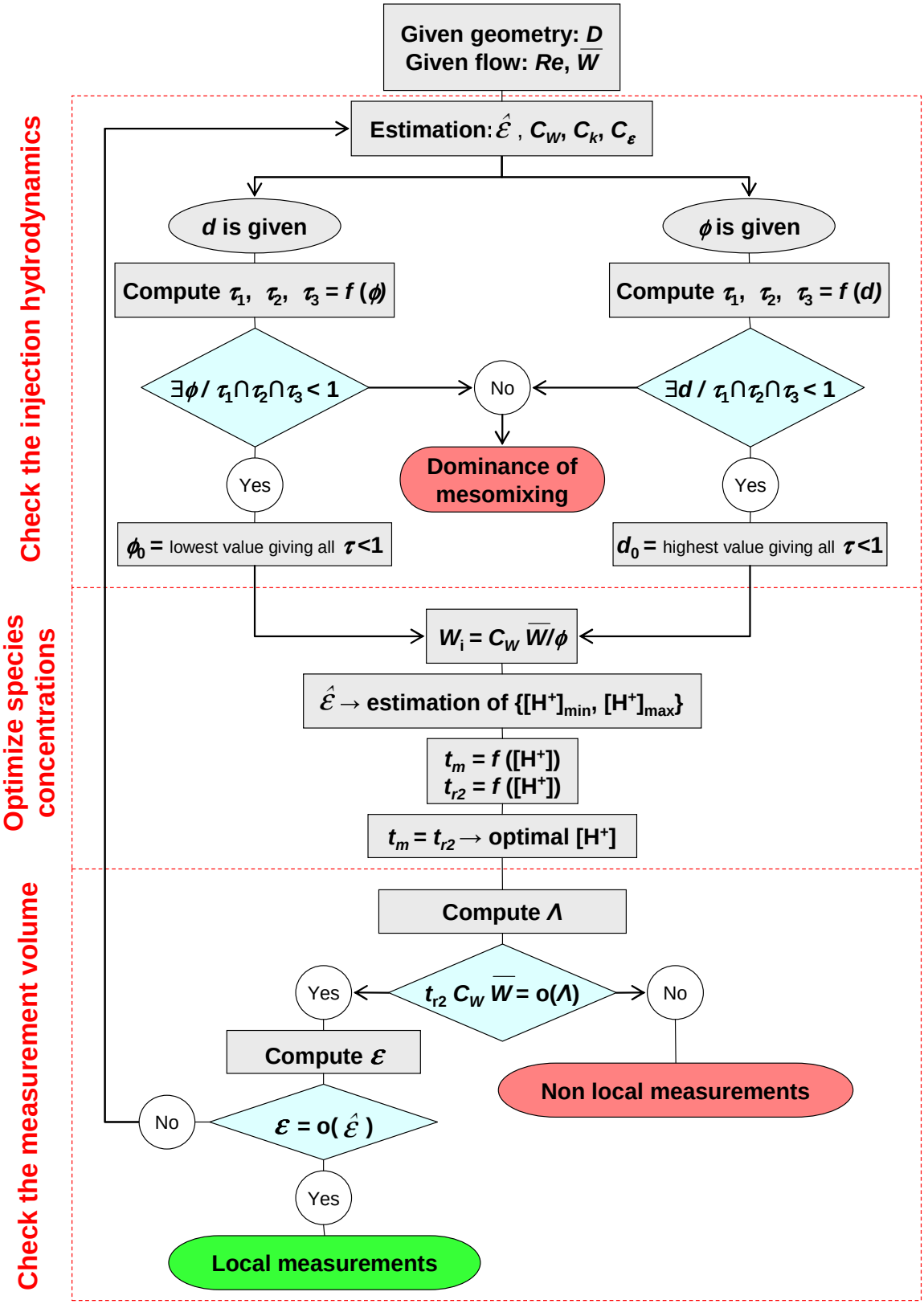

Figure 8 : Algorithme de mise en œuvre de la procédure expérimentale adaptative de la sonde chimique pour la mesure du micromélange

I.7. Procédure adaptative pour caractériser le micromélange

I.7.1. Géométrie étudiée et points de mesures

La sonde chimique iodure-iodate est appliquée au mélangeur HEV (high efficiency vortex (Chemineer, 2008)). Ce mélangeur est constitué d'un tube droit de section circulaire de 20 mm de diamètre, dans lequel plusieurs rangées de générateurs de vorticité sont fixées à la paroi. Chaque rangée est composée de quatre générateurs de tourbillons trapézoïdaux, diamétralement opposés et inclinés de 30° relativement à la paroi (voir Figure 9). Les détails concernant la géométrie de ce mélangeur et les dimensions du générateur de tourbillons sont donnés dans l'Annexe C. L'écoulement dans cette géométrie présente plusieurs régions de niveaux de turbulence différents (voir annexe B) (Lemenand *et al*, 2003, 2005 ; Dong and Meng, 2004). Ainsi, la procédure présentée au § 1.4 concernant le domaine de validité et la procédure adaptative peuvent être testés sur une large gamme de conditions hydrodynamiques et de niveaux de turbulence.

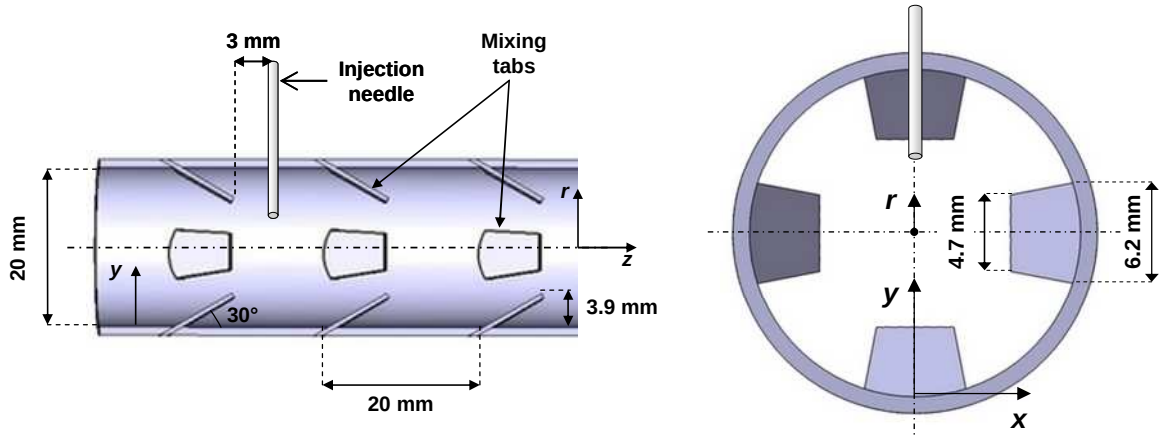

Figure 9 : (a) Section transversale de la section test sur les trois premières rangées, (b) Section perpendiculaire au sens de l'écoulement montrant les dimensions des générateurs de tourbillons

Suivant cette idée, trois positions de mesure situées à 3 mm en aval de l'ailette dans son plan de symétrie sont prises en considération, dont la Figure 10 montre le schéma de structure de l'écoulement :

- **B** : région au centre du tube (bulk region) avec les plus faibles niveaux de turbulence et positionnée à $y/R = 1$ (y est la position normale à la paroi et R le rayon du tube).

- **S** : zone située dans la couche de cisaillement (shear layer) développée à partir de l'extrémité haute de l'ailette et à $y/R = 0.4$. Cette région est caractérisée par un grand niveau de turbulence du à la présence de gradients de vitesse élevés.

- **W** : région située dans la zone de sillage (wake region) à $y/R = 0.2$ présentant un niveau de turbulence modérée.

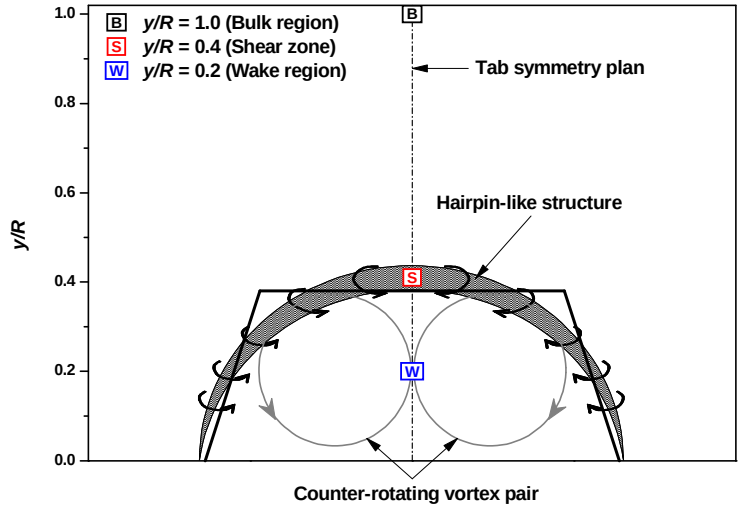

Figure 10 : Schéma de la structure de l'écoulement sur une section en aval d'un générateur de tourbillon trapézoïdal et les positions des points de mesure

Les caractéristiques hydrodynamiques de ces points sont décrites dans le Tableau 1 :

Point	Région	Position	Vitesse	Turbulence
B	Centre	y/R= 1,0	élevée	faible faibles gradients
S	Cisaillement	y/R= 0,2	modérée	élevée gradients élevés
W	Sillage	y/R= 0,4	faible	modérée faibles gradients

Tableau 1 : Caractéristiques hydrodynamiques des points de mesure

Les paramètres hydrodynamiques locaux (Eqs. (32)-(34)) pour les trois points de mesures B, S et W sont récapitulés dans le Tableau 2 pour une vitesse débitante $\overline{W} = 0{,}625\ \mathrm{m\,s^{-1}}$.

Positions de mesures	C_k	C_ε	C_W	k ($\mathrm{m^2\,s^{-2}}$)	ε ($\mathrm{m^2\,s^{-3}}$)	W ($\mathrm{m\,s^{-1}}$)
Bulk "**B**" $(y/R = 1.0)$	$4{,}42\times10^{-3}$	$4{,}21\times10^{-4}$	0,983	$1{,}73\times10^{-3}$	$5{,}14\times10^{-3}$	0,614
Shear "**S**" $(y/R = 0.4)$	0,24	0,70	0,169	$9{,}50\times10^{-2}$	8,60	0,106
Wake "**W**" $(y/R = 0.2)$	0,13	0.,51	0,312	$5{,}07\times10^{-2}$	6,20	0,195

Tableau 2 : Paramètres hydrodynamiques locaux pour les trois points de mesures obtenus à partir des simulations numériques pour Re= 12500

I.7.2. Hydrodynamique de l'injection

Dans notre cas, le diamètre d'injection est fixé à 0,6 mm, et un nombre de Reynolds fixé à 12500 : le seul paramètre qui peut être variable ici est le rapport de vitesse $\phi = W / W_i$. La Figure 11 représente les temps caractéristiques τ_1, τ_2 et τ_3, et indique dans la zone hachurée pour quelles conditions les trois temps caractéristiques sont inférieurs à 1 (τ_1, τ_2 et $\tau_3 < 1$).

Dans la Figure 11 (a), pour la position de mesure B, on peut observer que le rapport de vitesse ϕ_0 qui définit le domaine de validité tend vers 0 pour les conditions nominales, ce qui signifie que le micromélange est toujours le processus limitant en ce point. Dans le cas présent, les mesures sont effectuées avec ϕ = 7,61, ce qui est bien dans le domaine de validité.

Dans la Figure 11 (b), pour la position de mesure S, le rapport de vitesse nominale est $\phi_0 = 0{,}65$, et nos mesures sont effectuées à ϕ = 1,31 bien situé dans le domaine de validité.

La Figure 11 (c) montre l'évolution des rapports de temps caractéristiques pour la position W. On peut observer que τ_2 est toujours supérieur à 1 : pour ces conditions, quel que soit le rapport de vitesses ϕ, la sonde chimique ne peut pas être utilisée, sauf si le diamètre de l'aiguille d'injection est réduit pour que τ_2 devienne inférieur à 1.

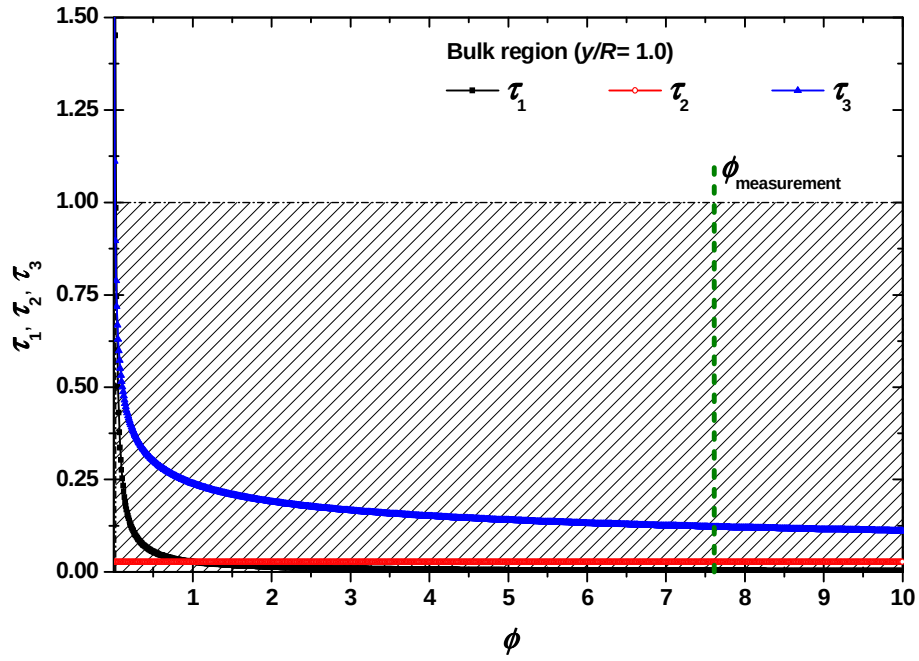

(a)

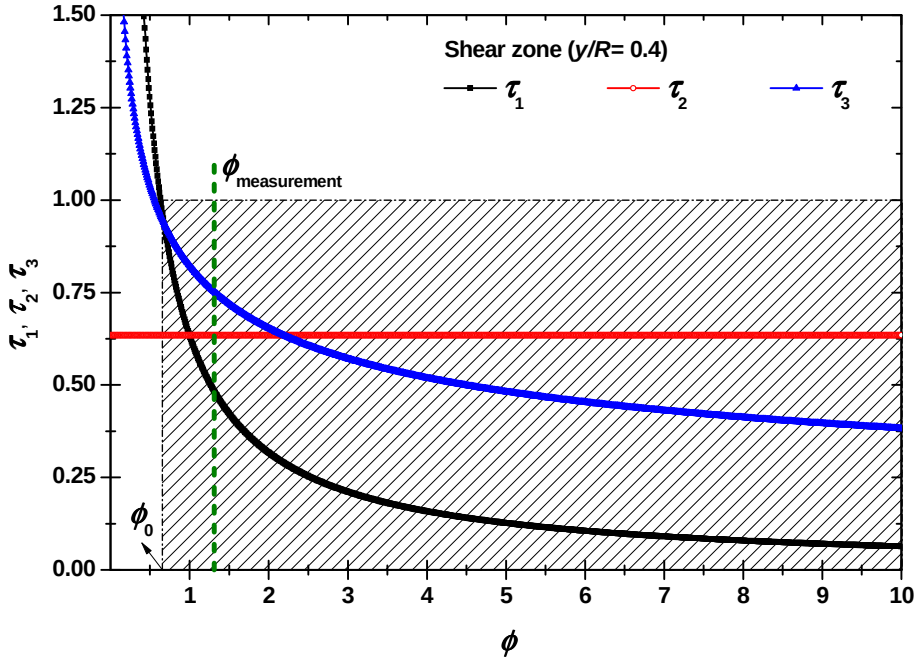

(b)

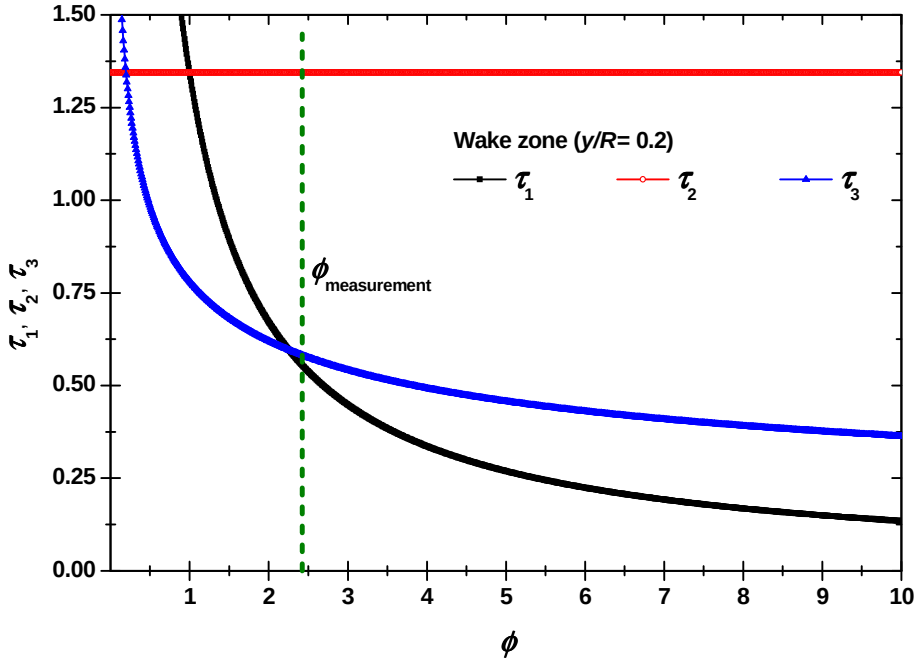

(c)

Figure 11 : Temps caractéristiques en fonction du rapport de vitesses ϕ pour les positions (a) B à $y/R = 1{,}0$, (b) S à $y/R = 0{,}4$, (c) W à $y/R = 0{,}2$

I.7.3. Ajustement de la concentration

Nous avons travaillé avec les mêmes les concentrations des réactifs définies par Mohand Kaci (2007) et présentés dans le Tableau 3. Seule la concentration de l'acide sulfurique H^+ est modifiable : elle est adaptée en fonction du niveau de turbulence selon la procédure expliquée au § I.6.

Réactifs	H_3BO_3	NaOH	KIO_3	KI^-	H^+
Concentrations (10^{-3} mol.L^{-1})	1,512	1,512	2,33	11,65	*variable*

Tableau 3 : Concentrations des réactifs pour la détermination du micromélange dans le mélangeur HEV

L'intervalle des concentrations de H^+ peut être estimé à partir des niveaux de la dissipation d'énergie cinétique turbulente dans l'écoulement obtenue à partir de la mesure de la perte de charge. Par exemple, connaissant l'ordre de grandeur de la dissipation d'énergie cinétique turbulente dans un écoulement donné, 10 m^{2}s^{-3}, le temps de micromélange sera, suivant l'Eq. (15), de 5,5 ms. Le critère $t_m = t_{r2}$ donne alors l'ordre de grandeur de t_{r2} et donc celui de la concentration en H^+ qui est environ 0,5 mol L^{-1} dans cet exemple. Nous proposons que l'intervalle des valeurs de $[H^+]$ soit défini par un facteur 5 généralement suffisant pour les écoulements en continu. Alors dans cet exemple on obtient $0.5 < [H^+] < 2.5$ mol L^{-1}. L'intersection des courbes de variation de t_m et t_{r2} indique ensuite la valeur optimale de $[H^+]$. Ici, la concentration de H^+ est balayée dans l'intervalle $0.2 < [H^+] < 1$ mol L^{-1} pour effectuer les mesures aux trois points B, S et W (voir Figure 12).

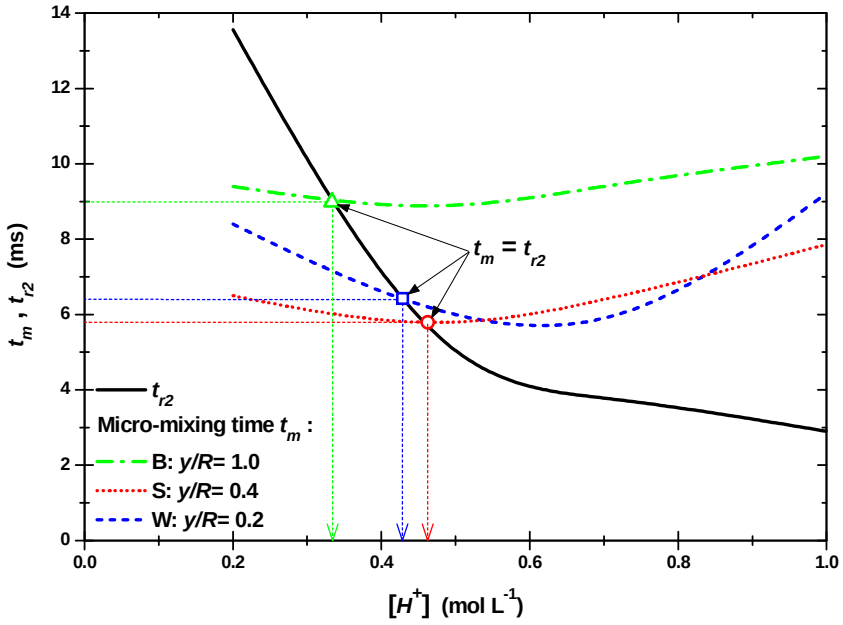

Figure 12 : Détermination de la concentration de H^+ pour $t_{r2} = t_m$ dans les trois points de mesures B, S et W pour $Re = 12500$

I.7.4. Volume de mesure

Selon les justifications données au § I.5, nous étudions la comparaison du volume de mesure $L_{r2} = W\, t_{r2}$ par rapport à l'échelle intégrale.

Pour la position B, la dissipation de l'énergie cinétique turbulente est très faible (5×10^{-3} m^2s^{-3}), ce qui donne un temps de micromélange de 0,24 s. Comme la vitesse locale est de 0,614 ms^{-1}, le volume de mesure est 14,77 cm qui est bien supérieur à l'échelle de mésomélange qui vaut 1,10 cm. A cause d'un volume de mesure trop important, la détermination du micromélange (mesure locale) dans le centre du réacteur est impossible par la sonde chimique.

Pour la position S dans la couche de cisaillement, $\varepsilon = 8{,}6\ m^2s^{-3}$ et le temps de micromélange correspondant est 5,88 ms, ce qui donne une longueur de mesure de 0,62 mm. L'échelle de mésomélange est 0,46 mm, ce qui indique que la réaction chimique prend place localement et la détermination de la valeur locale de ε est possible.

Au point W, nous avons vu que la sonde chimique n'est en tout état de cause pas valide (le diamètre de l'injection empêche de se positionner dans un domaine de validité) l'analyse du volume de mesure n'est alors pas menée.

I.7.5. Discussion

La Figure 13 permet de comparer les résultats de mesures chimiques avec la procédure adaptative à ceux obtenus par Mohand Kaci (2007) utilisant la procédure classique avec $[H^+] = 1\ mol\ L^{-1}$, et avec « l'arbitrage » de résultats obtenus par mesures LDA et par simulation numérique présentés dans les articles N°3, 4 et 5.

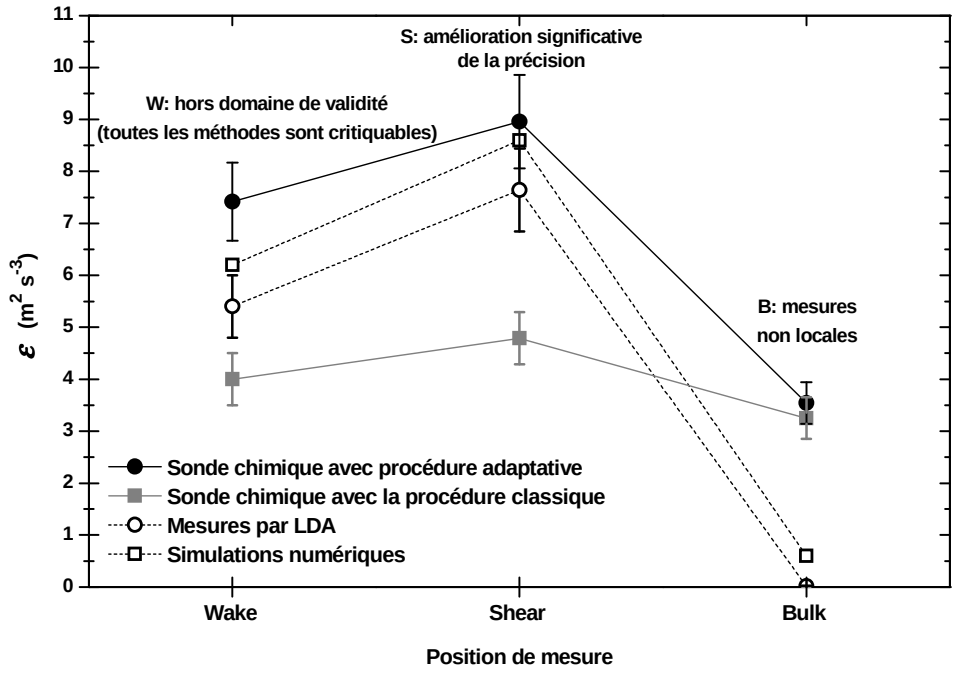

Figure 13 : Comparaison de la dissipation de l'énergie cinétique turbulente obtenue par différentes méthodes

On remarque l'utilité de la procédure adaptative proposée dans ce travail puisqu'on obtient des résultats sensiblement plus précis (5% au lieu de 20% précédemment) par rapport à ceux obtenus par mesures de LDA et simulations numériques pour la position S : la seule en situation de satisfaire toutes les conditions de validité de la sonde chimique.

Au point B, malgré de bonnes conditions pour l'hydrodynamique d'injection, il est impossible de faire des mesures locales. Aucune des deux procédures de sonde chimique ne donne de résultat satisfaisant car le temps de micromélange est comparable au temps de séjour, ce qui se produit quand la turbulence est faible et la vitesse élevée (voir le Tableau 1).

Au point W proche de la paroi, hors du domaine de validité (voir § I.7.2), les résultats ne sont pas non plus améliorés, mais à la fois les mesures de LDA et la simulation numérique peuvent être critiquables dans cette zone de vitesse moyenne nulle. Pour pouvoir effectuer des mesures fiables au point W il faudrait diminuer le diamètre d'injection d pour obtenir un temps caractéristique $\tau_2 < 1$ (voir Figure 11 (c)).

I.8. Procédure adaptative pour caractériser le mélange

Il s'agit de comparer le mélange global par la méthode de sonde chimique dans deux réacteurs à canaux ondulés de section rectangulaire (2×4 mm), de même diamètre hydraulique $D_h = 2.67$ mm , et dont les parois présentent une forte rugosité hydraulique afin d'intensifier la turbulence dans la gamme de nombre de Reynolds visée.

I.8.1. Description des géométries

La première géométrie, dite « canal ondulé », représentée dans la Figure 14 (a) présente 12 coudes arrondis de rayon de courbure $R_C = 10.50$ mm . Les positions d'injection de l'acide sulfurique P_i sont indiquées par des flèches rouges. Cette géométrie est utilisée pour mettre en place des mesures locales (micromélange) et des mesures globales (macromélange). La deuxième géométrie, le « canal zigzag » de la Figure 14 (b), est constituée de 27 coudes vifs à 90° de rayon de courbure $R'_C = 1.50$ mm . Dans cette géométrie un seul point d'injection est utilisé dans le premier coude.

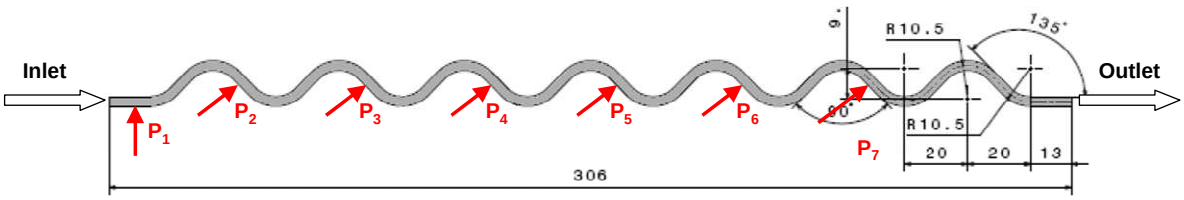

(a)

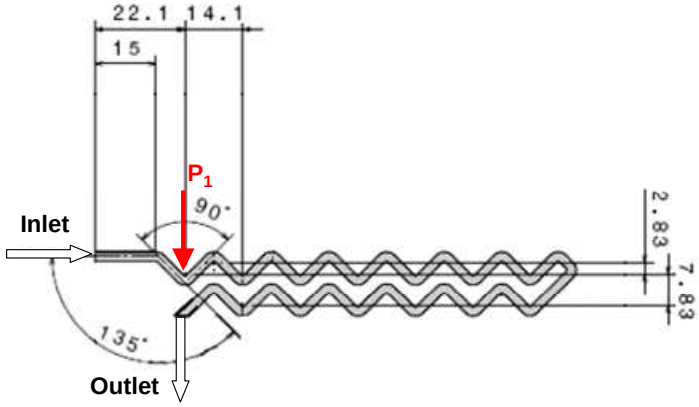

(b)

Figure 14 : Géométries étudiées et points de mesures P_i (a) « canal ondulé » à coudes arrondis, (b) « canal zigzag » à coudes vifs

I.8.2. Mesures de l'indice de ségrégation par la procédure adaptative

Des mesures locales sont effectués en plusieurs points d'injection tout le long du « canal ondulé » afin de caractériser le micromélange (voir l'article n°2 : Habchi *et al.*, 2010b)[6]. Nous avons montré qu'en utilisant une concentration d'acide sulfurique faible propre aux mesures locales, nous obtenons un X_S constant quelle que soit la position d'injection, et quel que soit le nombre de Reynolds. Cela est conforme à l'idée que la turbulence de paroi est faiblement dépendante du nombre de Reynolds, et fortement dépendante de la rugosité de paroi. L'effet du nombre de Reynolds est non détectable par la mesure de la sonde chimique, dans la gamme des nombres de Reynolds utilisés. Pour tenter de dégager les propriétés de mélange intrinsèques de ces deux réacteurs, nous présentons ici les résultats issus de mesures globales dans les deux géométries avec la procédure adaptative, permettant de caractériser le mélange à l'échelle du réacteur. La concentration de l'acide sulfurique injecté à l'entrée est calculée de façon à obtenir un volume de mesure correspondant à la taille du réacteur pour les différents nombre de Reynolds : $L_{r2} \approx t_{r2} W \approx$ constant égale à la longueur du réacteur (35 cm). Les concentrations des réactifs choisis sont récapitulées dans le Tableau 4.

Réactifs	H_3BO_3	NaOH	KIO_3	KI^-	H^+
Concentrations (10^{-3} mol L^{-1})	0.50	0.50	0.30	1.50	*variable*

Tableau 4 : Concentrations des réactifs pour les mesures de macromélange dans les deux géométries ondulées

Nous montrons dans l'article n°2 (Habchi *et al.*, 2010b) que la concentration en H^+ doit varier suivant l'expression suivante en fonction du nombre de Reynolds :

$$[H^+]_0 = 2.04\times10^{-4}\, Re^{0.975} \quad \text{pour} \quad 0 < Re < 4000 \tag{37}$$

[6] Habchi *et al.*, A new adaptive procedure for using chemical probes to characterize mixing, Chem. Eng. Sci., Submitted, 2010b

La Figure 15 montre l'indice de ségrégation dans les deux géométries en fonction du nombre de Reynolds. On peut observer que X_S diminue « rapidement » avec le nombre de Reynolds. En effet, plus la turbulence est intense, plus la qualité de mélange est bonne, ce qui est marqué par une diminution de X_S. La nouvelle procédure adaptative corrige la variation inexplicable de X_S qui était obtenue par la procédure classique (voir l'article n°2 : Habchi *et al.*, 2010b) et peut être utilisée pour comparer deux ERM similaires.

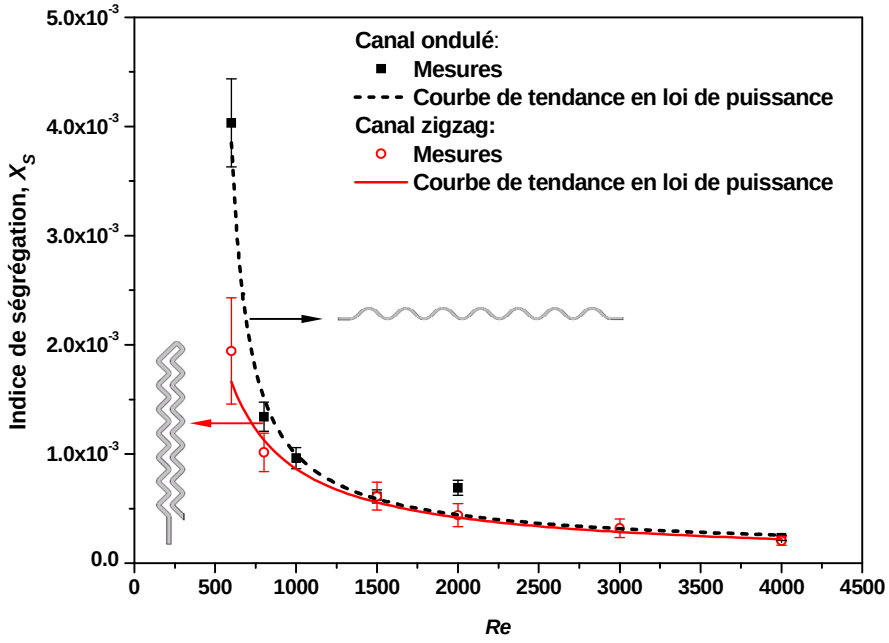

Figure 15 : Indice de ségrégation dans les deux géométries en fonction du nombre de Reynolds

I.8.3. Calcul du temps de mélange

Nous proposons de calculer le temps de mélange à partir des mesures précédentes de X_S dans les deux canaux ondulés : le nombre de Reynolds varie de 600 à 4000, le régime d'écoulement est donc soit laminaire soit turbulent.

En régime d'écoulement turbulent, le temps de micromélange t_m est proportionnel à $\varepsilon^{-1/2}$ d'après les modèles de Baldyga et Bourne (1989, 1999) et Fournier *et al.* (1996b). L'analyse dimensionnelle montrant que $\varepsilon \approx \overline{W}^3 / D_h$, on peut en déduire que t_m est proportionnel à $\overline{W}^{-3/2}$ et ainsi à $Re^{-3/2}$.

En régime laminaire, nous suivons le modèle proposé récemment par Falk et Commenge (2010), basé sur l'efficacité de l'étirement dans les écoulements laminaires. Baldyga et Bourne (1984) proposent de calculer le temps de mélange en écoulement laminaire suivant l'expression :

$$t_m = \frac{\operatorname{arcsinh}\left(\dfrac{0{,}76\,\dot{\gamma}\,\delta_0}{D_m}\right)}{2\,\dot{\gamma}} \tag{38}$$

avec δ_0 l'épaisseur initiale de striation qui est l'échelle spatiale de ségrégation avant le mélange, c'est-à-dire l'échelle d'injection de H^+, D_m la diffusion moléculaire, et $\dot{\gamma}$ le taux de cisaillement moyen dans le volume de l'écoulement. L'approche de Falk et Commenge (2010) se base sur une détermination approchée de $\dot{\gamma}$ par la loi de Hagen-Poiseuille, avec :

$$\varepsilon = \frac{32\upsilon\overline{W}^2}{D_h^2} \tag{39}$$

$$\dot{\gamma} = \left(\frac{\varepsilon}{2\upsilon}\right)^{\frac{1}{2}} \tag{40}$$

Falk et Commenge (2010) ont développé ce modèle pour l'étude du mélange dans des micromélangeurs dans lesquels la circulation de l'écoulement principal et l'injection de l'acide sulfurique se font dans des canaux de mêmes diamètres hydrauliques. Ainsi Falk et Commenge (2010) posent $\delta_0 = D_h$.

Dans la présente étude l'épaisseur de striation initiale est estimée égale au diamètre de l'aiguille d'injection de l'acide sulfurique d, d'où l'expression du temps de mélange pour notre cas :

$$t_m = \frac{D_h}{8\overline{W}}\operatorname{arcsinh}\left[3.04\left(\frac{d}{D_h}\right)^2 Pe\right] \tag{41}$$

avec $Pe = W_m D_h / D_m$ le nombre de Péclet.

Puisqu'une partie de l'énergie mécanique est consommée pour le mélange, Falk et Commenge (2010) utilisent le concept de l'efficacité énergétique proposé par Ottino *et al.* (1979) pour définir une nouvelle expression du temps de mélange, donné dans l'Eq. (44).

$$\eta = \frac{\dot{\gamma}}{\dot{\gamma}_{max}} = \frac{\dot{\gamma}}{\sqrt{\varepsilon/(2\upsilon)}} \tag{42}$$

avec $\dot{\gamma}$ le taux de cisaillement effectif

$$\dot{\gamma} = \sqrt{2\Re \bullet \Re} \tag{43}$$

et $\dot{\gamma}_{max}$ est le taux de cisaillement maximal dans l'écoulement (estimé à la paroi $\dot{\gamma}_{max} = 8\overline{W}/D_h$), et $\Re$ le tenseur de déformation.

$$t_m = \frac{D_h}{8\overline{W}\eta}\operatorname{arcsinh}\left[3.04\left(\frac{d}{D_h}\right)^2 Pe\,\eta\right] \tag{44}$$

Dans la Figure 16 les points expérimentaux pour les mesures globales sont obtenus par l'intégration des systèmes non linéaires de l'Eq. (16). En régime turbulent, nous traçons la courbe de tendance de ces points (droite noire) qui suit une loi de puissance en $Re^{-3/2}$. En régime laminaire on cale la formule théorique de l'Eq. (44) de Falk et Commenge (2010) qui suit une loi de puissance en Re^{-1}, en modifiant la valeur de η pour raccorder les courbes théoriques du régime laminaire et du régime turbulent.

Les valeurs de η sont ajustées dans l'Eq. (44) pour que la courbe théorique corresponde aux valeurs expérimentales. On trouve $\eta = 0.5$ pour les deux réacteurs, c'est-à-dire que 50% du taux de cisaillement est efficace pour le mélange, ce qui est très élevé par rapport aux 3% obtenus dans des micro-canaux étudiés par Falk et Commenge (2010) et à 1% dans l'extrudeuse bi-vis étudiée par Baldyga *et al.* (1998).

En comparant les mesures obtenues par l'intégration de l'Eq. (16) avec les tendances théoriques : en $Re^{-3/2}$ en régime turbulent, et en Re^{-1} en régime laminaire, on constate que l'intervalle de confiance à 90% est de ±30% comme mentionné par Falk et Commenge (2010) utilisant la même méthode chimique.

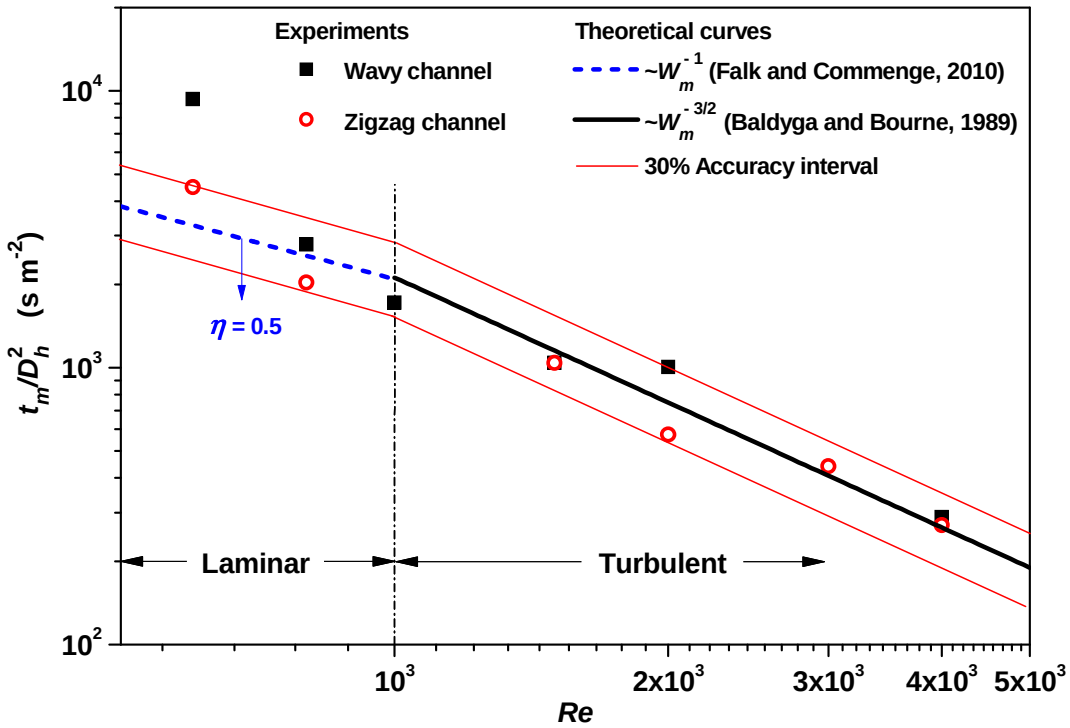

Figure 16 : Temps caractéristique de mélange divisé par le carré du diamètre hydraulique dans les deux géométries en fonction du nombre de Reynolds

I.9. Conclusion sur la sonde chimique

Nous présentons une procédure expérimentale adaptative pour mettre en place des mesures par sonde chimique de manière fiable et précise. Cette procédure adaptative se déroule en trois étapes :

- vérification de l'hydrodynamique de l'injection (§ I.3)
- ajustement de la concentration du réactif H^+ (§ I.4)
- vérification du volume de mesure (§ I.5)

Le but de cette étude sur la sonde chimique est de montrer qu'il est possible de s'assurer de la validité et d'une précision optimale de la caractérisation du micromélange pour laquelle elle est habituellement utilisée, mais également d'étendre son utilisation pour caractériser le mélange à des échelles plus globales.

Caractérisation quantitative et précise du micromélange

Ce premier point est mis en évidence dans le cas du mélangeur statique HEV (High Efficiency Vortex), en comparant la méthode adaptative à la méthode conventionnelle, en utilisant des valeurs de références obtenues par des méthodes optiques ou de simulation numérique. Trois cas de figures typiques ont été rencontrés :

- un point de mesure (S) pour lequel les valeurs des deux procédures sont concordantes, et où nous avons pu montrer en effet que les conditions de validité et de « localité » sont réunies avec la méthode classique, mais pour lequel la méthode adaptative apporte une amélioration sensible de la précision
- un point de mesure (W) pour lequel aucune des deux méthodes n'est véritablement assurée, et qui se trouve en dehors du domaine de validité de la sonde chimique
- un point de mesure (B) dans le domaine de faisabilité, mais pour lequel la méthode adaptative a pu apporter une interprétation « globale » des capacités de mélange

Caractérisation du mélange

Ce point a été testé dans le cas de deux ERM constitués par des canaux ondulés. Nous avons observé par la procédure classique qu'il n'y a pas d'effet significatif de la position de mesure ni du nombre de Reynolds sur les résultats de la sonde chimique en mesure locale, ce qui ne permet pas de comparer ces géométries. En effet, en injection pariétale, le domaine de mesure est proche de la paroi avec une turbulence contrôlée par la rugosité (article n°2 : Habchi *et al.*, 2010b). Nous proposons donc d'allonger le temps de la 2ème réaction pour que celle-ci se déroule dans tout le volume du réacteur. L'amélioration du mélange est ainsi nettement observée sur l'indice de ségrégation quand le nombre de Reynolds augmente.

Les temps de mélange obtenus par le modèle semi-empirique proposé par Falk et Commenge (2010), montrent une bonne cohérence avec les tendances théoriques dans les deux régimes laminaire et turbulent.

II. Méthodologie d'analyse des performances dans les ERM

II.1. Introduction

La problématique s'articule autour des transferts de masse et de chaleur dans les ERM en écoulement turbulent, car ce sont ces transferts qui vont induire les performances. Celles-ci sont liées aux capacités de mélange de l'écoulement aux différentes échelles. Comme il a été évoqué dans l'introduction, à l'échelle du réacteur c'est le macromélange qui caractérise la dispersion du fluide par le champ de vitesse moyenne. Le mésomélange se produit à l'échelle intégrale de la turbulence, et il correspond à l'advection par les fluctuations de vitesse. Le micromélange se situe à l'échelle dissipative, soit à l'échelle de Kolmogorov, il engage la destruction complète de la variance de la concentration des réactifs à l'échelle moléculaire.

Dans cette partie nous proposons une revue de l'ensemble des méthodes et démarches qui permettent de caractériser le fonctionnement d'un ERM en s'appuyant sur les trois étapes de la démarche présentée dans le diagramme de la Figure 17 :

- dans un premier temps la caractérisation du transfert de masse ou du mélange (articles 3 à 5 : Habchi *et al.*, 2010c-2010e)[7]
- dans un second temps la caractérisation du transfert thermique (article 6 : Mohand Kaci *et al.*, 2010)[8]
- enfin la caractérisation de l'intensification et de l'efficacité énergétique des ERM (article 7 : Habchi *et al.*, 2010f)[9]

Ces différentes méthodes sont illustrées dans le cas des trois géométries du mélangeur HEV étudiées dans le cadre de cette thèse, présentées dans l'Annexe C (page 65). Nous limitons notre présentation aux cas où la connaissance locale de l'écoulement est disponible pour analyser les performances. Cette connaissance préalable a pu être acquise expérimentalement (LDA, sonde chimique) et numériquement par CFD (Mohand Kaci *et al.*, 2010 ; Habchi *et al.*, 2010c-2010f). Nous envisageons de reprendre cette synthèse méthodologique dans un article, ce qui permettra d'inclure les méthodes expérimentales globales qui sont largement abordées dans la littérature, telles que la DTS par conductimètrie, l'indice de mélange par colorimétrie, ou la mesure des coefficients de transferts de chaleur.

---

[7] Habchi *et al.*, Turbulence behavior of artificially generated vorticity, J. Turbulence, Accepted, 2010c.
Habchi *et al.*, Alternating mixing tabs in multifunctional heat exchanger-reactor, Chem. Eng. Process., In press, 2010d.
Habchi *et al.*, Turbulent mixing and residence time distribution in novel configurations of multifunctional exchanger-reactor, Chem. Eng. Process., Submitted, 2010e.

[8] Mohand Kaci *et al.*, Flow structure and heat transfer induced by embedded vorticity, Int. J. Heat Mass Transfer 53 (2010) 3575-3584.

[9] Habchi *et al.*, Entropy production and synergy field principle in turbulent vortical flows, Int. J. Heat Fluid Flow, Submitted, 2010f.

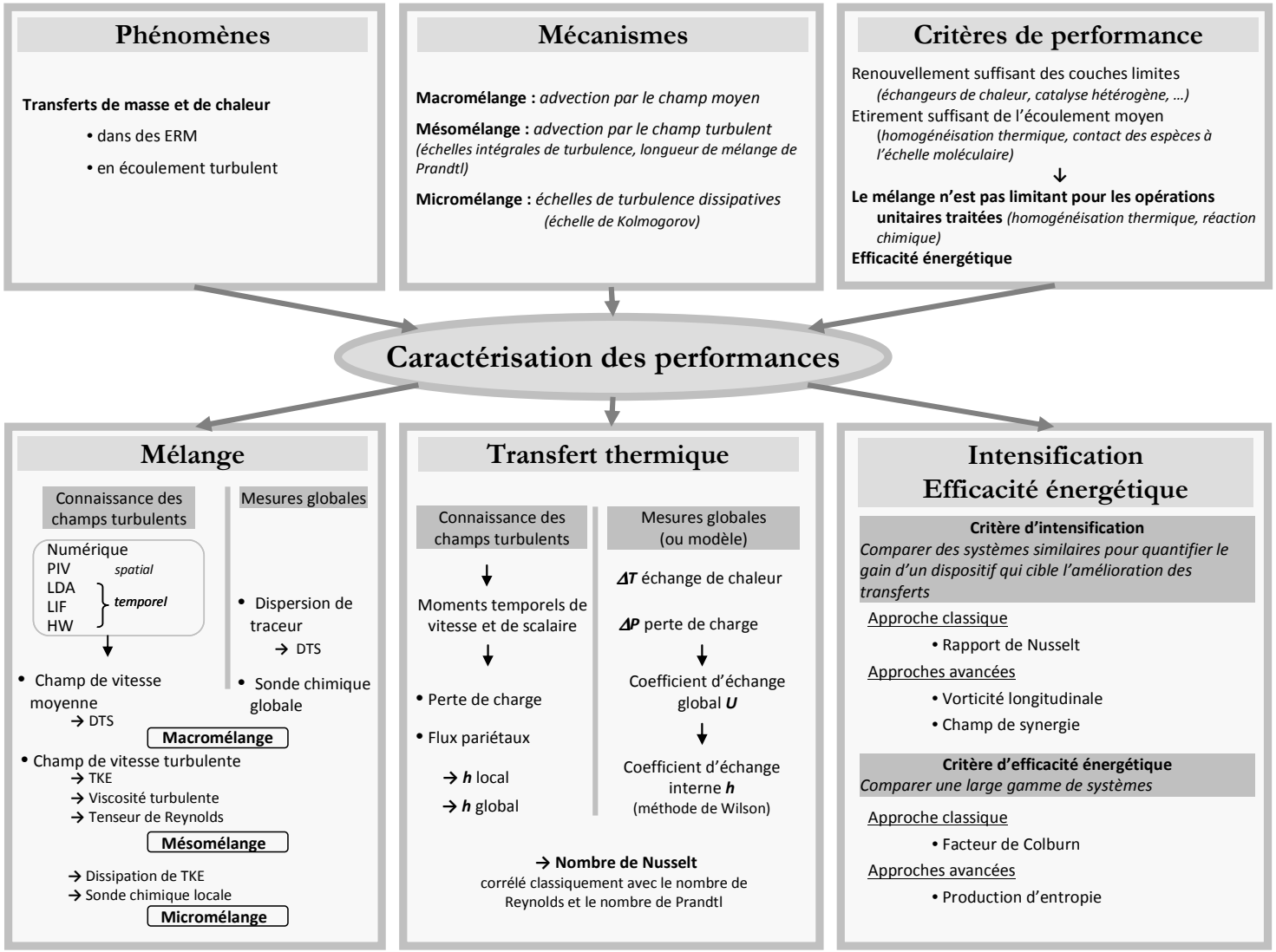

Figure 17 : Organigramme de caractérisation des performances des ERM

II.2. Caractérisation du mélange

II.2.1. Macromélange

Le macromélange, lié à l'advection par le champ de vitesse moyenne, peut être caractérisé par la distribution des temps de séjour (DTS). Celle-ci peut s'établir numériquement en post traitement du calcul hydrodynamique, en suivant la trajectoire de particules uniformément distribuées sur la section d'entrée. Les résultats concernant les trois géométries du mélangeur HEV (Figure 18) montrent la DTS pour les deux nombres de Reynolds $Re = 7500$ et $Re = 15000$. La distribution des temps de séjour reste très resserrée malgré son comportement bimodal. Ce comportement n'est donc pas rigoureusement piston comme on peut l'attendre d'un réacteur idéal, mais ce défaut ne concerne pas plus de 1,5 fois le temps de séjour moyen, ce qui est beaucoup mieux qu'en batch en tout état de cause.

Ces résultats sont analysés dans l'article n°5 (Habchi *et al.* ; 2010e).

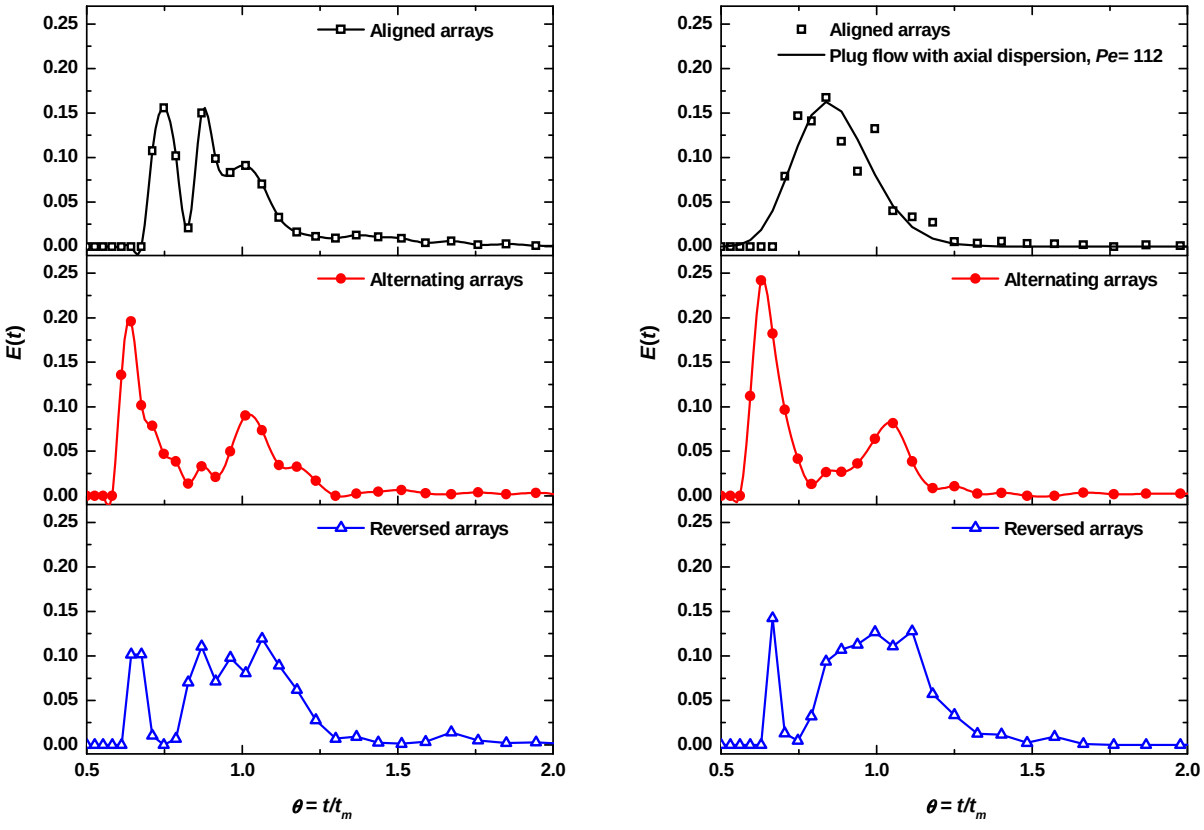

Figure 18 : Distribution des temps de séjour DTS dans les trois géométries à rangées alignées, alternées et inversées (a) $Re = 7500$, (b) $Re = 15000$

II.2.2. Mésomélange

Le mésomélange peut se caractériser par l'énergie cinétique de turbulence ou par le tenseur de Reynolds (article n°3 : Habchi *et al.*, 2010c).

Dans le cas des trois mélangeurs HEV, l'évolution longitudinale de l'énergie cinétique turbulente $k_{l,m}$ moyennée sur la section est présentée dans la Figure 19. Celle-ci présente des « oscillations spatiales » pour les trois configurations, avec des maxima locaux qui sont localisés au niveau des ailettes.

Un focus sur la 6ème rangée de perturbateurs fournit une observation plus précise sur le mécanisme du comportement de TKE. Dans les rangées alignées et alternées, la TKE augmente quand le fluide dépasse les perturbateurs, et aboutit à un maximum à l'extrémité supérieur de l'ailette où se situent les tourbillons « hairpins ». En effet, nous avons montré (article n°3 : Habchi *et al.*, 2010c,) que ces hairpins concentrent l'essentiel de la TKE.

En comparant les trois systèmes, on peut conclure que la géométrie de « rangées inversées » semble montrer la meilleure performance vis-à-vis du mésomélange, puisqu'elle présente des valeurs de $k_{l,m}$ jusqu'à 25% supérieures à celle de la géométrie à rangées alignées et de 16% supérieures à celle des rangées alternées.

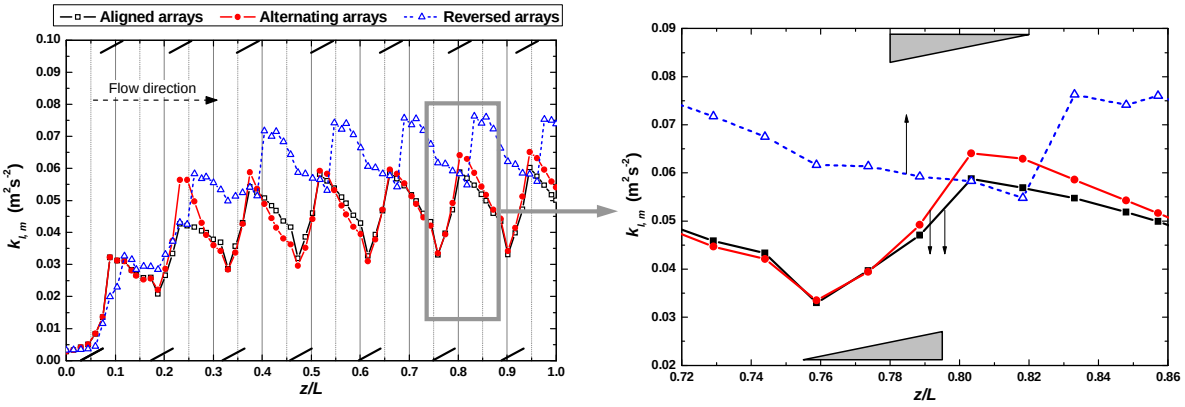

Figure 19 : Evolution longitudinale de l'énergie cinétique turbulente moyennée sur les sections des trois géométries avec un focus sur la 6ème rangée, $Re = 15000$

II.2.3. Micromélange

Le micromélange est caractérisé par les échelles de Kolmogorov ou par la dissipation de l'énergie cinétique turbulente.

L'évolution longitudinale de la dissipation de l'énergie cinétique turbulente moyennée sur les sections de chaque géométrie $\varepsilon_{l,m}$ est représentée dans la Figure 20. Une évolution périodique est également observée dans les ERM au passage des générateurs de tourbillons, créant un écoulement de type oscillatoire auto-entretenu tout au long des ERM. L'amplitude des oscillations est la même dans les trois géométries et égale à peu près à 35% de la valeur moyenne. Ceci est lié à la couche de cisaillement éjectée des extrémités des ailettes qui génère ainsi de grands gradients de vitesse, augmentant ainsi la dissipation turbulente. La première couche de cisaillement se développe à partir

du bord d'attaque et aboutit à son maximum au bord de fuite où les hairpins se développent. Les valeurs de $\varepsilon_{l,m}$ diminuent en s'éloignant de l'ailette.

En comparant les trois géométries, on peut conclure que la configuration des rangées inversées améliore le micromélange par rapport aux deux autres géométries puisqu'elle présente le plus haut niveau de dissipation turbulente. Dans cette configuration, $\varepsilon_{l,m}$ est environ 50% supérieur par rapport à la géométrie rangées alignées, et de 29% par rapport à la géométrie rangées alternées.

Ces résultats sont analysés dans l'article n°5 (Habchi *et al.* ; 2010e).

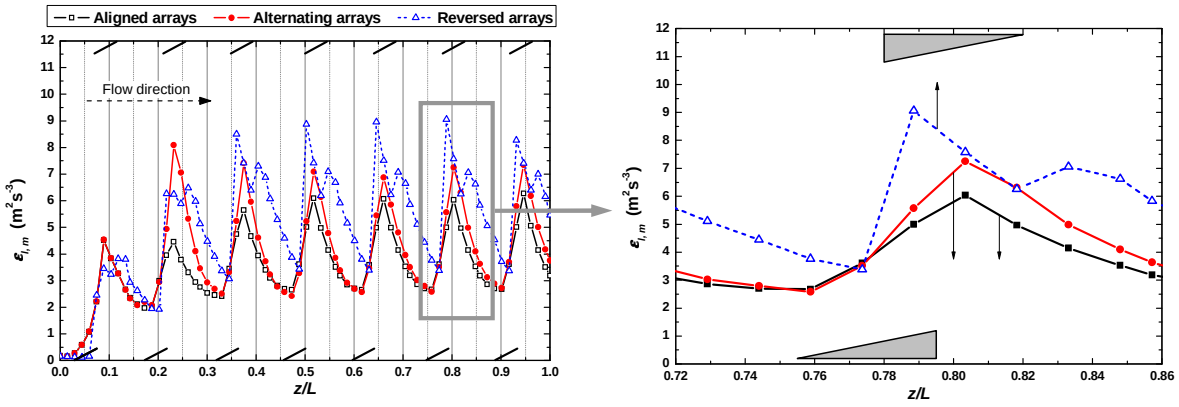

Figure 20 : Evolution longitudinale de la dissipation de l'énergie cinétique turbulente moyennée sur les sections des trois géométries avec un focus sur la 6ème rangée, $Re = 15000$

II.3. Caractérisation du transfert thermique

La caractérisation du transfert thermique est effectuée dans les articles n°6 et 7 (Mohand Kaci *et al.*, 2010 ; Habchi *et al.*, 2010f). A partir des résultats de CFD on peut établir des corrélations empiriques du nombre de Nusselt global dans les différents systèmes à partir de sa définition (Eq. (43)).

$$Nu = \frac{\dot{m}\, c_p}{\pi L \lambda} \frac{T_{b,outlet} - T_{b,inlet}}{T_w - T_{mean}} \tag{45}$$

où $T_{mean} = \left(T_{b,inlet} + T_{b,outlet}\right)/2$ et T_b est la température de mélange, λ la conductivité thermique de l'eau, $\dot{m}$ le débit massique et $T_{b,z}$ la température de mélange sur la section perpendiculaire à l'écoulement de coordonnée z et qui est obtenue à partir d'une UDF[10].

Les corrélations du nombre de Nusselt en fonction du nombre de Reynolds, obtenues dans les trois géométries sont présentées dans le Tableau 5, donnant une évolution en puissance 2/3.

Le facteur de frottement global f est aussi intéressant à calculer puisqu'il représente l'énergie dissipée dans un ERM et il est obtenu à partir de la différence de pression ΔP entre l'entrée et la

[10] User Defined Function dans Fluent™

sortie du système selon la définition donnée dans l'Eq. (44). Les corrélations du coefficient de perte de charge sont également présentées dans le Tableau 5.

$$f = \frac{2}{L/D}\frac{\Delta P}{\rho W_m^2} \tag{46}$$

Rangées alignées	Rangées alternées	Rangées inversées
$Nu_{alg} = 0.232\,Re^{2/3}\,Pr^{0.4}$	$Nu_{alt} = 0.274\,Re^{2/3}\,Pr^{0.4}$	$Nu_{rev} = 0.326\,Re^{2/3}\,Pr^{0.4}$
$f_{alg} = 0.858\,Re^{-0.057}$	$f_{alt} = 0.948\,Re^{-0.047}$	$f_{rev} = 0.761\,Re^{-0.004}$

Tableau 5 : Corrélations du nombre de Nusselt et du coefficient de perte de charge en fonction du nombre de Reynolds dans les trois géométries

Une deuxième méthode pour caractériser le transfert thermique consiste à calculer le coefficient de variance (COV) qui est une mesure de la dispersion relative par le rapport de l'écart-type et la moyenne de la température dans le volume de l'ERM. Ceci est présenté dans la Figure 21 pour les trois géométries du mélangeur HEV. En effet le COV est une signature du macromélange puisqu'il caractérise l'homogénéité d'un scalaire dans l'écoulement : $COV = 0$ signifie que l'homogénéité est idéale et la valeur 1 signifie une hétérogénéité totale. Ce coefficient classe les trois ERM de la même façon que le nombre de Nusselt : les rangées inversées sont les mieux classées et les rangées alignées les plus mal classées.

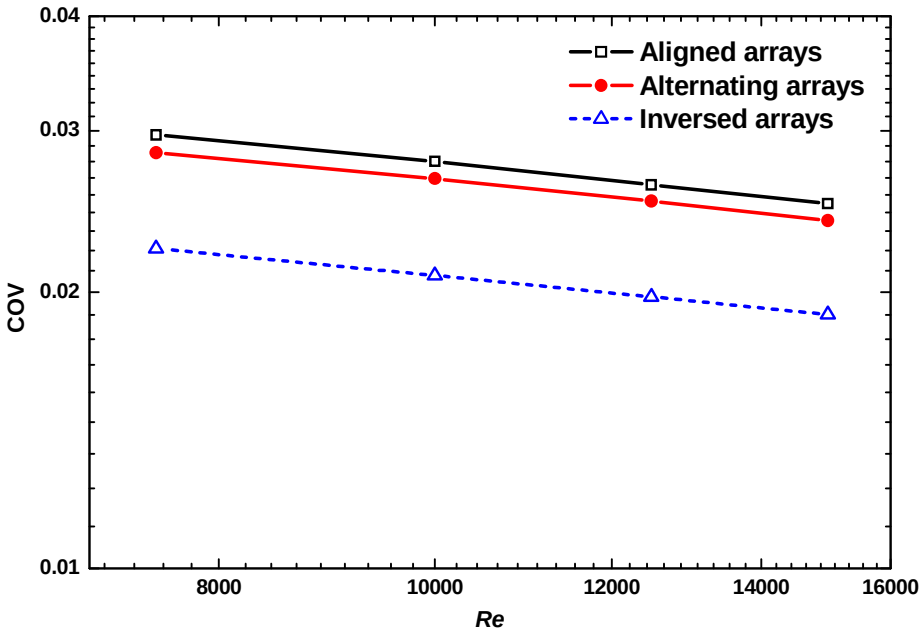

Figure 21 : Coefficient de variance (COV) dans les trois géométries du mélangeur HEV en fonction du nombre de Reynolds

II.4. Caractérisation de l'intensification et de l'efficacité énergétique

II.4.1. Critère d'intensification

L'intensification est un concept relatif : il permet de comparer des systèmes similaires en référence à l'un d'eux ou à une géométrie de base (Stankiewicz et Moulijn, 2000 ; Ferrouillat *et al.*, 2006a ; Moulijn *et al.*, 2008 ; Anxionnaz *et al.*, 2008). Les différents critères d'intensification sont présentés dans cette section.

II.4.1.1. Approche classique : rapport de Nusselt

On rapporte tout d'abord le nombre de Nusselt Nu d'un ERM à celui d'un tube circulaire Nu_0 en écoulement turbulent complètement développé pour caractériser l'intensification apportée par les générateurs de vortex du mélangeur HEV classique par rapport au tube droit.

Selon Kakac *et al.* (1987), on peut retenir comme valeur de nombre de Nusselt dans un tube vide Nu_0 la corrélation de Gnielinski (1976) (Eq. (47)) sur un intervalle de nombre de Prandtl de 0,5 à 200 et de nombre de Reynolds de 2300 à 5×10^6 :

$$Nu_0 = \frac{\left(f_0/8\right)}{1+12.7\left(f_0/8\right)^{1/2}}\frac{Pr}{\left(Pr^{2/3}-1\right)}\left(Re-1000\right) \tag{47}$$

avec f_0 le facteur de frottement dans un tube vide d'après la formule de Blasius :

$$f_0 = 0.079\,Re^{-0.25} \tag{48}$$

La Figure 22 (a) montre l'évolution longitudinale du nombre de Nusselt dans la géométrie « rangées alignées » normalisé par Nu_0. L'aspect périodique observé dans le paragraphe précédent est aussi présent dans la variation du nombre de Nusselt due à la présence périodique des ailettes. On observe que l'intensification locale du transfert thermique par rapport au tube droit est maximum proche du bord de fuite de chaque ailette et atteint une valeur d'environ 8. L'intensification minimale est dans la région entre deux perturbateurs à une distance $z/h \approx 5$ en aval du bord de fuite de l'ailette qui correspond à la distance à partir de laquelle les paires de tourbillons contrarotatifs perdent la plupart de leur intensité ou circulation (voir article n° 3 : Habchi *et al.*, 2010c).

Nous pouvons également caractériser l'intensification des géométries à rangées alternées et inversées par rapport à la géométrie alignée du mélangeur HEV, présentée dans la Figure 22 (b). La configuration à rangées inversées présente les meilleures performances thermiques, et donne un facteur d'intensification jusqu'à 2,50 alors qu'il atteint 1,75 dans les rangées alternées.

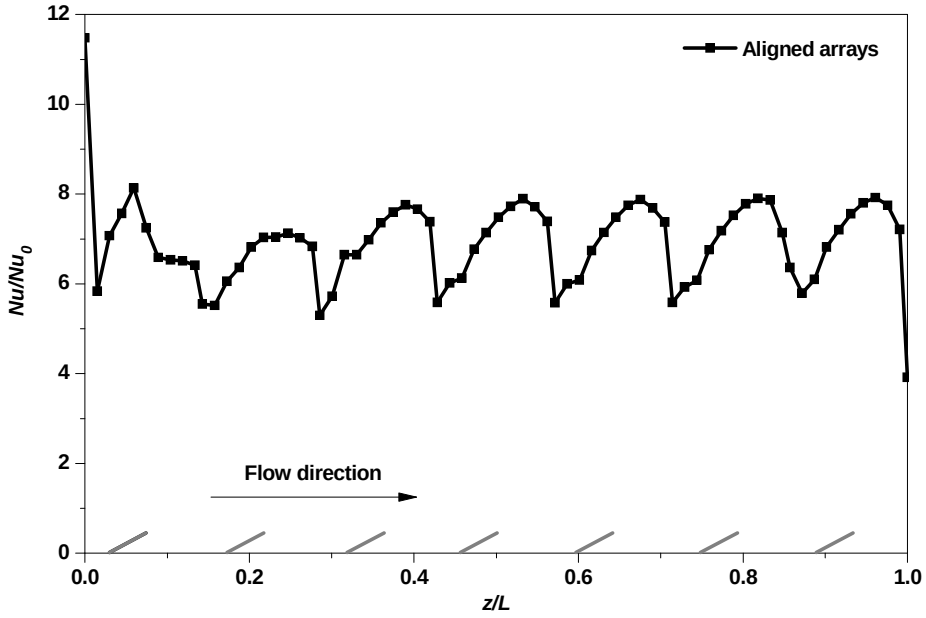

(a)

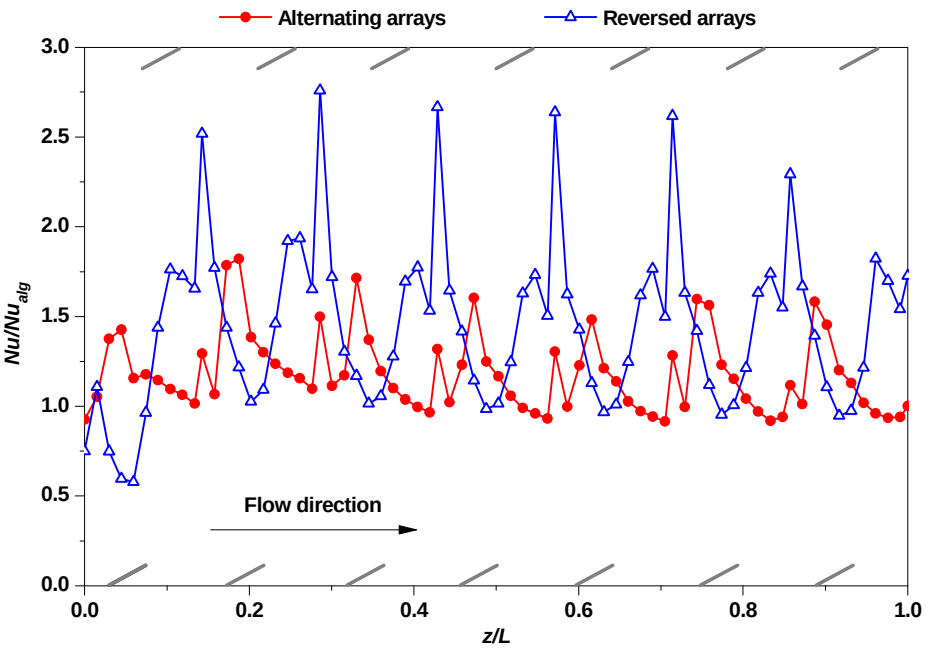

(b)

Figure 22 : Evolution longitudinale du nombre de Nusselt normalisé dans les trois géométries (a) intensification du mélangeur HEV classique par rapport au tube droit, (b) intensification des rangées alternées et inversées par rapport au mélangeur HEV classique, $Re = 15000$

II.4.1.2. Approches avancées

a) Vorticité longitudinale

La vorticité longitudinale a un effet important sur le transfert de chaleur en améliorant le mélange radial et les transferts de masse et de chaleur entre la paroi et l'écoulement (Fiebig, 1998 ; Ferrouillat, 2006b ; Anxionnaz, 2009). La question que l'on peut poser est de savoir si la circulation est un paramètre pertinent pour caractériser le transfert thermique. La Figure 23 représente le nombre de Nusselt en fonction de la circulation longitudinale (calculée par l'intégration de la vorticité dans l'enveloppe des tourbillons) dans les trois configurations du mélangeur HEV.

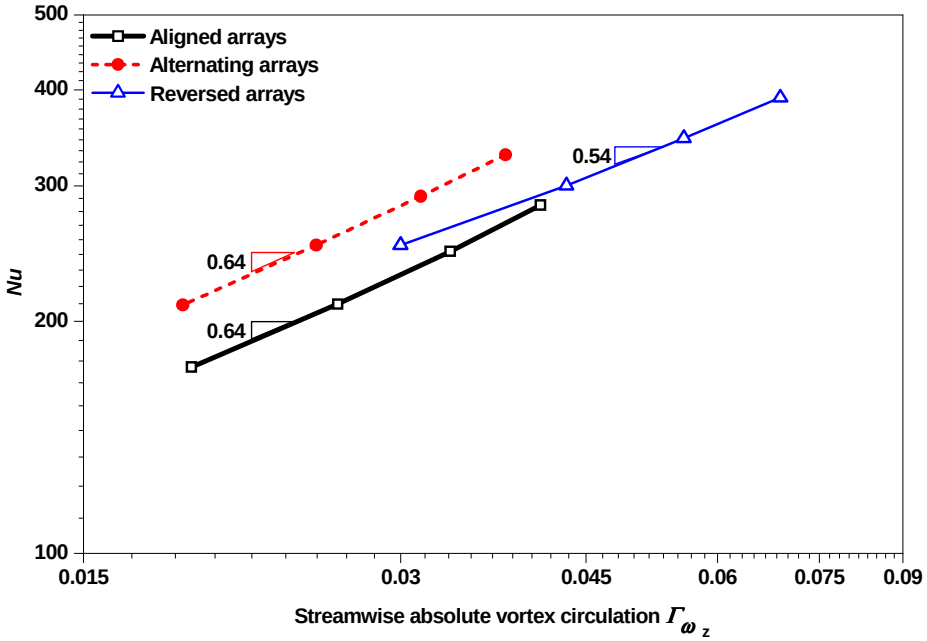

Figure 23 : Nombre de Nusselt en fonction de la circulation longitudinale

On remarque qu'il n'y a pas de courbe maîtresse qui pourrait indiquer que cette grandeur détermine le Nusselt. Dans la géométrie de « rangées inversées » la circulation est plus élevée, ainsi que le nombre de Nusselt par rapport aux autres géométries, à nombre de Reynolds donné. On peut seulement conclure que la circulation et le nombre de Nusselt sont liés mais que ce n'en est pas un paramètre totalement explicatif, puisque cette relation dépend de la géométrie.

Pour mieux comprendre la contribution relative des deux modes de transfert : convection radiale et turbulence, nous définissons un nouveau paramètre χ qui est le rapport de la convection des tourbillons aux grandes échelles, représentée par la circulation Γ_{ω_z} des tourbillons longitudinaux, sur la diffusivité turbulente υ_t (puisque le nombre de Schmidt turbulent est proche de 1, voir l'article n°7, Habchi *et al.* (2010f)). La signification physique de ce paramètre χ est proche de celle d'un nombre de Nusselt.

Ce paramètre χ est porté en fonction du nombre de Reynolds dans la Figure 24 pour les trois configurations du mélangeur HEV. Le mode de transfert convectif semble plus accentué dans la géométrie à rangées inversées, qui présente par ailleurs les nombres de Nusselt les plus élevés (§

II.4.1.1). Nous remarquons que χ augmente avec le nombre de Reynolds, ce qui signifie que la contribution de la vorticité longitudinale augmente en effet relatif sur la turbulence à grand nombre de Reynolds.

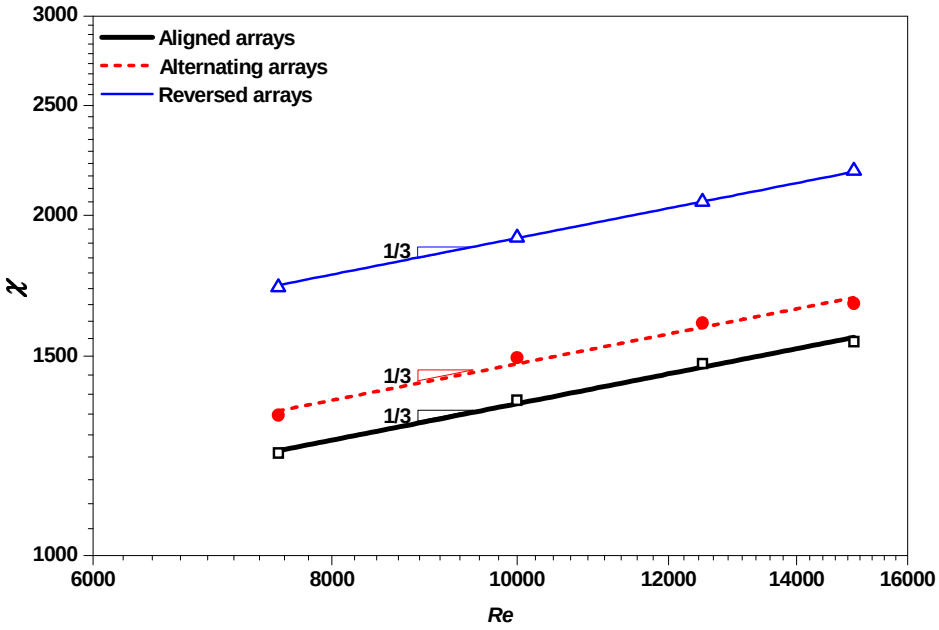

Figure 24 : Paramètre χ en fonction du nombre de Reynolds

b) Champ de synergie

Dans cette approche, l'idée de base est que l'alignement entre la vitesse et les gradients de température conditionne les transferts (Guo *et al.*, 1998; Tao *et al.*, 2002). De ce fait, le nombre de Nusselt dépend du produit scalaire $\vec{U}\cdot\vec{\nabla}T = \left|\vec{U}\right|\left|\vec{\nabla}T\right|\cos\theta$, où θ est l'angle d'intersection entre la vitesse et les gradients de température. Ainsi, pour des intensités données de vitesse et de gradients de température, plus θ est petit, plus le transfert convectif de chaleur est grand (article n° 7 : Habchi *et al.*, (2010f)). La valeur moyennée de cet angle sur le volume de l'écoulement θ_{Vol}, calculé par une UDF, est retenue comme paramètre caractéristique d'intensification.

Cet angle d'intersection global θ_{Vol} est représenté pour les trois géométries en fonction du nombre de Reynolds dans la Figure 25. Les plus grands θ_{Vol} sont obtenus dans les rangées alignées ayant le plus petit nombre de Nusselt, et les plus petites θ_{Vol} se trouvent dans les rangées inversées présentant les meilleures performances thermiques.

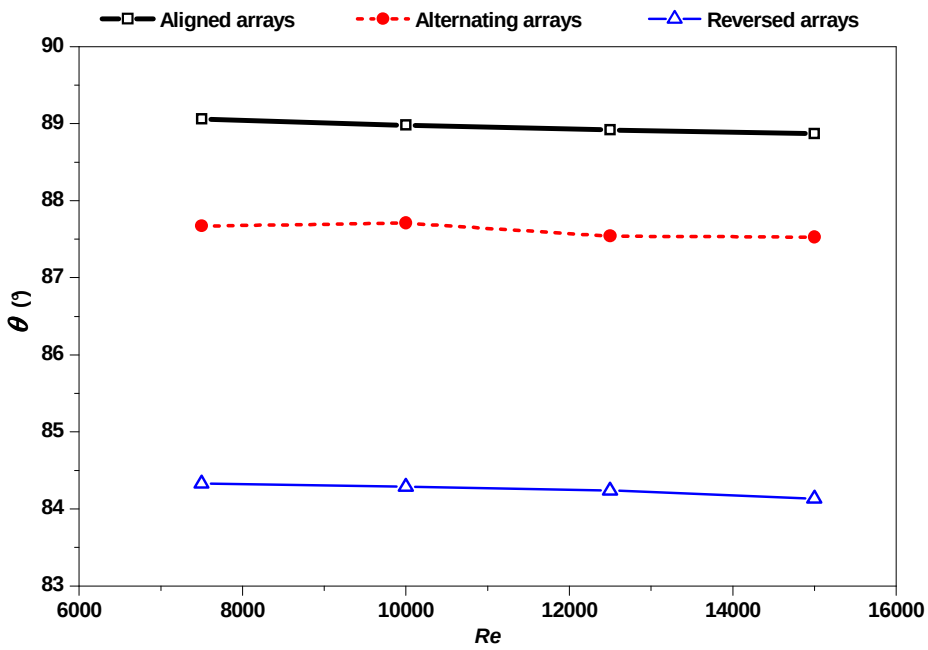

Figure 25 : Angle d'intersection global en fonction du nombre de Reynolds dans les trois géométries

II.4.2. Critère de l'efficacité énergétique

L'efficacité énergétique est un concept absolu : il permet de comparer plusieurs systèmes, puisqu'il prend en compte la consommation énergétique (Ferrouillat *et al.*, 2006a ; Anxionnaz *et al.*, 2008). Les différents critères de l'efficacité énergétique sont présentés ci-après.

II.4.2.1. Approche classique : facteur de Colburn

Pour comparer l'efficacité hydro-thermique des trois ERM, le facteur d'efficacité dit de Colburn η est utilisé : c'est le rapport de l'échange thermique convectif h sur celui dans un tube droit h_0 pour une puissance de pompage donnée (Promvonge and Thianpong, 2008; Rahimi *et al.*, 2009) :

$$\eta = \left(\frac{Nu}{Nu_0}\right)\left(\frac{f}{f_0}\right)^{-1/3} \tag{49}$$

La Figure 26 montre ce facteur d'efficacité η en fonction du nombre de Reynolds dans les trois géométries. On peut observer que η est toujours supérieur à 1. De plus η tend à diminuer avec le nombre de Reynolds (avec une loi de puissance de -1/3) ce qui signifie que le rôle des générateurs de vorticité dans l'intensification des transferts de chaleur est plus « rentable » pour les petits nombres de Reynolds. Le facteur d'efficacité η dans les rangées inversées est de 27% supérieur à celui des rangées alignées et de 12% supérieur à celui des rangées alternées.

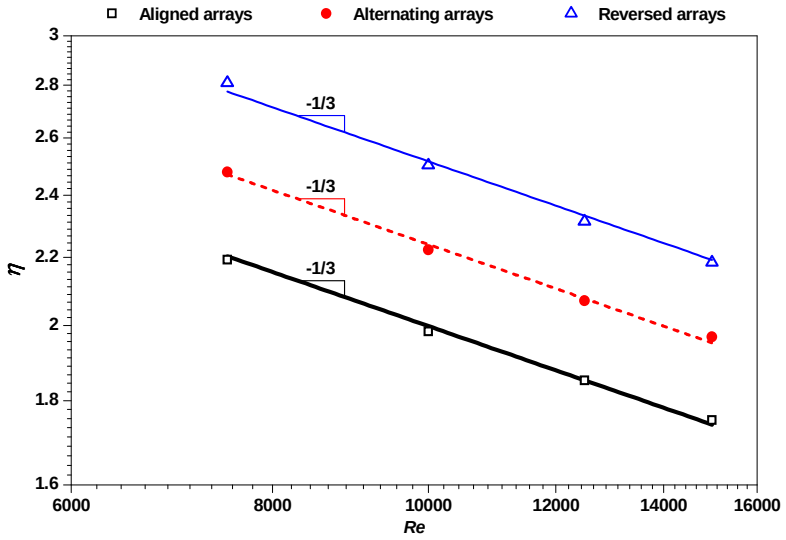

Figure 26 : Facteur d'efficacité η en fonction du nombre de Reynolds dans les trois géométries

Une présentation analogue est possible avec le nombre de Nusselt représenté en fonction de la dissipation énergétique par unité de masse. Ceci est proposé avec les données reconstituées de différents ERM de la littérature pour la même gamme de nombres de Reynolds $7500 < Re < 15000$: les appareils sont ainsi comparés à consommation énergétique égale Le tube à section circulaire correspond bien entendu au plus faible nombre de Nusselt et à la plus faible dissipation énergétique. Le Kenics™ et le HEV à géométrie de rangées alignées, présentent à peu près les mêmes performances. Ces performances sont améliorées par les rangées alternées, et encore plus par les rangées inversées (avec une augmentation quasiment négligeable de la consommation énergétique).

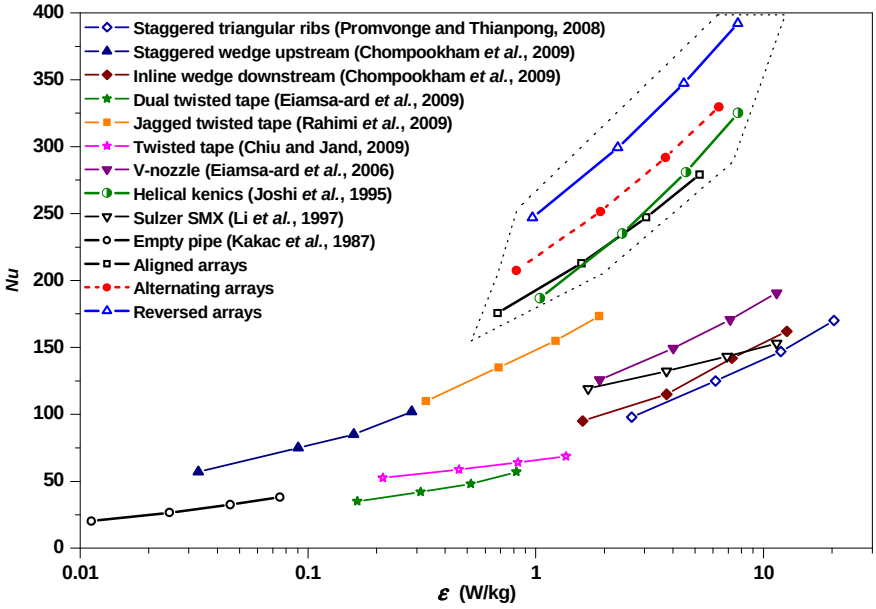

Figure 27 : Nombre de Nusselt en fonction de la consommation énergétique par unité de masse pour les trois géométries et plusieurs ERM de la littérature

II.4.2.2. Approches avancées : production d'entropie

Cette approche fait l'objet de l'article n° 7 (Habchi *et al.*, 2010f). La production d'entropie $\dot{S}_{pro}$ comprend à la fois le transfert de chaleur et les pertes de charges (Bejan, 1996), permettant ainsi la caractérisation des performances globales des ERM. Ce terme peut être calculé en utilisant le modèle de Kock et Herwing (2004, 2005), facilement intégré dans le post traitement des résultats de simulations numériques CFD.

Selon Hesselgreaves (2000), le nombre de production d'entropie $N_{\dot{S}_{pro}}$ est défini par l'expression suivante :

$$N_{\dot{S}_{pro}} = \frac{\dot{S}_{pro}\, T_w}{Q_w} \tag{50}$$

où Q_w et T_w sont respectivement la densité de flux et la température de paroi.

Le paramètre $N_{\dot{S}_{pro}}$ peut ainsi être utilisé pour la détermination des performances globales des ERM (Figure 28). Plus $N_{\dot{S}_{pro}}$ est élevé, moins l'efficacité énergétique est bonne. C'est la géométrie à rangées inversées qui présente la meilleure efficacité : $N_{\dot{S}_{pro},rev} > N_{\dot{S}_{pro},alt} > N_{\dot{S}_{pro},a\,lg}$ ce qui est cohérent avec les résultats précédents.

L'évolution de $N_{\dot{S}_{pro}}$ avec le nombre de Reynolds est plus forte dans les rangées alignées que les deux autres géométries, et l'augmentation de $N_{\dot{S}_{pro}}$ dans les rangées inversées est la plus lente, ayant une pente de 0.1. Plus cette pente est grande, plus on dissipe de l'énergie pour intensifier le transfert de chaleur.

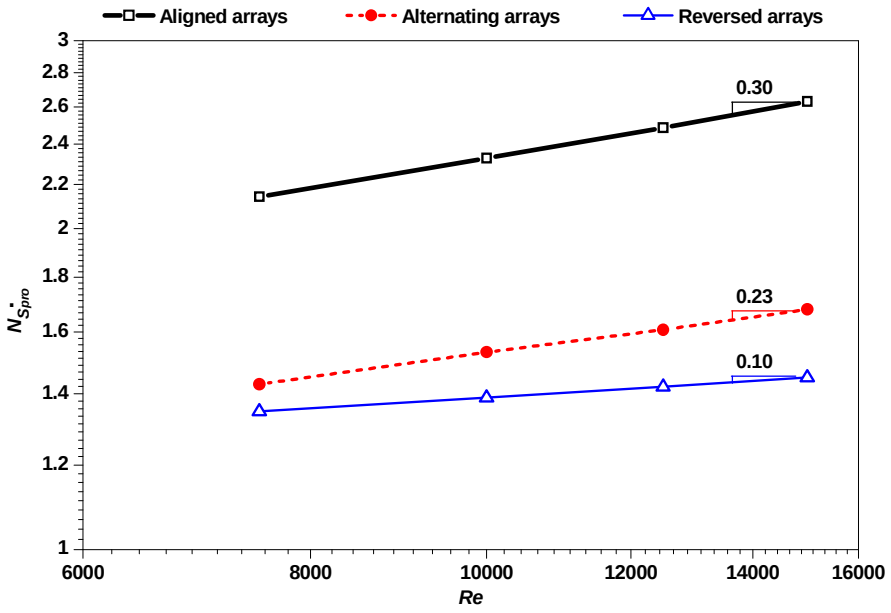

Figure 28 : Nombre de production d'entropie en fonction du nombre de Reynolds dans les trois géométries

II.5. Conclusion sur les critères de performances des ERM

Dans cette seconde partie nous proposons une revue de l'ensemble des méthodes et approches qui peuvent être utilisées pour la caractérisation des performances d'un ERM. Cette méthodologie est appliquée à trois géométries différentes d'ERM de type « générateur de vortex ».

Dans une première étape, la caractérisation du mélange turbulent est traitée en prenant en compte les trois échelles de ce mécanisme : macro, méso et micromélange. Chacun de ces mécanismes est caractérisé par un paramètre typique des phénomènes physiques qui le contrôlent.

Dans une seconde étape, nous présentons la caractérisation du transfert thermique par l'approche classique qui consiste à déterminer le coefficient longitudinal de transfert convectif et ainsi de proposer des corrélations empiriques globales pour le nombre de Nusselt global. Le coefficient de perte de charge est traité simultanément.

Ces études permettent d'aborder la caractérisation des performances d'intensification et d'efficacité énergétique des ERM. Tout d'abord, le concept d'intensification permet de comparer l'effet de différents dispositifs en référence à un système de base sur lequel on les applique. Les différents critères d'intensification présentés sont le rapport du nombre de Nusselt avec le système de base, et le champ de synergie entre les vecteurs vitesses et les gradients de température. Ensuite, la caractérisation de l'efficacité énergétique est effectuée par le facteur de Colburn, et par la production d'entropie. Celle-ci est un concept absolu, dans le sens où cela permet de comparer tous systèmes, dans toutes les gammes de productivité, puisqu'il prend en compte la perte énergétique.

La démarche présentée ici peut être suivie pour caractériser toute géométrie d'ERM dans le but de l'optimiser ou de la comparer à d'autres configurations existantes.

CONCLUSIONS ET PERSPECTIVES

Ce travail porte sur la compréhension des phénomènes de mélange turbulent et de transfert thermique dans des *échangeurs/réacteurs multifonctionnels* (ERM) en présence de vorticité générée artificiellement. Cette compréhension constitue un enjeu fondamental pour l'amélioration de l'efficacité énergétique de ces systèmes. Les objectifs et la démarche de la thèse sont articulés autour de deux axes :

- la méthodologie de *sonde chimique* utilisée pour la caractérisation de l'intensification des transferts dans les ERM (articles n°1 & 2),
- l'étude de *l'intensification et de l'efficacité énergétique* d'un ERM spécifique, basé sur le principe des générateurs de vortex (articles 3 à 7).

Dans la première partie, nous étudions l'utilisation de la sonde chimique pour caractériser le mélange dans des écoulements continus. Nous définissons un *domaine de validité* pour cette méthode dépendant uniquement des conditions hydrodynamiques et des dimensions de l'aiguille d'injection. Ceci est réalisé en nous appuyant sur la modélisation physique de l'interaction entre les différentes échelles du mélange turbulent. Nous proposons également une procédure expérimentale innovante dite *procédure adaptative* pour obtenir des résultats quantitatifs absolus lorsque cela est possible. L'approche expérimentale développée peut être transportée pour toute autre méthode de sonde chimique.

Cette démarche est appliquée au mélangeur statique HEV (high efficiency vortex) pour caractériser le *micromélange*, dont les résultats sont comparés à ceux obtenus à partir d'études antérieures, numériques et expérimentales (Mohand Kaci, 2007).

De plus, dans le cadre du projet ANR CP2D - RAPIC, la procédure expérimentale adaptative est appliquée pour caractériser le *mélange global* dans des mini-canaux ondulés, pour une large gamme de nombre de Reynolds qui couvre les régimes d'écoulement laminaire et turbulent. Ces applications nous montrent nettement l'intérêt de la procédure expérimentale adaptative par rapport à la procédure classique.

Dans la deuxième partie nous proposons une démarche de caractérisation des performances d'un ERM, dans le but de l'optimiser ou de le comparer à d'autres configurations existantes.

En premier lieu nous présentons les différentes approches pour caractériser le *mélange turbulent* en prenant en compte les trois échelles de ce mécanisme : macro, méso et micromélange. Chacun de ces mécanismes est caractérisé par une approche différente liée aux phénomènes physiques qui le contrôlent : la distribution du temps de séjour pour le macromélange, l'énergie cinétique de turbulence pour le mésomélange, et la dissipation de l'énergie turbulente pour le micromélange.

En deuxième lieu, nous nous intéressons à l'approche utilisée pour la caractérisation du *transfert thermique*, par la détermination du coefficient local de transfert convectif, qui permet d'établir les corrélations caractéristiques pour le nombre de Nusselt.

Enfin, nous présentons la caractérisation des performances globales des ERM. Pour caractériser *l'intensification* d'un ERM, différents critères sont utilisés : rapport de Nusselt et le champ de synergie entre les vitesses et les gradients de température. Les critères de *l'efficacité énergétique* utilisés sont le facteur de Colburn et la production d'entropie.

Cette démarche est appliquée à des ERM de type générateur de vortex dans trois configurations différentes. Les grandeurs physiques locales sont obtenues par mesure LDA et par simulation numérique CFD. L'application de cette démarche permet de mettre en évidence une géométrie, les rangées inversées, qui est mieux classée que d'autres ERM de la littérature.

D'autres formes de perturbateurs ont été envisagées pendant ce travail, imaginées en combinant le principe du jet et de la génération de vorticité. Une première maquette a été réalisée en créant une perforation au centre d'une ailette trapézoïdale (Figure 29 (a)) et a donné lieu à un Stage de Master pour les mesures de vitesse. Pour améliorer l'efficacité de ce système, nous envisageons de décaler le générateur de vorticité (plein ou perforé) de la paroi (Figure 29 (a)) de manière à réduire la zone de recirculation en aval du perturbateur en augmentant la quantité de mouvement dans l'interstice créé. Également, d'autres formes de générateurs de vorticité sont intéressantes à étudier, comme les perturbateurs flexibles (Figure 29 (b)) (Alben, 2009) : une géométrie HEV basée sur ce principe a fait l'objet du dépôt d'une enveloppe Soleau (Habchi *et al.*, 2009d) ainsi que l'obtention d'un Projet Exploratoire du PIE CNRS (Projet VORFLEX, 2010).

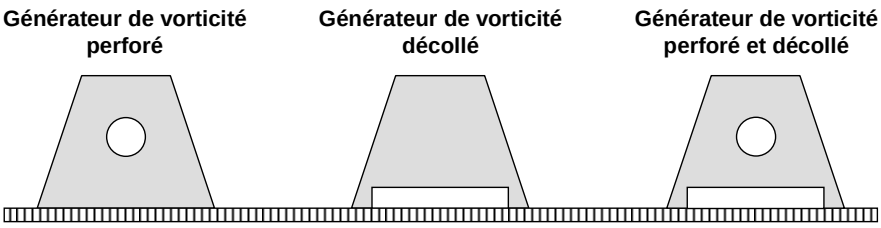

(a)

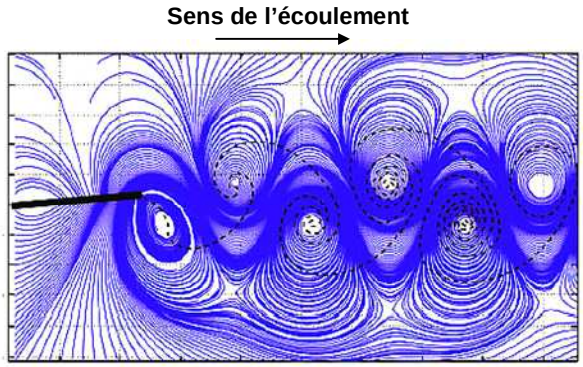

(b)

Figure 29 : (a) Nouvelles formes de générateurs de vorticité basées sur des perturbateurs trapézoïdaux, (b) lignes de courant en aval d'un générateur de tourbillon flexible (Alben, 2009)

Des travaux futurs concerneront des études thermiques expérimentales sur une maquette d'ERM qui a été conçue et construite pendant la thèse. Cette maquette est conçue de manière à pouvoir effectuer à la fois des mesures de flux et de température à la paroi grâce à 42 thermocouples insérés tout le long de l'ERM, ainsi que des mesures par PIV ou LDA en sortie du mélangeur pour avancer dans la compréhension de la structure de l'écoulement. La construction de cette maquette est terminée, l'expérimentation commencera en septembre 2010.

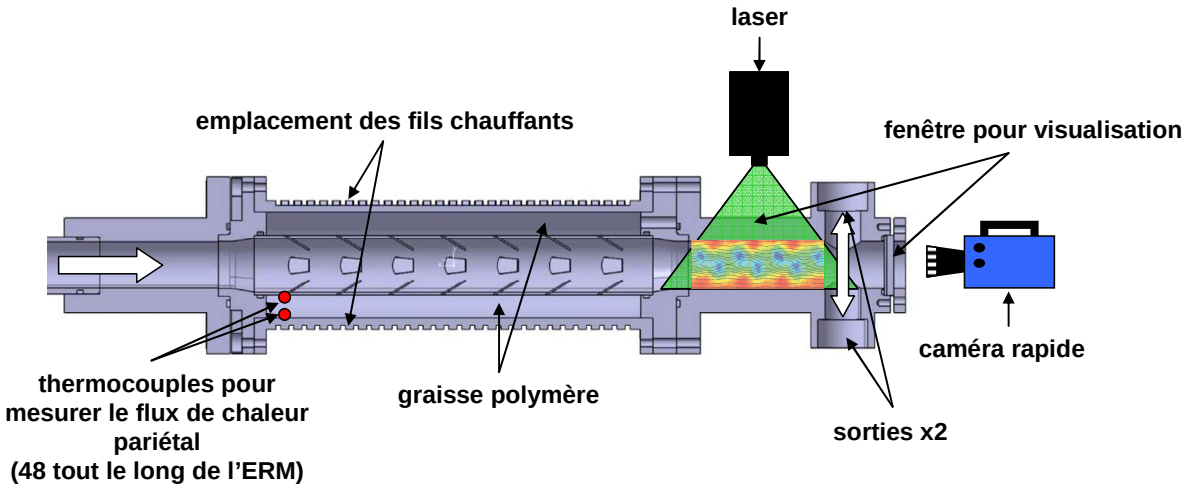

(a)

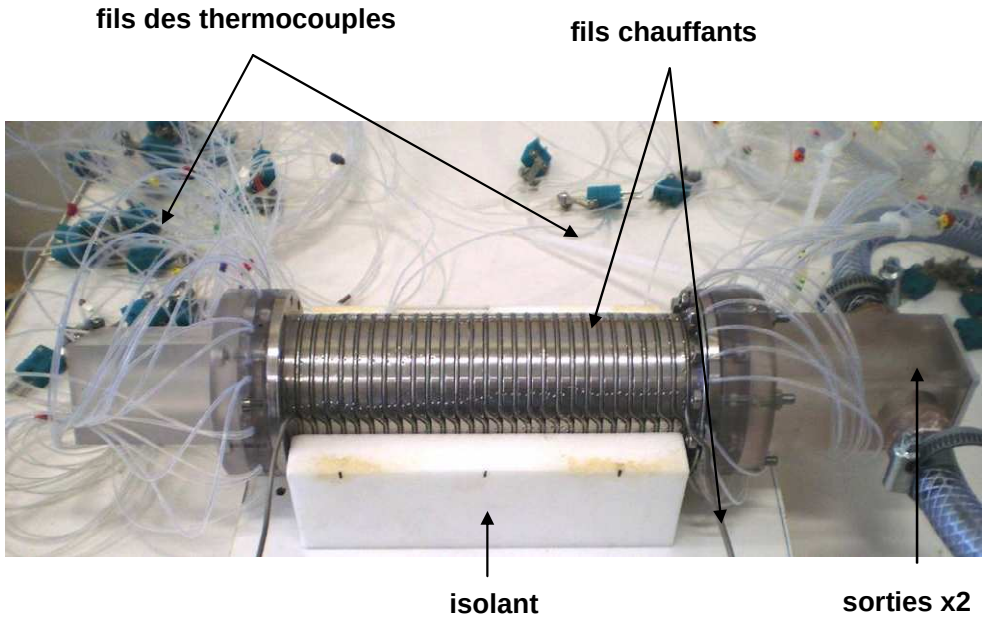

(b)

Figure 30 : (a) Dessin CAO du dispositif expérimental, (b) dispositif expérimental réel en cours de montage

LISTE DES PUBLICATIONS SELON LEUR ORDRE D'APPARITION DANS LE TEXTE

1. Assessment of micro-mixing in turbulent flows by chemical probe
C. Habchi, T. Lemenand, D. Della Valle, H. Peerhossaini
Chemical Engineering Journal, Submitted, 2010a

2. A new adaptive procedure for using chemical probes to characterize mixing
C. Habchi, T. Lemenand, D. Della Valle, Z. Anxionnaz, P. Tochon, M. Cabassud, C. Gourdon, H. Peerhossaini
Chemical Engineering Science, Submitted, 2010b

3. Turbulence behavior of artificially generated vorticity
C. Habchi, T. Lemenand, D. Della Valle, H. Peerhossaini
Journal of Turbulence 11 N°36 (2010c) 1-28

4. Alternating mixing tabs in multifunctional heat exchanger-reactor
C. Habchi, T. Lemenand, D. Della Valle, H. Peerhossaini
Chemical Engineering and Processing 49 (2010d) 653-661

5. Turbulent mixing and residence time distribution in novel configurations of multifunctional exchanger-reactor
C. Habchi, T. Lemenand, D. Della Valle, H. Peerhossaini
Chemical Engineering and Processing, 49 (2010e) 1066-1075

6. Flow structure and heat transfer induced by embedded vorticity
H. Mohand Kaci, **C. Habchi**, T. Lemenand, D. Della Valle, H. Peerhossaini
International Journal of Heat and Mass Transfer 53 (2010) 3575-3584.

7. Entropy production and synergy field principle in turbulent vortical flows
C. Habchi, T. Lemenand, D. Della Valle, H. Peerhossaini
International Journal of Thermal Science, Submitted, 2010f

8. Liquid/liquid dispersion in a chaotic advection flow
C. Habchi, T. Lemenand, D. Della Valle, H. Peerhossaini
International Journal of Multiphase Flow 35 (2009a) 485-497

CORPUS DES ARTICLES

1. Assessment of micro-mixing in turbulent flows by chemical probe

C. Habchi, T. Lemenand, D. Della Valle, H. Peerhossaini

Chemical Engineering Journal, Submitted (CEJ-D-10-01327), 2010a.

SUBMITTED TO

Chemical Engineering Journal

CEJ-D-10-01327

Assessment of micro-mixing in turbulent flows by chemical probe

Charbel Habchi[a,b], Thierry Lemenand[a], Dominique Della Valle[a,c], Hassan Peerhossaini[a,*]

[a] *Thermofluids, Complex Flows and Energy Research Group, LTN – CNRS UMR 6607, École Polytechnique – University of Nantes, rue Christian Pauc, 44306 Nantes, France*

[b] *Agence de l'Environnement et de la Maîtrise de l'Énergie (ADEME), 20 avenue du Grésillé, 49004 Angers, France*

[c] *ONIRIS Géraudière, 44322 Nantes, France*

ABSTRACT

Understanding and quantification of the micro-mixing mechanism is a fundamental issue in industrial chemical processes, especially for fast exothermal reactions. In fact, local mixing that is not "fast enough" compared with the reaction kinetics reduces the selectivity and hence the productivity of the reaction. Micro-mixing can be characterized by chemical probe methods based on observation of a local chemical reaction that results from the competition between turbulent mixing at micro-scales and the reaction kinetics. However, real-world experimental conditions rarely comply with the grounding hypotheses of this method, especially that the micro-mixing is really the limiting factor. Starting from physical considerations, the present study aims to establish some guidelines for obtaining quantitative information from the chemical probe when possible and for improving the accuracy of the method by an adaptive protocol. For the first aspect, an analytical approach is proposed to define the domain of validity based on analysis of the turbulent time scales. For the second, a novel experimental procedure is suggested that entails targeting the concentrations of the chemical species that most strongly affect the local turbulence energy dissipation rate. These rules, which can be generalized to any chemical-probe system and can be applied in any reactor geometry, are illustrated here for the case of an HEV exchanger/reactor with an iodide/iodate reaction system.

Keywords: Micro-mixing, iodide-iodate, chemical probe method, turbulence scales, static mixers, experimental procedure.

[*] Corresponding author: H. Peerhossaini
Phone: + (33)-240 683 124, Fax: + (33)-240 683 141
E-mail address: hassan.peerhossaini@univ-nantes.fr

1. Introduction

Characterizing micro-mixing is an important issue in the “Green Process” scheme, since it governs, in a broad class of industrial processes, byproduct effluents and consequently process efficiency. The selectivity of fast chemical reactions depends on reagent mixing at the molecular scale. In turbulent flows, the species aggregates are reduced in size by the turbulent cascade. In this process, the limiting mechanism occurs at smaller turbulence scales (Baldyga and Bourne [1]). Thus, the sequence of micro-mixing is: i) engulfment in the energetic vortices at Kolmogorov scale, ii) stirring in the viscous-convective subrange, where the fluid particles are subjected to laminar stretching (Batchelor [2]), and iii) molecular diffusion at sub-Batchelor scales that rapidly dissipates the variance in concentration. Understanding and quantifying this mechanism is essential in designing industrial processes involving fast reactions that can present characteristic reaction times smaller than the characteristic micro-mixing time.

The two steps in the micro-mixing mechanism described above are “faster” [1-4] than engulfment at the Kolmogorov scale: as a consequence, micro-mixing depends largely on the turbulence energy dissipation rate, which governs the time and length scale of the smaller eddies. This fundamental property of the turbulent field [5] can be determined by classical velocimetry methods such as laser Doppler anemometry, particle image velocimetry, or hot-wire anemometry, all of which give access, in three-dimensional space, to the nine contributions of the turbulent energy dissipation rate.

Alternative methods to characterize micro-mixing based on observations of a chemical system have been developed over the last few years, especially by Bourne [6] (coupling of naphtol-1 and -2 with diazot sulfanilic acid), and Fournier *et al.* [7] (Villermaux-Dushman reactions or the iodide/iodate method) [1, 9-15]. These techniques, called “chemical probe methods”, are based on the competition between micro-mixing and well known chemical kinetics by the straightforward observation of reaction selectivity, i.e. the secondary product concentrations. Such experiments must be performed under controlled conditions, first by ensuring that the reaction is not fully achieved: the selectivity must be “far” from 0 and 1 to make the reaction product sensitive to the micro-mixing. Under optimal conditions the slowest reaction time is equal to the micro-mixing time. From knowledge of the chemical reaction (mechanism, kinetics and stoichiometry), the local turbulent energy dissipation rate can readily be derived from the measured selectivity via phenomenological micro-mixing models [16].

The appropriate choice of operating conditions (initial reagent concentrations, injection flowrate, stoichiometry, ...) is not trivial and there is as yet no clear methodology for using chemical probes, especially for open-loop flows. The choice of initial concentrations is generally made by “trial and error” and sometimes is not convenient with respect to the reaction kinetics [14-21]. Accurate quantitative results can be obtained if certain conditions on the flow and the chemical system are fulfilled. The purpose of the present work is to examine the limitations of the chemical probe method, and to propose, when possible, solutions to overcome these limitations.

The iodide/iodate reaction system [7-11] and the E-model [18] employed in the present work are widely used to characterize the turbulent kinetic energy (TKE) mass dissipation rate, namely in batch and continuous-flow reactors [15, 22-25]. The chemical probe method and the micro-mixing model are succinctly reprised in section 2. Section 3, which discusses measurement limitations and proposed palliative solutions, has two main features. First, a scaling analysis of turbulence and the interactions among the different scales leads to definition of a validity domain for the chemical probe method. Second, a novel experimental procedure is proposed to adapt the reagent concentrations to the turbulence level and the desired measurement volume at the point in question. Section 4 is devoted to some examples of the improvement that can or cannot result from the present analysis, specifically targeted to the High-Efficiency Vortex (HEV) mixer as compared to previous experiments [15]. Concluding remarks about the application opportunities of the method are given in section 5.

2. Chemical probe: chemical system and micro-mixing model

2.1. The iodide/iodate method

The iodide/iodate system [10, 11, 19] is based on competitive parallel reactions: the quasi-instantaneous borate neutralization (Eq. (1)) and the Dushman reaction [26] (Eq. (2)), which is much slower. The balanced reactions can be modeled as follows:

$$H_2BO_3^- + H^+ \leftrightarrow H_3BO_3 \tag{1}$$

$$5I^- + IO_3^- + 6H^+ \leftrightarrow 3I_2 + 3H_2O \tag{2}$$

The iodine I_2 further reacts with iodide ions I^-, yielding I_3^- ions following the quasi-instantaneous equilibrium reaction:

$$I_2 + I^- \leftrightarrow I_3^- \tag{3}$$

The kinetics of the three reactions was established by Guichardon *et al.* [11]. Only the characteristic time of the slowest reaction in Eq. (2) is described here, since it is used for further calculations [7-11]:

$$t_{r2} = \frac{Min\left(\frac{3}{5}[I^-], 3[IO_3^-], \frac{1}{2}[H^+]\right)}{r_2} \tag{4}$$

where the brackets denote the reagent concentration and r_2 is the rate of the second reaction [11]:

$$r_2 = K_2 \left[I^-\right]^2 \left[H^+\right]^2 \left[IO_3^-\right] \tag{5}$$

In the above equation the constant K_2 is a function of the ionic strength λ as given by Palmer *et al.* [27] and Guichardon *et al.* [11]:

$$\begin{aligned} &\log_{10}(K_2) = 9.28105 - 3.664\sqrt{\lambda} && \text{for } \lambda < 0.166\,\text{M} \\ &\log_{10}(K_2) = 8.383 - 1.5112\sqrt{\lambda} + 0.23689\lambda && \text{for } \lambda > 0.166\,\text{M} \end{aligned} \tag{6}$$

To achieve these reactions, a small quantity of sulfuric acid providing H^+ ions in stoichiometric defect is added to an initial mixture of I^-, IO_3^- and $H_2BO_3^-$. When the micro-mixing is not limiting, the injected H^+ is totally consumed by the instantaneous reaction (1), as long as the borate negative ion is available, and there is no formation of iodine I_2. On the other hand, when the micro-mixing is limiting, a local overconcentration of H^+ can react after reaction (2) and produce iodine I_2, which itself reacts with iodide I^- and yields I_3^- ions (Eq. (3)). The presence of I_2 and I_3^- is hence the manifestation of a mixing time smaller than the second reaction time and can be quantified by a segregation index. In continuous systems, it is defined by Fournier *et al.* [19] and Mohand Kaci [15] as:

$$X_S = 2\frac{[I_2]+[I_3^-]}{[H^+]_0}\left(1+\frac{Q_p}{Q_{H^+}}\right)\left(1+\frac{[H_2BO_3^-]_0}{6[IO_3^-]_0}\right) \quad (7)$$

where Q_p and Q_{H^+} are respectively the principal flow rate of the initial mixture flow and the injection flow rate of sulfuric acid. $X_S = 0$ for perfect micro-mixing and $X_S = 1$ for total segregation on the molecular scale.

In order to determine the I_2 and I_3^- concentrations, the output flow is driven to a spectrometer cell where the light absorption, which is proportional to the concentration of I_3^- ions, is recorded. The iodine $[I_2]$ is derived from the mass balance on iodine, expressed by:

$$[I_2]^2 - \left(\frac{3}{5}[I^-]_0 - \frac{8}{5}[I_3^-]\right)[I_2] + \frac{3}{5}\frac{[I_3^-]}{K_B} = 0 \quad (8)$$

where K_B is the equilibrium constant of reaction (3) given by Palmer *et al.* [27]:

$$\log_{10}(K_B) = \frac{555}{T} + 7.355 - 2.575\log_{10}(T) \quad (9)$$

At 25°C, $K_B = 702\ \text{mol}^{-1}$.

2.2. Micro-mixing model

The segregation index X_S provides only qualitative information on micro-mixing since it depends on the initial concentrations and on the ratio between the main and injection flows. The related quantitative parameter is the intrinsic micro-mixing time, independent of the chemical system, which can be identified by a micro-mixing model devised on phenomenological grounds. Several micro-mixing models exist for determining micro-mixing time and turbulent energy dissipation rate. Villermaux and Devillon [28] developed the interaction by exchange with the mean (IEM) model, which was further simplified by Fournier *et al.* [19]. This model considers that the injected acid is broken up into aggregates that are progressively incorporated by the surrounding fluid containing the initial species. The characteristic incorporation time is related to the micro-mixing time [19, 28]. Baldyga and Bourne [17] have developed a more complex micro-mixing model, the engulfment-deformation-diffusion (EDD) model, based on the assumption of first-order-law growth of the incorporated reagent volume into spiral marbled structures (FIG. 1), which are later homogenized under the stretching effects until near-Batchelor scales, and then molecular diffusion. However, the same authors have established that for Schmidt numbers greater than 4000, the effects of laminar deformation as well as molecular diffusion are negligible relative to the engulfment process. Baldyga and Bourne [18] have hence proposed the simple engulfment model (E-model [18]) for high Schmidt fluids. They, and later Durandal [14], have confirmed that the E-model is more reliable than the EDD and IEM models. Since the E-model is used in the present work, let us recall its main steps. The first is the growth of the volume V_i containing the species i:

$$\frac{dV}{dt} = EV \quad (10)$$

where the engulfment rate E, the inverse of the micro-mixing time, is related to the TKE dissipation rate ε and the kinematic viscosity υ following the analysis of Baldyga and Bourne [18]:

$$E = \frac{1}{t_m} = 0.058\left(\frac{\varepsilon}{\upsilon}\right)^{\frac{1}{2}} \tag{11}$$

Expressing the Eq. (10) in terms of mass balance, the growth of the uniform mixing zone of concentration c_i is given by the TDE (temporal differential equation) [18]

$$\frac{d\,c_i}{d\,t} = E\left(< c_i > - c_i\right) + R_i \tag{12}$$

where $< c_i >$ refers to the mean value in the environment when mixing is completed and R_i is the rate of formation of substance i by chemical reaction.

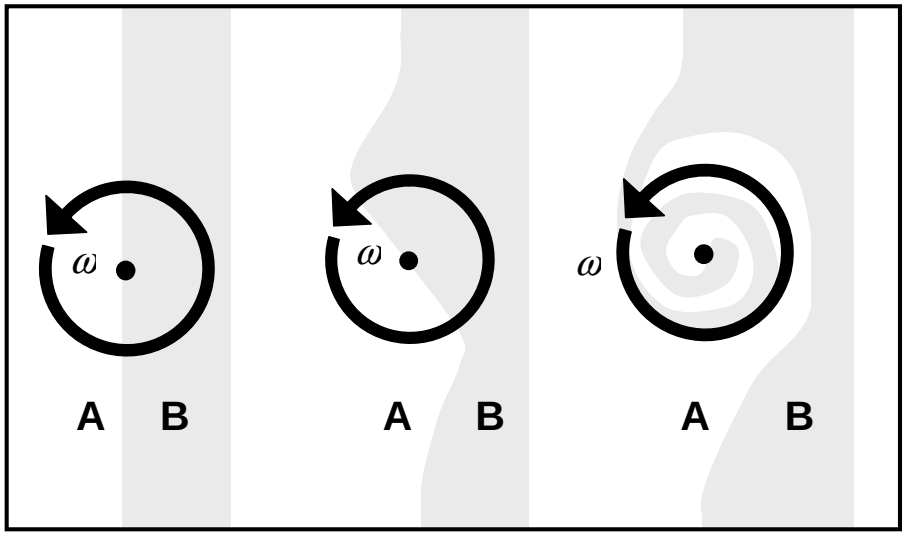

FIG. 1. Principle of the engulfment model (adapted from Baldyga and Bourne [1]).

To find the rate of variation of each species Eq. (12) should be solved for each substance, in the present case it would be a system of nine non-linear equations for the different reagents in the iodide/iodate reaction system. The Newton-Raphson iterative method is employed and computations are made with the software MATLAB™.

The calibration curve is obtained by the set of X_S solutions found by sweeping the mixing time parameter t_m. From the experimental X_S value (Eq. (7)), the micro-mixing time can be determined by the inverse function $X_S = f\left(t_m\right)$. Examples of calibration curves $X_S = f\left(t_m\right)$ for three different initial concentrations of sulfuric acid are shown in FIG. 2. It can be observed that the curve is very flat for both "small" and "large" t_m values. This can be explained from phenomenological considerations. For small t_m, $t_m << t_{r2}$, micro-mixing is very efficient and has no significant influence on X_S, because locally the reagents are "rapidly" homogenized. Eventually, if the large-scale transfers are limiting, the second reaction may develop on a larger volume and its selectivity is hence determined by the global mixing. At the other limit, for very large t_m, $t_m >> t_{r2}$, reaction selectivity is completely governed by the kinetics of the second reaction, and the hydrodynamics have only a weak effect on X_S.

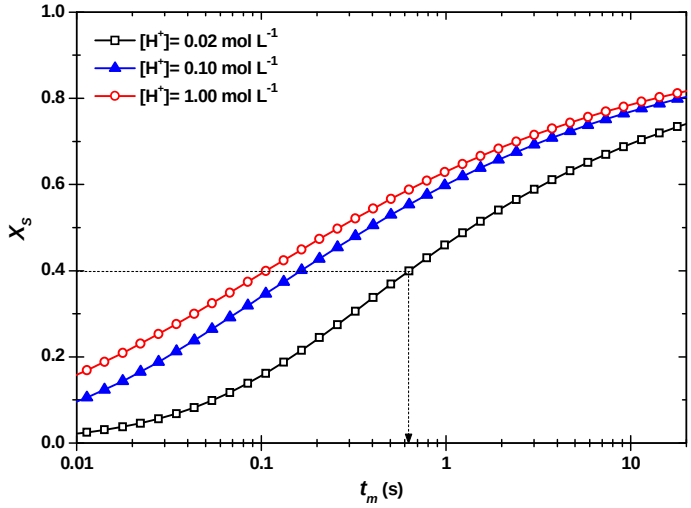

FIG. 2. Calibration curves from the E-model for different initial acid concentrations and for the following concentrations of initial reagents: $[KI]_0 = 0.01165$ mol L^{-1}, $[KIO_3]_0 = 0.00233$ mol L^{-1}, $[NaOH]_0 = [H_3BO_3]_0 = 0.001512$ mol L^{-1}, for $\phi = 15$, the ratio between the main flow velocity and the injection velocity.

3. Measurement limitations and palliative solutions

3.1. pH range

The production of I_2 ought to be due only to the micro-mixing following the development of the Dushman reaction (Eq. (2)). However, the pH of the initial mixture must be greater than pH*, the dissociation pH, where I_2 can be formed thermodynamically under pH* even in the absence of acid [7, 10, 15]. At the same time, the pH must not be too high, or else the iodine I_2 dissociation is not stable. Thus the best range for the initial solution is $8.5 < pH < 9.5$ [7, 10] for pH* near 7. More details about the pH-potential diagram appear in Guichardon and Falk [10].

3.2. Spectrometry range

The formation of I_3^- ions modifies the fluid color, so its absorbance can be measured by using a spectrometer. Obviously, the number of I_3^- ions formed must be in a range compatible with the optical density that can be detected accurately by the spectrometer. This depends, of course, on the spectrometer being used and should be adjusted by modifying the initial reagent concentrations. If the spectrometer detection system is saturated due to high optical densities, the acid concentration must be reduced as well as the iodine concentration, and the concentration of the boric acid must be increased to maintain stoichiometric equilibrium in the system and to respect the pH conditions cited above. This measurement issue was reported by Guichardon and Falk [10], who give some examples from experimental data and suitable adaptations.

3.3. Injection flow effects

3.3.1. Perturbation due to the injection flow

The chemical reactions occur near the injection region, so the hydrodynamics due to injection of the secondary reagent may in some cases affect the selectivity of the second reaction: micro-mixing must be due only to the main flow in the injection location, not to the extra turbulence energy due to the injection.

Let ϕ be the ratio of the local main flow velocity W to the injection flow velocity W_i:

$$\phi = \frac{W}{W_i} \tag{13}$$

To demonstrate that the injection flow can sometimes create artifacts in the chemical probe, measurements were carried out in a circular straight pipe flow for different combinations of main and injection flowrates. The injection is made in the pipe center (dimensions are given in Table 1), with constant concentrations for all Reynolds numbers.

	Pipe diameter D	Total length L	Tab inclination α
Straight pipe	20 mm	140 mm	-
HEV mixer	20 mm	140 mm	30°

Table 1. System dimensions

The selectivity is plotted versus the velocity ratio in FIG. 3. There is a critical value $\phi_o = 10$ beyond which the selectivity remains independent of ϕ, as is theoretically expected. For low ratios, on the other hand, the chemical reactions undergo intrusive effects from the injection. For the present example, the range $11-18$ appears to be the optimal velocity ratio for ϕ, first by ensuring that there is no influence of the injection, and also because for higher ϕ values, there is a risk of back-mixing in the injection needle.

Ferrouillat *et al.* [35] have made this test in a rectangular pipe flow and found a critical flow-rate ratio about 3000, which corresponds to velocity ratio ϕ_o about 15, consistent with our estimate.

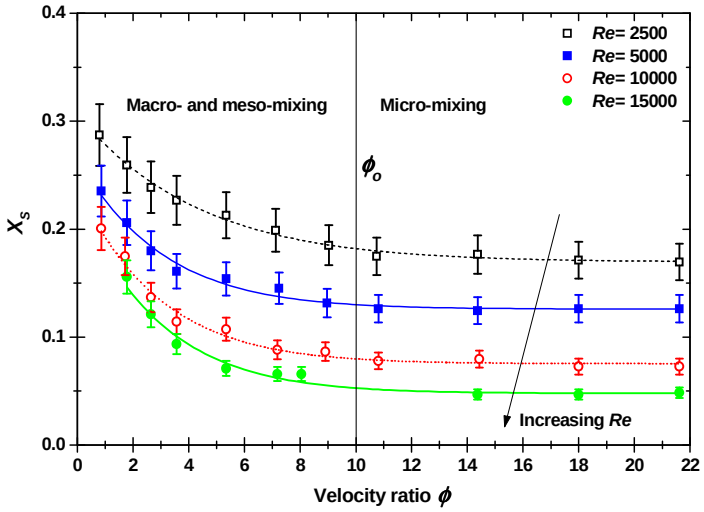

FIG. 3. Evidence of a critical velocity ratio ϕ_0 beyond which there is no effect of the injection on the selectivity (results adapted from Mohand Kaci [15]) for measurements in the center of an empty pipe for constant initial concentrations $[KI]_0 = 0.01165$ mol L^{-1}, $[KIO_3]_0 = 0.00233$ mol L^{-1}, $[NaOH]_0 = [H_3BO_3]_0 = 0.001512$ mol L^{-1}, $[H^+]_0 = 1$ mol L^{-1}.

3.3.2. Analysis of the meso-mixing scales

Two meso-mixing mechanisms have been identified by Baldyga *et al.* [31]: first, the turbulence dispersion of the feed stream into the main flow, in both the radial and streamwise directions, and second the break-down of injected aggregates in the turbulent cascade, from the large integral scale to the Kolmogorov scales. The corresponding time scales are computed in this section.

a) Time scales

Following concepts of Batchelor [2] and Corrsin [32], Baldyga and Bourne [31] defined two characteristic times for the turbulent dispersion mechanism, in the streamwise and radial directions relative to the injection, t_{D1} and t_{D2} respectively:

$$t_{D1} = \frac{Q_i}{W\, D_t} \tag{14}$$

$$t_{D2} = \frac{d^2}{4 D_t} \tag{15}$$

where d is the feed pipe internal diameter, Q_i is the injection flow rate and D_t is the turbulent diffusivity of the main flow, which is classically modeled with the TKE k and the dissipation rate ε [34]:

$$D_t = 0.1\frac{k^2}{\varepsilon} \tag{16}$$

The injection flow rate Q_i is expressed by the injection velocity:

$$Q_i = \frac{\pi d^2}{4} W_i \tag{17}$$

Replacing the velocity ratio W / W_i by ϕ, and the turbulent diffusivity coefficient by its expression in Eq. (16), t_{D1} and t_{D2} can be expressed by:

$$t_{D1} = \frac{\pi}{0.4}\frac{d^2}{\phi}\frac{\varepsilon}{k^2} \tag{18}$$

$$t_{D2} = \frac{d^2}{0.4}\frac{\varepsilon}{k^2} \tag{19}$$

When the injected feed stream is larger than the turbulent eddies, the concentration fluctuations break down from the integral scale Λ (convective-inertial large-scale) towards Kolmogorov's micro-scales by a mechanism called *inertial-convective meso-mixing*. For fully developed turbulence, the characteristic time (cascade time) is given by [2, 32]:

$$t_C = 2\left(\frac{\Lambda^2}{\varepsilon}\right)^{1/3} \tag{20}$$

If the injection momentum is moderate, the injected particles are instantaneously submitted to the main-flow velocity field. In this case, with L_0 the initial radius of the reactive jet that is convected with local velocity W, it follows by continuity that [31] $Q_i \approx \pi L_0^2 W$, by assuming that $\Lambda = L_0$ (Baldyga *et al.* [33]), leading to:

$$\Lambda = \sqrt{\frac{\phi d^2}{4}} \tag{21}$$

By combining Eq. (20) and Eq. (21), the inertial-convective meso-mixing characteristic time can be estimated by:

$$t_C = 1.26\left(\frac{d^2}{\phi\varepsilon}\right)^{1/3} \tag{22}$$

b) Comparison with micro-mixing time

In order to compare these different time scales with the micro-mixing time, three dimensionless parameters are defined, $\tau_1 = t_{D1}/t_m$, $\tau_2 = t_{D2}/t_m$ and $\tau_3 = t_C/t_m$, written as follows:

$$\tau_1 = 0.145\pi\frac{d^2}{\phi\upsilon^{1/2}}\frac{\varepsilon^{3/2}}{k^2} \tag{23}$$

$$\tau_2 = 0.145\frac{d^2}{\upsilon^{1/2}}\frac{\varepsilon^{3/2}}{k^2} \tag{24}$$

$$\tau_3 = 0.073\frac{d^{2/3}}{\phi^{1/3}\upsilon^{1/2}}\varepsilon^{1/6} \tag{25}$$

These parameters provide a criterion for the domain in which the chemical probe method can reach the micro-mixing time, that is when τ_1, τ_2 and $\tau_3 < 1$.

In this system, the independent parameters that may affect turbulent mixing near the injection are the feed needle diameter d and the velocity ratio ϕ for a given main flow rate. Eqs. (23)-(25) highlight the dependence on these parameters by expressing the turbulence kinetic energy and its dissipation rate with dimensional analysis, with the typical scales $\overline{W}$, the average flow velocity, and D, the reactor diameter. In the same way, the local velocity W is also normalized by the average velocity:

$$k = C_k\overline{W}^2 \tag{26}$$

$$\varepsilon = C_\varepsilon\frac{\overline{W}^3}{D} \tag{27}$$

$$W = C_W\overline{W} \tag{28}$$

Assuming dynamical similarity for a narrow range of Reynolds number, where the flow pattern does not change significantly, the coefficients C_k, C_ε and C_W depends only on location and not on the Reynolds number.

By substituting Eqs. (26) and (27) into Eqs. (23)-(25), the characteristic time ratios read:

$$\tau_1 = 0.145\pi \frac{C_\varepsilon^{3/2}}{C_k^2 D^{3/2} \upsilon^{1/2}} \frac{d^2}{\phi} \bar{W}^{1/2} \tag{29}$$

$$\tau_2 = 0.145 \frac{C_\varepsilon^{3/2}}{C_k^2 D^{3/2} \upsilon^{1/2}} d^2 \bar{W}^{1/2} \tag{30}$$

$$\tau_3 = 0.073 \frac{C_\varepsilon^{1/6}}{D^{1/6} \upsilon^{1/2}} \frac{d^{2/3}}{\phi^{1/3}} \bar{W}^{1/2} \tag{31}$$

An analytical study was carried out with Eqs. (29)-(31) to investigate the domain of validity in an arbitrary case. The example used here is flow in a straight pipe of hydraulic diameter $D = 20$ mm, with assumed local constants $C_k = 0.455$, $C_\varepsilon = 0.971$ and $C_W = 0.125$ (corresponding results are shown in FIG. 4) . The region where all the time ratios are less than 1 is hatched in FIG. 4, where the characteristic time ratios are plotted successively as a function of the three independent parameters ϕ, d, and $\bar{W}$, two of them assumed to be in the nominal state for each case. In FIG. 4a a critical value for the velocity ratio $\phi_o = 7$ is obtained from the criterion $\tau_3 < 1$, since it is the highest relative to τ_1 and τ_2. FIG. 4b shows that if the feed pipe diameter d is increased, meso-mixing overcomes micro-mixing as τ_2 becomes greater than 1. The higher main flow rates as well lead to $\tau_2 > 1$ in FIG. 4c, since the time ratios are an increasing function of $\bar{W}$. It is seen that, from this analysis, it is possible to evaluate theoretically the optimal value of the velocity ratio ϕ and of the feed pipe diameter d for given conditions.

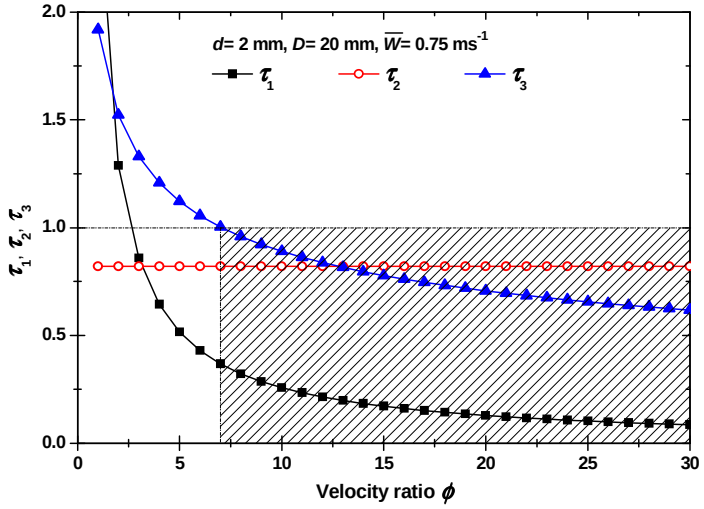

(a)

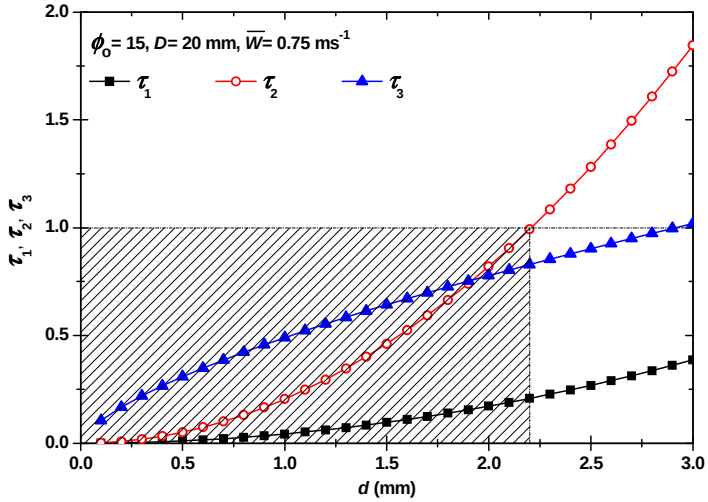

(b)

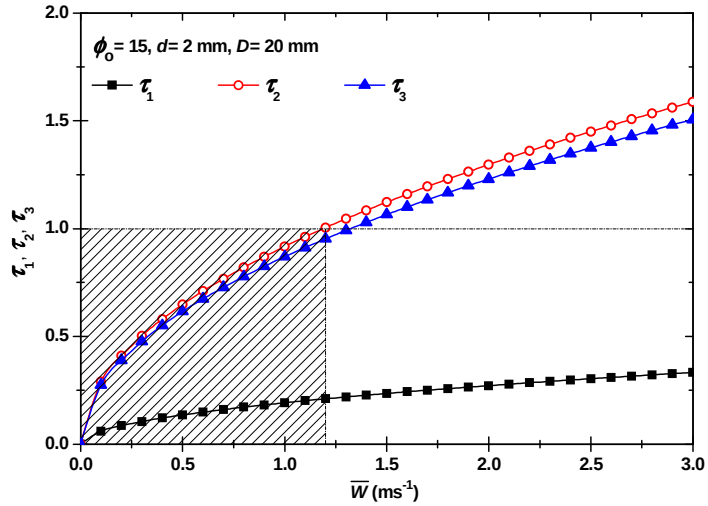

(c)

FIG. 4. Domain of validity of the chemical probe method for characterizing micro-mixing time depending on (a) velocity ratio, (b) feed pipe diameter and (c) mean flow velocity.

3.4. Measurement volume requirements

Micro-mixing is a local and small-scale mechanism, and thus should be achieved at a short distance from the injection point, meaning that convective transfer by the main stream velocity is small. Since the residence time in the reactor is $t_{Res} \approx L/\overline{W}$, it is self-evident that $t_{r2} << t_{Res}$ in order to get a second reaction time close to t_m.

Reciprocally, at velocity W, the second reaction length can be evaluated by $L_{r2} \approx W t_{r2}$. It is possible to "tune" t_{r2} so that L_{r2} is at the reactor scale, and in that case, the selectivity will be the signature of the global mixing properties. This could be a deliberate choice in experimental design in order to characterize the global mixing efficiency.

3.5. An adaptive method

This section proposes a practical method for experiments by exploring the different degrees of freedom influencing the selectivity of the chemical probe system, as summarized in the flowchart of FIG. 5.

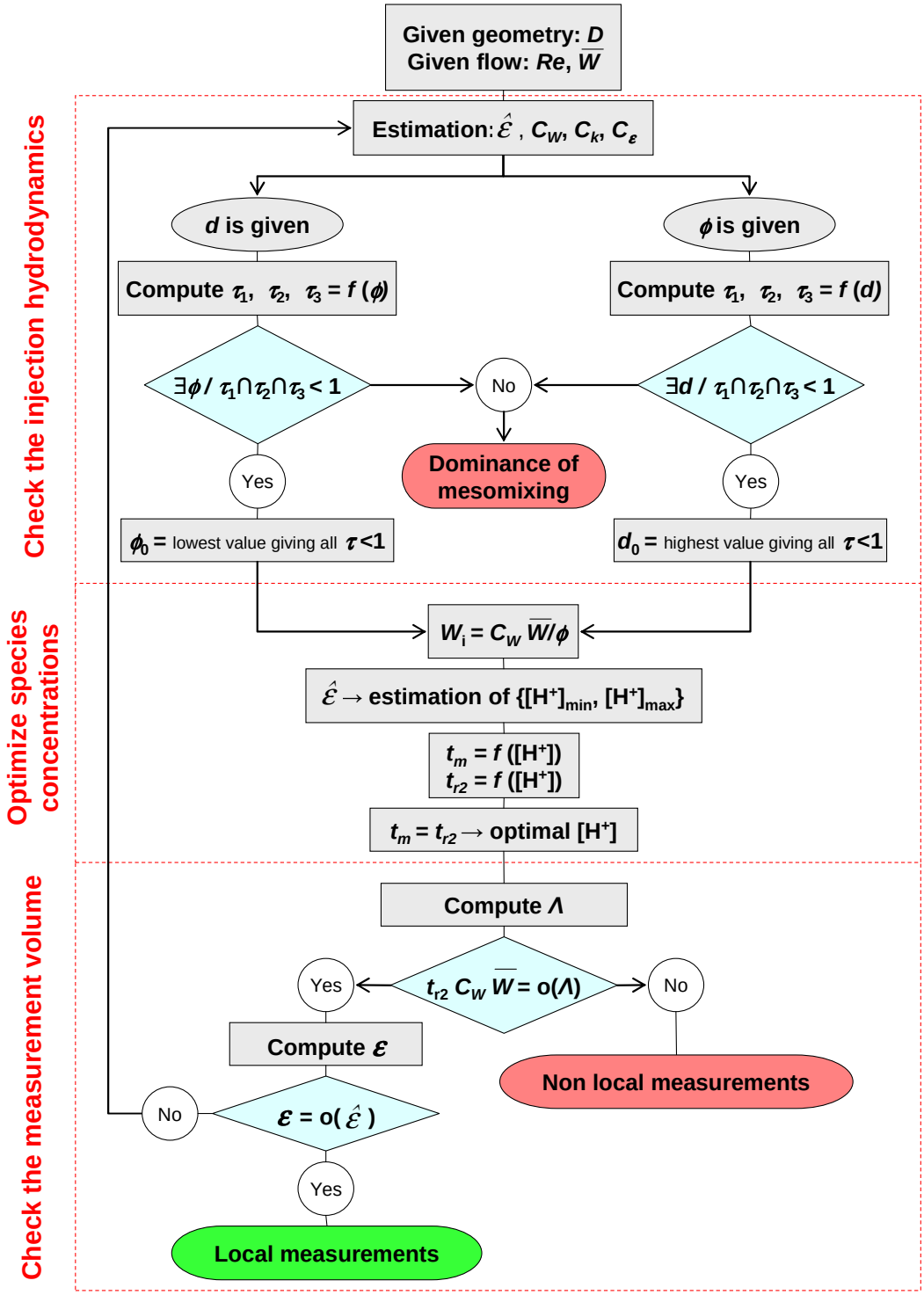

FIG. 5. Flowchart of the adaptive procedure for the chemical probe method for micro-mixing characterization.

First, to ensure that the flow is not perturbed by the injection, the velocity ratio ϕ must be higher than the critical value, and this condition must be checked for all operating conditions. For a full rig

design, the same logic allows evaluation of the maximal value of the feed pipe diameter d for a given ϕ. This case is relatively rare and the reasoning here is confined to a given needle size. The limiting mixing times can be computed from Eqs. (23)-(25) above.

In a second step, the reagent concentrations are varied to target the greatest sensitivity of the segregation index to the flow dynamics, and finally to the measurement of t_m, when $t_m = t_{r2}$. Hence, the initial reagent concentrations must be adapted for each location, especially if the hydrodynamic and turbulence levels are not homogeneous in the reactor. Since all the initial concentrations are linked (except for the sulfuric acid, which is contained in a separate tank), it is more tractable to modify the concentration of the $[H^+]$ ions, although the procedure might also be applied by modifying the other reactive concentrations (that would be necessary in any event if the convenient $[H^+]$ value does not correspond to a stoichiometric defect). Then the measured micro-mixing time t_m obtained by the engulfment model is plotted with the characteristic time for the second reaction t_{r2}, computed from Eq. (4), versus the H^+ concentrations. The experimental range of $[H^+]$ can be estimated from the turbulence energy dissipation rate in the flow from the pressure drop. For example, if it is known that in a given flow the turbulence energy dissipation rate is of the order of 10 m^2s^{-3}, then the micro-mixing time, following Eq. (11), is about 5.5 ms. The criterion $t_m = t_{r2}$ gives the order of magnitude of t_{r2} and thus the concentration of H^+, about 0.5 mol L^{-1} in this example. We suggest that the range of values of H^+ concentration in the FIG. 12 (5 fold) is generally sufficient to handle the local dissipation rate in an open-loop flow (a factor of ten would be desirable in a stirred tank), in the same example that leads to the interval $0.1 < [H^+] < 2.5$. The intersection between the curves t_m and t_{r2} indicates the optimal H^+ concentration, and the corresponding segregation index can be retained.

The last step is to check the local character of the probe by computing the measurement volume. If the measurement scale $L_{r2} \approx W t_{r2}$ is smaller than or of the order of magnitude of the meso-scale computed from Eq. (21), then the measurement can be considered local and only the micro-mixing process is characterized by the chemical probe method. Conversely, if the measurement scale L_{r2} is much larger than the meso-scale, then the measurement cannot be considered local and the chemical probe method must characterize not only the micro-mixing process but also the large-scale mixing. Hence, if the turbulence energy dissipation rate ε obtained is not in the order of magnitude of the estimate $\hat{\varepsilon}$, then a new estimate must be made to iterate the procedure for a new value of $\hat{\varepsilon}$.

4. Application to an online-mixer

4.1. Experimental setup and methods

4.1.1. Test section

The geometry of the HEV static mixer, used here, consists in a circular pipe equipped with seven rows of vortex generators placed at the wall; see FIG. 6 and Table 1. The so-called vortex generators induce coherent structures topologically similar to those found in concave boundary layers and in wall turbulence [36-45]. Two main features are identified (see FIG. 7):

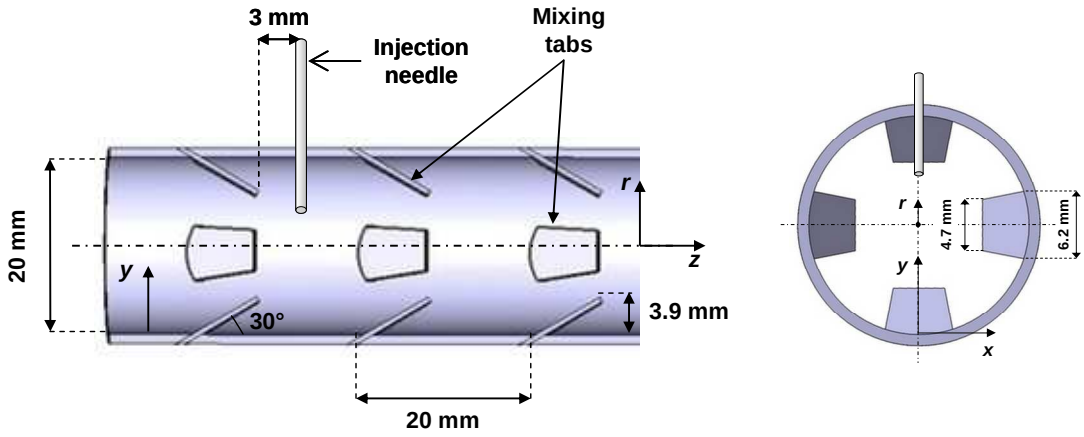

(a) (b)

FIG. 6. Schematic views of (a) the mixer cross section showing three elements and the injection needle location, and (b) the trapezoidal vortex generator dimensions.

- A streamwise counter-rotating vortex pair (primary CVP) with a common upflow in the tab symmetry plan, and a pair of secondary CVPs of very small volume close to the wall, with an associated common inflow
- A periodic sequence of hairpin vortices convecting downstream and riding on top of the CVP [39], corresponding to a maximum turbulence kinetic energy dissipation rate located at a radial position of around y/R= 0.4 [38, 40-42].

The measurements are taken in the typical locations B, S and W, given in Table 2, in the tab symmetry plane at the cross section, 3 mm downstream from the first tab array, as shown in FIG. 7.

B	Bulk flow region	y/R= 1.0	high velocity	low turbulence low gradients
S	Shear layer region	y/R= 0.2	moderate velocity	high turbulence high gradients
W	Wake of the tab	y/R= 0.4	low velocity	moderate turbulence low gradients

Table 2. Measurement locations

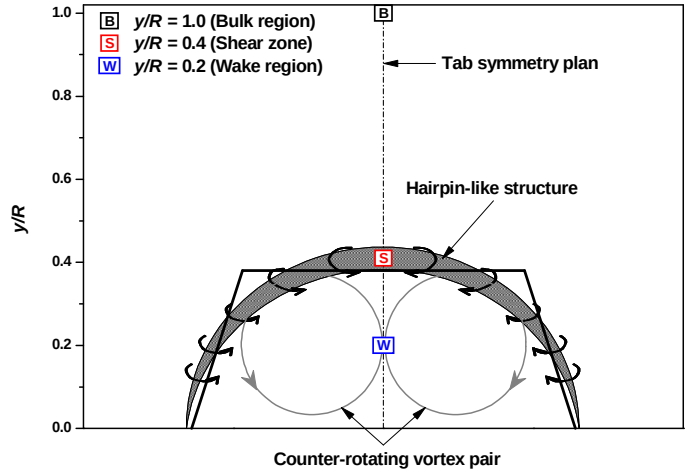

FIG. 7. Schematic view of the flow structure downstream from the vortex generator and the locations of the measurement points.

4.1.2. Reagent preparation

The initial reagents (KI, H_3BO_3, $NaOH$) are supplied as solid phase with purity ranges between 98% and 99.5% and are weighed with an analytical balance of 5×10^{-5} g accuracy. A resin is used to deionize the tap water (< 5 µ Siemens). The solution must be prepared according to the following procedure: all components are dissolved separately in the non-ionized water. First H_3BO_3 and $NaOH$ are poured in the main tank so the buffer solution achieves pH*. Then, KI and KIO_3 are successively added to the buffer solution. The concentrations are corrected by eventual addition of deionized water.

4.1.3. Hydraulic loop and injection system

The solution is mixed by an immersed pump and its temperature is kept constant at 298 K by a helical heat exchanger whose temperature is controlled by a thermostat (Crythermostat 71 Huber). As shown in FIG. 8, the mixture is driven by a rotary pump into the hydraulic loop. The main flow rate is determined by a precision balance and data acquisition is realized by Labview™ software.

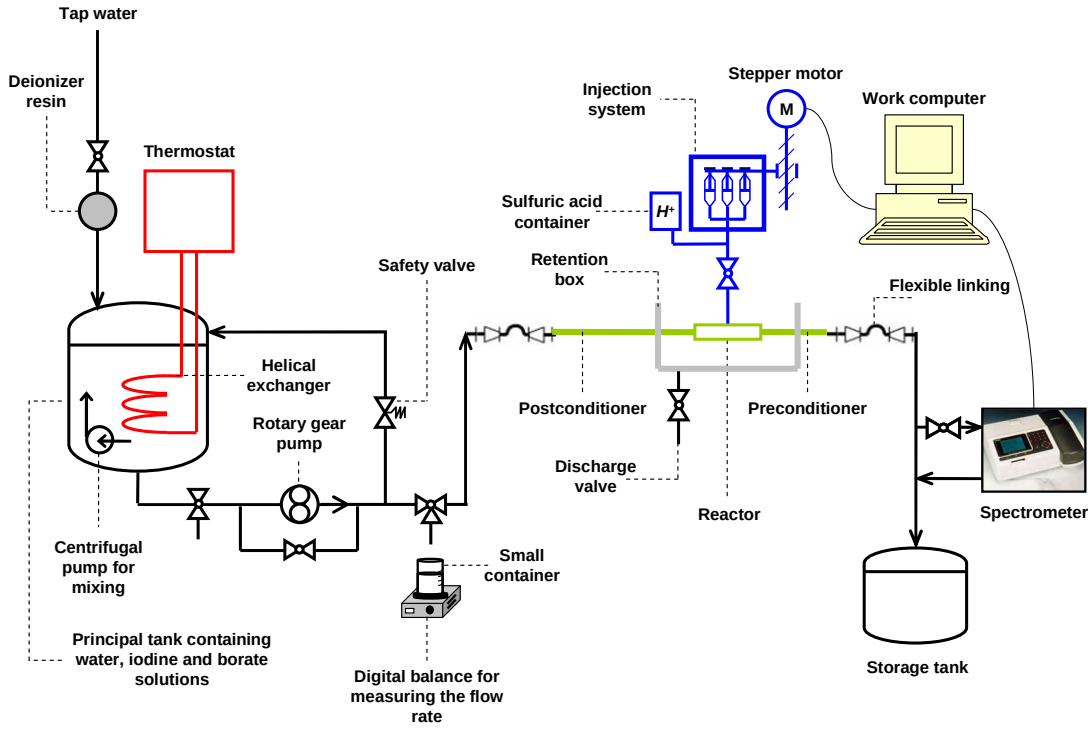

FIG. 8. Diagram of the hydraulic loop and injection system.

The sulfuric acid injection system consists of a regulated step motor connected to a multi push-syringe system: when the syringes are pushed down, sulfuric acid is injected into the reactor; when pulled up, the syringes are filled from the sulfuric acid container. The sulfuric acid is injected into the test section through an injection needle of 0.6 mm internal diameter connected to the syringes by flexible tubes.

The location of the needle in the reactor cross section is determined by a displacement mechanism, as shown in FIG. 6, with an accuracy of 10 µm. The flow rate of the acid injection is controlled by a velocity regulator on the angular velocity of the stepper motor via a PC.

The test section is incorporated in the hydraulic loop elements by flexible linking to avoid fluctuations due to pump vibration. The reactor is preceded by a straight-pipe preconditioner of 1.5 m length to ensure fully developed turbulent flow at the reactor inlet, and followed by a postconditioner of 0.3 m length.

The final products of the reaction are analyzed in continuous flow through a channel placed 0.3 m downstream from the reactor outlet and branched to a spectrometer (Jenway 6505™) of resolution 0.1 nm and bandwidth 1.8 nm whose wavelength ranges between 190 nm and 1100 nm. The measurable absorbance range of this spectrometer lies between 0 and 3, with 0.1% accuracy. The measurements of the I_3^- ion absorbance are performed in the UV domain.

4.2. Results and discussion

4.2.1. Context

In previous work [15], the chemical probe was used to study the micro-mixing properties of the HEV in the experimental rig described above. All runs were carefully performed with the set of constant concentration given in Table 3 [15]. In addition, the flow pattern and turbulent field of this reactor are thoroughly characterized by different velocimetry methods (LIF, PIV, LDA) and numerical analysis [15].

Reagents	H_3BO_3	NaOH	KIO_3	KI^-	H^+
Concentrations ($\times 10^3$ mol L^{-1})	1.512	1.512	2.33	11.65	1000

Table 3. Species concentrations

FIG. 9 plots the ratio between the chemical probe value and the reference value $\varepsilon_{chem} / \varepsilon_{num}$, versus the reference turbulence energy dissipation rate for all the runs, i.e., for Reynolds numbers between 7500 and 15000, in different locations. It can be observed from this figure that the "discrepancy factor" is clearly correlated with the level of turbulence: for the very low values, it makes intuitive sense that the injection strongly interferes with the main flow and that the chemical probe cannot measure the micro-mixing. At the other extreme, for the higher turbulence levels, the chemical probe is accurate in all cases, meaning that all the conditions are fulfilled. At intermediate values, here about $\varepsilon_0 \approx 2.5\ \mathrm{m^2\,s^{-3}}$, the discrepancies have a "stochastic" aspect and the question is thus to examine if these measurements can be improved.

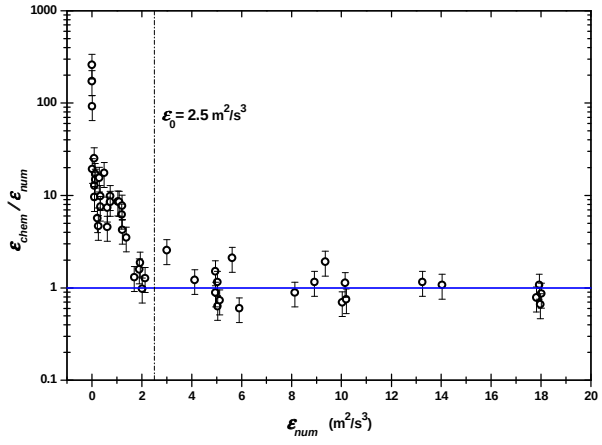

FIG. 9. Discrepancy ratio $\varepsilon_{chem} / \varepsilon_{num}$ vs. ε_{num} gathering the runs of Mohand Kaci (adapted from Mohand Kaci [15]).

The procedure is then applied in these conditions, when the Reynolds number is 12500, for the three locations B, S, and W (in the outlet cross section) shown in FIG. 7 (and Table 2). These positions are obtained in the previous numerical simulations [40-42], Table 4 recapitulates the constants C_W, C_k and C_ε, the effective velocity ratio ϕ used for the measurements, and the local velocity W for each location. In the present case, the injection diameter is $d = 0.6$ mm and the mean flow velocity is $\overline{W} = 0.625\ \mathrm{ms^{-1}}$.

Measurement location	C_k	C_ε	C_W	k ($\mathrm{m^2s^{-2}}$)	ε ($\mathrm{m^2s^{-3}}$)	W ($\mathrm{ms^{-1}}$)	ϕ_0
Bulk B $(y/R = 1.0)$	4.42×10^{-3}	4.21×10^{-4}	0.983	1.73×10^{-3}	5.14×10^{-3}	0.614	7.61
Shear S $(y/R = 0.4)$	0.24	0.70	0.169	9.50×10^{-2}	8.60	0.106	1.31
Wake W $(y/R = 0.2)$	0.13	0.51	0.312	5.07×10^{-2}	6.20	0.195	2.42

Table 4. Local hydrodynamic parameters independent of Reynolds number (adapted from Habchi *et al.* [40]) and local values for *Re*= 12500

4.2.2. Injection hydrodynamics

The domain of validity of the chemical probe method is determined by sweeping the only "free" parameter, the velocity ratio ϕ, as shown in FIG. 10. Following the approach described in section 3.5, the hatched regions represent the domain of validity in which the micro-mixing is unaffected by the injection. For measurements in the bulk region (point B in FIG. 10a), the velocity ratio ϕ_o that defines the validity domain tends to zero under the nominal conditions, meaning that the micro-mixing is always the limiting process at this location and that any velocity ratio ϕ value can be used for measurements here, where the local ϕ is $\phi_{measurement} = 7.6$. In FIG. 10b, for measurements in the shear region (point S), $\phi_0 = 0.65$ as given by τ_1, so that the local operating value $\phi_{measurement} = 1.31$ is consistent with the domain of validity. In FIG. 10c, in the wake region, it can be seen that τ_2 is always greater than 1. Therefore, whatever the velocity ratio in this region, the chemical probe method cannot be applied unless the needle diameter is refined to decrease τ_2.

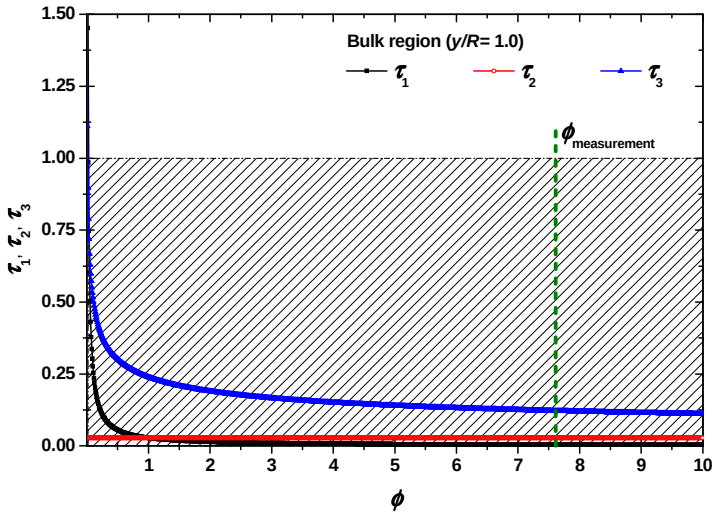

(a)

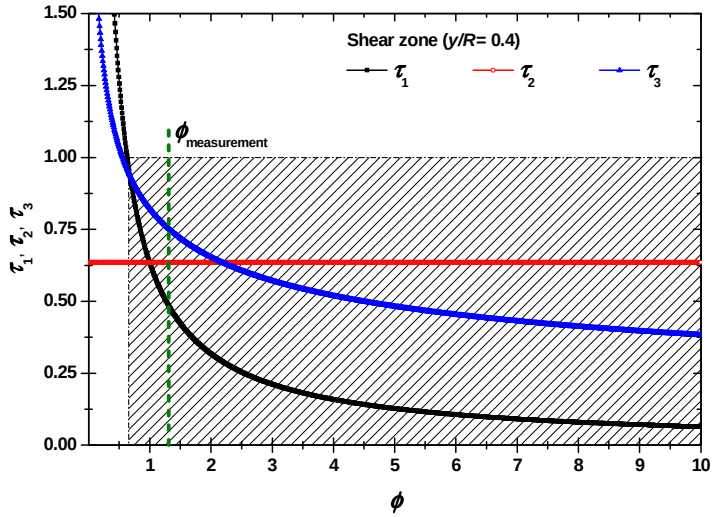

(b)

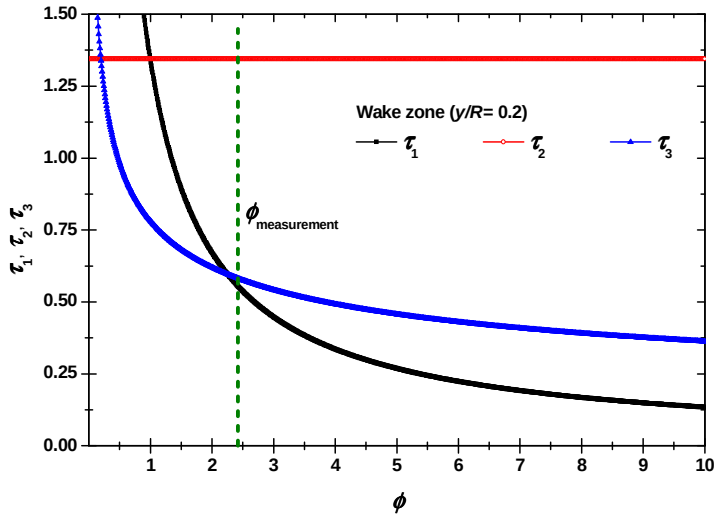

(c)

FIG. 10. Time ratio in the (a) bulk region, (b) shear region and (c) wake region as function of the velocity ratio, for *Re*= 12500.

4.2.3. Optimal [H+] for the micro-mixing time measurement

With the method discussed in section 3.5, the measurements are performed by sweeping the H^+ concentration between 0.2 and1 $\mathrm{mol\,L^{-1}}$. The second reaction time is computed by Eq. (4) as a function of $[H^+]$, and both are plotted in FIG. 11. The sulfuric acid concentration is taken where the second reaction time curve crosses the micro-mixing time. Hence, a convenient $[H^+]$ is determined for the three locations B, S, and W, and the corresponding mixing times and dissipation rates can be derived.

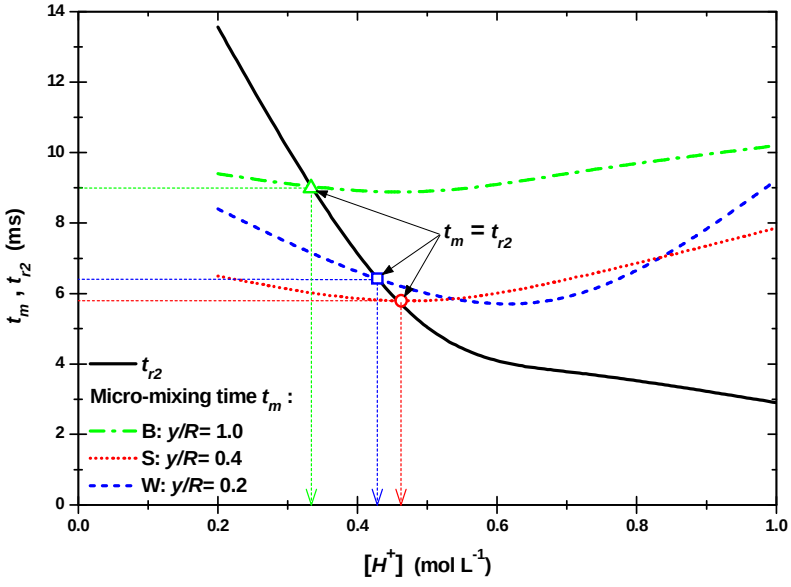

FIG. 11. Determination of suitable $[H^+]$ concentration for $t_m = t_{r2}$ in the bulk (B), shear (S) and wake (W) regions, for *Re*= 12500.

From these values of $[H^+]$ it is then possible to obtain the absolute value of the segregation index, which can then be used to compare the quality of the micro-mixing process in the three geometries, as shown in FIG. 12. These values are recapitulated in Table 5 for the three locations.

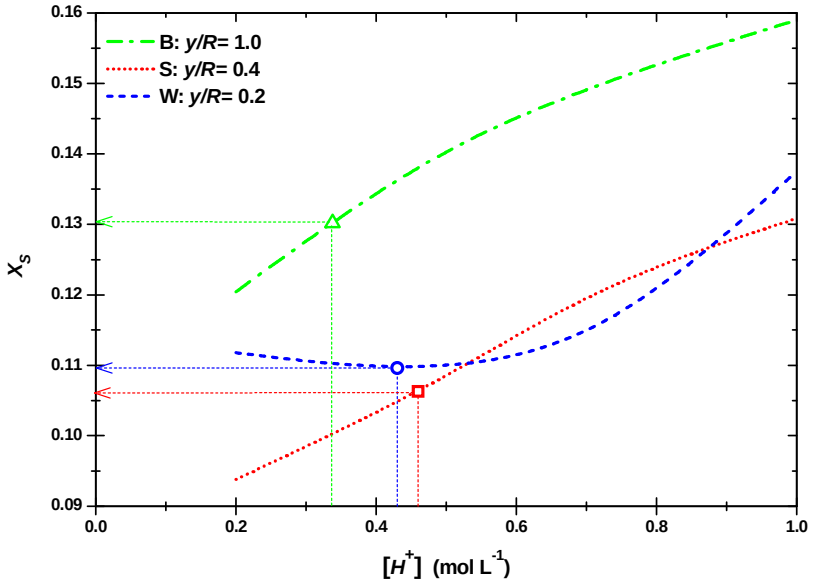

FIG. 12. Determination of the segregation index for $[H^+]$ in the bulk (B), shear (S) and wake (W) regions, for *Re*= 12500.

Measurement location	$[H^+]$ (mol L^{-1})	X_S	$t_m = t_{r2}$ (ms)	ε (m^2s^{-3})
Bulk B $(y/R = 1.0)$	0.336	0.130	9.111	3.581
Shear S $(y/R = 0.4)$	0.434	0.106	5.741	9.019
Wake W $(y/R = 0.2)$	0.462	0.110	6.338	7.400

Table 5. Nominal $[H^+]$ and results obtained from the chemical probe measurements in the three locations for *Re*= 12500

4.2.4. Measurement volume

This section analyzes the measurement volume $L_{r2} = W\, t_{r2}$ and its comparison to the meso-scale of Eq. (21). In the bulk region the effective turbulence energy dissipation rate obtained from numerical simulations [40-42] is rather small, about 5×10^{-3} m^2s^{-3}, yielding a mixing time of about 0.24 s. Since the local flow velocity is high (0.614 ms^{-1}), the measurement length is $L_{r2} = W\, t_{r2} = 14.77$ cm, much larger than the 1.10 cm meso-scale computed at this location. Thus, determination of the turbulent dissipation rate in the bulk region, B, is not possible when using the chemical probe method with this injection needle size.

For location S in the shear layer, the real turbulence energy dissipation rate is higher $(8.6\ m^2s^{-3})$ than that obtained from numerical simulations [40-42] and the corresponding mixing time is about 5.88 ms; the measurement length is close to $L_{r2} = W\, t_{t2} = 0.62$ mm. Meanwhile the meso-scale is 0.46 mm, indicating that the chemical reaction takes place locally and that the determination of the micro-mixing time and the local ε is meaningful.

The case of the wake location W is already disqualified, and thus analysis of the meso-scales is unnecessary.

4.3. Discussion

FIG. 13 compares the turbulent energy dissipation rates obtained by the adaptive method of chemical probe with those obtained from previous chemical probe measurements; these were carefully carried out by Mohand Kaci [15] using the classical procedure, but without rigorous analysis and understanding of the validity of the chemical method [15, 40-42]. The reference values in FIG. 13 are quoted from numerical and LDA measurements, remembering that these methods also have their own drawbacks.

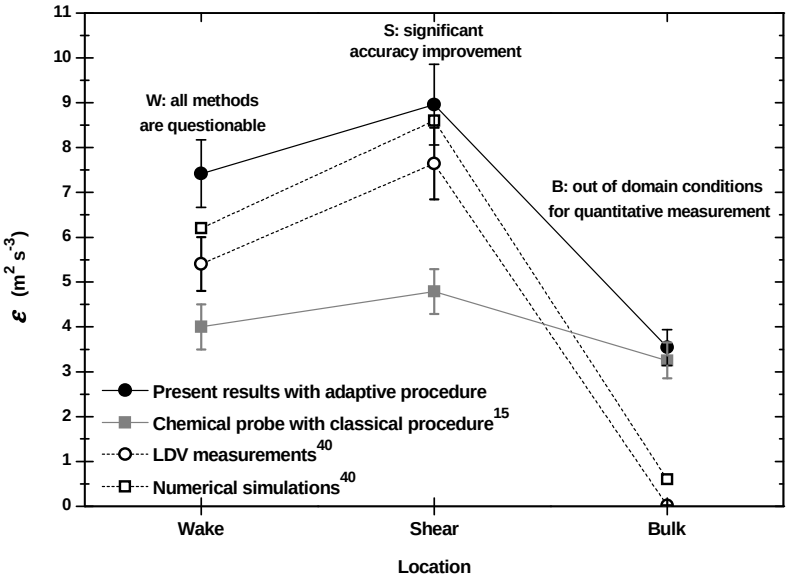

FIG. 13. Improvement in ε determination by the adaptive method for *Re*= 12500.

In the bulk zone (point B), we have shown that the limitation is the non-local character of the measurement, as the turbulence is not sufficient to compete with the convective effects. The new measurement is no closer to the reference points than the former, and cannot be improved with the present needle diameter.

In the wake zone (point W), the optimized method can bring no new information, as mentioned in the local analysis of time scales (section 4), but it can be noted that all the velocimetry methods lose their reliability in the case of zero average velocity fields.

The significant improvement is obtained in the shear zone (point S) by adapting the reaction kinetics. Compared with the more than 50% deviation in the classical method, the accuracy is now in the same range as that of optical and numerical methods (within 3%).

5. Concluding remarks

The present analytical and experimental investigation of micro-mixing quantification using chemical probe methods provides a better understanding of the different limitations that arise in the final determination of local turbulence energy dissipation rate. The first part of this study details the chemical-probe principle, focusing on the iodide/iodate method and its two parallel-competitive chemical reactions. This method suggests a segregation index that gives a measure of the selectivity

of the reaction system. The E-model, a phenomenological micro-mixing model developed by Baldyga and Bourne [18], is used to determine the turbulence energy dissipation rate.

This study proposes a synthetic experimental procedure to ensure the validity and enhance the accuracy of such methods. In the first step, an analytical study based on the hydrodynamics of the injection suggests checking if the three independent key parameters determining which mechanism controls the turbulence mixing are simply less than unity. By comparing the meso- and micro-time scales, these parameters define the domain of validity of the chemical probe. In the second step, optimal values for the operating conditions are set by sweeping the injected acid concentration in an appropriate range, estimated by the order of magnitude of the mass energy dissipation rate. The retained concentrations correspond to the crossover of the micro-mixing times and the predicted reaction time. The third and final step is to assess the measurement volume; i.e. to check whether the operating acid concentration corresponds to a reaction volume significantly under the reactor size. Accomplishing all these steps guarantees that the measurement is local and accurate.

The adaptive method is applied to the HEV (High-Efficiency Vortex) inline mixer to illustrate that in some cases the chemical probe measurements can be significantly improved by this adaptive method compared to previous measurements carried out by the classical method.

Acknowledgment

The authors gratefully thank Dr. H. Mohand Kaci for his help in measurements using the chemical probe method. The authors thank also the Technical Study and Manufacturing Service “SEF” of the LTN for the construction of the hydraulic loop and injection system.

References

[1] J. Baldyga, J. R. Bourne, Turbulent mixing and chemical reaction, Chichester, England: Wiley, 1999.

[2] G. K. Batchelor, The theory of homogeneous turbulence, Cambridge University Press, Cambridge, England, 1953.

[3] J. Baldyga and J. R. Bourne, Principles of micro-mixing, Encyclopedia of Fluid Mechanics, Gulf Publishing, Houston, TX, 1986.

[4] J. Baldyga and R. Pohorecki, Turbulent micro-mixing in chemical reactors – a review, The Chem. Eng. J. 58 (1995) 183.

[5] J. M. Wallace, Twenty years of experimental and direct numerical simulation access to the velocity gradient tensor: what have we learned about turbulence, Phys. Fluids 21 (2009) 021301.

[6] J. R. Bourne, An improved reaction system to investigate micro-mixing in high intensity mixers, Ind. Eng. Chem. Res. 32 (1992) 949.

[7] M. C. Fournier, L. Falk, and J. Villermaux, A new parallel competing reaction system for assessing micro-mixing efficiency – experimental approach, Chem. Eng. Sci. 51 (1996) 5053.

[8] G. I. Taylor, Statistical theory of turbulence, Proc. R. Soc. London, Ser. A 151 (1935) 421.

[9] S. Komori, T. Kanzaki, and Y. Murakami, Simultaneous measurements of instantaneous concentrations of two reacting species in a turbulent flow with a rapid reaction, Phys. Fluids A 3 (4) (1991) 507.

[10] P. Guichardon and L. Falk, Characterisation of micro-mixing efficiency by the iodide-iodate reaction system. Part I: Experimental procedure, Chem. Eng. Sci. 55 (2000) 4233.

[11] P. Guichardon, L. Falk, and J. Villermaux, Characterisation of micro-mixing efficiency by the iodide-iodate reaction system. Part II: kinetic study, Chem. Eng. Sci. 55 (2000) 4245.

[12] P.M. Oates and C. F. Harvey, A colorimetric reaction to quantify fluid mixing, Exp. Fluids 41 (2006) 673.

[13] P. M. Wheat and J. D. Posner, Quantifying mixing using equilibrium reactions, Phys. Fluids 21 (2009) 037101.

[14] C. Durandal, T. Lemenand, D. Della Valle, H. Peerhossaini, A chemical probe for characterizing turbulent micro-mixing, ASME FEDSM, (2006) 1091.

[15] H. Mohand Kaci, Caractérisation des capacités de micromélange des changeurs/réacteurs multifonctionnels par sonde chimique – Application au HEV, Ph.D. thesis, École Polytechnique de l'Université de Nantes, 2007.

[16] J. R. Bourne, Turbulent mixing and the selectivity of fast chemical reactions, Phys. Fluids A 3 (5) (1991).

[17] J. Baldyga and J. R. Bourne, A fluid mechanical approach to turbulent mixing and chemical reaction, Part II. Micro-mixing in the light of turbulence theory, Chem. Eng. Comm. 28 (1984) 242.

[18] J. Baldyga and J.R. Bourne, Simplification of micro-mixing calculations. I. Derivation and application of a new model, Chem. Eng. J. 42 (1989) 83.

[19] M.C. Fournier, L. Falk, and J. Villermaux, A new parallel competing reaction system for assessing micro-mixing efficiency – determination of micro-mixing time by a simple mixing model, Chem. Eng. Sci. 51 (1996) 5187.

[20] J.R. Bourne, Comments on the iodide/iodate method for characterising micro-mixing, Chem. Eng. J. 140 (2008) 638.

[21] A. Kölbl, Further comments on the iodide iodate reaction method for characterising micro-mixing, Chem. Eng. J. 145 (2008) 176.

[22] E. Schaer, P. Guichardon, L. Falk, E. Plasari, Determination of local energy dissipation rates in impinging jets by a chemical reaction method, Chem. Eng. J. 72 (1999) 125.

[23] A. Kölbl, M. Kraut, K. Schubert, The iodide iodate method to characterize microstructured mixing devices, AIChE J. 54 (3) (2008) 639.

[24] L. Nouri, J. Legrand, N. Benmalek, F. Imerzoukene, A. R. Yeddou, F. Halet, Characterisation and comparison of the micro-mixing efficiency in torus and batch stirred reactors, Chem. Eng. J. 142 (2008) 78.

[25] N. Baccar, R. Kieffer, and C. Charcosset, Characterization of mixing in a hollow fiber membrane contactor by the iodide–iodate method: numerical simulations and experiments, Chem. Eng. J. 148 (2-3) (2009) 517.

[26] S. Dushman, The rate of the reaction between iodic and hydriodic acids, J. Phys. Chem. 8 (1904) 453.

[27] D. A. Palmer, R. W. Ramette, and R. E. Mesmer, Triodide ion formation equilibrium and activity coefficients in aqueous solution, J. Solution Chem. 13 (1984) 673.

[28] J. Villermaux and J.C. Devillon, Représentation de la coalescence et de la redispersion des domaines de ségrégation dans un fluide par un modèle d'interaction phénomènologique, 2nd Int. Symp. Chem. Reaction Eng., Amsterdam, 1972.

[29] J. Baldyga and J. R. Bourne, Comparison of the engulfment and the interaction by exchange with the mean micro-mixing models, The Chem. Eng. J. 45 (1990) 25.

[30] J. Baldyga, J. R. Bourne, and Y. Yang, Influence of feed pipe diameter on meso-mixing in stirred tank reactors, Chem. Eng. Sci. 48 (1993) 3383.

[31] J. Baldyga, J. R. Bourne, and S. J. Hearn, Interaction between chemical reactions and mixing on various scales, Chem. Eng. Sci. 52 (1997) 457.

[32] S. Corrsin, The isotropic turbulent mixer: Part II. Arbitrary Schmidt number, AIChE J. 10 (1964) 870.

[33] J. Batdyga, J. R. Bourne, B. Dubuis, A. W. Etchells, R. V. Gholap, and B. Zimmermann, Jet reactor scale-up for mixing controlled reactions, Chem. Eng. Res. Des. 73 (1995) 497.

[34] P. Bradshaw, T. Cebeci, and J. H. Whitelaw, Engineering calculation methods for turbulent flow, Academic Press, London, 1981.

[35] S. Ferrouillat, P. Tochon, and H. Peerhossaini, Micro-mixing enhancement by turbulence: Application to multifunctional heat exchangers, Chem. Eng. Proc. 45 (2006) 633.

[36] J. Zhou, R. J. Adrian, and S. Balachandar, Autogeneration of near-wall vortical structures in channel flow, Phys. Fluids 8 (1) (1996) 288.

[37] R. J. Adrian, Hairpin vortex organization in wall turbulence, Phys. Fluids 19 (2007) 041301.

[38] T. Lemenand, D. Della Valle, Y. Zellouf, and H. Peerhossaini, Droplets formation in turbulent mixing of two immiscible fluids, Int. J. Multiphase Flow 29 (2003) 813.

[39] D. Dong and H. Meng, Flow past a trapezoidal tab, J. Fluid Mech. 510 (2004) 219.

[40] C. Habchi, T. Lemenand, D. Della Valle, and H. Peerhossaini, Alternating mixing tabs in multifunctional heat exchanger-reactor, Chem. Eng. Process., in press, doi:10.1016/j.cep.2009.07.003 (2009).

[41] H. Mohand Kaci, T. Lemenand, D. Della Valle, and H. Peerhossaini, Effects of embedded streamwise vorticity on turbulent mixing, Chem. Eng. Process. 48 (2009) 1457.

[42] H. Mohand Kaci, C. Habchi, T. Lemenand, D. Della Valle, and H. Peerhossaini, Flow structure and heat transfer induced by embedded vorticity, Int. J. Heat Mass Transfer 53 (2010) 3575.

[43] H. Peerhossaini, F. Bahri, On the spectral distribution of the modes in nonlinear Görtler instability, Exp. Therm. Fluid Sci. 16 (1998) 195-208.

[44] A. Ajakh, M.D. Kestoras, R. Toe, H. Peerhossaini, Influence of forced perturbations in the stagnation region on Görtler instability, AIAA J. 37 (1999) 1572-1577.

[45] R. Toe, A. Ajakh, H. Peerhossaini, Heat transfer enhancement by Görtler instability, Int. J. Heat Fluid Flow 23 (2002) 194-204.

CORPUS DES ARTICLES

2. A new adaptive procedure for using chemical probes to characterize mixing

C. Habchi, T. Lemenand, D. Della Valle, Z. Anxionnaz, P. Tochon, M. Cabassud, C. Gourdon, H. Peerhossaini

Chemical Engineering Science, Submitted (CES-D-10-00558), 2010b.

SUBMITTED TO

Chemical Engineering Science

CES-D-10-00558

A new adaptive procedure for using chemical probes to characterize mixing

Charbel Habchi [a, b], Dominique Della Valle [c], Thierry Lemenand [a], Zoé Anxionnaz [d], Patrice Tochon [d], Michel Cabassud[e], Christophe Gourdon[e], Hassan Peerhossaini [a,*]

[a] *Thermofluids, Complex Flows and Energy Research Group, LTN – CNRS UMR 6607, École Polytechnique – University of Nantes, rue Christian Pauc, 44306 Nantes, France*

[b] *Agence de l'Environnement et de la Maîtrise de l'Énergie (ADEME), 20 avenue du Grésillé, 49004 Angers, France*

[c] *ONIRIS Géraudière, 44322 Nantes, France*

[d] *Atomic Energy Commission – GREThh (CEA), 17 avenue des Martyrs, 38054 Grenoble, France*

[e] *Laboratoire de Génie Chimique, UMR 5503 CNRS/INPT/UPS, 5 rue P. Talabot, 31106 Toulouse Cedex 1, France*

ABSTRACT

The iodide-iodate chemical probe method is modified by a novel adaptive procedure to investigate the mixing abilities of two compact curved-duct reactors. Both reactors have a rectangular cross section; the first has smooth curvature (called the wavy duct) and the second has sharper bends (zigzag duct). In the conventional procedure, this method is used to characterize local micro-mixing, and for all experiments (for different Reynolds numbers and injection points) the reagent initial concentrations are kept at the same values. Even with wall injection, the selectivity of the chemical system is generally improved by increasing the flow Reynolds number. Nevertheless, two limitations encountered in using chemical probes (with the conventional protocol) to characterize the mixing abilities of the present reactors that prevent the conventional protocol of the chemical probe from discriminating between the mixing abilities of the two mockups. First, the duct walls are corrugated, so that the wall injection used to measure local micro-mixing is affected by the wall roughness, independently of the Reynolds number. Second, the flow Reynolds numbers are relatively low due to the small size of the duct sides, so that the measurements are inevitably hindered by meso-mixing effects. The challenge is thus to adapt the chemical method for characterizing the global mixing, by enlarging the measurement volume so as to capture and take into account all mixing scales. In the new adaptive procedure, the kinetics of the second reaction are adjusted in such a way as to impose the same reactive volume for different Reynolds numbers, leading to more relevant results for the segregation index X_S. Experimental results reveal that the mixing performance of the zigzag channel as assessed by this method is slightly above that of the wavy one. Finally, the segregation index in both reactors is related to the mixing time t_m by using a physical model in the literature.

Keywords: Turbulent mixing, micro-mixing, mass transfer, chemical reactor, static mixer, iodide-iodate chemical probe.

[*] Corresponding author: H. Peerhossaini
Phone: + (33)-240 683 124, Fax: + (33)-240 683 141
E-mail address: hassan.peerhossaini@univ-nantes.fr

1. Introduction

Mixing is a fundamental issue in process engineering and industrial fields such as chemistry, pharmaceutics and cosmetics (Stankiewicz and Moulijn, 2000; Anxionnaz *et al.*, 2008). The selectivity of the chemical reactions depends on the quality of mixing, from mixing at the reactor scale, sustained by the flow structures, down to mixing at molecular scales.

To describe the mixing mechanism, Fournier *et al.* (1996a) and Baldyga and Bourne (1999) have introduced macro-, meso- and micro-mixing as three parallel mixing stages at different scales. Macro-mixing concerns homogeneity at the reactor scale and is generally described by the residence-time distribution (RTD) method (Villermaux, 1986; Castelain *et al.*, 1997; Habchi *et al.*, 2009a) as a signature of velocity field uniformity. Macro-mixing can be enhanced by generating longitudinal vorticity, which intensifies radial mass and heat transfer (Fiebig, 1995; Ajakh *et al.*, 1999, Toé *et al.*, 2002, Lemenand *et al.*, 2003, 2005; Ferrouillat *et al.* 2006a; Mohand Kaci *et al.*, 2010; Habchi *et al.*, 2010).

Intermediate structures, which can be turbulent cascade vortices or fractal structures in a chaotic laminar flow (Aref, 1984; Jones *et al.*, 1989; Lemenand and Peerhossaini, 2002; Habchi *et al.*, 2009a, 2009b, Muzzio *et al.*, 1993), contribute to meso-mixing. In a chaotic laminar flow, the fractal structures are characterized by a Lyapunov exponent (Carrière, 2006), while in turbulent flows they can be characterized by the turbulent kinetic energy and the Reynolds strain-rate tensor (Schäfer *et al.* 1997; Mohand Kaci *et al.*, 2009; Habchi *et al.*, 2010).

Micro-mixing in turbulent flows takes place in the viscous-convective subrange, under the Kolmogorov scale, where laminar stretching leads to the molecular scales. The limiting step in micro-mixing is engulfment at the Kolmogorov scale (Baldyga and Bourne, 1999). In this sense, the Kolmogorov scale is a key parameter for the selectivity of chemical reactions in the turbulent regime that is determined by the dissipation rate of the turbulent kinetic energy (Villermaux, 1986; Baldyga and Bourne, 1989, 1999; Baldyga and Pohorecki, 1995; Fournier *et al.*, 1996a; Guichardon and Falk, 2000; Falk and Commenge, 2010).

Chemical probe methods are based on the competition between the mixing time and kinetics of one or more chemical reactions (Fournier *et al.*, 1996a; Guichardon and Falk, 2000). Several chemical systems can be used to characterize mixing efficiency (Wallace, 2009). Following Aubin *et al.* (2010), functional methods fall in three main categories. The first method is based on the color modification of a solution containing a reacting system directly injected in the flow, such as a pH indicator of an acido-basic solution. To obtain quantitative information about mixing efficiency, the mixing time is estimated by the ratio of the length of the color variation to the mean flow velocity (Kockmann *et al.* (2006), Branebjerg *et al.* (1996)). The second method involves a temporal-spatial recording of the concentrations in order to determine a coefficient of variance (COV) and then the segregation index (Hessel *et al.*, 2003) in stirred tanks (Paul *et al.*, 2004). The third technique, developed by Villermaux (1986) and reviewed by Fournier *et al.* (1996a) and Guichardon and Falk (2000), entails the competitive-consecutive or competitive-parallel reactions, which are based on the chemical result of the local injection of a reagent in stoichiometric deficit in the main flow. One of the two reactions is quasi-instantaneous with characteristic time t_{r1}; the second is slower and has characteristic time t_{r2} close to the mixing time t_m. The quality of the mixing process is measured by the segregation index X_S. In perfect mixing, the common reagent is totally consumed by the quasi-instantaneous reaction so that $X_S = 0$. In the total-segregation case, an overconcentrated zone of the injected common reagent occurs and the slower reaction can react with this common reagent, so that $X_S = 1$, as shown in Fig. 1. The segregation index can be related further to the mixing time by using physical models (Baldyga and Bourne, 1989, 1999; Fournier *et al.*, 1996b; Durandal *et al.*, 2006, Falk and Commenge, 2000). Section 2 presents in detail the iodide-iodate method, which is based on this concept.

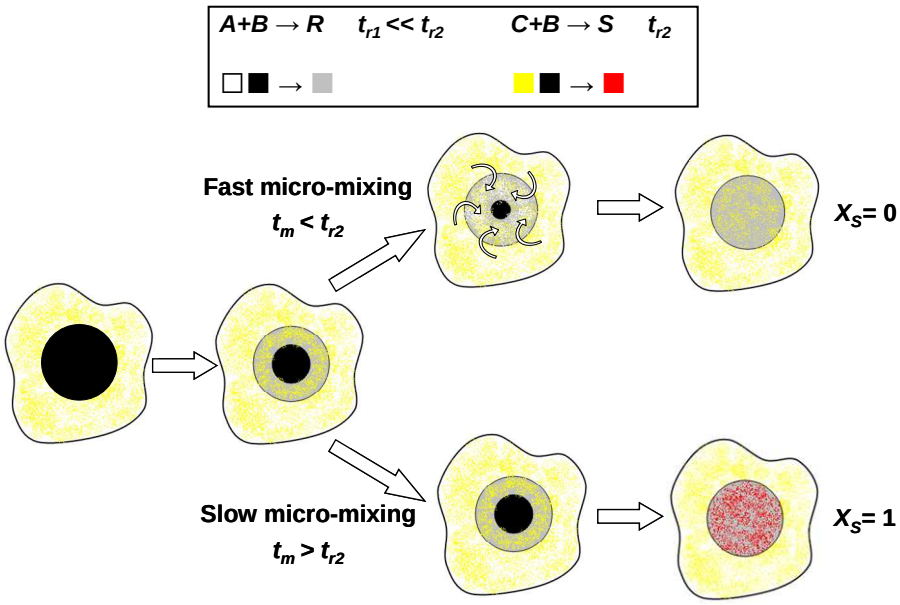

Fig. 1. Diagram of the micro-mixing process

The iodide-iodate method has been extensively used to study the mixing efficiency in different types of reactors (Kölbl *et al.*, 1998; Shaer *et al.*, 1999; Falk and Commenge, 2010; Ferrouillat *et al.*, 2006b; Mohand Kaci, 2007; Baccar *et al.*, 2009). This reaction system is used in the present study to compare the wavy and zigzag reactors, whose geometries are detailed in section 2.

The results are presented in section 3. A first experiment, with distributed wall injections and a given set of species concentrations fixing a "high rate" for the second reaction, demonstrates that selectivity does not vary with Reynolds number. In fact, the channel walls are corrugated, and near the solid walls the flow is governed by the roughness size. Even in the high-Reynolds-number flow regime, the chemical probe could not discriminate between the geometries when a wall injection was applied. A second experiment, with a slow ("low-rate") second reaction and a unique injection point at the duct inlet, does not even present any trend of variation with the Reynolds number, because the measurement volume depends precisely on the flow velocity. To overcome this difficulty, a new protocol is proposed here that involves *pre-adjusting* the measurement volume to the different Reynolds numbers by *adapting* the kinetics of the second reaction to each Reynolds number. This method lets us show the relative mixing improvement when the Reynolds number is increased by comparing the two duct geometries.

Finally, the measured segregation index is related to the mixing time by the engulfment model (Baldyga and Bourne, 1989) for turbulent configurations, and by the stretching model for laminar configurations. An attempt is made in section 4 to compare the experiments with the theoretical trends predicted by the model of Falk and Commenge (2010).

2. Materials and methods

2.1. Iodide-iodate method

This chemical method is based on competitive parallel reactions consisting in coupling the borate neutralization (Eq. (1)) and the Dushman (1904) reaction (Eq. (2)), as shown in the following scheme:

$$H_2BO_3^- + H^+ \leftrightarrow H_3BO_3 \qquad (1)$$

$$5\mathrm{I}^- + \mathrm{IO}_3^- + 6\mathrm{H}^+ \leftrightarrow 3\mathrm{I}_2 + 3\mathrm{H}_2\mathrm{O} \tag{2}$$

Reaction (1), of characteristic time t_{r1}, is quasi-instantaneous, and reaction (2) is much slower than the neutralization reaction (Eq. (1)): $t_{r2} >> t_{r1}$. These characteristic times are given by Guichardon *et al.* (2000) as follows:

$$t_{r1} = \frac{Min\left(\left[\mathrm{H}_2\mathrm{BO}_3^-\right], \left[\mathrm{H}^+\right] \right)}{r_1} \tag{3}$$

$$t_{r2} = \frac{Min\left(\frac{3}{5}\left[\mathrm{I}^-\right], 3\left[\mathrm{IO}_3^-\right], \frac{1}{2}\left[\mathrm{H}^+\right] \right)}{r_2} \tag{4}$$

where the brackets designate the reagent concentrations and r_1 and r_2 are respectively the reactions kinetics given by Eqs. (5) and (6):

$$r_1 = K_1 \left[\mathrm{H}_2\mathrm{BO}_3^-\right] \left[\mathrm{H}^+\right] \tag{5}$$

$$r_2 = K_2 \left[\mathrm{I}^-\right]^2 \left[\mathrm{H}^+\right]^2 \left[\mathrm{IO}_3^-\right] \tag{6}$$

Here $K_1 = 10^{11}\,\mathrm{L\,mol^{-1}\,s}$ and K_2 is a function of ionic strength λ as defined by Palmer *et al.* (1984) and Guichardon *et al.* (2000):

$$\begin{aligned} &\log_{10}(K_2) = 9.28105 - 3.664\sqrt{\lambda} && \text{for } \lambda < 0.166\,\mathrm{M} \\ &\log_{10}(K_2) = 8.383 - 1.5112\sqrt{\lambda} + 0.23689\lambda && \text{for } \lambda > 0.166\,\mathrm{M} \end{aligned} \tag{7}$$

The iodine I_2 generated from the second reaction in Eq. (2) reacts further with iodide ions I^- to yield I_3^- ions following the quasi-instantaneous equilibrium reaction

$$\mathrm{I}_2 + \mathrm{I}^- \leftrightarrow \mathrm{I}_3^- \tag{8}$$

The principle of this method is to add, in stoichiometric defect , a small quantity of sulfuric acid H^+ to an initial mixture of I^-, IO_3^- and $\mathrm{H}_2\mathrm{BO}_3^-$. In perfect mixing, the injected H^+ is totally consumed by the quasi-instantaneous reaction in Eq. (1) and hence there is no formation of iodine I_2. When the mixing process is not sufficiently fast to "feed" the first reaction, the local overconcentration of H^+ produces iodine I_2 by the second reaction (Eq. (2)), which reacts with iodide ions I^- to yield I_3^- ions (Eq. (8)). Therefore, the selectivity in I_2 is a measure of molecular-scale segregation and indicates mixing quality. To this end, the segregation index X_S is defined for open-loop flows (Villermaux, 1986) as

$$X_S = 2\,\frac{[\mathrm{I}_2] + [\mathrm{I}_3^-]}{[\mathrm{H}^+]_0} \left(1 + \frac{Q_p}{Q_{\mathrm{H}^+}} \right) \left(1 + \frac{[\mathrm{H}_2\mathrm{BO}_3^-]_0}{6\,[\mathrm{IO}_3^-]_0} \right) \tag{9}$$

where Q_p and Q_{H^+} are respectively the flow rate of the main stream (working fluid) and the flow rate of the injected sulfuric acid.

The mass balance on iodine I_2 atoms leads to the following expression (Fournier *et al.*, 1996a):

$$[I_2]^2 - \left(\frac{3}{5}[I^-]_0 - \frac{8}{5}[I_3^-]\right)[I_2] + \frac{3}{5}\frac{[I_3^-]}{K_B} = 0 \tag{10}$$

where K_B is the equilibrium constant of the reaction (8) defined by Palmer *et al.* (1984), which depends upon the fluid temperature:

$$\log_{10}(K_B) = \frac{555}{T} + 7.355 - 2.575\log_{10}(T) \tag{11}$$

At $T = 298\,\mathrm{K}$ the equilibrium constant $K_B = 702\ \mathrm{mol}^{-1}$.

2.2. Reagent preparation

The initial reagents (KI, KIO_3, H_3BO_3, $NaOH$) are in the solid phase, with purity between 98% and 99.5%. Their weight is measured by an analytical balance of 5×10^{-5}g precision. The buffer solution is first achieved with H_3BO_3 and $NaOH$, which are dissolved in deionized tap water (on a Siemens resin < 5 µ) and stored in the main tank shown in Fig. 2. The temperature is maintained constant at 298 K since the reaction kinetics are very sensitive to this parameter. KI and KIO_3 are dissolved separately in the deionized water, and are added consecutively to the buffer solution.

2.3. pH range

The formation of I_2 depends on the value of pH compared with pH* (Custer and Natelson, 1949; Pourbaix, 1963): if the initial mixture pH is below pH*, I_2 can form naturally even in the absence of acid molecules. Therefore, pH must be above pH*, but if the final pH value, after the reactions are completed in the flow, is much greater than pH* the iodine I_2 dissociation is not stable. Hence, the final pH must be close enough to pH*. The value of pH* is 7, and the ideal initial pH value is $8.5 < \mathrm{pH} < 9.5$ (Guichardon and Falk, 2000). For more details on the pH-potential diagram, see Guichardon and Falk (2000) and Mohand Kaci (2007).

2.4. Hydraulic loop

A schematic diagram of the hydraulic loop appears in Fig. 2a. The 200-liter tank containing the main flow reagent solution (KI, KIO_3, H_3BO_3, $NaOH$) has an immersed pump to homogenize the initial mixture before it enters the hydraulic loop driven by a rotary gear pump. The flow rate is controlled by the electrical power of the circulation pump and measured by a rotary flowmeter whose precision is 3%. The temperature in the system is kept constant at 298 K with an immersed helical heat exchanger whose temperature is controlled by a thermostat (Crythermostat 71 Huber).

The sulfuric acid H_2SO_4 injection system shown in Fig. 2b consists of a regulated stepper system plugged into a push-syringe. The sulfuric acid is injected into the test section by an injection needle of 0.5 mm internal diameter connected to the syringes by flexible tubes. To control the flow rate of the acid injection, the multi-syringe injection system shown in Fig. 2b was designed and constructed to provide a range of precisely controlled injection volume flow rates from 10 to 160 000 µl/min.

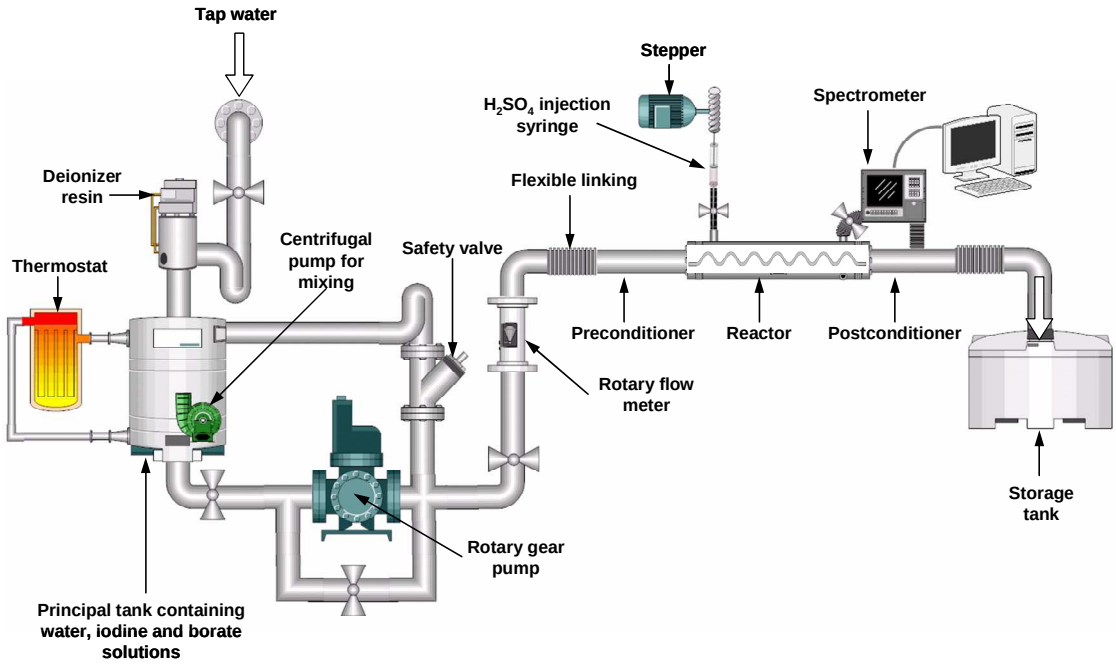

(a)

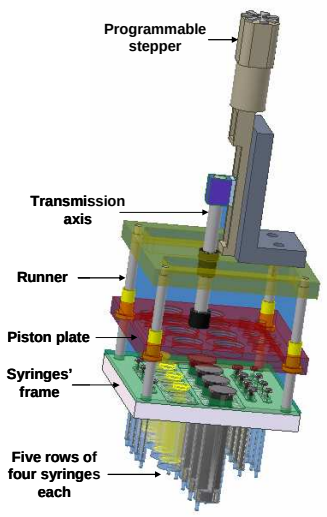

(b)

Fig. 2. Schematic diagram of (a) the hydraulic loop and (b) the injection system

2.5. Spectrometry analysis

The I_2 and I_3^- concentrations are experimentally determined by spectrometry. According to the Beer-Lambert law in Eq. (12), the light absorption A is proportional to the I_3^- concentration resulting from the equilibrium reaction (8):

$$[I_3^-] = \frac{A}{\xi \ell} \tag{12}$$

where ℓ is the optical length and ξ is the molar extinction coefficient of I_3^- at 353 nm equal to $\xi = 2597 \pm 148$ m^2/mol (Palmer *et al.*, 1984; Mohand Kaci, 2007).

The final products of the chemical reaction system are continuously analyzed through a channel placed 0.3 m downstream from the reactor outlet to a quartz recirculation cistern of capacity 750 µL. The spectrometer (Jenway 6505™) wavelength range is in the UV (ultraviolet) domain [190 nm, 1100 nm] and resolution is 0.1 nm with a bandwidth of 1.8 nm. The measurable absorbance range lies between 0 and 3 with 0.001 precision.

2.6. Test sections

The two reactor geometries investigated here are corrugated rectangular channels (2×4 mm cross section) of hydraulic diameter $D_h = 2.67$ mm. The Reynolds number in both geometries is defined by $Re = W_m D_h / \upsilon$, with W_m the mean flow velocity and υ the kinetic viscosity of the working fluid (water).

The wavy channel, shown in Fig. 3, has thirteen 90° curved bends of curvature radius $R_C = 10.50$ mm. The sulfuric acid injection holes are designated P_i in Fig. 3. This geometry is used both to study local mixing at different P_i (with i= 1 to 7) to assess the effect of injection location and also to appraise global mixing capacity by injecting the sulfuric acid only in P_1.

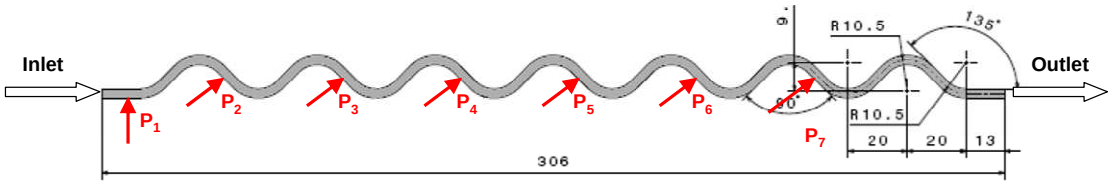

Fig. 3. Schematic diagram of the wavy channel showing the injection locations denoted P_i with i= 1 to 7

The zigzag channel, shown in Fig. 4, is made of 27 90° curved bends of curvature radius $R'_C = 1.50$ mm. Only one injection point is available in the first bend.

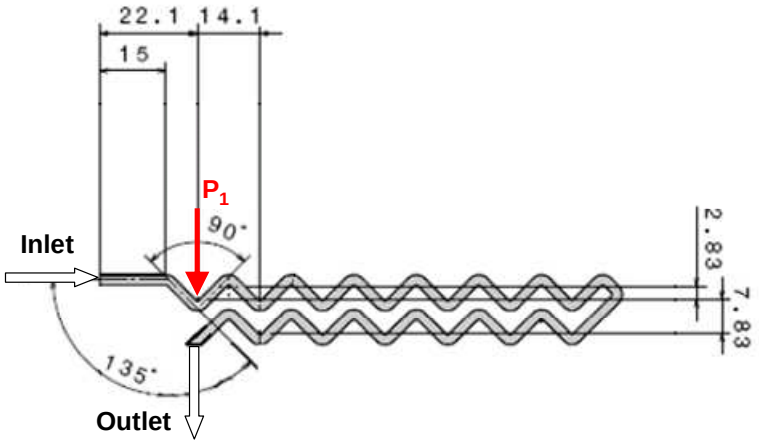

Fig. 4. Schematic diagram of the zigzag channel showing the injection in the first bend

Fig. 5 shows a photograph of the two reactors used in the present study and the locations of the sulfuric acid injection.

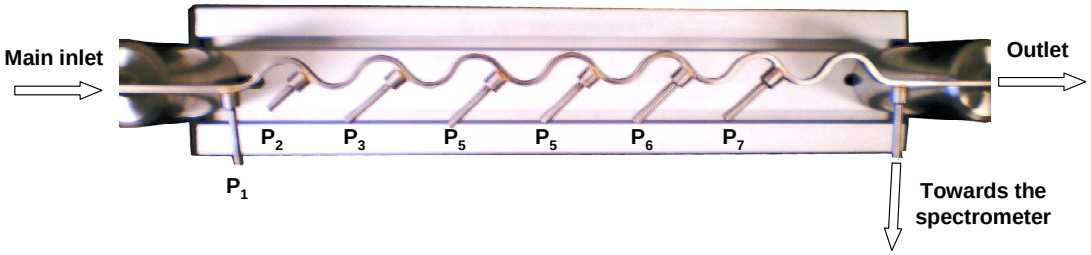

(a)

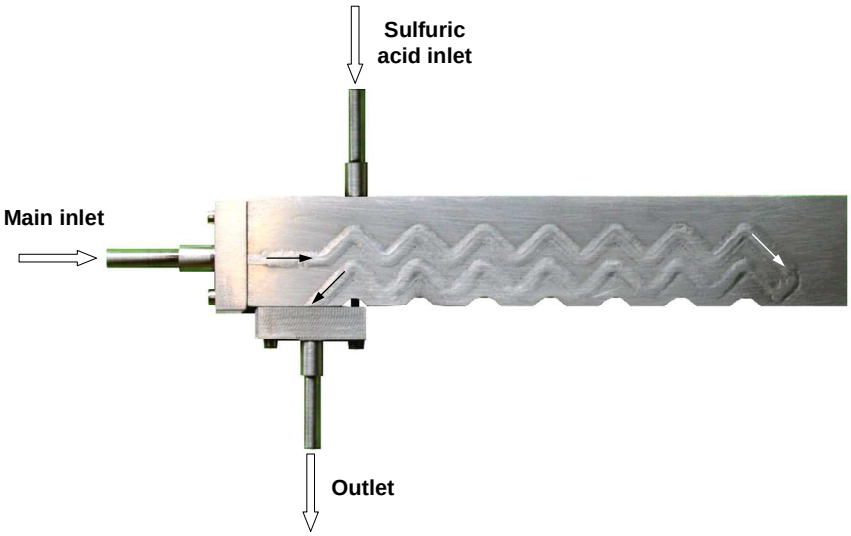

(b)

Fig. 5. Photograph of test sections: (a) wavy and (b) zigzag channels

3. Results and discussion

3.1. Measurement with conventional procedure in wavy channel

Local measurements

The conventional procedure here refers to a given set of values for the initial reagent concentrations. They are adapted from Mohand Kaci (2007) and are given in Table 1. In these experiments, small reaction times are desired, in order to get measurements that are as local as possible. The sulfuric acid is injected successively in the seven different locations P_i for the wavy channel, for two Reynolds numbers $Re = 2500$ and $Re = 4500$.

Species	*Initial concentrations* $\times 10^3$ *mol/L*
$H_2BO_3^-$	1.513
NaOH	1.513
IO_3^-	2.330
I^-	11.650
H^+	1000

Table 1. Initial concentrations of reagents of iodide-iodate method in wavy channel for micro-mixing characterization (adapted from Mohand Kaci, 2007)

The segregation index X_S defined in Eq. (9) is plotted in Fig. 6 at the different locations for the two Reynolds numbers. It is observed that neither the injection point nor the Reynolds number has a significant effect on X_S, which stays around the averaged value of 0.05.

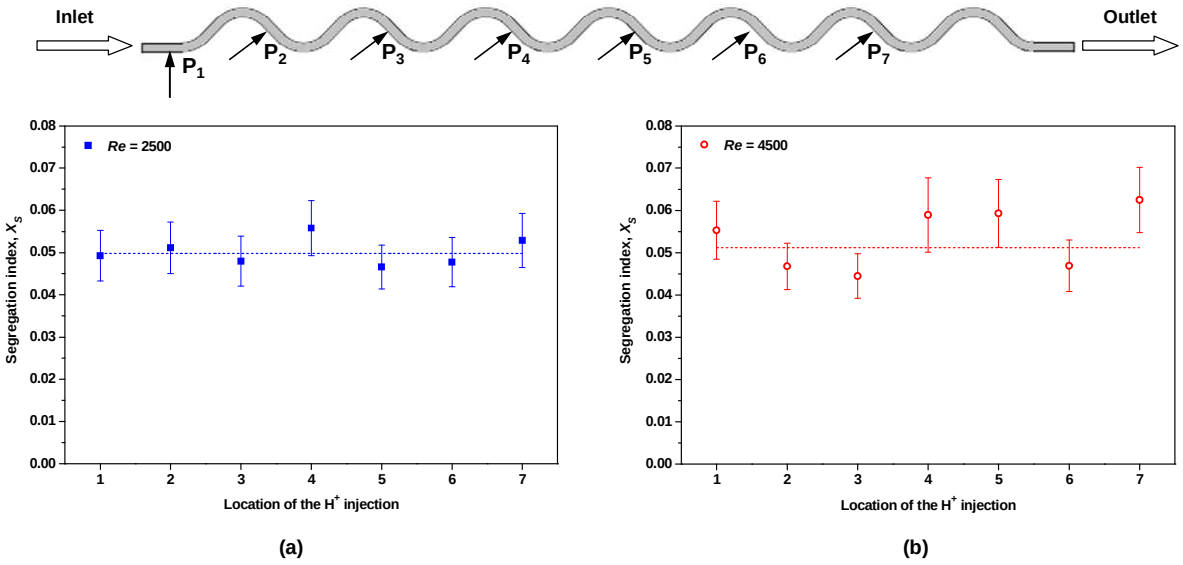

Fig. 6. Segregation index at different injection locations in the wavy channel for Reynolds numbers (a) $Re = 2500$ and (b) $Re = 4500$

Two conclusions can be drawn from these results. First, the X_S index is independent of location along the reactor, indicating that measurements are very local, as expected. For these concentrations, the characteristic time of the second reaction is obtained from Eq. (4) $t_{r2} \approx 3\,\text{ms}$. The reaction is achieved at a distance from the injection point approximated by $L_{r2} \approx t_{r2}\, w$, with w the advective velocity of the reacting volume, leading to a small value of L_{r2} (about 0.3 mm). Therefore, the measurement can be considered local, and the chemical probe characterizes the micro-mixing process.

Second, X_S is independent of Reynolds number. To explain this result, one should consider the turbulent environment at the injection point (in the wall region) where the turbulence is governed by the wall roughness. Therefore, the magnitude of ε and hence X_S remains almost constant for all Reynolds numbers.

Global measurements

Here the acid is injected at location P_1 (Fig. 3) for Reynolds numbers ranging between 600 and 4000. The standard experimental procedure is used with the initial reagent concentrations (Table 2) chosen so that the second reaction time is large enough to produce a large reaction volume. The corresponding second reaction time is about $t_{r2} \approx 0.17\,\mathrm{s}$ from Eq. (4).

Species	*Initial concentrations* $\times 10^3$ *mol/L*
$H_2BO_3^-$	0.50
NaOH	0.50
IO_3^-	0.30
I^-	1.50
H^+	1000

Table 2. Initial concentrations of reagents of iodide-iodate method in wavy channel for mixing characterization

Fig. 7 shows the segregation index X_S as a function of the Reynolds number. The X_S variation shows no coherent relation with the flow Reynolds number, considering the expected improvement in selectivity with Reynolds number. This feature is due to the reaction volume, which is proportional to the distance from the injection point, as previously mentioned: $L_{r2} \approx t_{r2} W$, with W the mean flow velocity. As the reagent concentrations are constant for all Reynolds numbers, the second reaction time is then constant, and the development length of the second reaction is proportional to W. Thus, X_S measurements are sensitive to two parameters: first, the Reynolds number has a decreasing effect on X_S because the higher the Reynolds number, the lower the segregation index X_S, and second, the measurement volume has an increasing effect because the greater the mean flow velocity *W*, the greater L_{r2}; L_{r2} varies from 0.03 m to 0.23 m. These two competitive effects are impossible to separate one from another and thus prevent inference of any physical understanding of the mixing quality.

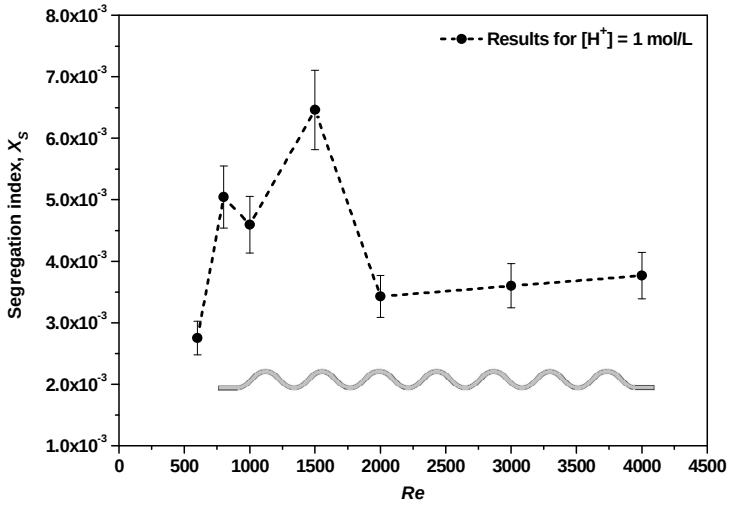

Fig. 7. Segregation index for different Reynolds numbers in the wavy channel using the conventional procedure

3.2. Global measurements with new protocol in the wavy and zigzag channels

Since with the conventional procedure the measurement volume is not the same for different Reynolds numbers (see section 3.1), the new procedure defined here aims to fix the measurement volume by varying the second reaction time t_{r2}, by adjusting the initial reagent concentrations. However, it is quite difficult to vary the initial concentrations of I^-, IO_3^- and $H_2BO_3^-$ constituting the initial solution because they are linked by the pH. It is more tractable to vary the H^+ concentration since it can be prepared separately from the other reagents before being injected into the main flow. For each Reynolds number, the second reaction time is computed in such a way as to obtain $L_{r2} \approx t_{r2} W \approx$ constant . Therefore, when Reynolds number increases by a factor α, the second reaction time t_{r2} is decreased by a factor $1/\alpha$ while increasing $[H^+]_0$ by a factor α. The set of concentrations for both geometries is the same as in section 3.1 (Table 2) except for $[H^+]_0$, which is adapted following Eq. (13) to obtain $t_m = t_{r2}$ for all Reynolds numbers:

$$[H^+]_0 = 2.04 \times 10^{-4}\, Re^{0.975} \text{ for } 0 < Re < 4000 \tag{13}$$

For the operating conditions of this study, the initial H^+ concentration $[H^+]_0$ varies from 0.087 to 0.6 63 mol L^{-1}.

Fig. 8 represents the segregation index X_S as a function of the Reynolds number in the reactors, by using the adaptive procedure with acid injection at the reactor inlets. The segregation indexes are lower in the new adaptive procedure (Fig. 8) than those obtained in the conventional procedure (Fig. 7) because the sulphuric acid concentration is lower in the adaptive procedure. It is clearly observed that X_S decreases exponentially with Reynolds number, showing the mixing enhancement with Reynolds number. The selectivity in the zigzag channel is better than in the wavy channel, especially in the laminar regime for $Re < 1000$, implying that the mixing quality in the zigzag reactor is higher than in the wavy channel. This result can be explained by the shape of each reactor. In the zigzag channel, the bends have a sharper curvature than in the wavy channel and therefore, produce higher Dean numbers:

i) in the laminar regime, the higher Dean number intensifies the secondary flow responsible for the radial transfer,

ii) in the turbulent regime, the induced gradients increase the turbulence production and consequently the turbulent-energy dissipation rate, which controls the mixing quality (Baldyga and Bourne, 1999).

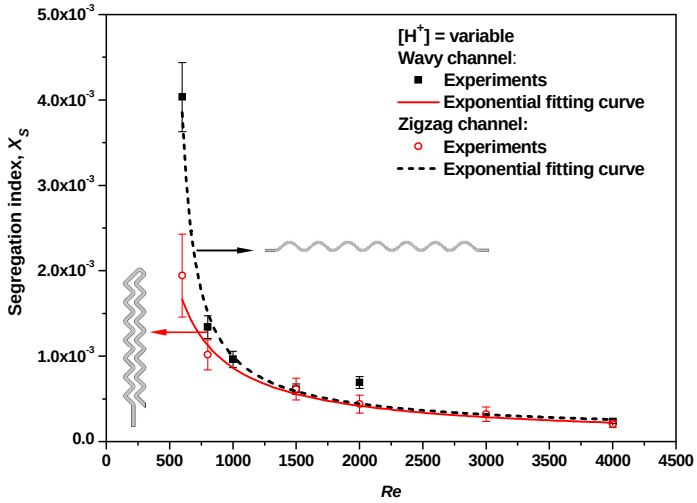

Fig. 8. Comparison between the segregation index of the wavy and zigzag channels using the adaptive procedure

4. Comparison with models

This section focuses on determining the mixing time from the measurements of the segregation index in both geometries, carried out over the total reactor volume. Therefore, in this case the mixing time characterizes the global mixing, accounting for the micro-, meso- and macro-mixing.

Two different flow regimes are involved. For $Re > 1000$, the engulfment model developed by Baldyga and Bourne (1989) is used to determine the mixing time in the turbulent regime. For $Re < 1000$, the mixing time is based on the physical model recently developed by Falk and Commenge (2010), based on the stretching mechanism in laminar duct flows.

With knowledge of the mixing time, the Falk and Commenge approach (2010) proposes building a characteristic parameter, homogeneous with the inverse of a "diffusion coefficient" t_m / D_h^2 resulting from the geometry and the operating conditions, which tends to the molecular diffusivity when the Reynolds number tends to zero.

4.1. Determination of mixing time by the engulfment model

The engulfment model (E-model) is based on the mass balance for each chemical species of the test reaction system (Baldyga and Bourne, 1984, 1989):

$$\frac{d C_i}{d t} = \frac{1}{t_m}\left(C_{i,0} - C_i\right) + r_i \tag{14}$$

where $C_{i,0}$ is the initial concentration of reagent i and C_i is its instantaneous concentration. r_i is the rate of formation of reagent i by chemical reaction, and t_m is the mixing time.

This model is based on the assumption of a first-order-law growth of the incorporated reagent volume into spiral marbled structures that are in turn homogenized under the stretching effects until near-Batchelor scales, when molecular diffusion comes into play. However, Baldyga and Bourne (1989) have established that for Schmidt numbers greater than 4000, the effects of laminar deformation as well as molecular diffusion are negligible relative to the engulfment process, and hence they proposed the simple E-model for high Schmidt number fluids. The E-model is shown in Fig. 9.

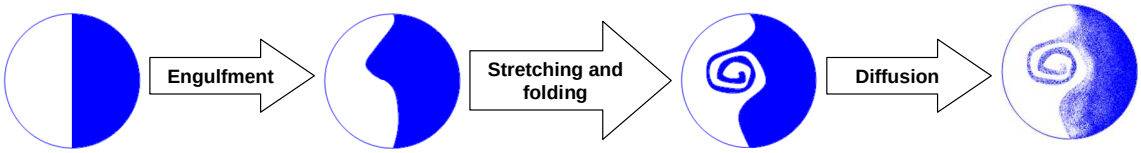

Fig. 9. Schematic of the E-model

In practice, for a given value of micro-mixing time t_m (representing the state of turbulence of the mixing environment), the system of Eqs. (14) is solved as a function of time for each species until the concentration of the sulfuric acid tends to zero; in the present case, nine nonlinear equations for the components of the iodide/iodate reaction system. The segregation index X_S is then calculated from the asymptotic values of the different concentrations. The Newton-Raphson iterative method is employed, and computations are performed using MATLAB™. If we repeat this procedure for different values of t_m, we then obtain a set of X_S values each corresponding to a t_m , as plotted in Fig. 10. This curve is used to find the micro-mixing time t_m of a mixing flow if the X_S value is available from experiment: $X_S = f(t_m)$.

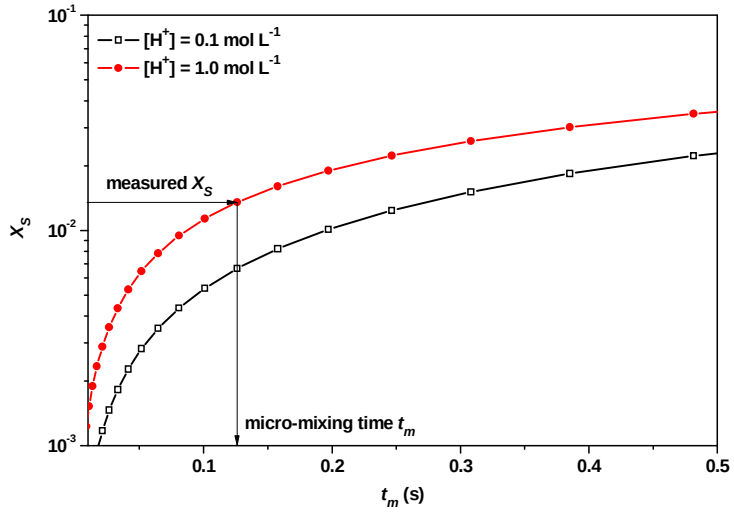

Fig. 10. Segregation index X_S plotted versus micro-mixing time t_m obtained from the E-model for concentrations given in Table 2 with two different H^+ concentrations

4.2. Determination of mixing time by stretching efficiency model

In this section, the stretching efficiency model proposed by Falk and Commenge (2010) is briefly recalled. Baldyga and Bourne (1984) suggest calcuating the mixing time in laminar flow by the following equation:

$$t_m = \frac{arcsinh\left(\dfrac{0.76\,\dot{\gamma}\,\delta_0}{D_m}\right)}{2\,\dot{\gamma}} \tag{15}$$

where δ_0 is the initial striation thickness, D_m the molecular diffusion of water and $\dot{\gamma}$ the mean shear rate in the reactor.

However, determination of δ_0 and $\dot{\gamma}$ is not trivial and numerical or analytical solutions are needed, so that Falk and Commenge (2010) estimate these parameters from the Hagen-Poiseuille law. Hence, the energy dissipation rate per unit mass of fluid ε and the shear rate $\dot{\gamma}$ can be derived:

$$\varepsilon = \frac{32\,\upsilon W^2}{D_h^2} \tag{16}$$

$$\dot{\gamma} = \left(\frac{\varepsilon}{2\upsilon}\right)^{\frac{1}{2}} \tag{17}$$

Moreover, by assuming that the initial striation thickness δ_0 is equal to half of the channel hydraulic diameter D_h, Falk and Commenge (2010) derive the following theoretical expression for mixing time:

$$t_m = \frac{D_h^2}{8D_m}\frac{ln(1.52\,Pe)}{Pe} \tag{18}$$

where $Pe = W_m D_h / D_m$ is the Péclet number.

Considering that only part of the consumed mechanical energy is spent on mixing, these authors used the concept of energetic efficiency proposed by Ottino *et al.* (1979) to derive a new expression for mixing time as given in Eq. (20).

$$\eta = \frac{\dot{\gamma}}{\dot{\gamma}_{max}} = \frac{\dot{\gamma}}{\sqrt{\varepsilon/(2\upsilon)}} \tag{19}$$

where $\dot{\gamma} = \sqrt{2\Re \bullet \Re}$ is the effective shear rate, $\dot{\gamma}_{max}$ is the maximum shear rate in the flow (computed at the wall $\dot{\gamma}_{max} = 8W / D_h$), and $\varepsilon = 2\upsilon(\Re \bullet \Re)$, with $\Re$ the deformation tensor, leading to:

$$t_m = \frac{D_h}{8W}\frac{ln(1.52\eta\,Pe)}{\eta} \tag{20}$$

4.3. Experimental results for the diffusion coefficient

Eq. (18) readily shows that for laminar flow t_m is inversely proportional to the Reynolds number (Falk and Commenge, 2010); indeed, for $Pe >> 100$, $ln(Pe)/Pe \propto 1/Pe$. In turbulent flows, the mixing time t_m must be proportional to $\varepsilon^{-1/2}$ (Baldyga and Bourne, 1989, 1999; Fournier *et al.*, 1996b). From a simple dimensional analysis, it is found that $\varepsilon \propto W^3 / D_h$, leading to t_m proportional to $W^{-3/2}$ and hence to $Re^{-3/2}$.

Fig. 11 represents the theoretical mixing time defined in Eq. (20) in the laminar flow regime, the trend curve $W^{-3/2}$ in the turbulent flow regime, and the measured mixing time versus Reynolds number for both wavy and zigzag channels. The experimental values of the inverse diffusion coefficients globally decrease with Reynolds number, signifying better mixing. For both reactor geometries studied here, the experimental results are in good agreement with the theoretical trends, especially in the turbulent regime. The accuracy interval is taken equal to ±30%, as mentioned by Falk and Commenge (2010) with the same test reaction section. The inverse diffusion coefficients for

the zigzag channel seem to be slightly below those for the wavy channel. In the present study all experimental points (except one) lie within the accuracy interval.

The value of η in Eq. (20) is fixed so that the theoretical curve given by this equation fits the experimental data in the laminar flow regime. For the present reactors $\eta = 0.8$, implying that 80% of the strain rate is efficient for the mixing process, which is quite high compared with the 3% in micro-mixers studied by Falk and Commenge (2010) and the 1% in the twin-screw extruder studied by Baldyga *et al.* (1998).

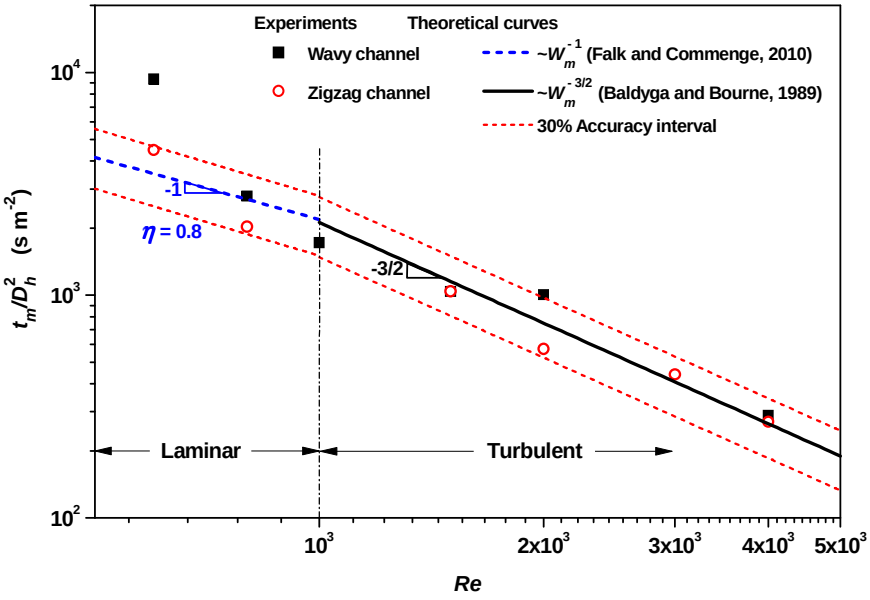

Fig. 11. Inverse diffusion coefficient versus Reynolds number for zigzag and wavy reactors

5. Concluding remarks

In the present study three different series of measurements are carried out to explore the ability of the iodide-iodate chemical probe method to characterize the mixing process and to discriminate between the mixing performances of two different reactor geometries.

First, local measurements are carried out in the wavy channel by wall injection of sulfuric acid at given locations along the reactor, with the aim of characterizing the micro-mixing process in this channel geometry for Reynolds numbers 2500 and 4500. It is shown that there is no significant effect of measurement location on the reaction result, and that Reynolds number does not significantly affect the segregation index. In the case of fast (high-rate) second reactions, the measurement volume is very close to the wall and dominated by the surface roughness, all along the channel walls. Therefore, X_S remains almost constant in all experiments.

The second series of measurements concerns using the conventional chemical-probe procedure in the wavy channel with large second reaction time, allowing the reaction to take place in the whole reactor volume. It is demonstrated that the segregation index presents no coherent trend versus the Reynolds number. This is attributed to the high sensitivity of the method to the measurement volume. Therefore, the measured X_S values are not comparable.

The final series of measurements is carried out in both zigzag and wavy reactors with the new adaptive procedure, which consists in fitting the concentrations of the injected sulfuric acid for each

Reynolds number. Mixing enhancement is then clearly observed on X_S when the Reynolds number increases.

This new procedure allows comparison between the wavy and zigzag channels. With equal hydraulic diameter, the better selectivity of the zigzag channel can be attributed to its sharper curvature, especially in the laminar regime, which may increase the Dean vortices compared to the wavy channel.

Finally, mixing time is determined in two models following the flow regime: the engulfment model in turbulent flow (Baldyga and Bourne, 1989) and the stretching efficiency in laminar flow. These results are compared to the semi-empirical model proposed by Falk and Commenge (2010) and seem to agree with the expected trends with efficiency 80%, which supports the validity of the adaptive method for determination of the mixing time.

The present study contributes to diversifying the application of the chemical probe method in the quantitative determination of the energy efficiency of MHER by global mixing time.

Acknowledgments

This work was carried out under a grant by ANR (Agence National de Recherche) through the project “RAPIC” in partnership with CEA-LETh, LGC CNRS UMR 5503, Fives Cryo and Rhodia R&D. The technical support of SEF (Design and Manufacturing Service of LTN) is greatly acknowledged, especially N. Lefevre, J. Delmas and O. Giboulot. C. Habchi was partially supported by ADEME (Agence de l’Environnement et de la Maîtrise de l’Énergie); we gratefully thank Dr. C. Garnier for monitoring this grant.

Nomenclature

A	light absorption
C_i	instantaneous concentration of reagent i (mol L^{-1})
$C_{i,0}$	initial concentration of reagent i (mol L^{-1})
D_h	hydraulic diameter (m)
D_m	molecular diffusion of water (m s^{-2})
K_B	equilibrium constant of reaction (3)
ℓ	optical length (m)
L_{r2}	measurement volume (m)
Pe	Péclet number $\left(=W_m D_h / D_m\right)$
Q_{H^+}	flow rate of injected sulfuric acid (m^3 s^{-1})
Q_p	flow rate of main flow (m^3 s^{-1})

r_1, r_2	test reaction kinetics (mol s^{-1})
R_C, R'_C	curvature radius (m)
Re	Reynolds number $(= W_m D_h / \upsilon)$
t_m	mixing time (s)
t_{r1}, t_{r2}	test reaction characteristic time (s)
w	advective velocity of measurement volume (m s^{-1})
W	mean flow velocity (m s^{-1})
X_S	segregation index

Greek symbols

δ_0	initial striation thickness (m)
ε	energy dissipation rate (m^2 s^{-3})
$\dot{\gamma}$	shear rate (s^{-1})
η	energy efficiency of mixing
υ	kinematic viscosity (m s^{-2})
$\Re$	deformation tensor (s^{-1})
ξ	molar extinction coefficient (m^2 mol^{-1})

Subscripts

0	initial value
max	maximum value

Notation

B	common injected reagent of test reaction
MHER	multifunctional heat exchanger-reactor
[ ]	concentration (mol L^{-1})

References

Ajakh A, Kestoras MD, Toe R, H. Peerhossaini, 1999, Influence of forced perturbations in the stagnation region on Görtler instability. AIAA Journal, 37, 1572-1577

Anxionnaz, Z., Cabassud, M., Gourdon, C., Tochon, P., 2008. Heat exchanger/reactors (HEX reactors): Concepts, technologies: State-of-the-art. Chemical Engineering and Processing 47, 2029-2050

Aref, H., 1984. Stirring by chaotic advection. Journal of Fluid Mechanics 143, 1-21.

Aubin, J., Ferrando, M., Jiricny, V., 2010. Current methods for characterising mixing and flow in microchannels. Chemical Engineering Science doi:10.1016/j.ces.2009.12.001.

Baccar, N., Kieffer, R., Charcosset, C., 2009. Characterization of mixing in a hollow fiber membrane contactor by the iodide–iodate method: Numerical simulations and experiments. Chemical Engineering Journal 148, 517-524.

Baldyga, J., Bourne, J.R., 1984. Mixing and fast chemical reaction--VIII: Initial deformation of material elements in isotropic, homogeneous turbulence. Chemical Engineering Science 39, 329-334.

Baldyga, J., Bourne, J.R., 1989. Simplification of micro-mixing calculations: I. Derivation and application of a new model. Chemical Engineering Journal 42, 83-92.

Baldyga, J., Rozen, A., Mostert, F., 1998. A model of laminar micro-mixing with application to parallel chemical reactions. Chemical Engineering Journal 69, 7-20.

Baldyga, J., Bourne, J.R., 1999. Turbulent Mixing and Chemical Reactions, Wiley, Chichester.

Baldyga, J., Pohorecki, R., 1995. Turbulent micro-mixing in chemical reactors - a review. The Chemical Engineering Journal 58, 183-195.

Bourne, J.R., 2008. Comments on the iodide/iodate method for characterising micro-mixing. Chemical Engineering Journal 140, 638-641.

Branebjerg, J., Fabius, B., Gravesen, B., 1995. Application of miniature analysers: from microfluidic components to µTAS. Van den Berg A., Bergfeld P. (Eds.), Micro Total Analysis Systems, Kluwer, Dordrecht, 141-151.

Carrière, P., 2006. Lyapunov spectrum determination from the FEM simulation of a chaotic advecting flow. International Journal of Numerical Methods in Fluids 50, 555-577.

Castelain, C., Mokrani, A., Legentilhomme, P., Peerhossaini, H., 1997. Residence time distribution in twisted pipe flows: helically coiled system and chaotic system. Experiments in Fluids 22, 359-368

Custer, J.J., Natelson, S., 1949. Spectrophotometric determination of micro quantities of iodine. Analytical Chemistry 21, 1005-1009.

Durandal, C., Lemenand, T., Della Valle, D., Peerhossaini, H., 2006. A chemical probe for characterizing turbulent micro-mixing. ASME Fluids Engineering Division Summer Meeting, 1091-1099.

Dushman, S., 1904. The rate of the reaction between iodic and hydriodic acids. Journal of Physical Chemistry 8, 453-482.

Falk, L., Commenge, J.M., 2010. Performance comparison of micro-mixers. Chemical Engineering Science 65, 405-411.

Ferrouillat, S., Tochon, P., Garnier, C., Peerhossaini, H., 2006a. Intensification of heat transfer and mixing in multifunctional heat exchangers by artificially generated streamwise vorticity. Applied Thermal Engineering 26, 1820-1829.

Ferrouillat, S., Tochon, P., Peerhossaini, H., 2006b. Micro-mixing enhancement by turbulence: Application to multifunctional heat exchangers. Chemical Engineering and Processing 45, 633-640.

Fiebig, M., 1995. Embedded vortices in internal flow: heat transfer and pressure loss enhancement. International Journal of Heat and Fluid Flow 16, 376-388.

Fournier, M.C., Falk, L., Villermaux, J., 1996a. A new parallel competing reaction system for assessing micro-mixing efficiency - Experimental approach. Chemical Engineering Science 51, 5053-5064.

Fournier, M.C., Falk, L., Villermaux, J., 1996b. A new parallel competing reaction system for assessing micro-mixing efficiency - Determination of micro-mixing time by a simple mixing model. Chemical Engineering Science 51, 5187-5192.

Guichardon, P., Falk, L., 2000. Characterisation of micro-mixing efficiency by the iodide-iodate reaction system. Part I: Experimental procedure. Chemical Engineering Science 55, 4233-4243.

Guichardon, P., Falk, L., Villermaux, J., 2000. Characterisation of micro-mixing efficiency by the iodide-iodate reaction system. Part II: kinetic study. Chemical Engineering Science 55, 4245-4253.

Habchi, C., Lemenand, T., Della Valle, D., Peerhossaini, H., 2009a. Liquid/liquid dispersion in a chaotic advection flow. International Journal of Multiphase Flow 35, 485-497.

Habchi, C., Ouarets, S., Lemenand, T., Della Valle, D., Bellettre, J., Peerhossaini, H., 2009b, Influence of viscosity ratio on droplets formation in a chaotic advection flow. International Journal of Chemical Reactor Engineering 7, A50.

Habchi, C., Lemenand, T., Della Valle, D., Peerhossaini, H., 2010. Alternating mixing tabs in multifunctional heat exchanger-reactor, Chemical Engineering and Processing, doi:10.1016/j.cep.2009.07.003.

Hessel, V., Hardt, S., Löwe, H., Schönfeld, F., 2003. Laminar mixing in different interdigital micro-mixers: I. Experimental characterization. American Institute of Chemical Engineering Journal 49, 566-577.

Jones, S.W., Thomas, O.M., Aref, H., 1989. Chaotic advection by laminar flow in a twisted pipe. Journal of Fluid Mechanics 209, 335-357.

Kockmann, N., Kiefer, T., Engler, M., Woias, P., 2006. Silicon microstructures for high throughput mixing devices. Microfluid Nanofluid 2, 327-335.

Kölbl, A., Kraut, M., Schubert, K., 2008. The iodide iodate method to characterize microstructured mixing devices. American Institute of Chemical Engineering Journal 54, 639-645.

Kölbl, A., 2008. Further comments on the iodide iodate reaction method for characterising micro-mixing. Chemical Engineering Journal 145, 176-177.

Lemenand, T., Peerhossaini, H., 2002. A thermal model for prediction of the Nusselt number in a pipe with chaotic flow. Applied Thermal Engineering 22 (15), 1717-1730.

Lemenand, T., Della Valle, D., Zellouf, Y., Peerhossaini, H., 2003. Droplets formation in turbulent mixing of two immiscible fluids in a new type of static mixer. International Journal of Multiphase Flow 29, 813-840.

Lemenand, T., Dupont, P., Della Valle, D., Peerhossaini, H., 2005. Turbulent mixing of two immiscible fluids. Journal of Fluids Engineering 127 (6), 1132-1139.

Mohand Kaci, H., 2007. Caractérisation des capacités de micromélange des changeurs/réacteurs multifonctionnels par sonde chimique -- Application au HEV. Ph.D. thesis, École Polytechnique, University of Nantes.

Mohand Kaci, H., Lemenand, T., Della Valle, D., Peerhossaini, H., 2009. Effects of embedded streamwise vorticity on turbulent mixing. Chemical Engineering and Processing 48, 1457-1474.

Mohand Kaci, H., Habchi, C., Lemenand, T., Della Valle, D., Peerhossaini, H., 2010. Flow structure and heat transfer induced by embedded vorticity. International Journal of Heat and Mass Transfer, doi:10.1016/j.ijheatmasstransfer.2010.04.029.

Muzzio, F.J., Meneveau, C., Swanson, P.D., Ottino, J.M., 1992. Scaling and multifractal properties of mixing in chaotic flows. Physics of Fluids A 4, 1439-1456.

Ottino, J.M., Ranz, W.E., Macosko, C.W., 1979. A lamellar model for analysis of liquid- liquid mixing. Chemical Engineering Science 34, 877-890.

Palmer, D.A., Ramette, R.W., Mesmer, R.E., 1984. Triodide ion formation equilibrium and activity coefficients in aqueous solution. Journal of Solution Chemistry 13, 673-683.

Paul, E.L., Atiemo-Obeng, V., Kresta, S.M., 2004. Handbook of Industrial Mixing. Wiley, Hoboken, NJ.

Pourbaix, M., 1963. Atlas d'équilibres électrochimiques, Gauthier-Villars, Paris.

Schaer, E., Guichardon, P., Falk, L., Plasari, E., 1999. Determination of local energy dissipation rates in impinging jets by a chemical reaction method. Chemical Engineering Journal 72, 125-138.

Schäfer, M., Höfken, M., Durst, F., 1997. Detailed LDV measurements for visualization of the flow field within a stirred-tank reactor equipped with a Rushton turbine. Transaction of the Institution of Chemical Engineers 75, 729-736.

Stankiewicz, A., Moulijn, J., 2000. Process Intensification: transforming chemical engineering, Chemical Engineering Progress 96, 22-34.

Toe R, Ajakh A, Peerhossaini H, 2002. Heat transfer enhancement by Görtler instability. Int. J. Heat Fluid Flow, 23, 194-204.

Villermaux, J., 1986. Micro-mixing phenomena in stirred reactors, Encyclopedia of Fluid Mechanics, Houston, Gulf Publishing Company.

Wallace, J.M., 2009. Twenty years of experimental and direct numerical simulation access to the velocity gradient tensor: What have we learned about turbulence. Physics of Fluids 21, 021301.

CORPUS DES ARTICLES

3. Turbulence behavior of artificially generated vorticity

C. Habchi, T. Lemenand, D. Della Valle, H. Peerhossaini

Journal of Turbulence 11 N°36 (2010c) 1-28.

Journal of Turbulence
Vol. 11, No. 36, 2010, 1–28

Taylor & Francis
Taylor & Francis Group

Turbulence behavior of artificially generated vorticity

Charbel Habchi[a,b], Thierry Lemenand[a], Dominique Della Valle[a] and Hassan Peerhossaini[a*]

[a] *Thermofluids, Complex Flows and Energy Research Group, LTN, CNRS UMR 6607, École Polytechnique – University of Nantes, rue Christian Pauc, B.P. 50609, 44306 Nantes, France;* [b] *Agence de l'Environnement et de la Maîtrise de l'Énergie (ADEME), 20 avenue du Grésillé, B.P. 90406, 49004 Angers, France*

(*Received 05 January 2010; final version received 17 July 2010*)

Longitudinal vortices and hairpin-like structures are generated in an open loop flow by a row of vortex generators inserted on the inner wall of a circular pipe; the vortex generator row is made up of four diametrically opposed trapezoidal tabs tilted from the wall. Steady counter-rotating vortex pairs and periodic hairpin-like structures develop downstream from each tab. The flow pattern of these vortical structures has been studied extensively [D. Dong and H. Meng, *Flow past a trapezoidal tab*, J. Fluid Mech. 510 (2004), pp. 219–242]; nevertheless, the specific contributions of these structures to the mixing process have not yet been elucidated, especially with regard to global improvement of the transfer coefficients compared to a straight pipe. This study aims at exploring the turbulent mixing mechanisms caused by artificially generated vorticity, especially at the different mixing scales (macro-, meso- and micro-mixing), using both numerical simulations and laboratory experiments. Instantaneous velocities and spectral analysis using Laser Doppler Velocimetry are carried out for axial velocity components. Numerical simulations using the Reynolds stress turbulence model are also performed to investigate the effect of the different flow structures on the averaged Reynolds stress tensor and the turbulent kinetic energy dissipation rate. The development and decay of the counter-rotating vortices are also investigated using a recent pseudo-viscous model [O. Lögdberg, J.H.M. Fransson, and P.H. Alfredsson, *Streamwise evolution of longitudinal vortices in a turbulent boundary layer*, J. Fluid Mech. 623 (2009), pp. 27–58]. Here we modify this model to predict the center path of the streamwise vortices in a turbulent boundary layer. It is also shown that the hairpin-like structures govern both meso- and micro-mixing mechanisms, while the counter-rotating vortices act as internal agitators in the flow by creating convective transfer between the wall region and the flow core. This investigation is fundamental for optimizing static mixers based on vortex generators and for control of separation in aerodynamic applications.

Keywords: longitudinal vortices; streamwise vortices; transverse vortices; hairpin-like structures; vortex generators; turbulent mixing; turbulent mass transfer; multifunctional heat exchangers/reactors

1. Introduction

The streamwise and transverse vortical structures can be artificially generated in turbulent flows by inserting sharp-edged obstacles that cause local pressure gradients and shear

*Corresponding author. hassan.peerhossaini@univ-nantes.fr

ISSN: 1468-5248 online only

DOI: 10.1080/14685248.2010.510841
http://www.informaworld.com

instabilities [1–14]. These vortices, which efficiently enhance radial heat and mass transfer, can be readily used in industrial processes simply by mounting inclined tabs on the channel wall. The main applications are in heat and mass transfer intensification [1, 7–9] and drag reduction, and control of flow separation in aeronautics and automotive aerodynamics [13] as well as for flow control over three-dimensional bluff bodies [14].

Various geometries are available for the vortex generators; the present study focuses on the trapezoidal ones used in the high-efficiency vortex (HEV) static mixer [15]. Gretta and Smith [4] investigated the flow pattern in such a configuration and identified two types of flow structures: a counter-rotating vortex pair (CVP), formed in the wake of the tab because of the pressure difference between the low-momentum region under the tab and the high-momentum region above the tab, and a periodic sequence of hairpin-like structures (or horseshoe vortices) riding on top of the CVP and being convected downstream. The interactions of these structures and the main flow significantly enhance mixing by mass exchange between the near-wall region and the core flow [4–7]. This mechanism is employed in the HEV mixer, where several arrays of trapezoidal tabs produce a complex vortex system [8–12].

Numerous studies underline the existence of Ω-shaped hairpin packets in the near-wall layers and analyze their dynamics and mechanisms of turbulence production [16–19]. Kim and Adrian [16] have characterized very large-scale motions (VLSM) in the outer layer of fully developed turbulent pipe flow formed by long packets of hairpin-like structures. Zhou, Adrian and Balachandar [17] have identified auto-generation mechanisms of a symmetric quasi-streamwise vortex pair in the near-wall turbulent boundary layer by using direct numerical simulation (DNS), showing that these vortices expand into primary hairpins that grow and generate secondary hairpin structures as they are convected downstream. While the hairpins are being lifted up, a new pair of streamwise vortices forms on their "legs," providing a self-sustaining mechanism.

Similar dynamics were observed by Dong and Meng [7] for flow past a trapezoidal tab. While propagating downstream, the CVP distorts and splits into hairpin vortex legs because of the instability caused by the difference of vorticity in the vortex core and surrounding fluid. Moreover, when the flow encounters the mixing tab, a three-dimensional shear layer is formed around the tab that becomes more unstable and generates hairpin structures, a phenomenon caused by the Kelvin–Helmholtz instability in a free shear flow. Primary hairpins can further generate secondary vortices in the tab wake [6–7]. As observed by Yang, Meng and Sheng [6] and Dong and Meng [7], these secondary vortices have a hairpin-like shape (as shown in Figure 14). Other secondary instabilities can also occur to generate reverse vortices in the tab wake [6–7]. The growth of the hairpin strength is here attributed [6–7] to ejection and entrainment of new vorticity from the near-wall local boundary layer toward the hairpin head. Figure 1 shows the main flow structures.

These embedded structures contribute to the transfer of momentum, heat and mass that can be analyzed in terms of mixing. More precisely, they specifically contribute to the different scales of mixing in the turbulent flow, namely macro-, meso- and micro-mixing. Following the classification introduced by Villermaux and Devillon [20], macro-mixing characterizes flow homogeneity at the reactor scale. The related mechanism is advection by the mean flow, generally characterized by a Péclet number. Meso-mixing is the process of disintegration of large eddies in the inertial sub-range of the energy cascade; a typical meso-mixing parameter can be any component of the Reynolds stress tensor, which determines the concomitant destruction of a tracer concentration variance [21–22] by the turbulence. Meanwhile, the viscous–convective deformation of the fluid under the Kolmogorov scale accelerates mass diffusion and brings about homogenization in the molecular scale. This

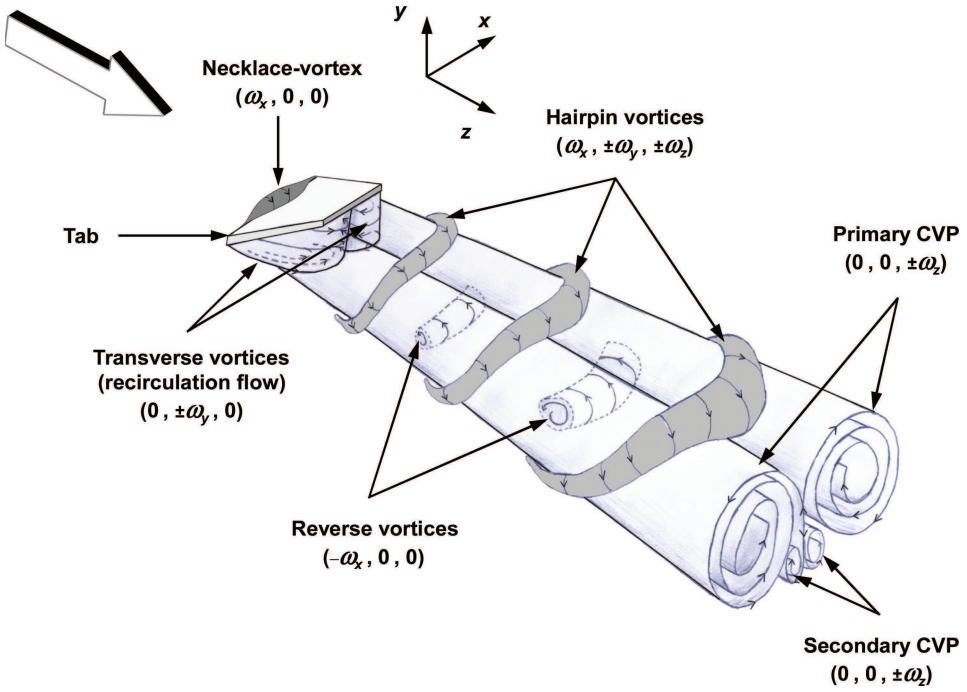

Figure 1. The main flow structures generated by a trapezoidal vortex generator.

last mechanism is the micro-mixing, decisive in fast chemical reactions [23] and drop equilibrium diameter in multiphase flows [24]. In the turbulent regime, micro-mixing has a typical time scale based on the turbulent energy dissipation rate; this parameter is therefore retained here in the analysis. In practical mixing situations, it is important to note that the higher scales "feed" the lower scales and that the ultimate performance of a reactor depends on the three steps mentioned above.

The present study gives an experimental and numerical analysis of the contribution of the different flow structures to the mixing process, including a spectral analysis of the shear instability in the flow downstream from the vortex-generating tabs. Streamwise vortices are generated by a row of four diametrically opposed trapezoidal mixing tabs inserted at an angle on the inner wall of a circular pipe.

The instantaneous velocity measurements and spectral analysis are carried out using laser Doppler velocimetry (LDV); the experimental test section and hydraulic loop are described in Section 2. The velocity and turbulence fields are also simulated numerically, using the Reynolds stress model (RSM), in order to obtain the three-dimensional flow structures. The numerical procedure and implementation are presented in Section 3.

After discussing the experimental validation of the numerical results in Section 4, the flow topology induced by the vortex generators is described, as is the individual contribution of the different flow structures to the turbulent mixing. Moreover, a pseudo-viscous model, recently developed by Lögdberg, Fransson and Alfredsson [2] by extending the analysis in Jones [25], is used to study the longitudinal development of the CVP. This model allows description of the vortex strength decay and the streamwise asymptotic limit of the vortex center and brings out fundamental knowledge useful in various applications,

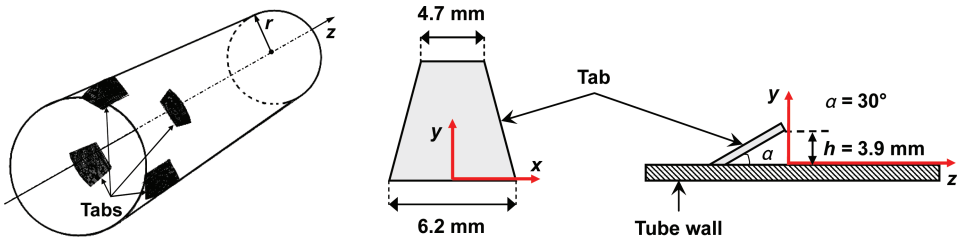

(a) (b)

Figure 2. (a) Schematic of the test section; (b) mixing tab dimensions.

such as separation control in aerodynamics and design optimization of static mixers and multifunctional heat exchangers/reactors.

2. Experimental setup

2.1. *Test section and hydraulic loop*

The test section consists of a straight circular pipe of 20-mm inner diameter in which a row of four diametrically opposed mixing tabs is fixed (Figure 2(a)). The tabs are inclined at 30° with respect to the tube wall (Figure 2(b)).

As shown in Figure 3, the test section is preceded by a preconditioner (2000-mm straight Plexiglas pipe) to generate a fully developed turbulent flow at the test section inlet, and is followed by a postconditioner (200-mm straight Plexiglas pipe). The connections between the different elements carefully avoid any protuberance that could disturb the flow. A safety

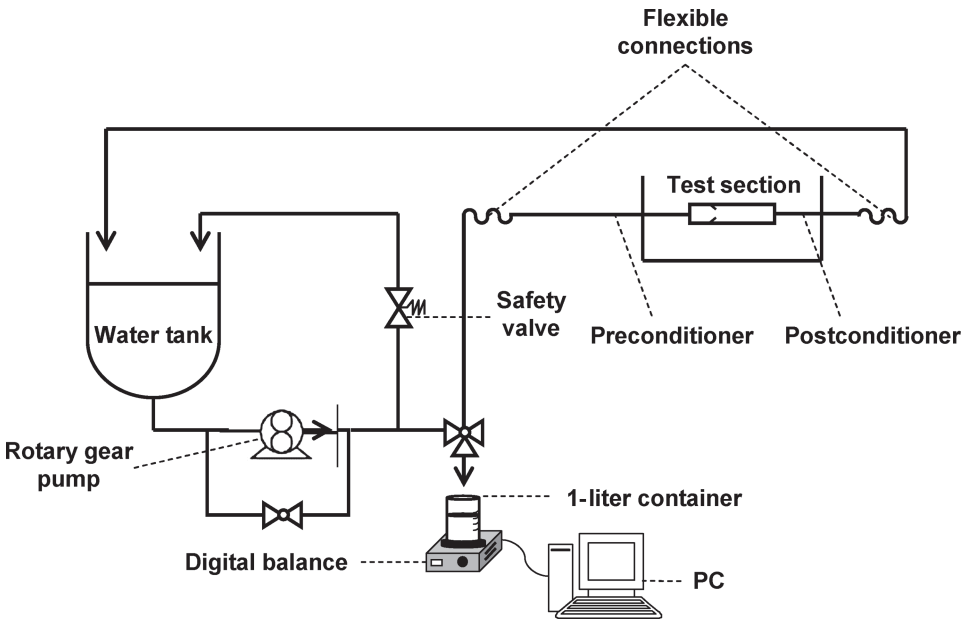

Figure 3. Hydraulic loop.

Table 1. Details of LDV setup and particle seeding.

	LDV system
Laser type	Two-component optic-fiber system operated in back-scattered light mode.
Wavelengths	514.5 nm (green)–488 nm (blue)
Shift frequency	40 MHz (Bragg cell)
Measurement volume Positioning	Manual (3D) + automatic with 12.5-μm precision.
Beam separation	40 mm
Beam diameter before lens	3.8 mm
Beam intersection angle	13.55°
Measurement volume length	404 μm
Measurement volume width	48 μm
Measurement volume height	48 μm
Fringes number	21
Fringes spacing	2.18 μm
	Seeding particles
Type	Merck Iriodine: small spangled particles of mica coated in titanium oxide.
Size	0.1–0.5 μm
Density	3 g.m^{-3}
Response frequency	1 kHz

valve is added to the circuit, as well as a pulsation damper to limit the pressure fluctuations produced by the pump and thus ensure stable flow in the test section.

The temperature of the working fluid (water) is maintained constant at 298 K. The experiments are carried out in a turbulent flow with Reynolds numbers based on the pipe diameter in the range of 7500–15,000.

2.2. *LDV measurements and data acquisition*

Measurements are made using a Dantec LDV system equipped with a 10-W argon-ion laser source and two BSA-enhanced signal-processing units (57N20 BSA and 57N35 BSA enhanced models); the measurement head is equipped with a 160-mm focal lens. The measuring volume of the LDV is positioned with a three-dimensional lightweight precision traversing system controlled via a PC. Owing to the cylindrical shape of the pipe, and in order to avoid light beam refraction, only the axial component of the Reynolds stress and mean velocity are measured in the radial direction. The details of the LDV setup and particle seeding are shown in Table 1.

The statistical convergence criteria are achieved on the velocity fluctuations and the mean velocity. It was shown that a validated sampling particle number 30,000 is needed to obtain the statistical convergence. The associated measurement time ranges between 60 s and 360 s, which is about 6×10^3 to 36×10^3 times the integral time scale, thus ensuring statistical convergence. The data-acquisition rate is 1–4 kHz.

The LDV system calibration, including Bragg-cell oscillation and orientation sensitivity, light beam power, reference point and optics alignment, was performed. The precision error was estimated at about 2.5%. Moreover, to ensure the reproducibility of LDV measurements, experiments were iterated four times for radial profiles at different positions for Reynolds number 15,000. The relative standard deviation for the mean and RMS velocities depends on location in the measurement volume: it reaches 10–12% in the near-wall region and

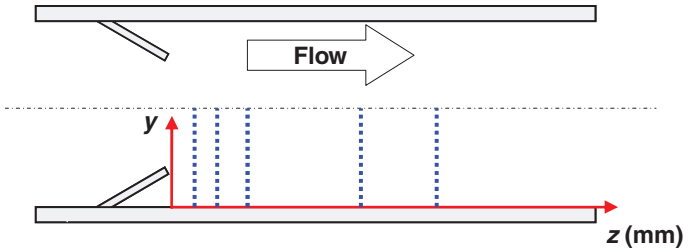

Figure 4. Measurement points on the radial profiles (dotted blue lines) in the symmetry plane of the tab.

in the shear layer, a low-velocity, high-turbulence-intensity zone, and stays at about 2.5% in the flow core region. The global mean standard deviation does not exceed 6% for the mean velocity or for the turbulent fluctuations. Thus, the uncertainty can be calculated as $\sqrt{2.5^2 + 6^2} = 6.5\%$.

Using the sampling rate uncertainty method of Benedict and Gould [26], the confidence level is determined to be 95%; in addition, 15% of the measured data had an error less than 1% and 85% less than 10%.

The integral time scale can be evaluated from the temporal correlation function, which requires velocity measurements with only a single probe. Measurements must be performed at sufficiently short time intervals to detect high-frequency fluctuations. Laser Doppler velocimetry allows such fast measurements by optimizing seeding and optical adjustments. However, as LDV measurements are not performed at constant time intervals, the data must be sampled again. In the present study, all data were resampled according to a method suggested by Høst-Madsen and Caspersen [27].

Measurements are taken on radial profiles in the center plane of one mixing tab, at 3, 6, 10, 25 and 35-mm downstream from the tab tip, as shown in Figure 4.

2.3. *Turbulent energy dissipation rate*

We compute the turbulent energy dissipation rate from the following expression, using Batchelor's [28] model based on dimensional analysis:

$$\varepsilon = A\,\frac{u'^3}{\Lambda}. \tag{1}$$

The constant A was determined by Mokrani, Castelain and Peerhossaini [29] as 1.85, and this value has been used subsequently [8–12] for turbulent flow in similar configurations. Λ represents the integral length defined by Batchelor [28]:

$$\Lambda = \int_0^\infty \frac{\overline{u'(x)\,u'(x+r)}}{\overline{u'^2(x)}}\,dr. \tag{2}$$

Evaluating Λ using Equation (2) requires the spatial or temporal autocorrelation, which is available by LDV in the present study. The temporal macroscale is determined by Equation

(3) and leads to the spatial macroscale by (4):

$$\tau = \int_0^\infty \frac{\overline{u'(t)\,u'(t+T)}}{\overline{u'^2(t)}}\,dT, \tag{3}$$

$$\Lambda = \tau\ U_{\text{conv}}. \tag{4}$$

The convective velocity U_{conv} is estimated by the Van Doorn model [30] and has been successfully used [8–12] for the HEV static mixer, assuming local isotropy of the turbulence in a one-dimensional mean flow:

$$U_{\text{conv}} = U^2\left(1 + 5\frac{\overline{u'^2}}{U^2}\right). \tag{5}$$

3. Numerical simulation

3.1. *Solution method*

A numerical simulation of the incompressible flow is carried out using the CFD program Fluent® 6.3 to access the three-dimensional turbulent fields, because LDV measurements are feasible only in two dimensions. The continuity equations for mass and momentum are solved sequentially with double precision, segregated and second-order UPWIND [31]. Pressure-velocity coupling is performed by finite volume with the SIMPLE algorithm [32]. The second-order precision is obtained by calculating the quantities on the cell faces using the multidimensional linear approach [33].

3.2. *Turbulence model and boundary conditions*

Mohand Kaci et al. [11], studying flow dynamics in the HEV static mixer and testing five different models in the HEV configuration, found that the standard $k-\varepsilon$ [34, 35] and RSM models (Boussinesq closure hypothesis for the third-order moments) [36–38], associated with a two-layer model to compute the wall region, provide a satisfactory description of the flow pattern in the HEV geometry. In the present study the RSM model is preferred because knowledge of Reynolds stresses is required to understand the turbulent mixing process.

The RSM model involves the calculation of the individual Reynolds stresses $\overline{u_i'\,u_j'}$ by solving seven differential transport equations without using the Boussinesq hypothesis for the turbulent viscosity. The individual Reynolds stresses are then used to obtain closure of the Reynolds averaged momentum equation. The pressure–strain terms in the transport equations are treated by the linear model proposed by Gibson and Launder [36], Launder, Reece and Rodi [37] and Launder [38]. The turbulent diffusion terms are modeled by the generalized gradient-diffusion model of Daly and Harlow [39].

The near-wall region is modeled by a two-layer model, or enhanced wall treatment. In this approach, the near-wall region is divided into a viscous sublayer and a turbulent region. The delimitation of these two regions is determined by the turbulent Reynolds number based on the distance normal to the wall y, which is defined as $Re_y = \rho\, y\, \sqrt{k}/\mu$. In the turbulent region ($Re_y > 200$), the RSM model equations are solved. In the viscous sublayer ($Re_y < 200$) the one-equation model of Wolfstein [40] is used, where only the momentum

and turbulent kinetic energy transport equations are solved. However, the turbulent viscosity is computed from the empirical correlation defined by $\mu_t = \rho\, C_\mu\, \ell_\mu\, \sqrt{k}$, where ℓ_μ is the length scale defined by Chen and Patel [41] as $\ell_\mu = y\, C_\ell^* [1 - \exp(-Re_y/A_\mu)]$. When using the enhanced wall treatment, a zero flux for the Reynolds stresses $\overline{u_i' u_j'}$ is applied at the wall boundaries. The constants C_ℓ^* and $C_\mu A_\mu$ are given by Chen and Patel [41].

A no-slip boundary condition is applied to the solid surfaces and a 1/7 power-law velocity profile $W = W_{\max}(1 - y/R)^{1/7}$ is imposed at the tab array inlet [42]. The turbulent kinetic energy and the dissipation rate are fixed by the turbulence intensity I and are respectively $k = 3\,(W_m\, I)^2/2$ and $k = C_\mu^{3/4}\, k^{3/2}/0.07\, D$, where $I = 0.16\, Re^{-1/8}$ is derived from the empty-tube equilibrium state [42]. C_μ is a constant equal to 0.09.

3.3. *Computational domain and meshing*

Exploiting the symmetry of the mixer, the studied section is reduced to the $\pi/4$ sector shown by the gray area in Figure 5(a). Previous studies by Mokrani et al. [29] and Mokrani [43] showed that in stationary numerical simulations, this tangential symmetry does not affect the numerical results, as the coherent structures grow downstream of the tab. However, this symmetry cannot be used when performing transient numerical simulations in attempting to capture the interaction among the transient flow structures [4–7].

Using the software Gambit®, a nonuniform unstructured three-dimensional mesh with hexahedral volumes is adopted and refined at all solid boundaries (wall and tab surfaces) so as to take into account the strong gradients in this region. The mesh on the tabs' symmetry plane is shown in Figure 5(b). The two-layer approach requires estimation of the wall adjacent cell size, corresponding to an ideal dimensionless wall distance y_c^+ that would not exceed 5, guaranteeing that the viscous sub-layer is meshed [44]. The mean final value of y_c^+ for the actual numerical simulations is about 2.1 and its maximum value is 3.2.

To determine the appropriate mesh, the simulation is run with increasing mesh densities until no effect on the results is detected. The criterion for the grid sensitivity test is based on velocity profiles and turbulence dissipation rate at 3, 6, 10, 25, 35 and 50-mm downstream from the tab tip. The final mesh contains 484,352 cells. The mesh quality was quantified

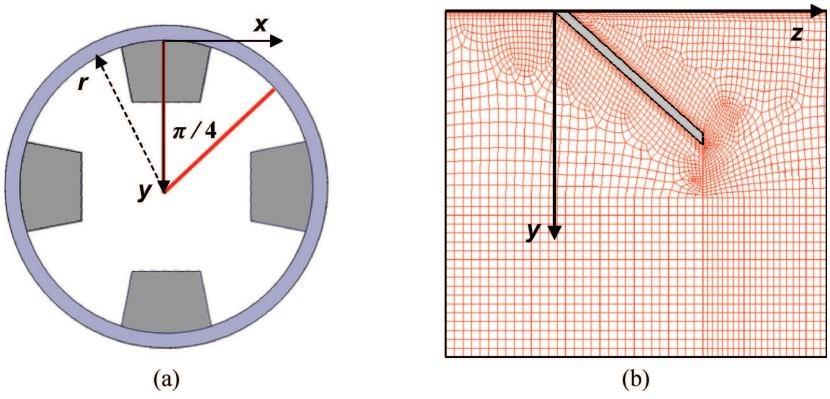

Figure 5. (a) Computational domain (gray area); (b) mesh (transverse cross section).

by using equi-angle skew parameter. Results show 73.9% high-quality cells, 23.6% good quality cells and 2.5% acceptable quality cells.

3.4. *Convergence and accuracy criteria*

In order to determine an adequate convergence criterion, a series of simulations for different stop-criterion values ranging from 10^{-3} to 10^{-9} was carried out. Beyond a convergence criterion of 10^{-6}, no significant changes were observed in the velocity field or turbulence quantities; this value was therefore retained as the convergence criterion.

Numerical accuracy is checked with the numerical global mean energy dissipation $\bar{\varepsilon}$, integrated on the whole geometry volume, and compared with equation (6) from the computed pressure drop level:

$$\bar{\varepsilon} = \frac{W\ \Delta P}{\rho\, L}, \tag{6}$$

where W is the axial mean velocity, ΔP the pressure drop, ρ, the fluid density and L, the test section length. Results are in good agreement, with relative deviation 10^{-4}, showing that the numerical deviation remains low in the simulations.

4. Results and discussion

4.1. *Experimental validation*

The physical relevance of the CFD simulations is shown in Figure 6, which compares experimental and numerical radial profiles for the streamwise mean and fluctuating velocities for two different axial positions downstream from the tab at $z = 0$. Figure 5 shows that numerical simulations predict the flow pattern in the studied test section quite well: the overall relative standard deviation does not exceed 8%. It is maximal in the shear zone ($0.36 < y/R < 0.55$), low velocities inducing reduced LDV precision, and minimal in the core region ($0.55 < y/R < 1$).

A significant damping of the mean velocity gradients is observed between $z/h = 0.75$ and $z/h = 8.75$, where h is the tab height (see Figure 2). Near the tab, the flow can be divided into three different regions: the shear region around $y/R \approx 0.4$, where high gradients are observed, the flow core region in the pipe center for $y/R \approx 1$ and the wake region behind the tab for $y/R \approx 0.2$. Regarding the RMS velocity, the shear region is marked by a maximum, the flow core and the wake region by low and moderate turbulence intensity respectively. Downstream, the mean velocity profile tends to the 1/7 power law of a fully developed turbulent flow.

4.2. *Upstream necklace vortex and downstream recirculation flow*

Figure 7 shows the distribution of the mean streamwise velocity and the flow streamlines for Reynolds number 15,000. In Figure 7(a) a necklace vortex is observed upstream of the tab that also appears in the DNS by Dong and Meng [7]. Actually, in this region, the interaction between the main flow and the low-momentum fluid in the corner between the tab and the pipe wall develops high-velocity gradients that generate a transversal vorticity, giving rise to the necklace vortex. In the near wake of the tab, a dead zone is also observed. As shown in Figure 7(b), a recirculation flow formed of two symmetrical counter-rotating vortices is generated behind the tab (on both sides of the tab symmetry plane at ($x/R = 0$)).

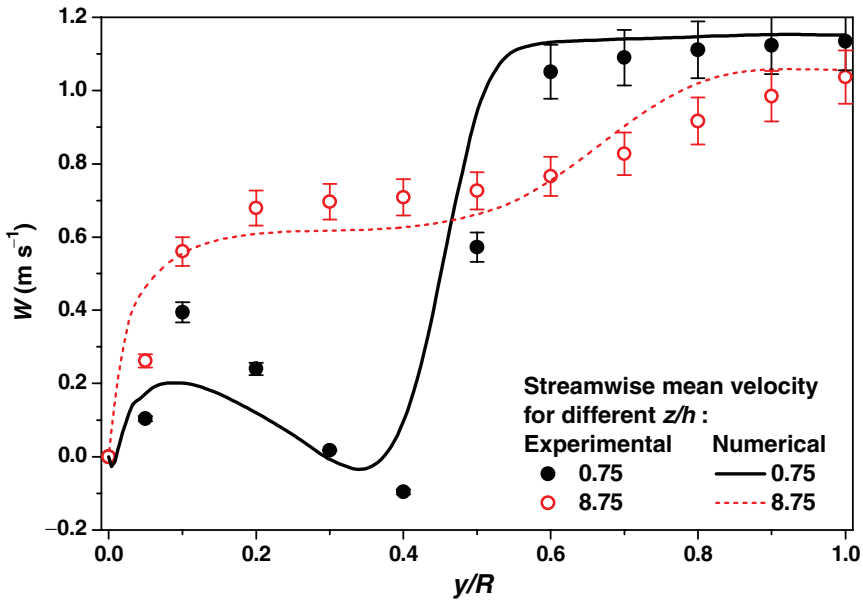

(a)

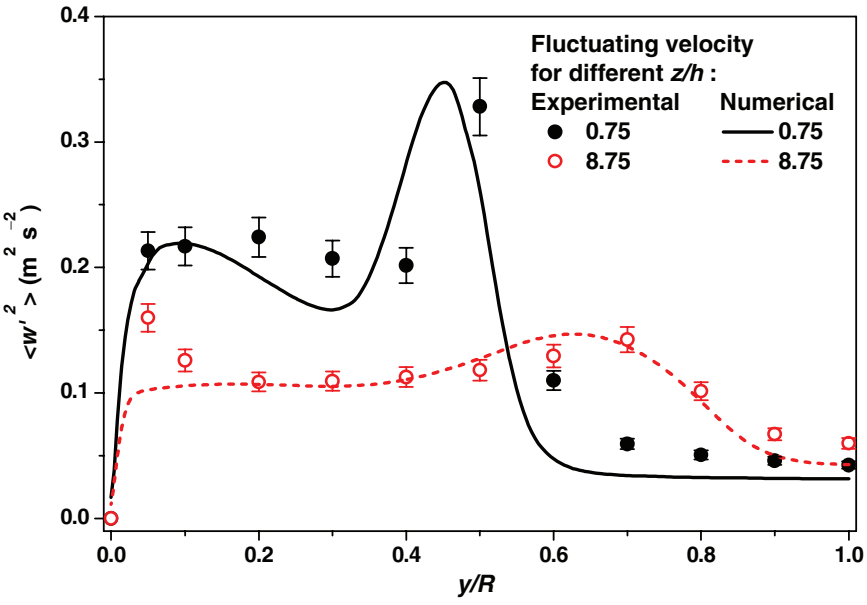

(b)

Figure 6. Experimental validation: streamwise (a) mean and (b) fluctuating velocity radial profiles, $z/h = 0.75$ and 8.75, Re = 15, 000.

These transverse vortices are caused by the wake effect due to the tab, whereby the flow stream must detour around the obstacle. These two flow structures form stagnation regions that trap the fluid particles. These regions can lead to overheating in exothermal chemical reactions and have a negative effect on macro- and meso-mixing.

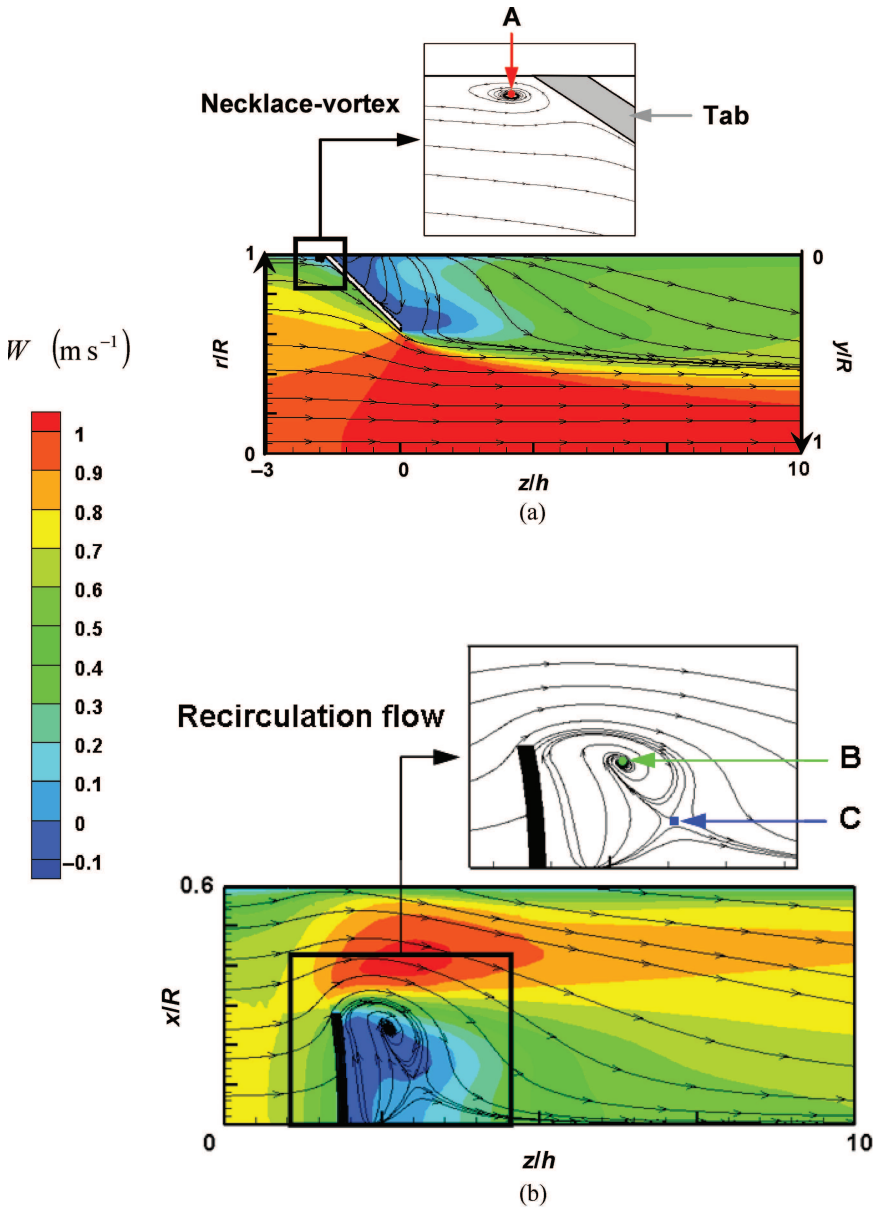

Figure 7. Axial mean velocity distribution and streamlines for $Re = 15{,}000$ in (a) tab symmetry plane and (b) horizontal plane at radial distance $r/R = 0.8$.

Several critical points are observed in Figure 7. In fact, a stable focus A on the tab symmetry plane is identified by a red dot in Figure 7(a) within the necklace-vortex center; another stable focus B is marked by a green dot in Figure 7(b) within the downstream recirculation flow. These foci identify the generation of hairpin vortices [44, 45]. The blue square C is a saddle point locating the separation of the recirculation flow.

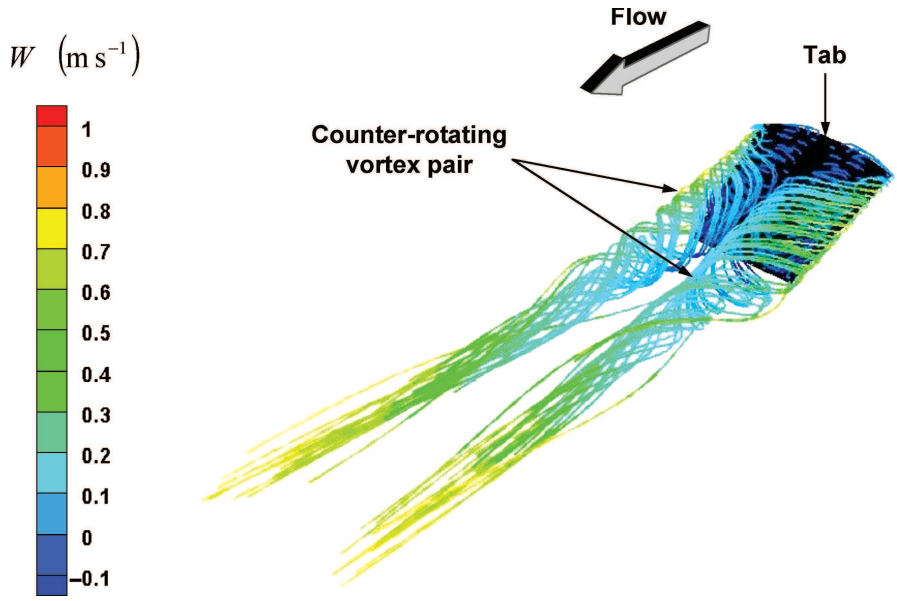

Figure 8. Perspective view of pathlines injected from the tab edges: a counter-rotating vortex pair is developing in the near tab wake, $Re = 15{,}000$.

4.3. *Counter-rotating vortex pair (CVP)*

4.3.1. *Flow topology of the CVP*

The spiral motion on the tab edges generated by the two counter-rotating streamwise vortices is shown in Figure 8.

The cross-section view of these two longitudinal vortices in Figure 9 shows the flow pattern downstream from the tab. The negative bifurcation line L^- in the wake of the tab indicates the generation of an uplifting CVP, and a positive bifurcation line L^+ is also observed in the tab symmetry plane at the tab top edge. At the limit of bifurcation lines

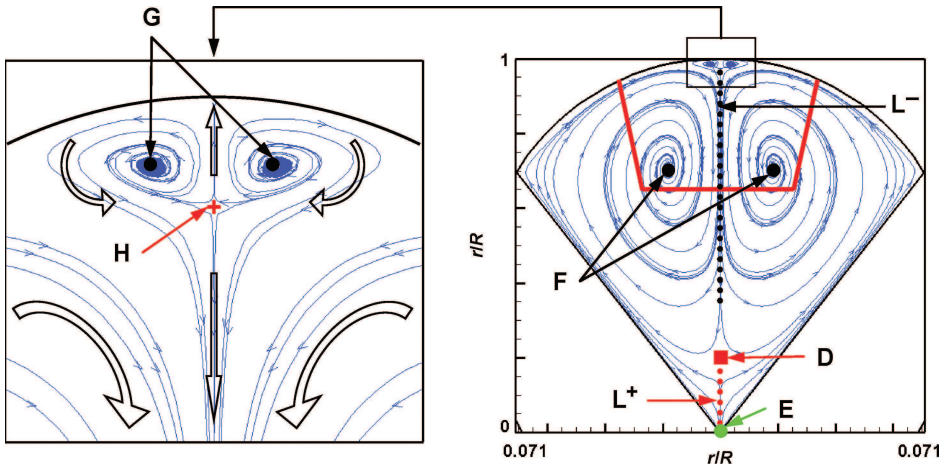

Figure 9. Streamlines in a tube cross section at $z/h = 0.75$ downstream from the tab.

L^+ and L^-, the saddle point of separation D (marked by a red square) corresponds to the splitting of the CVP on the tab symmetry plane. In the center of each CVP, a stable focus F is observed (black circle). Moreover, a separation or unstable node E in the tube center because of the CVP is generated by the four tabs, which sweep the fluid from the flow core toward the wake region. A pair of secondary streamwise CVPs, identified for the first time by Dong and Meng [7], is also observed near the wall behind the tab. Their vorticity is in the opposite direction to the primary CVPs because they are created by the interaction of the accelerated fluid on the circumference of the primary CVPs and the slow fluid near the wall. The common flow of the secondary CVPs prevents transfer of the low-momentum fluid in this region to the core flow by the primary CVPs and hence reduces the mixing efficiency of the vortex generator. Unlike the primary CVPs, which show stable foci in their centers, unstable foci G (black circles) occur in each secondary CVP center. A saddle point H, indicated by a red $+$, marks the splitting of secondary and primary CVP common flows.

Similar critical points have also been found for flows around a solid obstacle, such as a low-aspect ratio pyramid [3], a backward-facing step [45], a flow separation over a three-dimensional axisymmetric hill [46] and in-flow past a delta wing with a sinusoidal leading edge [47]. More details and physical analyses of critical points are provided by Bakker and de Winkel [48].

4.3.2. *Streamwise evolution of the CVP by the Jones–Lögdberg method*

The evolution of the longitudinal vortices and their decay in strength are investigated by studying the streamwise evolution of their circulation Γ and the path of their centers in the tube volume. This method was developed by Lögdberg et al. [2] by adding a pseudo-viscous term to the Jones [25] potential-flow approach, and has been successfully implemented for the case of rectangular wings [2].

For this purpose, the circulation of the CVP is determined following the general definition:

$$\Gamma = \int_S \omega_z \, dS, \tag{7}$$

where ω_z is the streamwise vorticity and S is the vortex area. The vortex S core is the contour delimited by a fraction of 5% of the maximum invariant Q_z [2, 49]. In fact, once the Q_z contour is plotted, the vortex core is where Q_z is reduced to 5% of its maximal value at the vortex center:

$$Q_z = -\frac{1}{2}\frac{\partial V}{\partial x}\frac{\partial U}{\partial y}. \tag{8}$$

Figure 10 shows the longitudinal evolution of Γ for $Re = 15{,}000$. Here Γ_0 is the vorticity circulation when z tends to be zero at the first point where the vortex core is detected. The exponential decay of Γ is clearly observed, as reported by Lögdberg et al. [2] for the flow downstream of a rectangular vortex generator. The circulation decay, caused by the dissipative effects of the turbulent stresses, appears to undergo very steep asymptotic damping, and shows the "scope of action" of the vortex generator. It can be concluded from Figure 10 that to maintain the macro-mixing level in the flow section, another vortex generator must be located at a dimensionless distance of $z/h \approx 5$, where the vortex strength has decreased to about 50% of its initial value Γ_0. From experimental flow visualizations,

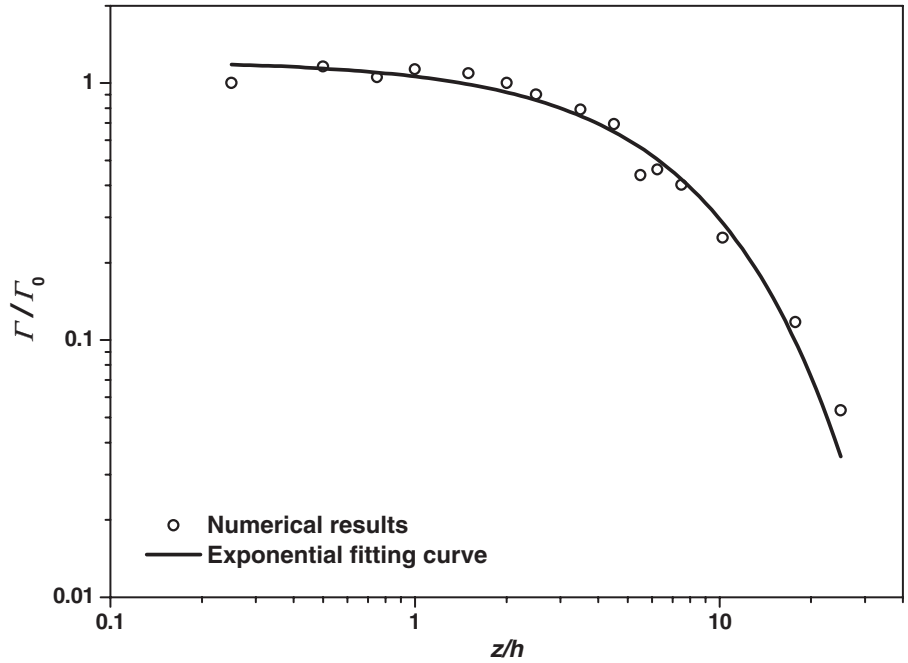

Figure 10. Exponential decay of the vortex strength, $Re = 15{,}000$.

Elavarasan and Meng [5] and Yang et al. [6] have found that CVPs lose most of their strength at about $z/h \approx 2$. In the HEV static mixer [8–11] the vortex generators are spaced by $z/h \approx 6$, so this geometry could be optimized by moving the vortex generators arrays closer.

The vortex center is computed as the location of the maximum absolute streamwise vorticity $|\omega_z|_{\max}$ in the cross section. Actually, $|\omega_z|_{\max}$ decreases downstream from the tab, and the vorticity distribution becomes more uniform in the cross section. This feature reduces the accuracy of the determination of the vortex center "far" from the tab [2].

From Jones' analytical solution [25], the vortex center in the cross section (x, y) is given by Equation (9), while its path slopes projected in the transverse sections (x, z) and (y, z) are obtained from Equations (10) and (11):

$$\frac{1}{\sin^2(x_c)} + \frac{1}{\sinh^2(y_c)} = C, \tag{9}$$

$$\frac{dx_c}{dz_c} = \frac{\Psi \ \tan^2(x_c)}{\sinh(2y_c)\,[\tan^2(x_c) + \tanh^2(y_c)]}, \tag{10}$$

$$\frac{dy_c}{dz_c} = \frac{\Psi \ \tanh^2(y_c)}{\sin(2x_c)\,[\tan^2(x_c) + \tanh^2(y_c)]}. \tag{11}$$

The dimensionless Cartesian coordinates (x_c, y_c, z_c) of the vortex center are $x_c = 2\pi\, x/D$, $y_c = 2\pi\, y/D$ and $z_c = 2\pi\, z/D$, and the dimensionless vortex strength is $\Psi = \Gamma/(D\, W_h)$, where W_h is the streamwise velocity at tab height $(x = 0,\ \ y = h)$. The constants C and Ψ are the model calibration parameters, as explained below.

Jones' model [25] neglects viscosity effects, and hence the model parameters are constant downstream from the tab ($C = C_0$ and $\Psi = \Psi_0$), where C_0 and Ψ_0 are the initial values calculated at the first location where the CVPs are identified. Lögdberg et al. [2] modify the Jones solution [25] by taking into account the damping of the vortex strength because of viscosity, called the pseudo-viscous model. Assuming exponential decay, Ψ is expressed as

$$\Psi = \Psi_0 \exp[\sigma\,(z_c - \delta)]. \tag{12}$$

The model parameters are obtained by fitting the curve in Figure 10, giving $\Psi_0 = 0.28$, $\sigma = -0.12$ and $\delta = 0.15$.

From experimental results, Lögdberg et al. [2] conclude that, in the cross section, the CVP center asymptote moves closer downstream. Thus, using this argument, the C parameter is modeled by [2]:

$$C = (C_0 - C_\infty) \exp[\varphi\,(z_c - \beta)^2]^+ C_\infty, \tag{13}$$

where C_∞ is the asymptotic value of C in the far region for $x_c = x_{c,\infty}$ and $y_c = y_{c,\infty}$, C_0 is the value of C at the origin, and both are determined by replacing (x_c, y_c) respectively by $(x_{c,\infty}, y_{c,\infty})$ and $(x_{c,0}, y_{c,0})$ in Equation (9). Nevertheless, with this model, the CVP center path is not well represented: in Figure 11 the Lögdberg model poorly reproduces the shape of the numerical results. In fact, Lögdberg et al. [2] defined the expression of the model parameter C in a turbulent boundary layer flow with rows of rectangular vortex generators.

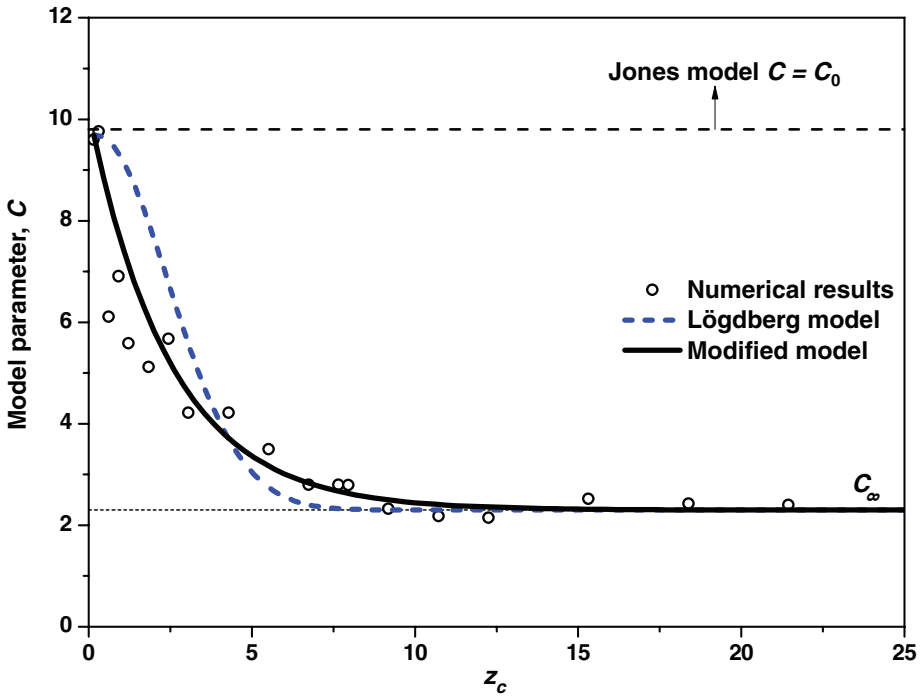

Figure 11. Streamwise variation of the model parameter C.

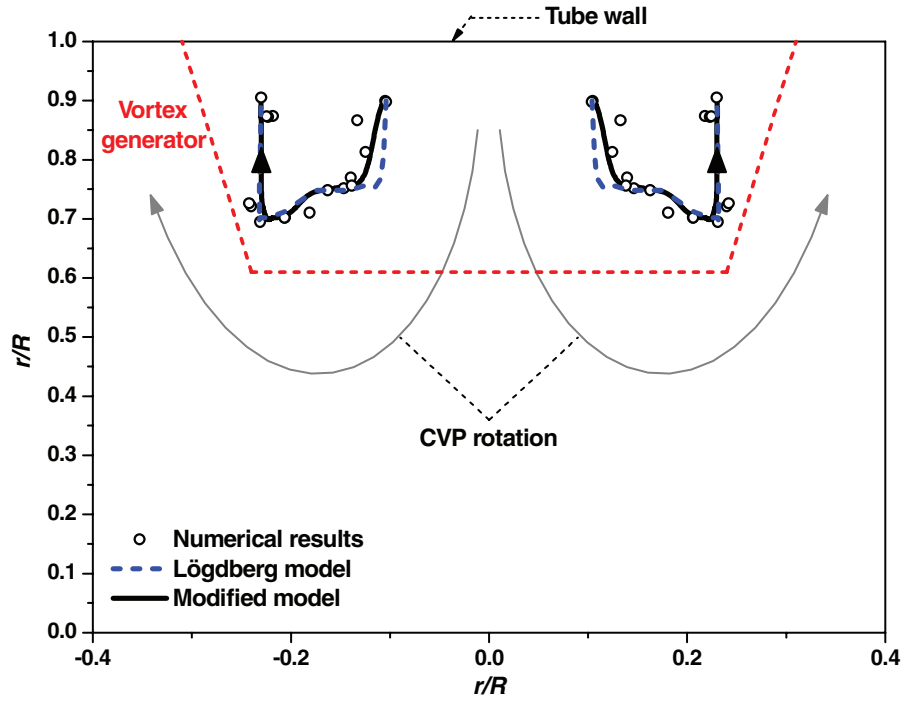

Figure 12. Path of vortex centers projected in the flow cross-section plane (x, y) from numerical results and pseudo-viscous model [2], $Re = 15{,}000$.

In the present case the flow configuration studied is different from that of Lögdberg et al. [2] because trapezoidal vortex generators are inserted in a circular pipe. Hence, here we attempt a slightly different model to better describe the path of the CVP centers:

$$C = (C_0 - C_\infty)\,\exp[\varphi\,(z_c - \beta)]^{+} C_\infty, \tag{14}$$

where the model parameters are fitted to the experimental profile in Figure 11, giving $C_0 = 9.7$, $C_\infty = 2.3$, $\beta = 0.15$ and $\varphi = -0.4$. Both models for C (Equations (13) and (14)) are plotted in Figure 11: We can observe that the present modified model fits the numerical results better than the original model of Lögdberg et al. [2].

Figure 12 presents the projection of the vortex center path in a plane normal to the flow to permit comparison among the original and modified Lögdberg models and the numerical simulations. Figure 12 shows that the path rotation sign of the vortex centers is the same as the rotation sign of the CVP. While being convected downstream, the vortex centers rapidly move away from the tube wall. Coming up to the tab lateral edges, the centers stop their displacement in the x direction and travel quickly toward the wall with constant slope. It is also observed that the vortex path obtained from the model equations perfectly agree with the numerical results, especially with the modified Equation (14).

Figure 13 shows the projection of the vortex center paths in the horizontal plane (x, z). It is observed that this path diverges from its initial position at $r/R \approx 0.1$ on the x-axis to reach an asymptotic direction at $r/R \approx 0.25$ corresponding to the limit of the tab tip

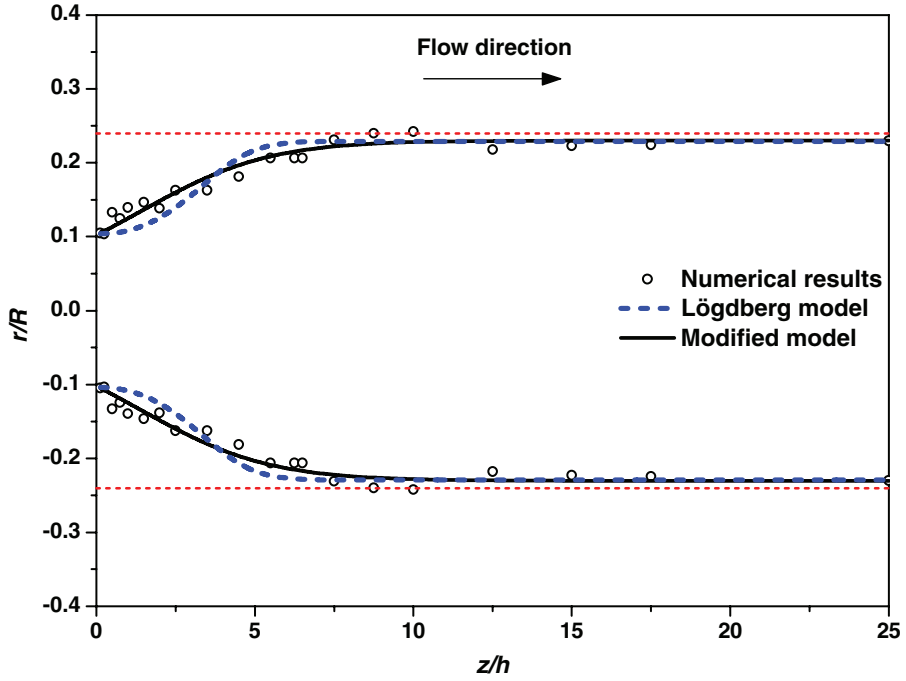

Figure 13. Path of vortex centers projected in the plane (x, z) obtained from numerical results and pseudo-viscous model [2], $Re = 15{,}000$. Red dotted lines show limits of tab tip location.

location. In this projection, agreement with the numerical results is better with the present modified model.

4.4. *Hairpin-like structures and reverse vortices*

4.4.1. *Hairpin structures*

As noted in the introduction, hairpins are transient structures. A schematic view of these vortices, essentially decomposed into head and leg, is given in Figure 14 for better visualization of their topology to understand their effects on turbulent mixing. In what follows, the turbulence energy dissipation rate ε is used as a criterion to investigate the micro-mixing process, and the stress tensor components $< u_i' \, u_j' >$ for the meso-mixing process, as well as turbulent kinetic energy, the trace of this tensor.

4.4.2. *Hairpin legs*

Figure 15 plots the Reynolds shear stress $< u' \, v' >$ distribution for different cross sections downstream from the tab. The statistical path of the hairpin vortex legs is defined by the inflection points obtained from $\partial^2 W / \partial^2 x = 0$, as suggested by Yang et al. [6]. These inflection points are marked by red circles corresponding to the secondary hairpin legs and blue circles corresponding to the primary hairpin legs.

From this figure, it can be noted that the higher $< u' \, v' >$ values coincide with the region of the statistical path of the secondary hairpin legs (blue contours). The other maximum $- < u' \, v' >$ values are observed in the region of primary hairpin legs, with lower energy

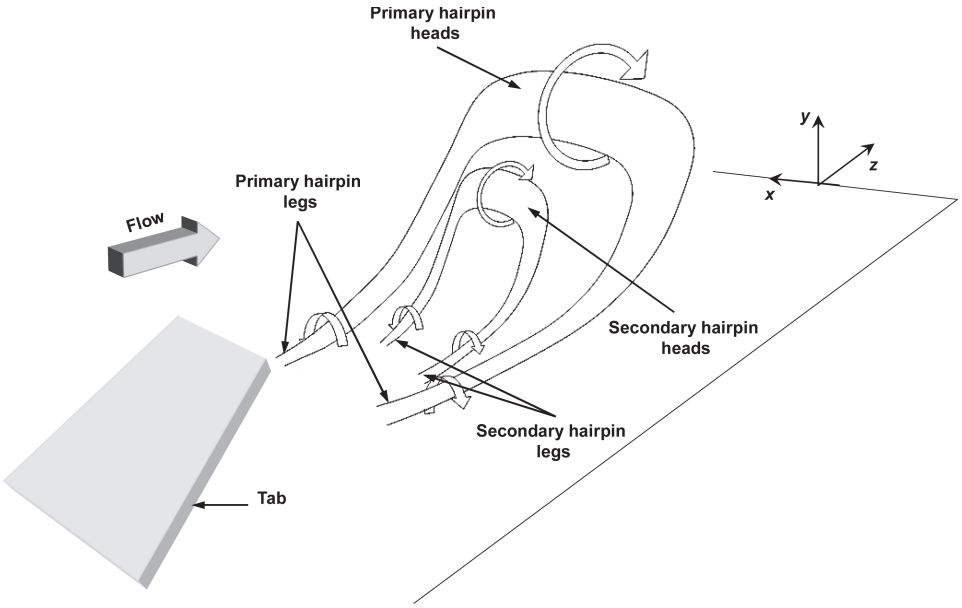

Figure 14. Three-dimensional sketch of primary and secondary hairpins.

level than that of secondary hairpins (red contours). This suggests that the secondary and primary hairpin legs contribute to meso-mixing in the near-wall region. These results are in agreement with those of Dong and Meng [7], who showed that higher kinetic energy is observed in the region of primary hairpin legs; however, their study did not show an effect of secondary hairpin legs on the meso-mixing process.

4.4.3. *Hairpin heads and reverse vortices*

The radial profiles of the mean streamwise velocity are plotted for different flow cross sections in Figure 16(a). A steep gradient is observed in the mean streamwise velocity profiles at the shear zone $0.4 < y/R < 0.6$, because of the interaction between high-momentum fluid in the flow core and low-momentum fluid beneath the shear layer shed from the tab. The presence of the hairpin head in the shear layer is reflected by the upper inflection point $\left(\partial^2 W/\partial y^2 = 0\right)$, which can be analytically computed by a polynomial fitting, following Yang et al. [6]. Thus the solid red line in Figure 16(a) coincides with the statistical path of the primary hairpin heads, showing that they move away from the wall downstream from the tab. A lower inflection point appearing below the hairpin heads denotes the presence of the reverse vortices. The particle image velocimetry (PIV) measurements by Yang et al. [6] and DNS by Dong and Meng [7] have shown that these secondary structures have vorticity opposite to the hairpin heads and are convected downstream below the hairpins before vanishing. From this argument, these inflection points can be used to analyze the effect of flow structures on turbulent mixing without transient modeling.

To analyze the effects of hairpins and reverse vortices on the turbulent meso-mixing, radial profiles in the tab symmetry plane of the Reynolds shear stress $< w'^2 >$ are plotted in Figure 16(b) for different axial positions, z/h. These profiles clearly indicate that the hairpin head coincides with the higher peak of $< w'^2 >$ and the reverse vortex coincides

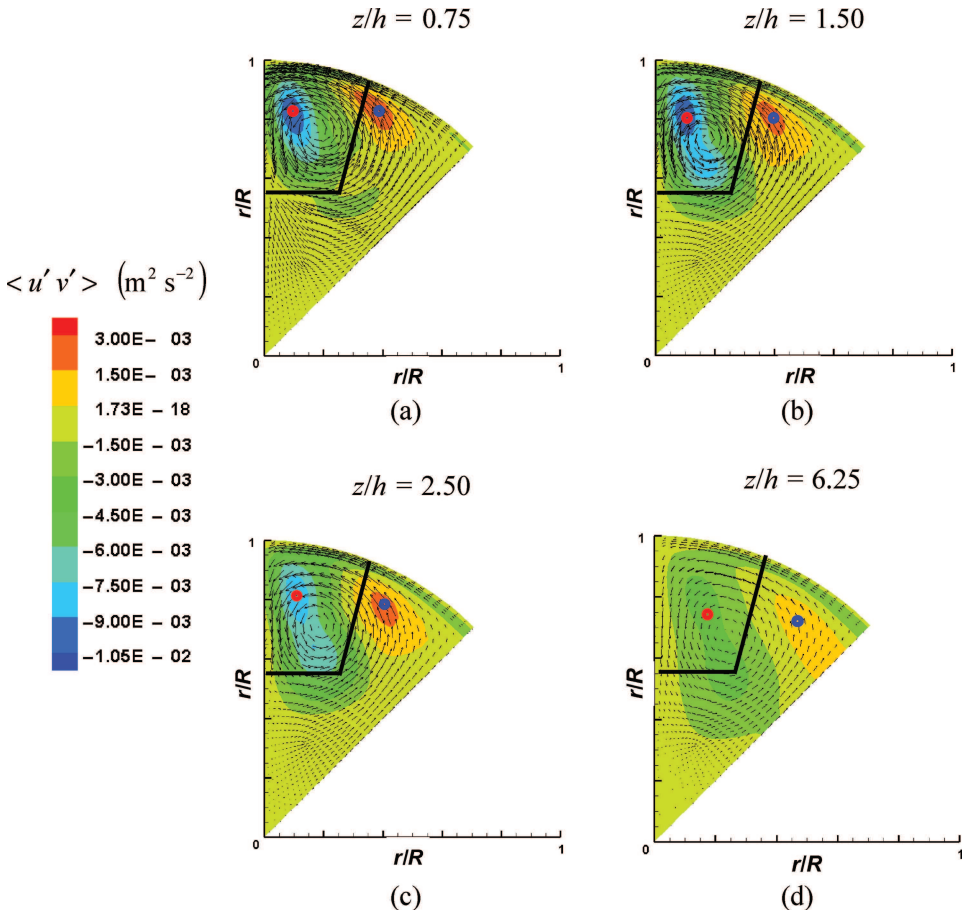

Figure 15. Reynolds shear stress distribution on different cross sections downstream from the tab, $Re = 15{,}000$. u' and v' are the fluctuating velocity components in the Cartesian coordinates x and y, respectively. Red and blue circles correspond, respectively, to the statistical path of the secondary and primary hairpin legs.

with the secondary peak. This suggests that both primary hairpin heads and reverse vortices participate in the meso-mixing process in the tab wake. The contribution of the reverse vortices to meso-mixing in the region directly below the hairpins is rapidly damped beyond an axial distance of $z/h \approx 3$. Meanwhile, the meso-mixing process in the shear zone caused by the primary hairpin heads remains active downstream from the tab up to $z/h \approx 8$, as observed from the higher peaks in the radial $< w'^2 >$ profiles (Figure 16(b)), while the CVP effect vanishes beyond an axial distance of $z/h \approx 5$, as shown in the previous section. Moreover, the peaks of $< w'^2 >$ move closer to the pipe center downstream because of the uplift of the hairpin heads.

Figure 16(c) plots the radial profiles of the turbulent energy dissipation rate for various distances z/h from the tab. The maximum values of ε coincide with the statistical path of the primary hairpin heads, as shown in Figure 16(c). The second extremum of ε is located in the near-wall region where the turbulence production is due to the wall gradients.

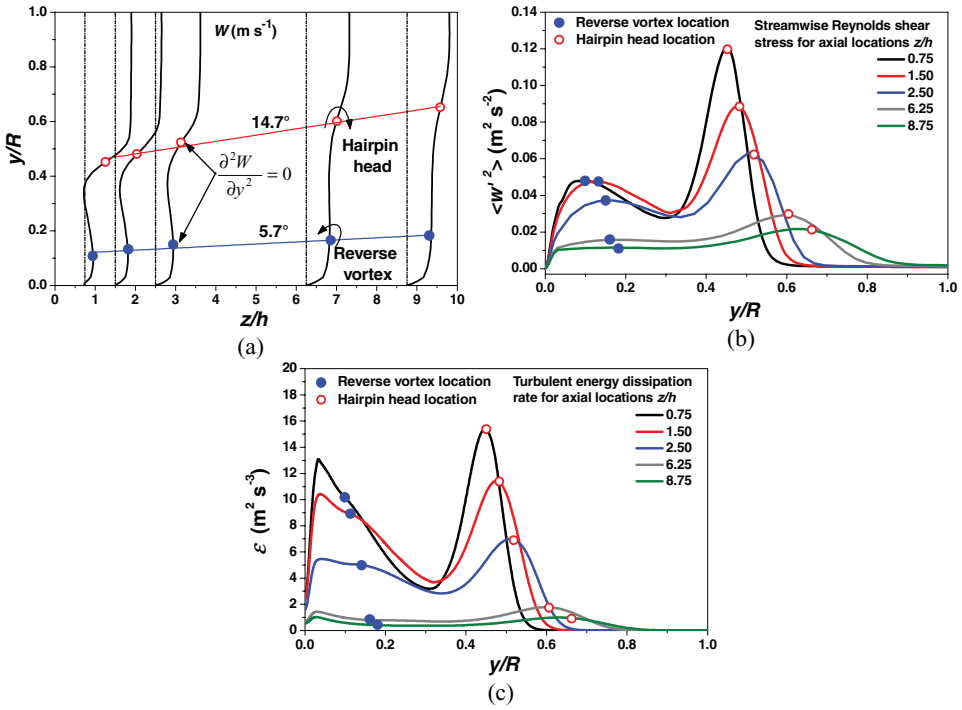

Figure 16. Experimental radial profiles. (a) Mean streamwise velocity, (b) axial component of the Reynolds stress $< w'^2 >$ and (c) turbulent energy dissipation rate, showing development of primary hairpin heads and reversed vortices and their individual contribution to turbulent mixing for different z/h downstream from the tab, $Re = 15{,}000$.

In Figure 17, the numerical contours of Reynolds stresses and turbulent energy dissipation rate are represented on a tab symmetry plane. We can verify from Figure 17(a) that high negative values of Reynolds shear stress coincide with the position of the reverse vortices identified from Figure 16(a), in the region below the path of hairpin heads, as observed by Yang et al. [6] and Dong and Meng [7]. The maximum Reynolds shear stress values coincide with the statistical location of the hairpin heads and persist much further downstream than the reverse vortices. We see in Figure 17(b) that the maximum values of turbulent energy dissipation persist in the shear layer near-tab region, but on a shorter length than the Reynolds shear stress. This observation is consistent with the experimental results and corroborates the different contributions of the flow structures to meso- and micro-mixing. The other zones of high turbulence energy dissipation are observed below the shear layer near the wall region. These high ε are caused by the coupling of turbulence energy production in the near-wall region and the interactions between primary and secondary CVP, which increase the velocity fluctuation gradients. When the CVP strength is almost null, the fluctuations gradient induced by the common upflow of the CVP is reduced, leading to a decrease in ε, as shown in Figure 17(b).

As shown in Figure 18, the arc of maximum ε is the projection of the statistical path of the hairpin heads on the pipe cross sections. Moreover, it is observed that the maximum ε ride on the top of the CVP and migrate toward the pipe centerline while being convected downstream, in a way similar to the dynamics of hairpin heads in Yang et al. [6] and Dong and Meng [7]. Owing to viscous damping effects, the turbulent energy dissipation rate ε is

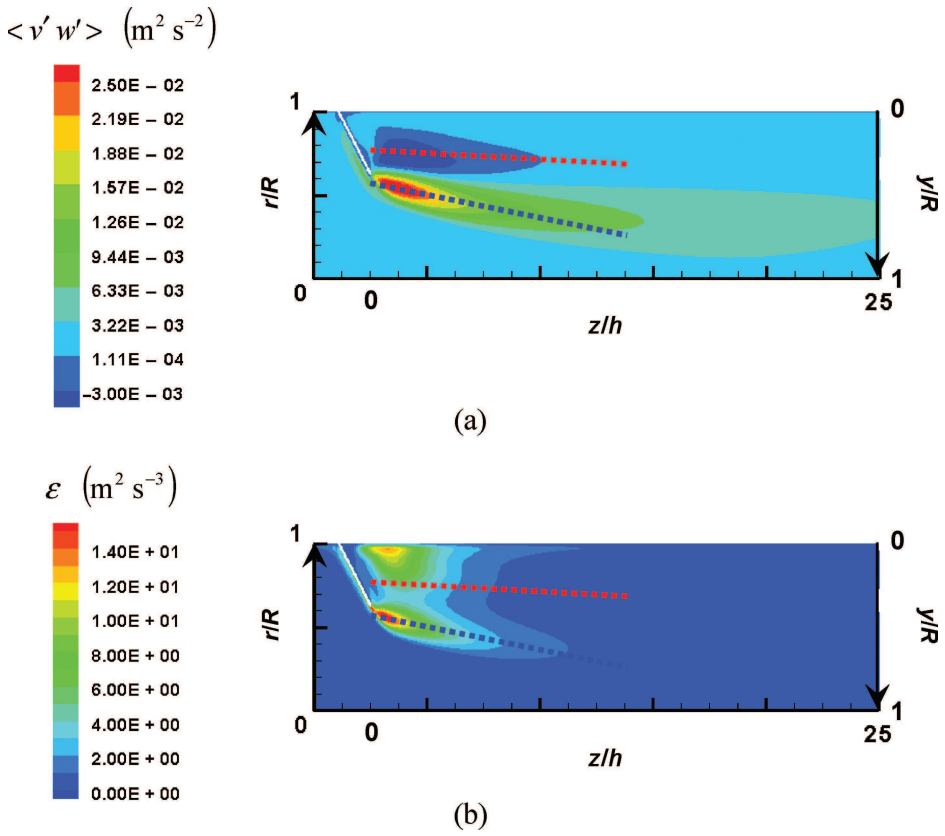

Figure 17. Contours of (a) Reynolds shear stress and (b) turbulent energy dissipation rate computed in the tab symmetry plane for $Re = 15{,}000$. u' and v' are the fluctuating velocity components in the Cartesian coordinates x and y, respectively. Red and blue dotted lines correspond, respectively, to the statistical path of the secondary and primary hairpin heads.

further reduced at increasing axial locations z/h and its distribution becomes more uniform, especially for $z/h \approx 6.25$, as shown in Figure 18(d). This latter marks the disintegration and breakup of the hairpin structures, as has been shown by Dong and Meng [7].

Finally, as the evolution of the maximum values of ε is analogous to the dynamics of the hairpin heads [6–7], it can be concluded that these structures are of considerable importance in the micro-mixing process by transporting fluid toward the shear zone, where the turbulence energy dissipation rate is high.

4.4.4. *Spectral analysis*

The energy spectra E for different axial locations z/h, obtained on the upper inflection point identified from Figure 16(a), are presented in Figure 19(a). Figure 19(b) shows the premultiplied energy spectra $f\ E(f)/U_{\text{conv}}$; the advantage of this presentation is that it shows the turbulent kinetic energy (TKE) by the area under the curve in log scale. This can be seen in Equation (15), which relates the TKE to the integral of the pre-multiplied energy

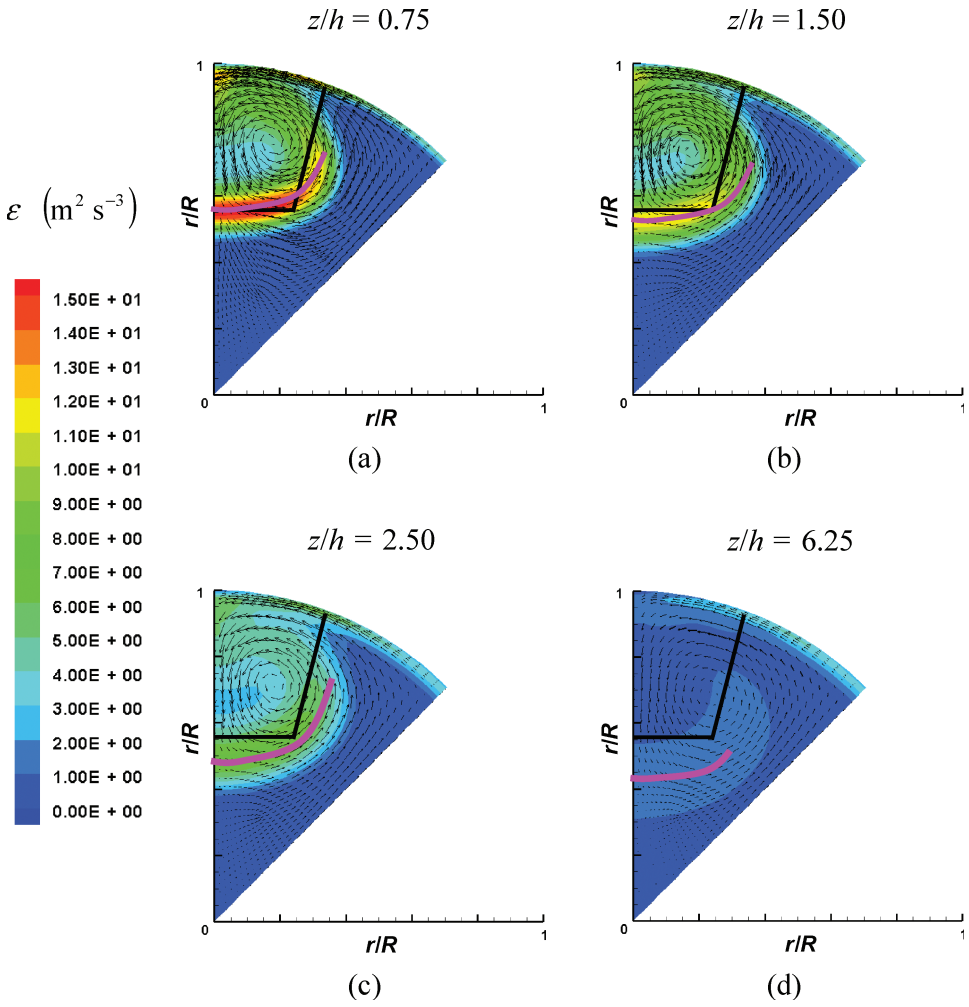

Figure 18. Distribution of turbulent energy dissipation rate computed on different cross sections downstream from the tabs, for $Re = 15{,}000$. The statistical path of the hairpin heads is obtained from the upper inflection point derived from $(\partial^2 W/\partial y^2 = 0)$.

spectrum, on the right-hand side:

$$TKE = \frac{2\pi}{U_{\text{conv}}} \int_0^\infty E(f)\, df = \frac{2\pi}{U_{\text{conv}}} \int_0^\infty f\ E(f)\, d(\ln(f)). \tag{15}$$

The red circles in Figure 19(a) correspond to the limit of the $-5/3$ power law in the energy spectrum, i.e. to the turbulent macro-scale Λ defined in Equation (2), which is the limit of the convective inertial sub-range. These points also correspond to higher values of TKE, as seen in Figure 19(b). This suggests that the hairpin heads are the more energetic vortices and that they appear in the energy spectra although they are coherent structures.

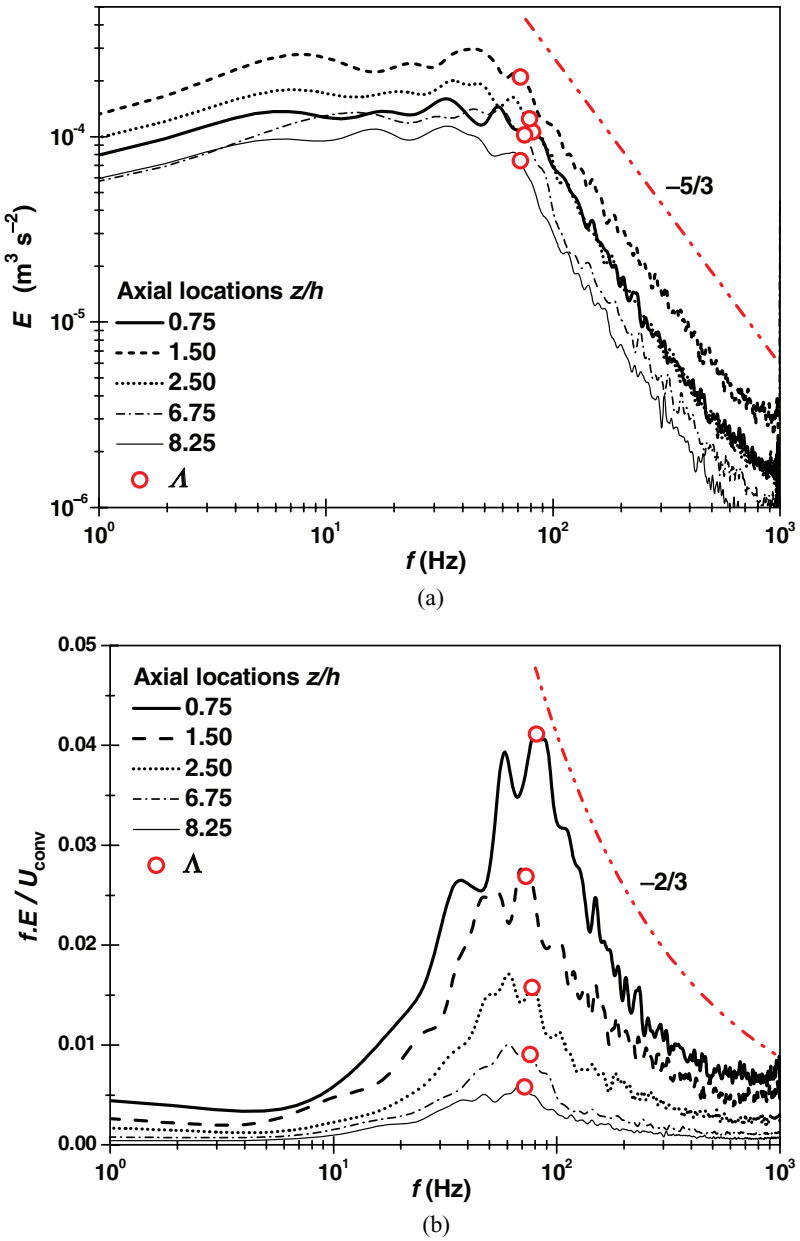

Figure 19. (a) Energy spectra of streamwise velocity and (b) pre-multiplied spectra at different axial locations, $Re = 15{,}000$, at radial coordinate of inflexion point.

This feature is confirmed by the numerical three-dimensional contour in Figure 20 showing the turbulent kinetic energy field downstream of the tab; the turbulent kinetic energy contour takes the shape of the hairpin structures. Moreover, the maximum turbulent kinetic energy coincides with the upper inflection points that form the statistical path of the hairpin heads.

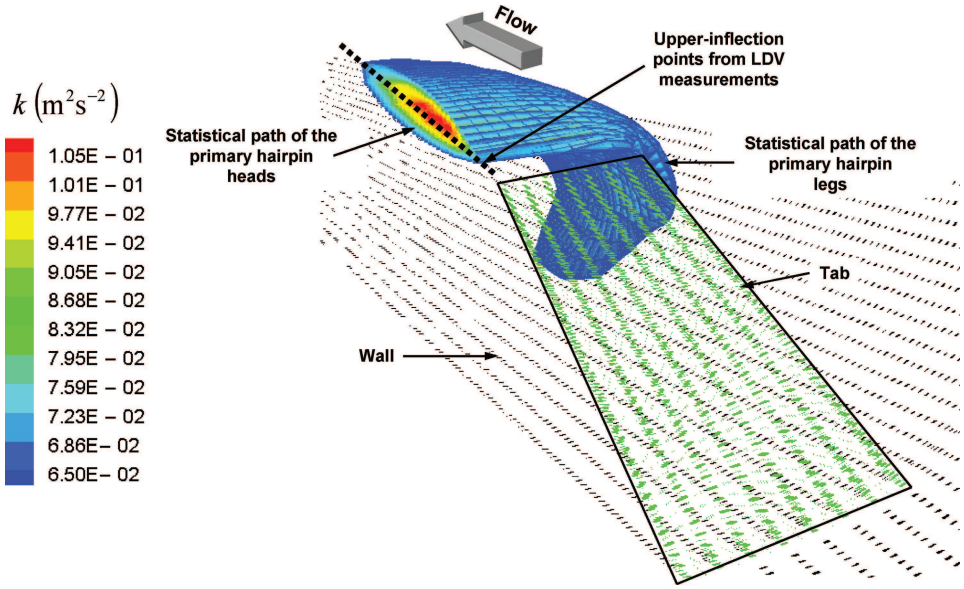

Figure 20. Hairpin statistical path identification from contour of turbulent kinetic energy in the range k (0.06–0.11) m^2 s^{-2}, for Re =15,000.

Figure 21 shows the streamwise evolution of the large eddy scales Λ obtained from the energy spectra; this is also the hairpin characteristic scale, as it is merged with the spatial macro-scale. This macro-scale corresponds to the higher limit of the inertial sub-range, determined by the intersection between the energy spectra and the $-5/3$ power law.

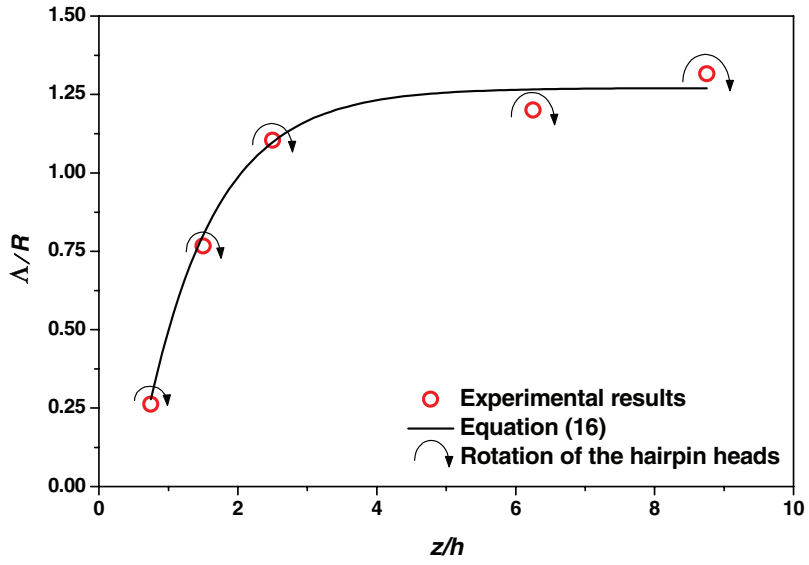

Figure 21. Integral length for different axial distances z/h from the tab, Re = 15,000.

The typical size of the hairpin heads grows downstream from $\Lambda/R \approx 0.25$ at $z/h \approx 1$ to $\Lambda/R \approx 1.30$ at $z/h \approx 9$. The evolution of the spatial macro-scale Λ shown in Figure 21 is fitted to an exponential curve:

$$\frac{\Lambda}{R} = 1.27 - 2.1 \exp\left(-\frac{z}{h}\right). \tag{16}$$

In Figure 21, the growth in Λ/R appears very rapid but saturates for $z/h > 3$ to an asymptotic value $\Lambda/R \approx 1.3$.

5. Conclusions

The turbulent flow pattern generated by a row of vortex generators inserted in a straight pipe is investigated by LDV measurements and numerical simulations. Analysis of this complex flow suggests an explanation of the individual contribution of the different flow structures to macro-, meso- and micro-mixing mechanisms.

It is shown that the primary CVP generated by the pressure gradient across the tab plays an essential role in macro-mixing by radial mass exchange. This mass exchange is reduced by the secondary CVPs that are present below the primary CVP in the tabs' symmetry plane and rotate in opposite directions. A modification of the model of Lögdberg et al. [2] is proposed here: $C = (C_0 - C_\infty)\ \exp[\varphi\,(z_c - \beta)]^+ C_\infty$, where the model parameters are fitted with the experimental profiles, giving $C_0 = 9.7$, $C_\infty = 2.3$, $\beta = 0.15$ and $\varphi = -0.4$. This model satisfactorily predicts the streamwise development of the CVP, especially the vortex strength decay and the path of the vortex centers downstream from the tab. It is shown that the strength of the CVP, i.e. the vortex circulation, loses more than 50% of its initial magnitude after an axial distance of $z/h \approx 5$. The vortex centers path projected in the tube cross section asymptotically approach the level of the tab top.

The statistical path of the transient vortices, hairpins and reverse vortices in the shear and wake regions is identified by inflection points in the radial profiles of mean streamwise velocity. The primary hairpin heads coincide with the maximum values of the turbulent kinetic energy and its dissipation rate. Hence the hairpin heads seem to be primarily responsible for the meso-mixing process in the shear region. Reverse vortices also contribute, to a lesser extent, to meso-mixing in the wake of the tab, as their statistical paths coincide with the local maxima of Reynolds shear stresses.

In the tube cross section, the statistical paths of the primary and secondary hairpin legs also coincide with the higher values of Reynolds shear stresses and therefore contribute to meso-mixing in the wake region. We have shown that the *secondary* hairpin legs are more energetic than the *primary* ones.

The spectral analysis of LDV measurements shows that the primary hairpin heads carry most of the turbulent kinetic energy. The characteristic size of the primary hairpin heads is in the macro-scale range of the spectra; it is demonstrated that they are coherent structures in the turbulence field.

The analysis of the turbulence mixing process presented here should be useful in future studies aimed at designing intensified multifunctional heat exchangers/reactors. In addition to the artificially generated streamwise vortices, a relevant issue here is the mixing and heat transfer by naturally generated streamwise vortices, such as the Görtler vortices that occur in a boundary layer over a concave wall [50–54]. Though not all the features of the artificially generated vortices are present in naturally occurring streamwise vortices, it seems that the analysis presented here can capture some main features of natural streamwise

vortices in the turbulent regime. This subject merits examination in the light of the results presented here.

Acknowledgements

The authors would like to thank Dr. E. Gadoin and Dr. H. Mohand Kaci for fruitful discussions on the numerical simulation procedures. The authors are also grateful for the technical support of the Service d'Études et de Fabrication (SEF) for LDV measurements. This work was financially supported by the Programme Interdisciplinaire Energie du CNRS, under the Multifunctional Heat Exchanger project. C. Habchi would like to acknowledge the financial support of CNRS and ADEME.

References

[1] M. Fiebig, *Vortices, generators and heat transfer*, Chem. Eng. Res. Des. 76 (1998), pp. 108–123.
[2] O. Lögdberg, J.H.M. Fransson, and P.H. Alfredsson, *Streamwise evolution of longitudinal vortices in a turbulent boundary layer*, J. Fluid Mech., 623 (2009), pp. 27–58.
[3] R.J. Martinuzzi, *Dual vortex structure shedding from low aspect ratio, surface-mounted pyramids*, J. Turbulence 9 (2008), pp. 1–16.
[4] W.J. Gretta and C.R. Smith, *The flow structure and statistics of a passive mixing tab*, Trans. ASME J. Fluids Eng. 115 (1993), pp. 255–263.
[5] R. Elavarasan and H. Meng, *Flow visualization study of role of coherent structures in a tab wake*, Fluid Dyn. Res. 27 (2000), pp. 183–197.
[6] W. Yang, H. Meng, and J. Sheng, *Dynamics of hairpin vortices generated by a mixing tab in a channel flow*, Exp. Fluids 30 (2001), pp. 705–722.
[7] D. Dong and H. Meng, *Flow past a trapezoidal tab*, J. Fluid Mech. 510 (2004), pp. 219–242.
[8] T. Lemenand, D. Della Valle, Y. Zellouf, and H. Peerhossaini, *Droplets formation in turbulent mixing of two immiscible fluids*, Int. J. Multiphase Flow 29 (2003), pp. 813–840.
[9] T. Lemenand, P. Dupont, D. Della Valle, and H. Peerhossaini, *Turbulent mixing of two immiscible fluids*, J. Fluids Eng. 127 (2005), pp. 1132–1139.
[10] H. Mohand Kaci, C. Habchi, T. Lemenand, D. Della Valle, and H. Peerhossaini, *Flow structure and heat transfer induced by embedded vorticity*, Int. J. Heat Mass Transfer, 53 (2010), pp. 3575–3584.
[11] H. Mohand Kaci, T. Lemenand, D. Della Valle, and H. Peerhossaini, *Effects of embedded streamwise vorticity on turbulent mixing*, Chem. Eng. Process. 48 (2009), pp. 1457–1474.
[12] C. Habchi, T. Lemenand, D. Della Valle, and H. Peerhossaini, *Alternating mixing tabs in multifonctional heat exchanger/reactor*, Chem. Eng. Process. (in press), doi:10.1016/j.cep.2009.07.003.
[13] T. Duriez, J.L. Aider, and J.E. Wesfreid, *Non-linear modulation of a boundary layer induced by vortex generators*, 4th Flow Control Conference, Seattle, Washington, June 23–26, AIAA 2008-4076, pp. 1–7.
[14] J.L. Aider, J.F. Beaudoin, and J.E. Wesfreid, *Drag and lift reduction of a 3D bluff-body using active vortex generators*, Exp. Fluids 48 (2010), pp. 771–789.
[15] Chemineer, Kenics, *Static Mixing Technology*, Bulletin 800 (commercial documentation), Chemineer Inc., Dayton, OH,1998.
[16] K.C. Kim and R.J. Adrian, *Very large-scale motion in the outer layer*, Phys. Fluids 11 (1999), pp. 417–422.
[17] J. Zhou, R.J. Adrian, and S. Balachandar, *Autogeneration of near-wall vortical structures in channel flow*, Phys. Fluids 8 (1996), pp. 288–290.
[18] K.T. Christensen and R.J. Adrian, *Statistical evidence of hairpin vortex packets in wall turbulence*, J. Fluid Mech. 431 (2001), pp. 433–443.
[19] M. Lesieur, P. Begou, E. Briand, A. Danet, F. Delcayre, and J.L. Aider, *Coherent-vortex dynamics in large-eddy simulations of turbulence*, J. Turbul. 4 (2003), pp. 1–24.
[20] J. Villermaux and J.C. Devillon, *Représentation de la coalescence et de la redispersion des domaines de ségrégation dans un fluide par un modèle d'interaction phénoménologique*, Proceedings *of the* 2nd International Symposium *on* Chemical Reaction Engineering, Amsterdam, the Netherlands, 1972.
[21] M. Gonzalez, *Kinematic properties of passive scalar gradient predicted by a stochastic Lagrangian model*, Phys. Fluids 21 (2009), pp. 055104.

[22] L. Danaila, P. Le Gal, F. Anselmet, F. Plaza, and J.F. Pinton, *Some new features of the passive scalar mixing in a turbulent flow*, Phys. Fluids 11 (1999), pp. 636–646.
[23] J. Baldyga and J.R. Bourne, *Turbulent Mixing and Chemical Reactions*, Wiley, Chichester, UK, 1999.
[24] J.O. Hinze, *Fundamentals of the hydrodynamic mechanism of splitting in dispersion processes*, AIChE J. 1 (1955), pp. 289–295.
[25] J.P. Jones, *The calculation of paths of vortices from a system of vortex generators, and a comparison with experiment.* Tech. Rep. C.P. No. 361, Aeronautical Research Council, UK, 1957.
[26] L.H. Benedict and R.D. Gould, *Towards better uncertainty estimates for turbulence statistics*, Exp. Fluids 22 (1996), 129–136.
[27] A. Høst-Madsen and C. Caspersen, *The limitations in high-frequency turbulence spectrum estimation using the laser Doppler anemometer*, 7th International Symposium on Application of Laser Techniques to Fluid Mechanics, Lisbon, Portugal, 1994, ISBN 3540602364.
[28] G.K. Batchelor, *The Theory of Homogeneous Turbulence*, Cambridge University Press, Cambridge, UK, 1953.
[29] A. Mokrani, C. Castelain, and H. Peerhossaini, *Experimental study of the influence of the rows of vortex generators on turbulence structure in a tube*, Chem. Eng. Proc. 48 (2009), pp. 659–671.
[30] M. Van Doorn, *On Taylor's hypothesis in turbulent shear flows*, Internal Note 811123, University of Missouri-Rolla, Rolla, MO, 1981.
[31] R.F. Warming and R.M. Beam, *Upwind second-order difference schemes and applications in unsteady aerodynamic flows*, in *Proceedings of AIAA 2nd Fluid Dynamics Conference*, Hartford, CT, 1975, pp. 17–28.
[32] S.V. Patankar, *Numerical Heat Transfer and Fluid Flow*, Hemisphere, New York, 1980, pp. 330–351.
[33] J.T. Barth and D. Jespersen, *The design and application of upwind schemes on unstructured meshes*, Proceedings of AIAA 27th Aerospace Sciences Meeting, Reno, Nevada, 1989.
[34] B.E. Launder and D.B. Spalding, *The numerical computation of turbulent flo*ws, Comp. Meth. Appl. Mech. Eng. 3 (1974), pp. 269–289.
[35] H.K. Versteeg and W. Malalasekera, *An Introduction to Computational Fluid Dynamics, the Finite Volume Method*, Prentice Hall, New York, 1995, pp. 62–146.
[36] M.M. Gibson and B.E. Launder, *Ground effects on pressure fluctuations in the atmospheric boundary layer*, J. Fluid Mech. 86 (1978), pp. 491–511.
[37] B.E. Launder, G.J. Reece, and W. Rodi, *Progress in the development of a Reynolds stress turbulence closure*, J. Fluid Mech. 68 (1975), pp. 537–566.
[38] B.E. Launder, *Second-moment closure: Present . . . and future?* Int. J. Heat Fluid Flow 10 (1989), pp. 282–300.
[39] B.J. Daly and F.H. Harlow, *Transport equations in turbulence*, Phys. Fluids 13 (1970), pp. 2634–2649.
[40] M. Wolfstein, *The velocity and temperature distribution of one-dimensional flow with turbulence augmentation and pressure gradient*, Int. J. Heat Mass Tran. 12 (1969), pp. 301–318.
[41] H.C. Chen and V.C. Patel, *Near-wall turbulence models for complex flows including separation*, AIAA J. 26 (1988), pp. 641–648.
[42] J.O. Hinze, *Turbulence*, 2nd ed., McGraw-Hill, New York, 1975.
[43] A. Mokrani, *Analyse expérimentale et numérique de deux procédés complémentaires de mélange et de transfert thermique en écoulement tridimensionnel ouvert: advection chaotique laminaire et écoulement turbulent Eulérien*, thesis, University of Nantes, France, 1997.
[44] M.A. Elyyan and D.K. Tafti, *A novel split-dimple interrupted fin configuration for heat transfer augmentation*, Int. J. Heat Mass Tran. 52 (2009), pp. 1561–1572.
[45] C.E. Tinney and L.S. Ukeiley, *A study of a 3-D double backward-facing step*, Exp. Fluids 47 (2009), pp. 427–438.
[46] M. Garcia-Villalba, N. Li, W. Rodi, and M.A. Leschziner, *Large-eddy simulation of separated flow over a three-dimensional axisymmetric hill*, J. Fluid Mech. 627 (2009), pp. 55–96.
[47] T. Goruney and D. Rockwell, *Flow past a delta wing with a sinusoidal leading edge: near-surface topology and flow structure*, Exp. Fluids 47 (2009), pp.321–331.
[48] P.G. Bakker and M.E.M. de Winkel, *On the topology of three-dimensional separated flow structures and local solutions of the Navier–Stokes equations*, in *Proceedings of the IUTAM Symp.,*

Topological Fluid Mechanics, August 1989, Cambridge, UK., HK Moffatt and A Tsinober, eds., Cambridge University Press, Cambridge, UK, 1989, pp. 13–18.
[49] J. Jeong and F. Hussain, *On the identification of a vortex*, J. Fluid Mech. 285 (1995), pp. 69–94.
[50] R. Toe, A. Ajakh, and H. Peerhossaini, *Heat transfer enhancement by Görtler instability*, Int. J. Heat Fluid Flow 23 (2002), pp. 194–204.
[51] A. Ajakh, M.D. Kestoras, R. Toe, and H. Peerhossaini, *Influence of forced perturbations in the stagnation region of Görtler instability*, AIAA J. 37 (1995), pp. 1572–1577.
[52] H. Peerhossaini and F. Bahri, *On the spectral distribution of the modes in nonlinear Görtler instability*, Exp. Thermal Fluid Sci. 16 (1998), pp. 195–208.
[53] L. Momayez, P. Dupont, and H. Peerhossaini, *Effects of vortex organization on heat transfer enhancement by Görtler instability*, Int. J. Thermal Sci. 43 (2004), pp. 753–760.
[54] L. Momayez, P. Dupont, and H. Peerhossaini, *Some unexpected effects of wavelength and perturbation strength on heat transfer enhancement by Görtler vortices*, Int. J. Heat Mass Transfer 47 (2004), pp. 3783–3795.

CORPUS DES ARTICLES

4. Alternating mixing tabs in multifunctional heat exchanger-reactor

C. Habchi, T. Lemenand, D. Della Valle, H. Peerhossaini

Chemical Engineering and Processing 49 (2010d) 653-661.

Chemical Engineering and Processing 49 (2010) 653–661

Contents lists available at ScienceDirect

Chemical Engineering and Processing: Process Intensification

journal homepage: www.elsevier.com/locate/cep

Alternating mixing tabs in multifunctional heat exchanger-reactor

Charbel Habchi[a,b], Thierry Lemenand[a], Dominique Della Valle[a], Hassan Peerhossaini[a,*]

[a] Thermofluids, Complex Flows and Energy Research Group, Laboratoire de Thermocinétique de Nantes (LTN), CNRS UMR 6607, École Polytechnique de l'Université de Nantes, rue Christian Pauc, B.P. 50609, 44306 Nantes, France
[b] Agence de l'Environnement et de la Maîtrise de l'Énergie (ADEME), 20 avenue du Grésillé, B.P. 90406, 49004 Angers, France

ARTICLE INFO

Article history:
Received 17 April 2009
Received in revised form 1 July 2009
Accepted 2 July 2009
Available online 10 July 2009

Keywords:
Turbulence energy dissipation
Vortex generators
Micromixing
Process intensification
Multifunctional heat exchanger/reactor
Static mixer

ABSTRACT

Streamwise vortices are used in many applications for mixing processes, fast chemical reactions and heat-transfer enhancement. In this work we studied experimentally and numerically the effects of vorticity field redistribution on the turbulence energy dissipation rate in a modified geometry of the high-efficiency vortex (HEV) mixer, in which the mixing tab arrays are periodically rotated by 45° to better distribute the vorticity field. Attention focuses on the evolution and distribution of turbulence energy dissipation, since this describes quantitatively the drop breakup and turbulent micromixing mechanism, which controls fast chemical reactions. It is found that redistribution of the vorticity field locally intensifies turbulent micromixing relative to the classical HEV mixer, producing a local mixing intensification of up to 120%. In addition, the alternating vortex generator arrays improve homogenization of the turbulence field in the mixer.

1. Introduction

Streamwise vortices are used in many applications for mixing processes, fast chemical reactions and heat-transfer enhancement. Streamwise vorticity can be generated in essentially two ways:

- Streamline curvature (Görtler, Dean roll-cells), where centrifugal force generates the streamwise vortices. Heat-transfer intensification in these flows has been studied extensively by Peerhossaini [1], Toé et al. [2] and Momayez et al. [3,4]. Mixing by Görtler instability has been studied by Girgis and Liu [5], among others. This method of generating streamwise vortex is more appropriate for boundary layer flows.
- In the domain of online mixers and multifunctional heat exchangers, longitudinal vortices can readily be generated by vortex generators, in particular the high-efficiency vortex (HEV) mixer [6]. In HEV mixers several arrays of trapezoidal mixing tabs [7] produce a complex vortex system consisting of steady longitudinal counter-rotating vortex pairs and transient hairpin structures in one array [7–10] (see Fig. 1) that are modified, further downstream, by the subsequent arrays [11–14].

Flow past trapezoidal mixing tabs has been studied extensively due to its ability to enhance turbulent mixing, mass transfer and phase dispersion and to its generation of coherent structures similar to those found in natural turbulent boundary layers [7–14].

As generally observed [7–10], a counter-rotating vortex pair (CVP) is generated at each side of the tab. A common radial flow in the tab center-plane is induced, transporting low-momentum fluid from the near-wall region toward the high-momentum fluid at the mixer centerline. This mechanism greatly enhances radial transfer. While fluid passes through the tab wake zone, it is stretched and folded over due to the swirling motion induced by the CVP. This mechanism also occurs over the tabs further downstream. A second type of periodic vortex develops from the edges of the mixing tabs, riding on the top of CVP and flowing downstream. These vortices, called hairpin-like structures, have been the subject of several studies [8–10].

In this work we study experimentally and numerically the effects of vorticity field redistribution on turbulence energy dissipation in a modified-geometry HEV. The HEV consists of a circular pipe in which tabs arrays are fixed. Each array is composed of four trapezoidal inclined tabs that are diametrically opposed. In the modified geometry we applied a 45° periodic rotation on the arrays with respect to one another in order to achieve a better vorticity field distribution in the mixer volume. Experiments were carried out by measuring instantaneous velocities using laser Doppler velocimetry (LDV). Numerical simulations of the velocity distribution and turbulence field inside the flow were also used to better understand the flow mechanism and turbulent flow structures in this new type of mixer. Attention focused on the evolution and distribution of

* Corresponding author. Tel.: +33 2 40 68 31 24; fax: +33 2 40 68 31 41.
E-mail address: hassan.peerhossaini@univ-nantes.fr (H. Peerhossaini).

0255-2701/$ – see front matter © 2009 Elsevier B.V. All rights reserved.
doi:10.1016/j.cep.2009.07.003

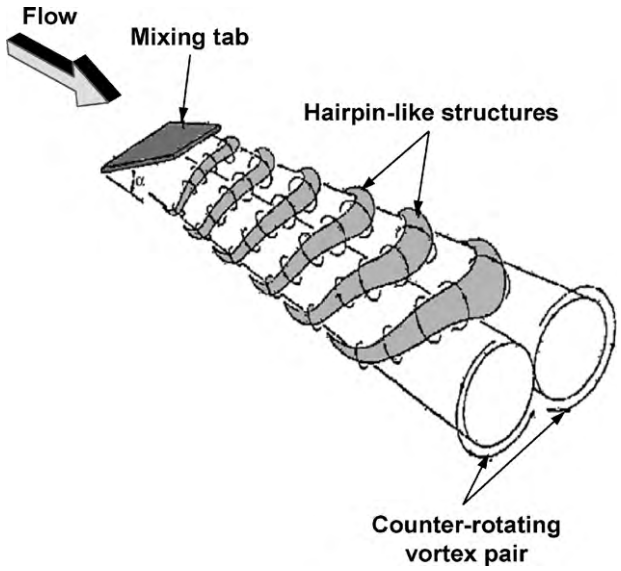

Fig. 1. Flow structure behind a trapezoidal mixing tab proposed by Gretta and Smith [7]. Periodic hairpin vortices are generated by the free shear layer instability, while counter-rotating vortex pairs are produced by the pressure difference between the front and back tab surfaces.

turbulence energy dissipation, since this describes quantitatively the mechanisms of drop breakup and turbulent micromixing.

In fact, an efficient reactor is characterized by producing mixing on the microscale before the reaction takes place. This fact is described by the micromixing time, t_m, which is related to the turbulence energy dissipation ε by models such as the engulfment–deformation–diffusion (EDD) model [15]. The kinetic energy produced in the macroscale eddies is transferred to microscale (i.e. Kolmogorov-scale) eddies, where it is dissipated in viscous form.

The paper is organized as follows: the experimental study is described in Section 2. Section 3 gives the numerical procedure and results, and Section 4 contains concluding remarks.

2. Experimental study

2.1. Experimental apparatus and data acquisition

2.1.1. Test section and hydraulic loop

The test section is a straight circular pipe of 20 mm inner diameter along which seven rows of vortex generators are fixed. Each vortex generator array is rotated 45° with respect to the neighboring array. Each of the seven arrays consists of four diametrically opposed trapezoidal mixing tabs. Fig. 2 shows schematically both the aligned and alternating tab arrays, which are inclined 30° with respect to the mixer wall. Their role is to generate longitudinal vortical structures that enhance the turbulence and radial transfer over that in the empty duct [7–13]. The test section is preceded by a preconditioner (200 mm straight Plexiglas pipe) to produce a fully developed turbulent flow at the test section inlet, and is followed by a postconditioner (200 mm straight Plexiglas pipe). Care is taken that the connections between the different elements do not disturb the flow. A safety valve is added to the circuit as well as a pulsation absorber whose role is to limit the pressure fluctuations produced by the pump and thus ensure continuous, stable flow in the test section. The dimensions of a trapezoidal mixing tab are represented schematically in Fig. 3.

The temperature of the working fluid (water) is maintained constant at 298 K, so there is no significant effect of the physical

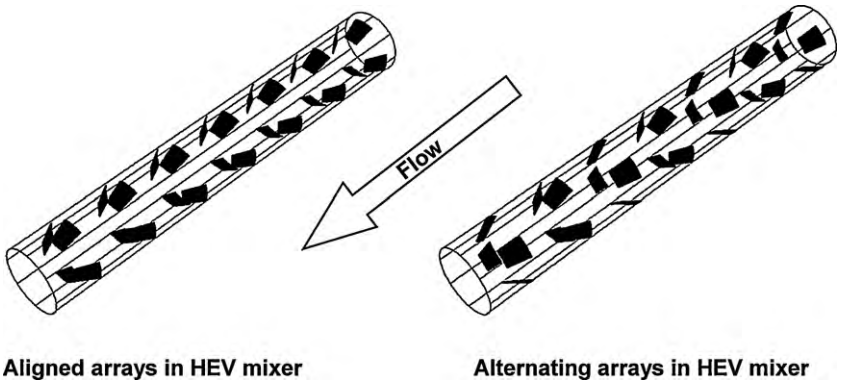

Fig. 2. Aligned and alternating arrays of mixing tabs in HEV static mixer.

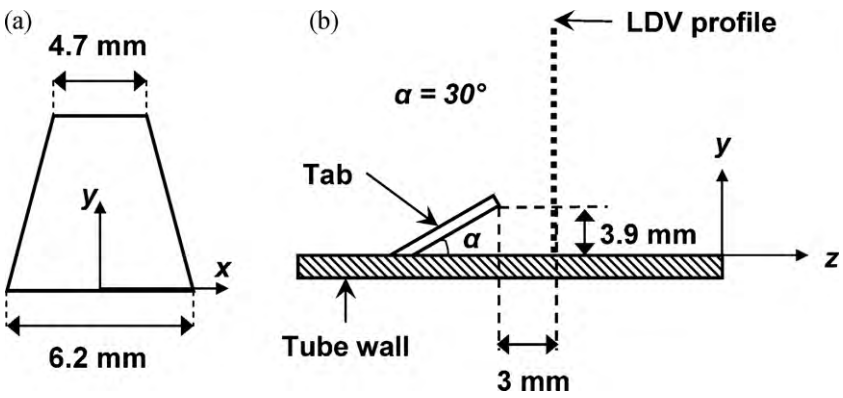

Fig. 3. Dimensions of mixing tab: (a) front view, (b) side view and position of LDV radial profile.

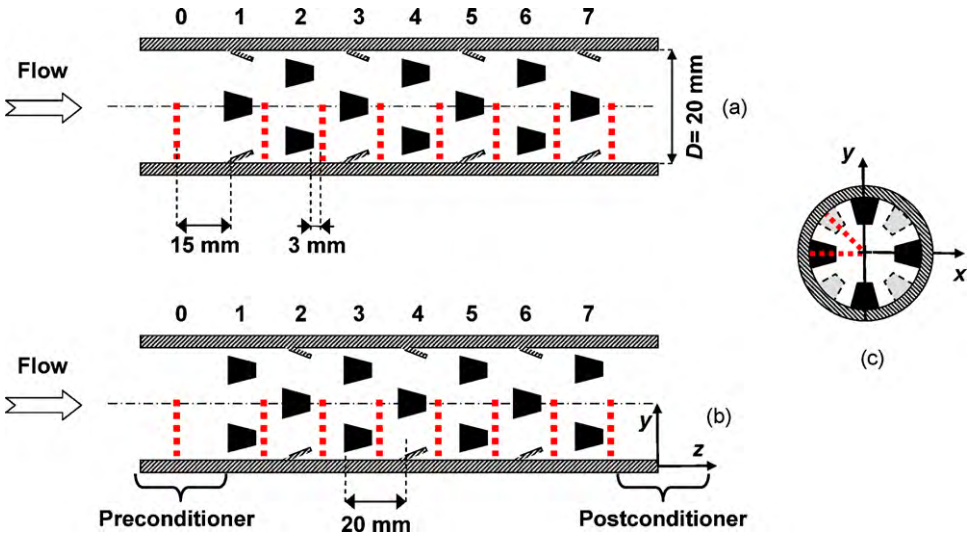

Fig. 4. Location of radial profiles for LDV measurements on different cross-sections: side views: (a) configuration 1, (b) configuration 2, and (c) front view of the mixer.

properties of the working fluid on the turbulence. The experiments are carried out in a fully developed steady turbulent flow with Reynolds numbers 7500, 10,000, 12,500 and 15,000. All measurements are taken on radial profiles 3 mm downstream from each array (Fig. 4).

2.1.2. LDV system and data acquisition

The measurements are performed using a Dantec LDV system equipped with a 10 W argon-ion laser source and two BSA-enhanced signal-processing units (57N20 BSA and 57N35 BSA enhanced models). A lens of 160 mm focal distance is used. A lightweight precision three-dimensional traversing mechanism controlled via a personal computer is used to displace the measurement volume. The data-acquisition rate is 1–4 kHz and the sampling particle number is 30,000.

3. Results and discussion

3.1. Reproducibility test

To ensure the repeatability of LDV measurements, experiments were iterated four times for radial profiles at different cross-sections, for Reynolds number 15,000. The relative standard deviation for the mean and RMS fluctuating velocities depends on the location of the measurement volume. It is maximal in the near-wall region, a low-velocity zone, and minimal in the flow core region. The global mean standard deviation is 6% for the mean velocities and 5% for the fluctuating velocities.

3.2. Mean and fluctuating velocity measurements

Fig. 5 shows profiles of mean and fluctuating axial velocities and a schematic description of the hairpin-like structures in the flow. When the fluid passes through a tab array, the mean axial velocity accelerates due to the decrease in the flow cross-section. In the bulk region for $y/R > 0.5$, the mean velocity is high and quasi-constant and the RMS velocity is low. In the "shear" zone near the tab upper edge, $0.3 < y/R > 0.5$, an important velocity gradient and a peak in the fluctuating velocities can be observed. This peak coincides with the head of hairpin-like structures where an inflection in the mean velocity profile takes place, i.e. $\partial^2 U/\partial^2 y = 0$ (see Fig. 5). The second inflection point is a sign of a reversed vortex below the hairpin heads in the region $0 < y/R > 0.3$, as identified from PIV measurements by Yang et al. [9].

As shown in Fig. 5b and c, the maximum values of fluctuating velocities coincide with the statistical path of hairpin heads, suggesting that these structures contribute strongly to the mesomixing. The reversed vortex apparently does not contribute to this process.

Mean and fluctuating axial velocities increase with Reynolds number, but have similar profiles. The flow seems to be established beyond the fourth array, so that the profiles at the seventh row correspond to the equilibrium situation.

3.3. Turbulent intensity evolution

To evaluate the turbulent intensity, the convection velocity U_{conv} must be determined. Here the convective velocity was estimated using the method proposed by Van Doorn [16] and successfully used

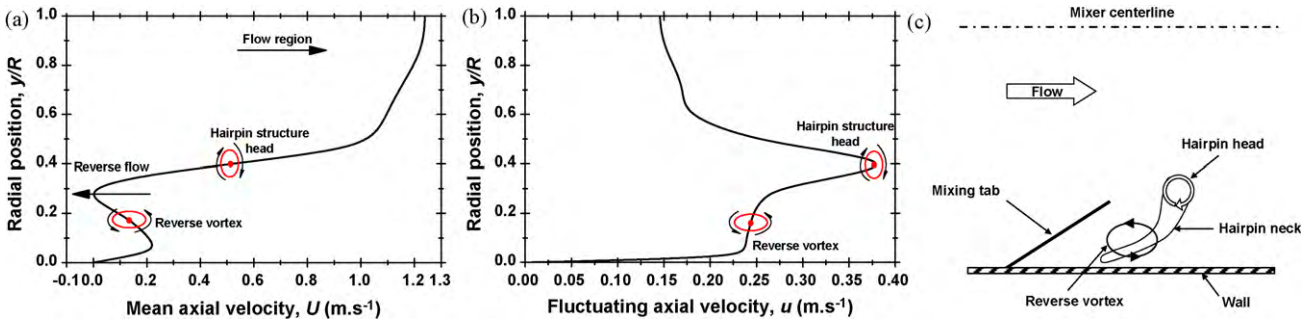

Fig. 5. (a) Mean and (b) fluctuating axial velocities 3 mm downstream from seventh tab array for $Re = 15{,}000$, and (c) schematic of hairpin structures and reversed vortex.

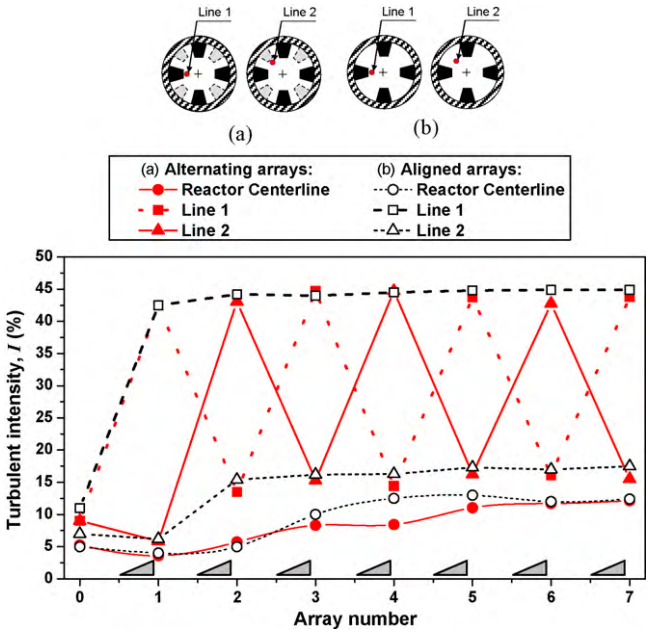

Fig. 6. Evolution of turbulence intensity at 3.5 mm from tube wall and at centerline in (a) aligned and (b) alternating arrays. Triangles indicate locations of vortex generators; $Re = 15{,}000$.

by Lemenand et al. [11], Mohand Kaci et al. [12] and Mokrani et al. [13] for measurements in the HEV mixer, assuming local isotropy of the turbulence in a one-dimensional mean flow:

$$U_{conv} = U^2\left(1 + 5\frac{\overline{u^2}}{U^2}\right) \tag{1}$$

where u is the fluctuating velocity and U is the mean velocity.

Fig. 6 shows the longitudinal evolution of turbulence intensity defined by $I = \sqrt{\overline{u^2}}/U_{conv}$ measured 3.5 mm from the tube wall and at the centerline, in both aligned and alternating rows of vortex generators, for Reynolds number 15,000. It can be seen that the turbulence intensity in alternating arrays oscillates between that of aligned arrays. This periodic oscillation, which is due to the periodic redistribution of the vorticity field in the mixer volume, enhances the homogeneity in the mixing process.

3.4. Integral time and length scales

To evaluate the integral time scale (Eq. (2)) from LDV measurements, time sampling must be regular and short enough to detect high-frequency fluctuations. As LDV systems do not function at fixed time intervals, all results were resampled using the "sample and hold" technique proposed by Host-Madsen and Caspersen [18]:

$$\tau = \int_0^\infty \frac{\overline{u(t)\,u(t+T)}}{\overline{u^2(t)}}dT \tag{2}$$

Fig. 7 shows the temporal autocorrelation coefficients 15 mm upstream of the mixer and 3 mm downstream of the seventh tab array. The exponential trend of the curves is similar to typical autocorrelation functions in classical turbulent flows. It can be seen in this figure that in the shear zone ($y/R = 0.4$) downstream of the seventh array, the temporal autocorrelation coefficient decreases more quickly than at the centerline, and still faster than in the straight pipe, whatever the position. In fact, short tails in temporal autocorrelation function curves indicate more intensified turbulence, thus confirming the turbulence-enhancing effect of the coherent structures generated by trapezoidal tabs.

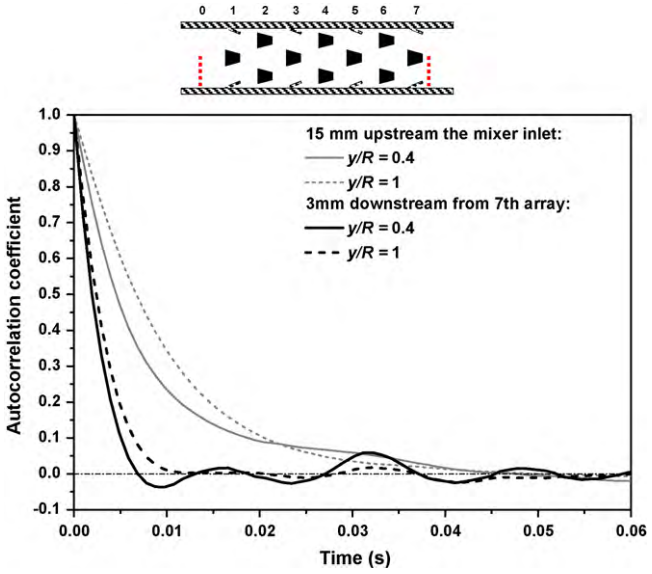

Fig. 7. Evolution of temporal autocorrelation coefficient in straight pipe upstream the mixer, and 3 mm downstream from the seventh array at tab's centerline, $Re = 15{,}000$.

In homogenous turbulent flows, the integral length scale Λ is defined as

$$\Lambda = \int_0^\infty \frac{\overline{u(x)\,u(x+r)}}{\overline{u^2(x)}}dr \tag{3}$$

Evaluating Λ using Eq. (3) requires a spatial autocorrelation (following Batchelor [17]). In the present study, the spatial macroscale is derived from the integral time scale in Eq. (2):

$$\Lambda = \tau U_{conv} \tag{4}$$

The spatial macroscale Λ, evaluated from Eq. (4), is plotted in Fig. 8 versus distance from the wall for three different radial profiles and at Reynolds number 15,000. In the preconditioner pipe, 15 mm upstream of the mixer inlet, the integral length scale increases with distance from the tube wall to attain a maximum of about $2.4R$ at $y/R \approx 0.8$, and then decreases at the tube center to $0.9R$, where

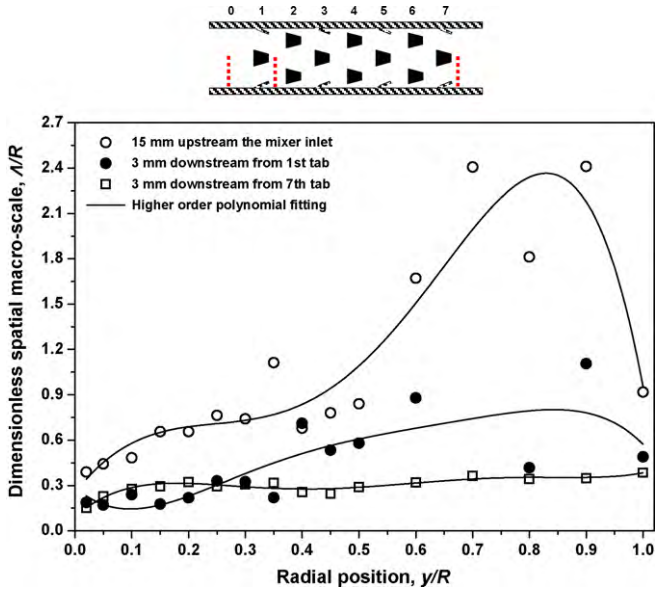

Fig. 8. Effect of vortex generators on the distribution of turbulence spatial macroscale, $Re = 15{,}000$.

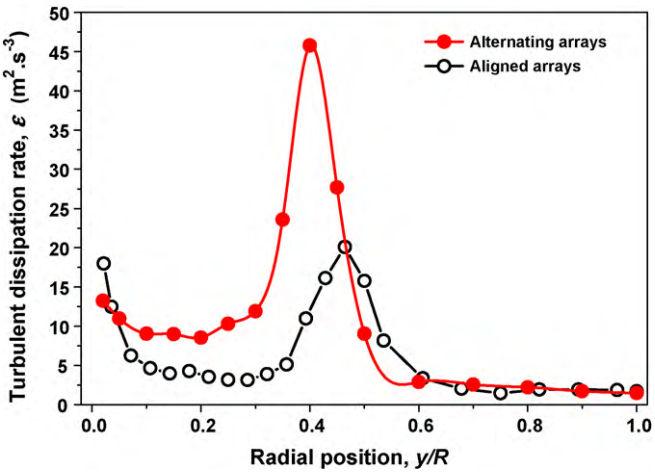

Fig. 9. Radial profiles of turbulence energy dissipation rate 3 mm downstream from the seventh tab array in aligned and alternating rows for Re = 15,000.

the convective velocity is maximum. Integral length scale values are reduced further downstream from the successive arrays, due to the turbulence intensification. For radial profiles downstream from first and seventh arrays, the variation of Λ is flatter than that at the mixer inlet, indicating more homogenous turbulent production distribution in the mixer cross-section.

3.5. Distribution of the local turbulence energy dissipation

Here the turbulence energy dissipation is evaluated using Batchelor's [17] model based on dimensional analysis:

$$\varepsilon = A\frac{(\overline{u^2})^{3/2}}{\Lambda} \quad (5)$$

where Λ represents the scale of the energetic structures, which is the upper limit of the inertial domain in Kolmogorov energy cascades. The constant A, determined by Mokrani et al. [13] as 1.8, has been used by Lemenand et al. [11] and Mohand Kaci et al. [12] for turbulent flow in aligned rows of vortex generators. In the present study we use the same value for A.

Fig. 9 shows radial profiles of the turbulence energy dissipation ε calculated from Eq. (5), 3 mm downstream from the seventh tab array, in both aligned and alternating rows geometries. It is clear that the presence of vortex generators strongly intensifies the turbulence energy dissipation in both geometries. In the alternating rows of mixing tabs, ε is much greater than in classical aligned rows. The maximum energy dissipation is located near the tabs' edges, where the statistical passage of the hairpin-like structures heads visualized by Mokrani et al. [13] in aligned rows of vortex generators (Fig. 5). These turbulent structures destabilize the flow by adding high-frequency fluctuations. The turbulence energy dissipation ε is related to the micromixing process, i.e. mixing on the Kolmogorov scale, and the heads of the hairpins passage coincide with higher values of ε where the best micromixing occurs.

From Fig. 9, it can be observed that in comparison with the alternating array, the location of the maximum value of ε in the aligned array geometry is shifted towards the mixer centerline by a small distance of y/R = 0.06, i.e. y = 0.6 mm, which is in the range of uncertainty in the LDV measurement volume positioning. Therefore, this small shift is not caused by a physical phenomenon due to the flow interaction with the tab, but it is attributed to the positioning errors of the LDV measurement volume in the pipe cross-section which has a radius of 10 mm.

The turbulence energy dissipation ε was also evaluated for the other Reynolds numbers (7500, 10,000 and 12,500); no qualitative effect of Reynolds number on ε was found in this range, but the turbulence energy dissipation rate was found to increase globally with Re.

4. Numerical study

In this study, a three-dimensional numerical simulation of the hydrodynamics and flow pattern in the alternating-array geometry is carried out using the CFD code Fluent®. The continuity equations for mass, momentum and energy are solved sequentially with double precision, segregated and second-order accuracy. Pressure–velocity coupling is performed by finite volumes with the SIMPLE algorithm.

4.1. Numerical procedure

4.1.1. Turbulence model

Mohand Kaci et al. [12] showed that for the flow pattern in aligned rows of vortex generators, the standard k–ε turbulent model [19], associated with a two-layer model to compute the wall region, produces flow simulation results of accuracy comparable to that obtained with other tested turbulence models, with reduced computing time and easier implementation. The same turbulent model is used here to analyze the fluid dynamics in alternating rows of vortex generators.

4.1.2. Boundary conditions

The velocity profile for fully turbulent developed flow in a pipe is used at the HEV inlet. The turbulence kinetic energy and the dissipation rate are fixed by the turbulence intensity I, derived from the tube flow equilibrium state [20].

The flow in the near-wall region is described by the "two-layer model", where the Navier–Stokes equations are solved in the viscous sublayer. The two-layer model obviates use of the empirical wall standard functions, which are not valid in complex flows. No-slip boundary conditions are applied to the solid surface of the tabs and at the pipe wall.

4.1.3. Grid system and convergence criterion

Due to flow axisymmetry, the geometry studied is reduced to 1/8 of the tube cross-section. An unstructured three-dimensional mesh with hexahedral volumes is adopted and refined at all solid boundaries. The CFD code is tested for several mesh densities and refined until no effect on the numerical results is detected. The appropriate meshing contains 724,174 cells. Mesh quality is quantified by using equiangle skew parameter; results show that 78.1% of the cells are of very good quality, 18.4% of good quality and 3.5% of mean quality. Several simulations are carried out by varying the convergence criterion values from 10^{-4} to 10^{-9}. Beyond a convergence criterion of 10^{-6} there are no significant changes in the turbulence quantities; therefore, a convergence criterion value of 10^{-6} is used.

To validate the accuracy of the simulation, the global mean energy dissipation obtained from numerical simulations was compared to that obtained from the pressure-drop equation calculated numerically between the test section inlet and outlet. Results were in good agreement, with a relative standard deviation of 10^{-4}.

5. Results and discussion

5.1. Experimental validation

Experiments were carried out to determine velocity and turbulence properties in the streamwise direction due to the test section geometry. Fig. 10, showing experimental and numerical results for Reynolds number 15,000, demonstrates that numerical simulations

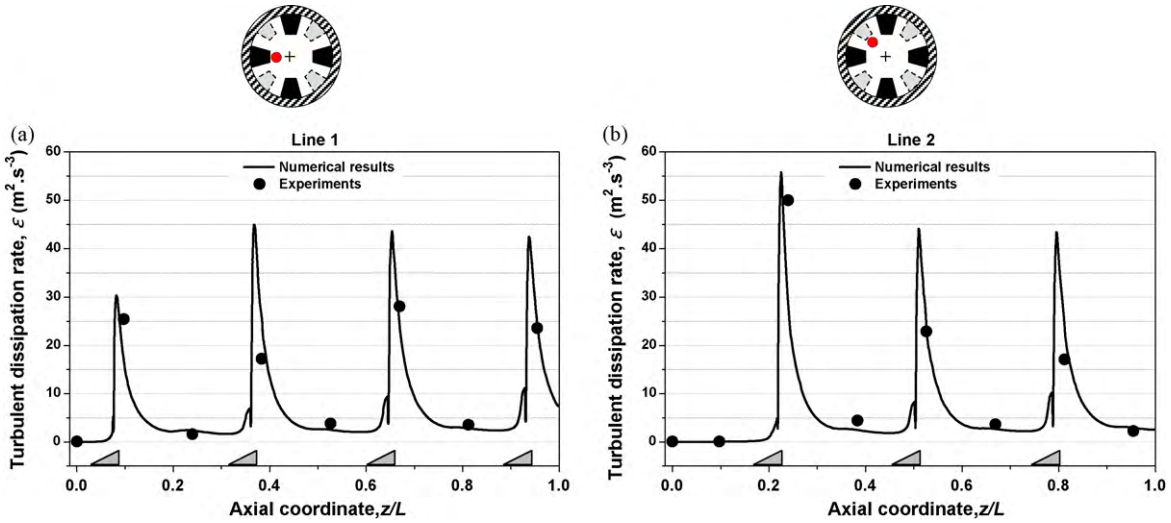

Fig. 10. Experimental validation of longitudinal distribution of turbulence energy dissipation ε for line 1 (a) and line 2 (b) schematically represented, Re = 15,000.

are in good agreement with the experimental results obtained from LDV measurements.

5.2. Turbulent flow structures

Fig. 11 shows the flow streamlines downstream of the seventh tab array. The swirling motion of the CVP is clearly observed: it entrains radial mass transfer between the near-wall low-velocity flow and the high-momentum flow in the mixer centerline.

Fig. 12 shows numerical simulations and LIF visualization (Mokrani et al. [13]) of the CVP and hairpin-like structures developed slightly downstream from the first tab array. The common upflow induced by CVP ejects the near-wall fluid and forms the head of the hairpin-like structures, which interact further with CVP to intensify mixing. At the splitting point, the common upflow velocity induced by the CVP divides into two opposite tangential velocities in the flow cross-section.

Fig. 13 shows contour plots of energy dissipation rate 3 mm downstream from each row of vortex generators: maximum values of ε are at a distance from the wall equal to that of the hairpin heads' statistical path identified in Section 2 (Fig. 5). It is clearly seen that the head of the hairpin vortices corresponds to positions of higher turbulence energy dissipation, confirming the peaks in the kinetic energy dissipation profiles obtained from LDV measurements, which are located at the height of the tab. Numerous studies [8–10] have shown that while flowing downstream from the tabs, CVPs are transformed into hairpin-like structures that become the main contributors to the turbulent mixing process. Fig. 11, showing flow pathlines downstream from the seventh tab array, demonstrates the effect of counter-rotating vortices on entraining the fluid in a swirling motion downstream from the tab, and thus enhancing the radial mass transfer in the tab wake.

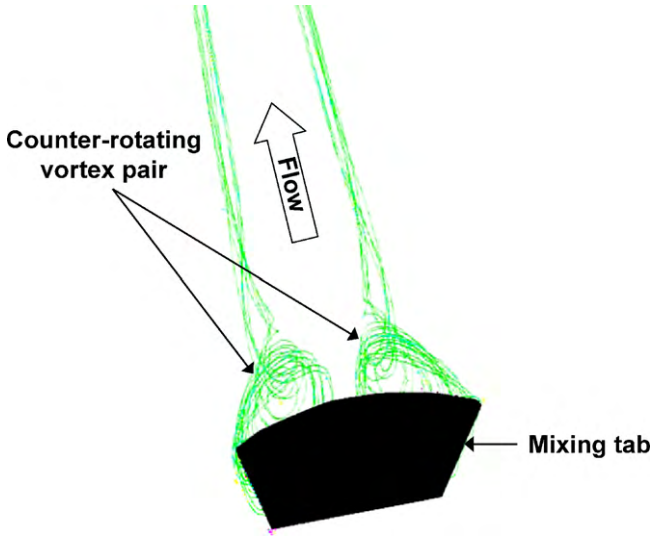

Fig. 11. Pathlines downstream from seventh tab array showing a counter-rotating vortex, Re = 15,000.

5.3. Efficiency of streamwise vortex redistribution

Fig. 14 compares the local turbulence energy dissipation rate ε_ℓ, averaged on tube cross-sections along the mixer, in the aligned and alternating configurations obtained from numerical simulations. When the flow encounters the first array, ε_ℓ sharply increases and then periodically attains its maximum value at each tab row in both cases. Minimum values are located upstream of each tab array. The advantage of the alternating geometry is clear from this figure: compared to the aligned geometry, ε_ℓ more than doubles at the second tab array, and increases by a factor 1.7 for the following tab arrays. Local turbulence energy dissipation is strongly intensified by the redistribution of streamwise vortices caused by the alternating rows of vortex generators.

In fact, the extra ε_ℓ generation produced by the alternating geometry is due to better exposure of the tabs to the flow. In the aligned geometry, the tabs are located in the wake of their upstream tabs and therefore are less exposed to the flow: they thus have less chance to interact with the fluid and generate lower turbulence energy dissipation. This is not the case in the turbulence intensity shown in Fig. 6, where the maximum turbulence intensity generated by the alternating geometry is the same as that of the aligned geometry. This is because I is proportional to u/U_{conv}; when u increases in the alternating case, U_{conv} increases as well, in such a way that the turbulence intensity at a given location stays the same for the alternating and aligned cases.

The energy consumption ($\Delta P/\rho$) is directly proportional to the global mean value of the turbulence energy dissipation calculated on the mixer volume ($\bar{\varepsilon}$). The global relative energy consumption ζ, defined by Eq. (6), is the ratio of the difference between the global dissipation rates in the alternating and aligned geometry over the

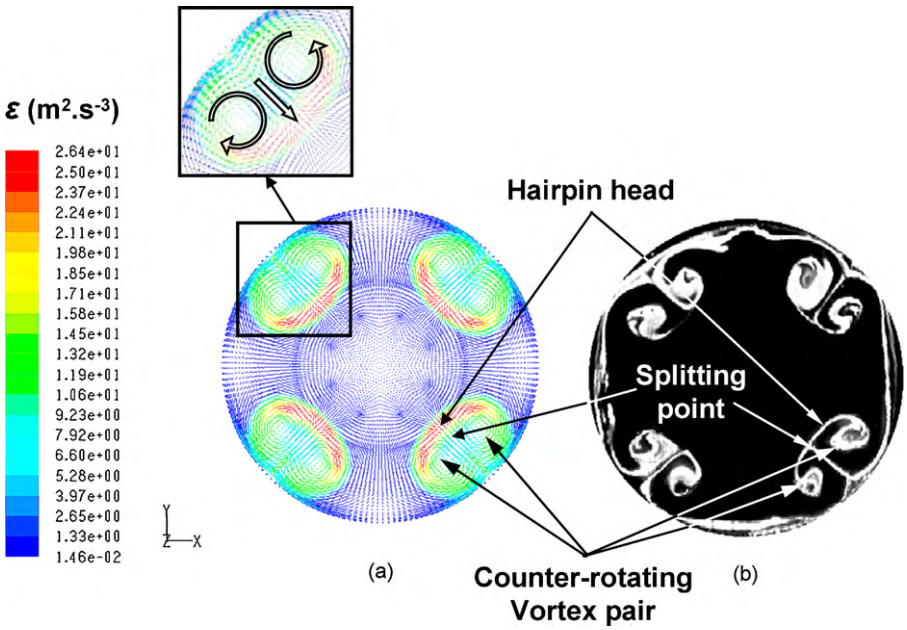

Fig. 12. Interaction of hairpin-like structures with counter-rotating vortex pair (CVP), at a cross-section 3 mm downstream from first array, (a) present numerical results for $Re = 15{,}000$ and (b) LIF measurements by Mokrani et al. [13] for $Re = 1000$.

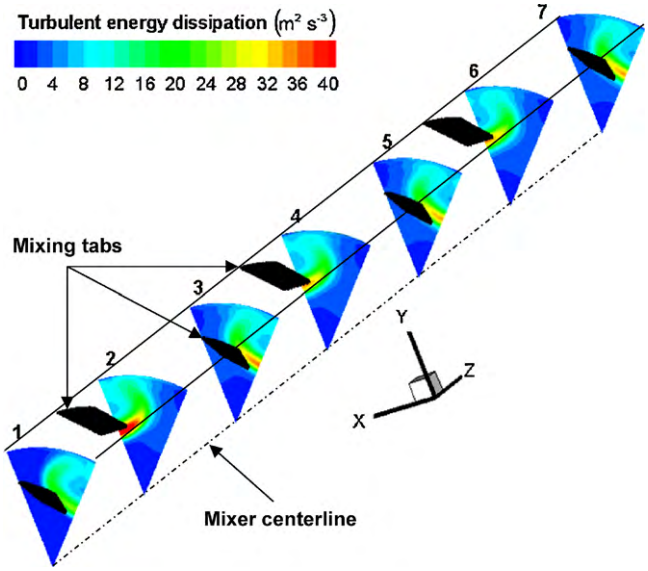

Fig. 13. Evolution of turbulence energy dissipation 3 mm downstream from tab arrays ($m^2\ s^{-3}$), $Re = 15{,}000$.

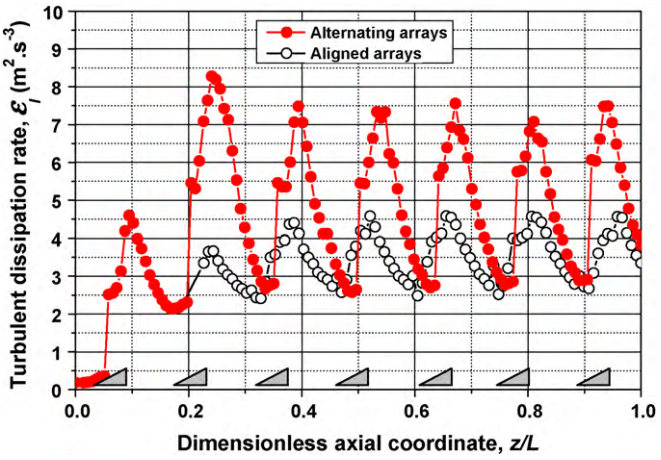

Fig. 14. Comparison of the ε_ℓ averaged on tube cross-sections for aligned and alternating rows of vortex generators, $Re = 15{,}000$.

global dissipation rate in aligned geometry:

$$\zeta = \frac{\bar{\varepsilon}_{alternated} - \bar{\varepsilon}_{aligned}}{\bar{\varepsilon}_{aligned}} \tag{6}$$

Fig. 15 shows global relative energy consumption ζ for Reynolds numbers from 7500 to 15,000. It can be noted that ζ increases with the Reynolds number. For $Re = 7500$, ζ is still low ($\zeta = 5\%$), but as the Reynolds number increases it reaches $\zeta = 18.5\%$ for $Re = 15{,}000$. This tendency of ζ suggests that it will increase for higher Re; however, the present study is limited to $Re = 15{,}000$ due to pumping system limitations. The increase in the relative energy consumption between the aligned and alternating geometry arises from the intensified local values of turbulence energy dissipation discussed above and shown in Fig. 14.

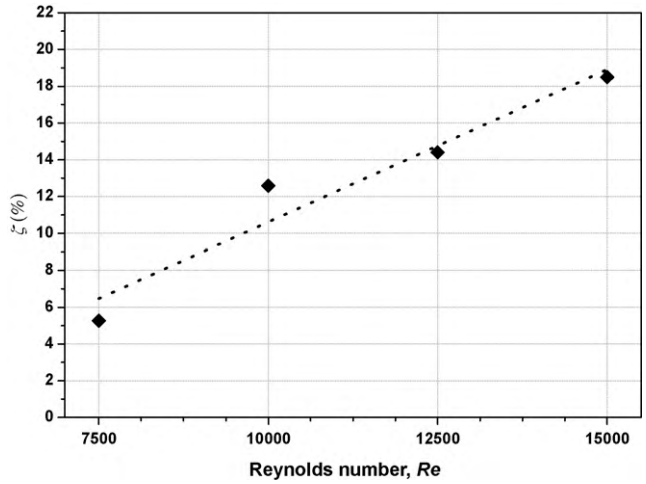

Fig. 15. Global relative energy consumption.

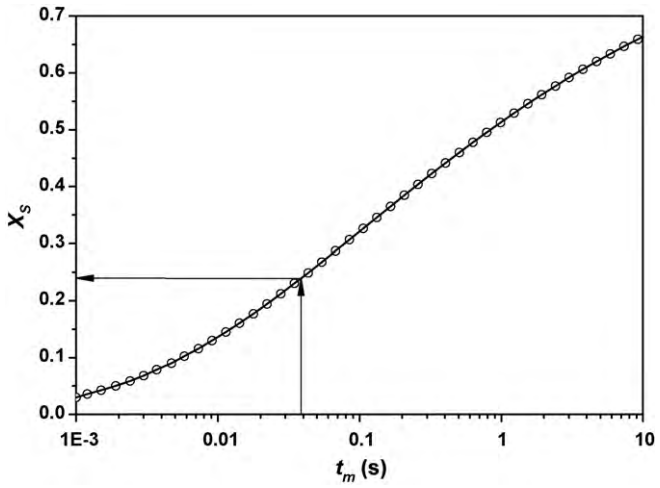

Fig. 16. Evolution of the segregation index X_S with respect to the micromixing time t_m obtained from the E-model and for the following sets of concentrations: [KI] = 0.0116 mol L^{-1}, [KIO_3] = 0.00233 mol L^{-1}, [NaOH] = 0.00605 mol L^{-1}, [H_3BO_3] = 0.0121 mol L^{-1} and [H_2SO_4] = 0.5 mol L^{-1}.

5.4. Determination of the segregation index

In experimental studies, chemical probe methods can be used to determine a segregation index by measuring the selectivity of fast chemical reactions. This segregation index can be related further to a micromixing time or to the turbulence energy dissipation rate to quantify the micromixing. In the present study, and having numerically computed the turbulence energy dissipation rate, a segregation index is calculated by considering the iodide–iodate reaction method developed by Fournier et al. [22] and by using the engulfment model, or E-model, originated by Baldyga and Bourne [23].

For the iodide–iodate reaction method, the segregation index, X_S, can be written as

$$X_S = 2\,\frac{[I_2]+[I_3^-]}{[H^+]_0}\left(1+\frac{Q_m}{Q_{H^+}}\right)\left(1+\frac{[H_2BO_3^-]_0}{6\,[IO_3^-]_0}\right) \quad (7)$$

where Q_m is the flow rate of the main flow in the reactor, and Q_{H^+} is the flow rate of the sulfuric acid, which is injected into the main flow. In fact, and following Ferrouillat et al. [24] and Mohand Kaci [25], the ratio Q_m/Q_{H^+} is chosen equal to 5000 to insure that macro and mesomixing play no significant role during the injection.

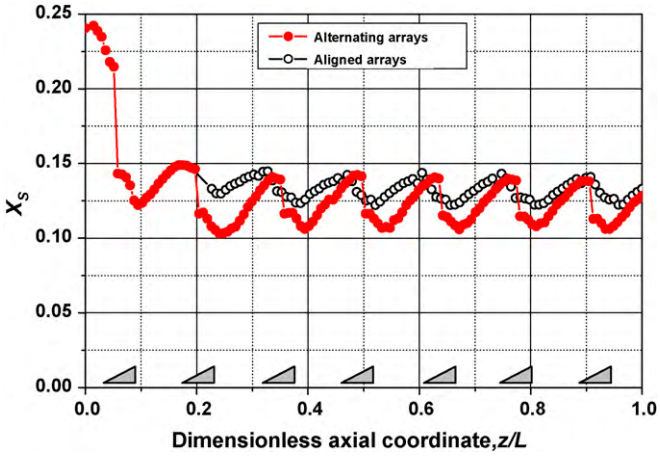

Fig. 17. Comparison of the X_S obtained from ε_ℓ averaged on tube cross-sections for aligned and alternating rows of vortex generators, Re = 15,000.

Segregation index X_S, is used in order to compare the quality of micromixing in both aligned and alternating arrays. In perfect micromixing, there is no formation of I_2 and I_3^-, and hence $X_S = 0$. In the opposite case, i.e. in total segregation $X_S = 1$.

In the present work, the set of concentrations is chosen based on the experiments of Mohand Kaci [25] who used the iodide–iodate test reaction to quantify experimentally the micromixing in a multifunctional heat exchanger-reactor. The evolution of X_S with respect to t_m, as shown in Fig. 16, is then determined by using the E-model [23] which consist in solving the non-linear differential equations of the evolution of each specie in the reaction system, until that the total quantity of the sulfuric acid is consumed.

The micromixing time t_m is then determined by using Eq. (8) given from the E-model [23], where ε is obtained from the numerical results. Hence, knowing t_m, the segregation index X_S can be determined from Fig. 16.

$$t_m = 17.24\left(\frac{\upsilon}{\varepsilon}\right)^{1/2} \quad (8)$$

Fig. 17 compares the segregation index X_S averaged on tube cross-sections along the mixer, in the aligned and alternating configurations. A periodic variation is observed in both aligned and alternating arrays due to the presence of the vortex generators. Following the same trend of ε (Fig. 14), the lowest values of X_S are observed downstream of each tab array, due to the generation of shear layers in these regions. It is also observed that in the alternating arrays the improvement of X_S is of about 20% relative to that in the aligned arrays.

6. Conclusions

The classical HEV static mixer is based on aligned arrays of mixing tabs. We applied a 45° periodic rotation on the arrays to build a new type of static and investigated whether it improved the vorticity field distribution in the mixer volume.

Studying the influence of vorticity redistribution in this new configuration on the local turbulence energy dissipation was the main objective of this work, since this characterizes the mixing on Kolmogorov scale (which controls fast chemical reactions) and the drop equilibrium diameter in multiphase dispersion. Experiments were carried out using LDV measurement to study the turbulent properties of the flow, and numerical simulations were performed to access the three-dimensional turbulent and velocity field.

The turbulence energy dissipation rate was estimated using Batchelor's [17] dimensional analysis based on the turbulence kinetic energy and a characteristic length scale. Using Taylor's hypothesis, this length scale was determined from the temporal autocorrelation measured by LDV.

It was found that the redistribution of the vorticity field intensifies the local turbulence energy dissipation by more than 120% relative to that in the classical HEV static mixer, with a maximum increase in energy consumption of 20%. In addition, the alternating arrays better homogenize the mixing process through more uniform redistribution of the turbulence field in the mixer. Intensification of the turbulence energy dissipation intensifies the micromixing and emulsification processes. In fact, the characteristic micromixing time is inversely proportional to $\varepsilon^{1/2}$. Therefore, enhancement of ε by a factor of 2.2 (for Re = 15,000) leads to 1.5-fold faster micromixing process. Moreover, from Hinze's [21] theory, the equilibrium diameter, which corresponds to the maximum drop size that can withstand the turbulent forces, is inversely proportional to $\varepsilon^{0.4}$, so that higher turbulence energy dissipation intensifies emulsification and leads to smaller drop diameters.

Acknowledgements

This work was partially supported by ADEME. Authors would like to acknowledge the continuous support of Dr. Gwenaël Guyonvarch, head of industrial and agricultural processes department of ADEME and also Dr. Cédric Garnier for monitoring this grant. CH is supported by ADEME and CNRS.

Appendix A. Nomenclature

A	constant
D	mixer diameter
ΔP	pressure drop
Q	flow rate
R	empty pipe radius
Re	Reynolds number $\left[\mathrm{Re} = \frac{UD}{\nu}\right]$
t_m	micromixing time
U_{conv}	convective velocity
U	axial mean velocity
u	axial fluctuating velocity
x, y, z	cartesian coordinates
X_S	segregation index

Greek letters

ε_ℓ	local turbulence energy dissipation rate
$\bar{\varepsilon}$	global turbulence energy dissipation rate $\left[\bar{\varepsilon} = \frac{U\Delta P}{\rho L}\right]$
Λ	integral length scale
υ	kinematic viscosity
τ	integral time scale
ζ	global relative energy consumption

Notations

0	initial value
[ ]	concentration of species

References

[1] H. Peerhossaini, On the effect of streamwise vortices on wall heat transfer, in: R. Shah (Ed.), Compact Heat Exchangers for Process Industries, Begell House Publishers, New York, 1997.
[2] R. Toé, A. Ajakh, H. Peerhossaini, Heat transfer enhancement by Görtler instability, Int. J. Heat Fluid Flow 23 (2002) 194–204.
[3] L. Momayez, P. Dupont, H. Peerhossaini, Effects of vortex organization on heat transfer enhancement by Görtler instability, Int. J. Therm. Sci. 43 (2004) 753–760.
[4] L. Momayez, P. Dupont, H. Peerhossaini, Some unexpected effects of wavelength and perturbation strength on heat transfer enhancement by Görtler instability, Int. J. Heat Mass Transf. 47 (2004) 3783–3795.
[5] I.G. Girgis, J.T.C. Liu, Mixing enhancement via the release of strongly nonlinear longitudinal Görtler vortices and their secondary instabilities in the mixing region, J. Fluid Mech. 468 (2002) 29–75.
[6] Chemineer, Kenics: Static Mixing Technology, Chemineer Inc., 1998, Bulletin 800 (commercial documentation).
[7] W.J. Gretta, C.R. Smith, The flow structure and statistics of a passive mixing tab, J. Fluids Eng. 115 (1993) 255–263.
[8] R. Elavarasan, H. Meng, Flow visualization study of role of coherent structures in a tab wake, Fluid Dyn. Res. 27 (2000) 183–197.
[9] W. Yang, H. Meng, J. Sheng, Dynamics of hairpin vortices generated by a mixing tab in a channel flow, Exp. Fluids 30 (2001) 705–722.
[10] D. Dong, H. Meng, Flow past a trapezoidal tab, J. Fluid Mech. 510 (2004) 219–242.
[11] T. Lemenand, D. Della Valle, Y. Zellouf, H. Peerhossaini, Droplets formation in turbulent mixing of two immiscible fluids, Int. J. Multiphase Flow 29 (2003) 813–840.
[12] H. Mohand Kaci, T. Lemenand, D. Della Valle, H. Peerhossaini, Enhancement of turbulent mixing by embedded longitudinal vorticity: a numerical study and experimental comparison, in: Proceedings of ASME FEDSM, Miami, Florida, July 17–20, 2006, pp. 115–125.
[13] A. Mokrani, C. Castelain, H. Peerhossaini, Experimental study of the influence of the rows of vortex generators on turbulence structure in a tube, Chem. Eng. Process. 48 (2009) 659–671.
[14] T. Lemenand, P. Dupont, D. Della Valle, H. Peerhossaini, Turbulent mixing of two immiscible fluids, J. Fluids Eng. 127 (2005) 1132–1139.
[15] J. Baldyga, J.R. Bourne, Turbulent Mixing and Chemical Reactions, Wiley, Chichester, 1999.
[16] M. Van Doorn, On Taylor's hypothesis in turbulent shear flows, Internal note 811123, University of Missouri-Rolla, 1981.
[17] G.K. Batchelor, The Theory of Homogeneous Turbulence, Cambridge University Press, New York, 1953, pp. 1–197.
[18] A. Host-Madsen, C. Caspersen, The limitations in high frequency turbulence spectrum estimation using the laser Doppler anemometer, in: Seventh International Symposium on Application of Laser Techniques to Fluid Mechanics, Lisbon, 1994.
[19] B.E. Launder, D.B. Spalding, Lectures in Mathematical Models of Turbulence, Academic Press, London, 1972.
[20] J.O. Hinze, Turbulence, 2nd ed., McGraw-Hill, New York, 1975, pp. 223–225.
[21] J.O. Hinze, Fundamentals of the hydrodynamic mechanism of splitting in dispersion processes, AIChE J. 1 (1955) 289–295.
[22] M.C. Fournier, L. Falk, J. Villermaux, A new parallel competing reaction system for assessing micromixing efficiency—experimental approach, Chem. Eng. Sci. 51 (1996) 5053–5064.
[23] J. Baldyga, J.R. Bourne, Simplification of micromixing calculations. I. Derivation and application of a new model, Chem. Eng. J. 42 (1989) 83–92.
[24] S. Ferrouillat, P. Tochon, H. Peerhossaini, Micromixing enhancement by turbulence: application to multifunctional heat exchangers, Chem. Eng. Process. 45 (2006) 633–644.
[25] M. Mohand Kaci, Caractérisation des capacités de micromélange des échangeurs/réacteurs multifonctionnels par sonde chimique—Application au HEV, Ph.D. Thesis, École Polytechnique de l'Université de Nantes, 2007.

CORPUS DES ARTICLES

5. Turbulent mixing and residence time distribution in novel configurations of multifunctional exchanger-reactor

C. Habchi, T. Lemenand, D. Della Valle, H. Peerhossaini

Chemical Engineering and Processing 49 (2010e) 1066-1075.

Chemical Engineering and Processing 49 (2010) 1066–1075

Contents lists available at ScienceDirect

Chemical Engineering and Processing: Process Intensification

journal homepage: www.elsevier.com/locate/cep

Turbulent mixing and residence time distribution in novel multifunctional heat exchangers–reactors

Charbel Habchi[a,b], Thierry Lemenand[a], Dominique Della Valle[a], Hassan Peerhossaini[a,*]

[a] Thermofluids, Complex Flows and Energy Research Group, Laboratoire de Thermocinétique, CNRS UMR 6607, École Polytechnique de l'Université de Nantes, rue Christian Pauc, B.P. 50609, 44306 Nantes, France

[b] Agence de l'Environnement et de la Maîtrise de l'Énergie (ADEME), 20 Avenue du Grésillé, B.P. 90406, 49004 Angers, France

ARTICLE INFO

Article history:
Received 25 February 2010
Accepted 2 August 2010
Available online 10 August 2010

Keywords:
Multifunctional heat exchanger/reactor
Micro-mixing
Mixing intensification
Longitudinal vortices
Vortex generators
LDA

ABSTRACT

Multifunctional heat exchanger–reactors show significant promise in increasing the energy efficiency of industrial chemical processes. The performance of these systems is conditioned by flow properties and is strongly geometry dependent. Here CFD simulation and laser Doppler anemometry (LDA) measurements are used to investigate the redistributing effects of the longitudinal vorticity generated by rows of inclined trapezoidal tabs on turbulent mixing in static mixers. Studies are carried out on three different configurations: in the first, the tabs are aligned and inclined in the direction of flow (the reference geometry for a high-efficiency vortex (HEV) static mixer), in the second, a periodic 45° tangential rotation is applied to the tab arrays with respect to one another, and in the third the reference geometry is used in the direction opposite to the flow direction (reversed direction). The mixing efficiency, taken as the resultant of the momentum-transfer efficiency of the "mean" flow at different scales, is studied. Macro-mixing entails the dispersive capacity of the flow at the heat exchanger–reactor scale, and is generally measured by the residence time distribution (RTD). At the intermediate scale, meso-mixing is governed by the turbulent fluctuations; this process of turbulent mixing can be characterized by the turbulence kinetic energy (TKE). Micro-mixing is characterized by the local rate of turbulence energy dissipation and is related to the progress of fast chemical reactions and selectivity. It is shown here that the reversed-array arrangement (the third configuration) provides the best performance in micro- (50%) and meso-mixing (25%), but exhibits an approximately 40% increase in power consumption over the classical HEV (reference) geometry and somewhat pronounced bimodal behavior in the RTD.

1. Introduction

The effects of symmetric and asymmetric longitudinal vortices on heat and mass transfer and on the mixing process have widely been studied due to their ability to increase velocity fluctuations and flow momentum redistribution, leading to better convective transfer and turbulent mixing without the need of external mechanical forces [1–4]. Several types of vortex generators are used to generate longitudinal vorticity and complex flow structures topologically similar to those encountered in the near-wall region of turbulent boundary layers [1,5–7]. These artificially generated structures can be used to intensify the convective heat and mass transfer in open flows or in internal flows such as in multifunctional heat exchangers/reactors (MHE/R).

MHE/Rs are widely used in industry because they can efficiently accomplish several unit operations such as mixing, heat and mass transfer, phase dispersion and chemical reactions, with low power consumption, better compactness and higher productivity than stirred vessels [1–4]. Process intensification is a rapidly growing field aiming to develop new high-performance super-compact MHE/Rs [8–17]. However, better performance is generally accompanied with an increase in pressure drop [2,4]. The mixing capacity of MHE/Rs is a determining factor in the thermal and chemical performance of these devices.

The mixing process depends directly on the transfer efficiency of the "mean" flow at different scales [18]. Macro-mixing consists in the dispersive capacity of the flow at the heat exchanger/reactor scale, and is generally measured by the residence time distribution (RTD). In fact, the RTD is directly related to the global motion of the flow since it represents the time the fluid particles take to migrate from the device inlet to the outlet. This large-scale motion, caused by the flow mean velocity, convects the fluid particles between high- and low-momentum regions in the heat exchanger/reactor volume, determining the large-scale convective transfer called macro-mixing. At intermediate scale, meso-mixing is governed by the turbulent fluctuations; this is the process of turbulent diffusion

* Corresponding author. Tel.: +33 240 683 124; fax: +33 240 683 141.
E-mail address: hassan.peerhossaini@univ-nantes.fr (H. Peerhossaini).

0255-2701/$ – see front matter © 2010 Elsevier B.V. All rights reserved.
doi:10.1016/j.cep.2010.08.007

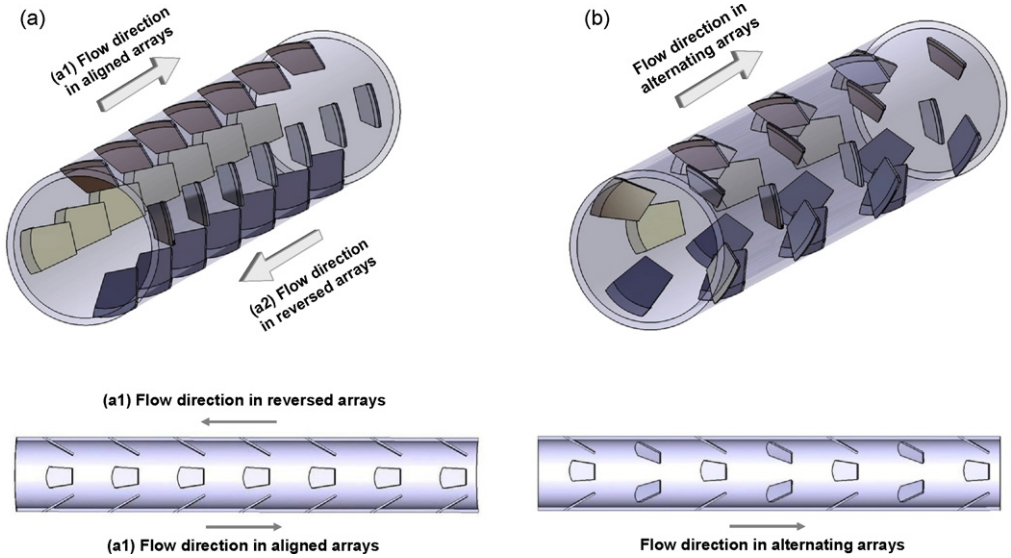

Fig. 1. Three-dimensional and top views of the geometries studied: (a1) aligned arrays, (a2) reversed arrays, and (b) alternating arrays.

that can be characterized by the turbulent kinetic energy (TKE). The selectivity of chemical reactions depends on how the reagents mix on the molecular scale [18]. This mechanism, called micro-mixing, entails the engulfment and deformation of Kolmogorov micro-scale eddies and is the limiting process in the reduction of local concentration gradients. This mechanism can be characterized by a micro-mixing time that is directly related to the turbulence energy dissipation rate [18]. Following the theory of Hinze and Kolmogorov, which is based on the idea of energy cascade, the drop breakup in multiphase flows can also be characterized by the turbulence energy dissipation rate [19–21]. Thus, an increase in turbulence energy dissipation accelerates the micro-mixing process, enhancing the selectivity of fast chemical reactions and also reducing the maximum drop size in multiphase flows.

The present study uses the high-efficiency vortex (HEV) static mixer as a generic device to study the effects of vortex generator architecture on mixing. HEV has the lowest energy consumption among commercial MHE/R (of about 75% lower power consumption [9,22]). The tab row configurations were modified in order to generate more energetic flow structures so as to intensify turbulent mixing and mass transfer. The classical HEV mixer (Chemineer Inc.™ [22]) consists of a circular pipe equipped with rows of mixing tabs. Each row is made up of four trapezoidal inclined tabs diametrically opposed in the tube cross-section and fixed on the pipe wall. This basic geometry, in which the tabs are aligned in the flow direction, is used here as the reference geometry. In the first geometry variant, each tab array is rotated tangentially by 45° with respect to its neighboring array, leading to a periodic rotation of the arrays; this we call *alternating arrays*. In the second variant, the tab arrays are aligned as in the classical HEV mixer, but the flow direction is reversed; this geometry we call *reversed arrays*.

Several studies aimed at investigating the flow pattern and fluid mixing efficiency of the HEV static mixer [9,17,23] have shown its high efficiency in emulsification and mass transfer. Other studies [5,6,24,25] focused on the flow dynamics downstream from one trapezoidal tab and suggest redesign of the HEV mixer to optimize meso- and micro-mixing.

To analyze the performance of these different geometries in turbulent regime, a three-dimensional numerical simulation is performed of the local flow pattern. For validation, the results of these simulations are then compared with laser Doppler anemometry measurements of the flow field in the same geometry. These studies are performed in a turbulent regime where the Reynolds numbers based on the inner pipe diameter are 7500, 10,000, 12,500 and 15,000.

In Section 2, the different geometries and their dimensions, the numerical method and the experimental setup are described. The results are presented and discussed in Section 3 in terms of flow structure (numerical and experimental) and turbulence mixing performance (TKE, turbulence energy dissipation, RTD and pressure drop). Section 4 presents our conclusions.

2. Materials and methods

2.1. MHE/R geometries

The three different configurations of the HEV static mixer studied here are shown in Fig. 1.

- Configuration a1: circular pipe equipped with seven rows of trapezoidal mixing tabs. The tabs are fixed to the wall and inclined at 30° in the flow direction.
- Configuration a2: reversed-tab array in which the flow is in the opposite direction to that in the basic HEV (a1).
- Configuration b: the arrays in the basic HEV are periodically rotated at 45° angles.

The dimensions of the geometries are given in Table 1.

2.2. Numerical method and turbulence model

The numerical simulation is carried out using the CFD code Fluent® 6.3 [26]. The continuity and momentum equations are solved sequentially with double precision [27], segregated and second-order accuracy [28]. Pressure–velocity coupling is performed by finite volumes with the SIMPLE algorithm [29].

It has been shown by Mohand Kaci et al. [23] that the standard $k-\omega$ [30] and the RSM models (Boussinesq closure hypothesis for the third order moments) [31–33], both associated with the "two-layer model" [34,35], provide a satisfactory description of the flow pattern and turbulence properties in the wall region of the HEV static mixer. The $k-\varepsilon$ turbulence model provides similar accuracy to other models (RNG $k-\varepsilon$, *standard* $k-\omega$, SST $k-\omega$ and RSM model) but requires far less computational time. Thus the $k-\varepsilon$ model will be used to study the three geometries in the present work. Moreover, the RSM model is used to simulate the higher

Table 1
Mixing tab geometry and dimensions.

Pipe inside diameter (D)	20 mm
Distance between consecutive arrays	20 mm
Total pipe length (L)	140 mm
Tab height (tab edge from the wall) (h)	3.9 mm
Larger base of the trapezoidal tab (a)	6.2 mm
Smaller base of the trapezoidal tab (b)	4.7 mm

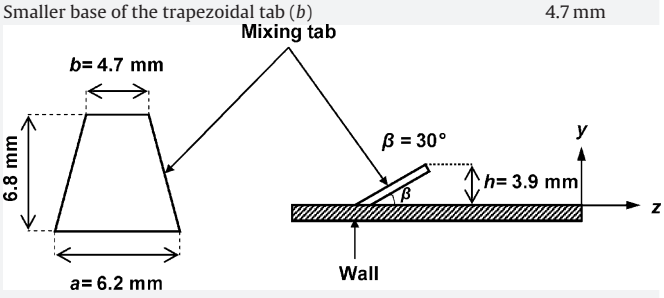

Reynolds numbers in the three geometries to validate the results obtained from the $k-\varepsilon$ model. Once the validation is done, the $k-\varepsilon$ model is used to simulate all other Reynolds numbers.

The flow in the near wall region is modeled by the two-layer model to avoid using the empirical wall standard functions, which are not valid for three-dimensional complex flows. No-slip boundary conditions are applied to the solid surface of the tabs and of the pipe wall. At the computational domain inlet, a fully developed turbulent flow velocity profile is used; the TKE and the turbulence energy dissipation rate at the inlet are fixed by the turbulence intensity derived from the equilibrium turbulent tube flow [36].

Taking into account the periodicity (axial symmetry) of the geometries reduces the computational domain to $\pi/4$ of the mixer total volume, as shown in Fig. 2. An unstructured three-dimensional mesh with hexahedral volumes refined at the solid boundaries is adopted.

A grid dependency study was carried out for the three geometries; the simulations were tested for several mesh densities and refined until the relative difference between the numerical results for two consecutive mesh densities did not exceed 1%. The final values of y^+ in the first grid points and the numbers of cells retained after refinement for the numerical simulations in the three geometries are given in Table 2. The maximum value of y^+ does not exceed 4, guaranteeing that at least one mesh point exists inside the viscous sub-layer [23,37].

Simulations are carried out by varying the convergence stop-criterion values from 10^{-4} to 10^{-9}. Beyond a convergence criterion of 10^{-6} there are no significant changes on the turbulence field, so that this is the value used in the simulations.

Table 2
Mean and maximum values of y^+ in the first grid cells near the solid surfaces, and number of cells in the computational domain.

Geometry	Number of cells	Mean value of y^+	Maximum value of y^+
Aligned arrays	695,178	2.1	3.4
Alternating arrays	724,174	2.2	3.2
Reversed arrays	723,778	2.2	3.0

2.3. Experimental setup and methods

The hydraulic loop is shown in Fig. 3. The test section is preceded by a preconditioner (1500 mm straight Plexiglas pipe) to produce a fully developed turbulent flow at the test section inlet. The test section is followed by a postconditioner (500 mm straight Plexiglas pipe). A safety valve is added to the circuit as well as a pulsation absorber whose role is to limit the pressure fluctuations produced by the pump and thus ensure a continuous and stable flow in the test section. The flow rate is measured by a digital balance via a PC. The working fluid is tap water whose temperature is maintained constant at 298 K, controlled by a thermostatic Huber Crythermostat71 (temperature can be controlled to 0.05 K accuracy).

Flow measurements are performed using a Dantec laser Doppler anemometry system. The LDA system is equipped with a 10 W argon-ion laser source and two BSA-enhanced signal-processing units (57N20 BSA and 57N35 BSA enhanced models). A lens of 160 mm focal distance is used. A lightweight precision three-dimensional traversing mechanism controlled via PC is used to displace the measuring volume. The data-acquisition rate was 1–4 kHz and the sampling particle number was 30,000. Measurements are taken along different radial profiles in each array, at 3 mm downstream from the tab.

Due to the cylindrical shape of the test sections, only the axial mean and fluctuating velocities were measured by the LDA system. To ensure repeatability of LDA measurements, experiments were iterated four times for radial profiles at different positions for Reynolds number 15,000. The global mean standard deviation is 6% for the mean velocity and 5% for the fluctuating velocity.

3. Results and discussions

3.1. Experimental validation

For Reynolds number 15,000, Fig. 4 shows the streamwise mean velocity (Fig. 4(a)) and turbulence energy dissipation rate (Fig. 4(b)) profiles obtained from LDA measurements and numerical simulations, both RSM and $k-\varepsilon$ model. The mean axial velocity obtained

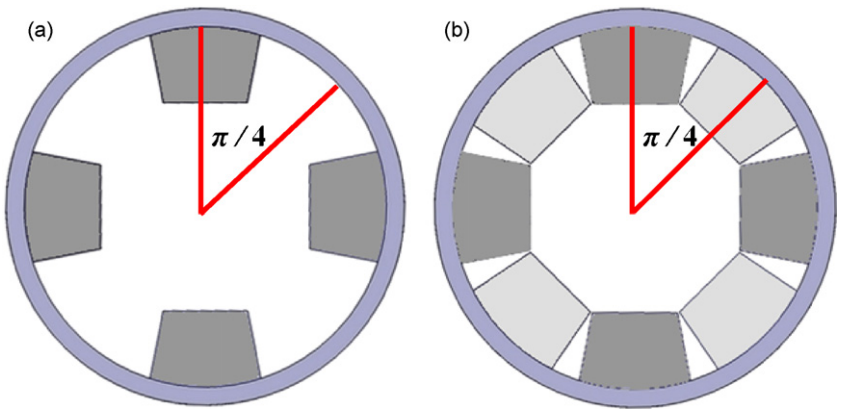

Fig. 2. Front view of the computational domain in a $\pi/8$ sector of the (a) aligned and reversed arrays and (b) alternating arrays.

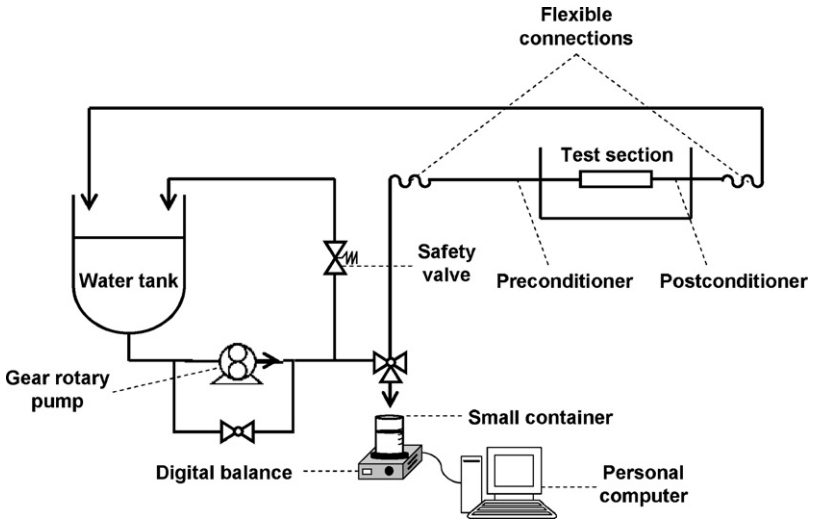

Fig. 3. Experimental rig.

numerically reproduces fairly well the experimental data as shown in Fig. 4(a). Moreover, the mean axial velocities obtained numerically from both turbulence models are very close to each other. Also from Fig. 4(b), it is observed that both turbulence models reproduce well the experimental results, especially in the flow core ($0 < r/R < 0.4$) and in the shear region ($0 < r/R < 0.7$). However, in the wake region near the wall, the numerical results do not correlate very well with experimental ones. This fact can be attributed to the noises in the LDA measurements in the near wall region as reported previously [23]. Moreover, the experimental turbulence energy dissipation is obtained by using Taylor hypothesis of "frozen turbulence" which requires the definition of a convective velocity. This hypothesis works well in the flow core and shear region since the convective velocity is not much different from the mean axial velocity. However, in the wake region, the mean axial velocity is negative due to recirculation flow, and hence Taylor hypothesis is not appropriate to be used in this flow region.

The qualitative shapes of the velocity and turbulence energy dissipation profiles are well reproduced by the numerical simulations using $k-\varepsilon$ model; the maximum relative standard deviations between the numerical and experimental results do not exceed 10%. This guarantees that the numerical simulation is a sufficiently reliable tool to investigate the three configurations. In the rest of the paper only results obtained from the $k-\varepsilon$ model are shown

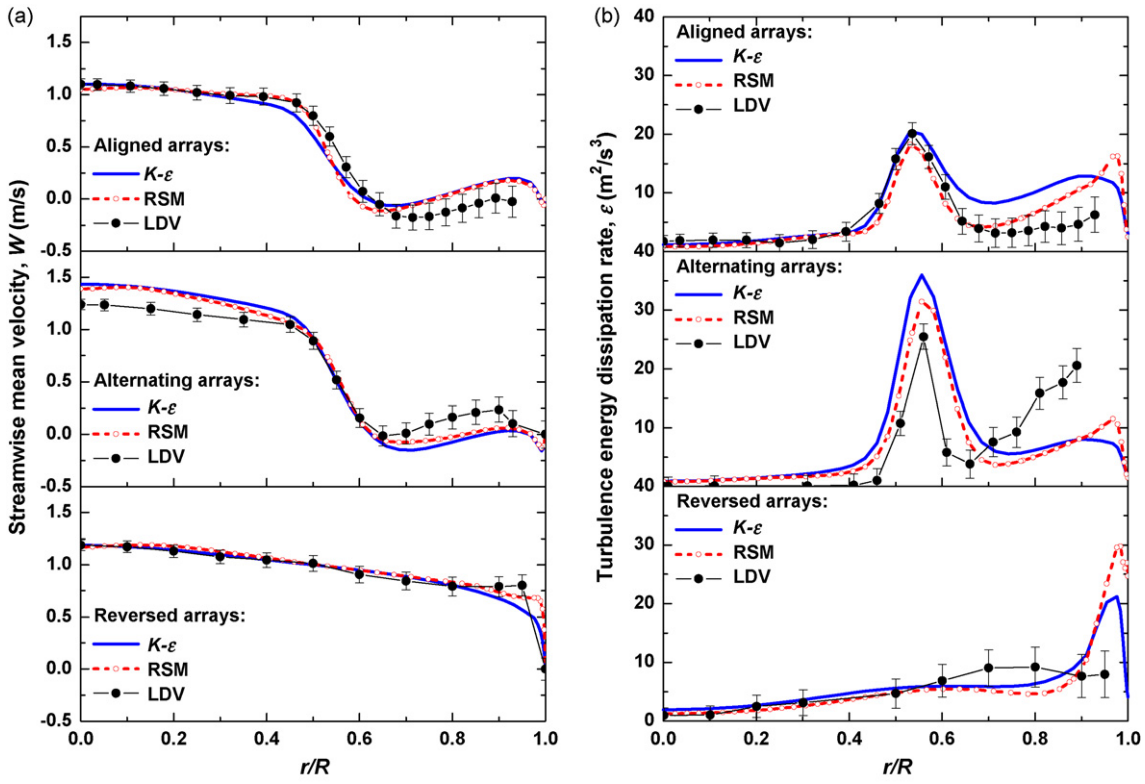

Fig. 4. Numerical and experimental (a) mean streamwise velocity profiles and (b) turbulence energy dissipation rate for the three configurations 3 mm downstream from the 7th tab; Re = 15,000.

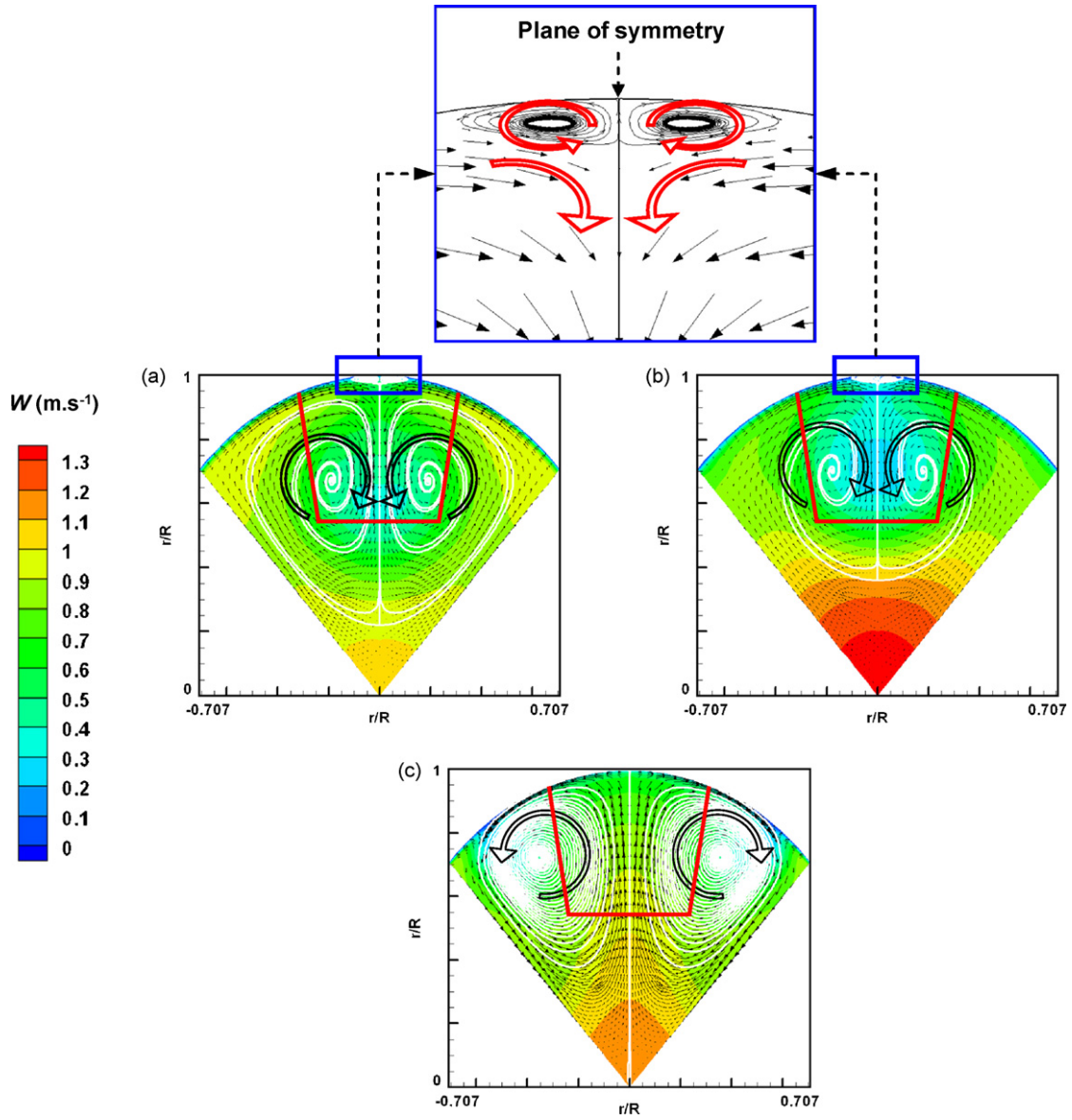

Fig. 5. Counter-rotating vortex pairs in (a) aligned, (b) alternating and (c) reversed arrays at 9 mm downstream of the 7th tab array, Re = 15,000.

since it was less computer time consuming, and hence was used to simulate all the Reynolds numbers in the three geometries.

3.2. Flow pattern

The velocity vector field and axial mean velocity distribution in the cross-section at the outlet of each geometry (9 mm downstream from the 7th tab array) are presented in Fig. 5. In all configurations, a counter-rotating vortex pair (CVP) shown by the white streamlines can be observed behind each tab. The longitudinal vortices are generated by the pressure gradient caused by the velocity difference between the lower and upper tab sides. In the aligned and alternating arrays, the tabs are inclined in the flow direction; hence the flow velocity above the tab is greater than that below, so that a pressure gradient appears that initiates a swirling motion forming further downstream of the CVP and taking the form of a mushroom-like structure. These vortices occupy a larger area in the aligned arrays than in the alternating array. However, it can be observed from the distribution of the axial mean velocity that the flow in the alternating tab array is more energetic than in the aligned arrays because the periodic rotation of the tab arrays redistributes the flow momentum in the reactor cross-section. A small CVP also develops near the wall region behind the tabs that arises from entrainment by the large CVP of the fluid trapped in the corner behind the tab: the swirling motion of the large CVP creates a swirling motion in the corner and gives rise to a smaller CVP. This structure can be seen from the streamlines plotted in the zoom view in Fig. 5(a) and (b).

In the reversed array (Fig. 5(c)), the tabs are inclined in the opposite direction to the flow. Hence, the flow velocity on both tab sides (left and right) is larger than that behind the tab surface and causes a pressure gradient. As a consequence, the fluid particles are sucked into both tab sides. This entrains a fluid flow from the core region towards the tab wake to replace the fluid particles sucked into the tab sides, initiating a swirling motion that is convected downstream. This swirling motion gives raise to a CVP that rotates in the opposite direction to those in the two previous configurations. In the reversed array, the CVP occupies a larger area than in the other configurations and extends further into the core flow on both sides of the tab. These vortices are more energetic than those in the other two geometries, as evidenced by the velocity vector sizes in Fig. 5. The counter-rotating vortex pair enhances radial mass transfer between the tab wake and the flow core in the

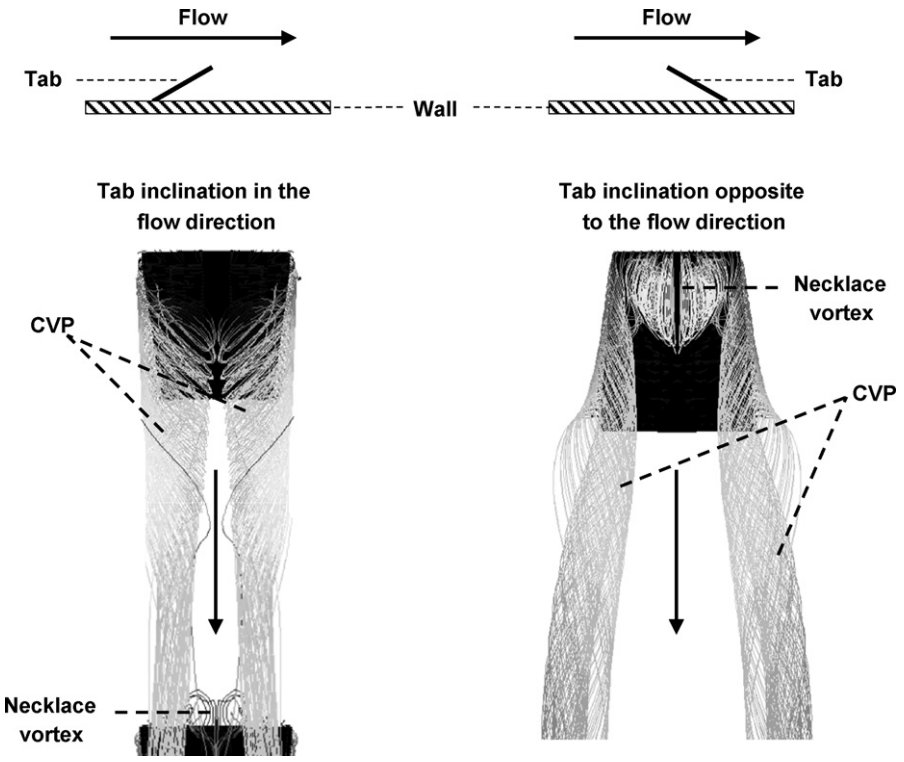

Fig. 6. Mean flow structure for different tab inclinations in the 6th tab array, Re = 15,000.

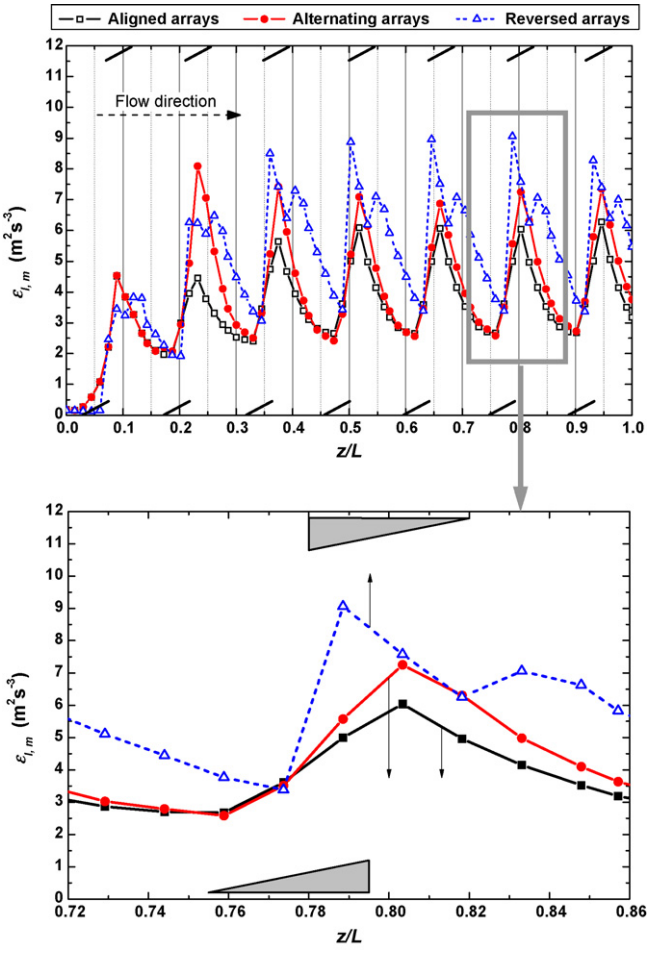

Fig. 7. Longitudinal evolution of turbulence energy dissipation averaged on the reactor cross-sections, Re = 15,000.

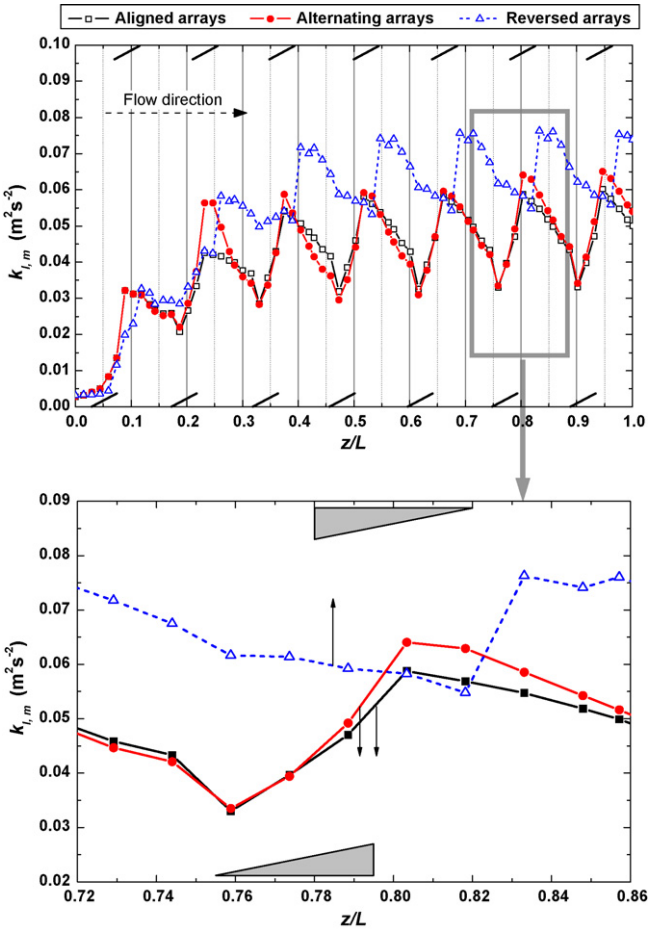

Fig. 8. Longitudinal evolution of the TKE averaged on reactor cross-sections for the three tab arrays, Re = 15,000.

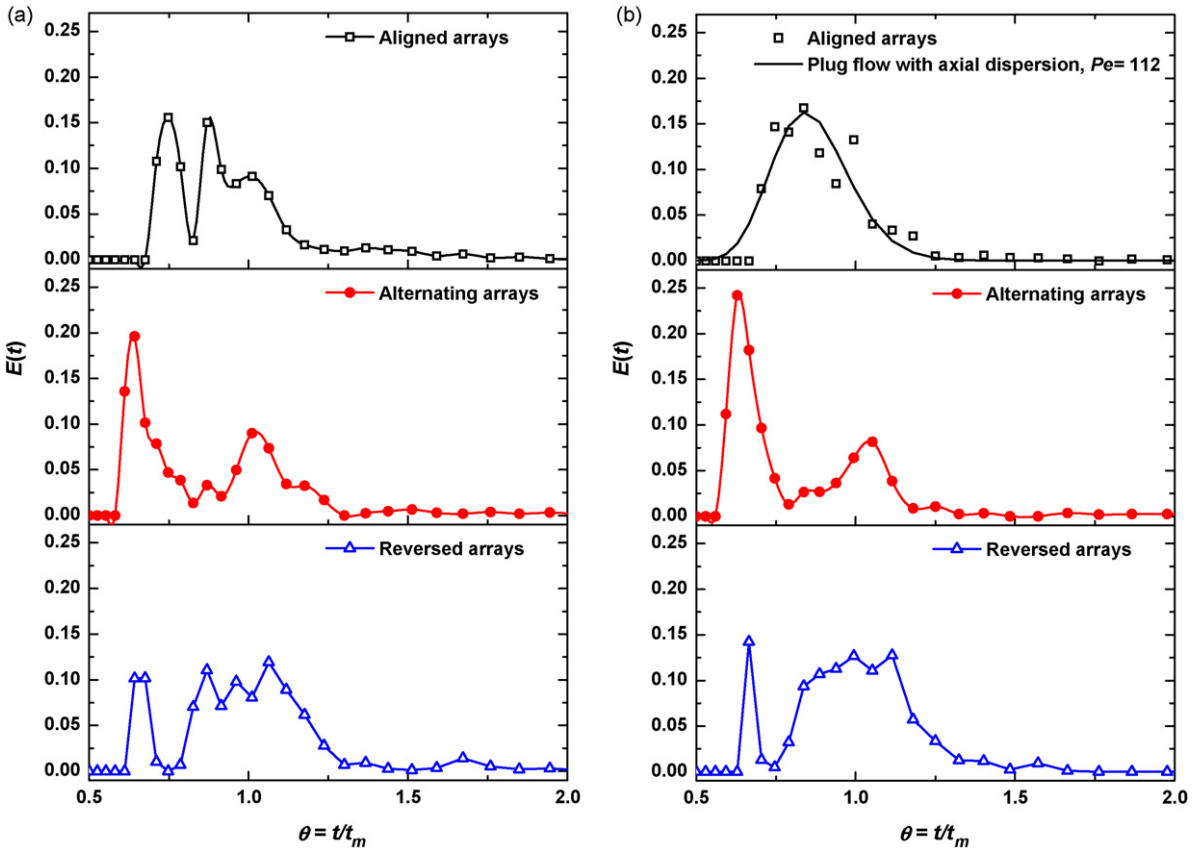

Fig. 9. (a) PDF of the RTD in the three geometries smoothed using FFT, Re = 7500.

pipe centerline by increasing mass and energy exchange between the low-momentum fluid in the near-wall region and the high-momentum fluid in the reactor core. Thus, the CVPs play the role of internal agitators in the flow.

The three-dimensional streamlines in Fig. 6 also show the role of the CVP in convecting fluid particles in both radial and streamwise directions and reveal the presence of new vortices. A small necklace vortex forms upstream of a tab inclined in the flow direction (aligned and alternating arrays). For the reversed tabs, a large necklace vortex exists at the upper tab edge that further enhances mass exchange between the tab wake region and the core flow. In fact, the flow structure changes radically when the tab inclination is reversed. The CVP vanishes after a certain distance from the tabs because its momentum is damped as it migrates away from the tab. We discuss below the effect on the turbulent mixing of the different flow structures in the three geometries.

3.3. Turbulence energy dissipation and micro-mixing skills

The local turbulence energy dissipation rate, which can be used to quantify micro-mixing, is:

$$\varepsilon_l = \frac{1}{2}\upsilon\overline{\left(\frac{\partial u_i}{\partial x_j} + \frac{\partial u_j}{\partial x_i}\right)^2} \quad (1)$$

The local turbulence energy dissipation rate averaged on cross-sections ($\varepsilon_{l,m}$) (Eq. (2)) is used to compare micro-mixing efficiency in the three geometries:

$$\varepsilon_{l,m} = \frac{\sum_{k=1}^{n}\varepsilon_{l,k}}{n} \quad (2)$$

where n is the total node number in the tube cross-section.

The longitudinal evolution of the local turbulence energy dissipation rate averaged on the tube cross-sections ($\varepsilon_{l,m}$) in the three configurations is shown in Fig. 7. A periodic evolution is observed along the MHE/R due to the presence of the mixing tabs at constant intervals, creating a self-sustained oscillatory-like flow along the reactor. The amplitude of the oscillations is the same in the three configurations and reaches about 35% of the mean global value; for the reversed arrays two maxima are observed. To analyze the effect of different tab arrangements on the dissipation of turbulence energy, an enlargement of the curves on the 6th array is shown in Fig. 7. The shear layer shed from the tab edges creates high-velocity fluctuation gradients, thus increasing the dissipation of the turbulence energy. The first shear layer develops downstream from the tab leading edge. In the aligned and alternating arrays similar behavior is observed: $\varepsilon_{l,m}$ begins to increase from the tab leading edge and reaches its maximum value at the trailing edge where the hairpin vortices develop due to Kelvin-Helmholtz instability [6]. The values of $\varepsilon_{l,m}$ decrease further downstream due to the breakdown of turbulence production between two tabs. Despite the same tab orientation in these two configurations, the values of $\varepsilon_{l,m}$ in alternating arrays are greater than in aligned arrays. In fact, the flow impacting a tab in the alternating arrays arises because the region between two tabs in the previous array carries higher momentum and energy due to the reduction of the flow cross-section. In the aligned rows, on the other hand, the momentum and energy of the flow impacting a tab is reduced by the previous array, since the tabs are aligned.

In the reversed arrays, $\varepsilon_{l,m}$ starts to increase from the tab leading edge (which is in fact the tab tip). Further downstream, the velocity fluctuation gradient is damped, leading to a decrease in $\varepsilon_{l,m}$. The second maximum of $\varepsilon_{l,m}$ in the reversed arrays is due also

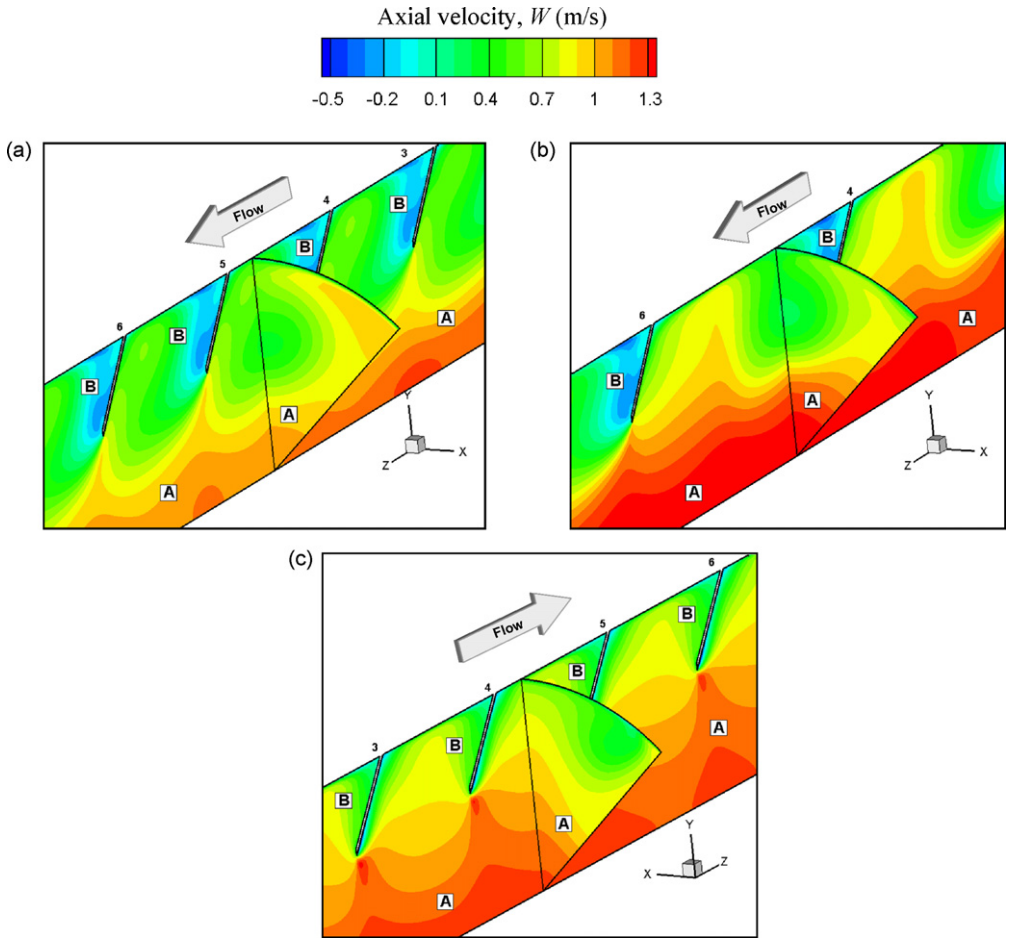

Fig. 10. Distribution of axial velocity in tab symmetry plane and on the reactor cross-section for (a) aligned, (b) alternating and (c) reversed arrays (Re = 15,000).

to the shear layer shed from the trailing edge, i.e. the base of the trapezoidal tabs.

From the above observations it can be concluded that when the flow encounters the tab tip (the upper side of the trapezoidal tab in the reversed arrays) abruptly, the flow streamlines do not have time to adjust their curvature and higher fluctuation-velocity gradients are generated that intensify the dissipation of turbulence energy. On the other hand, when the flow encounters the tabs in the aligned and alternating arrays, the flow streamlines have enough time to adjust themselves to the wall curvature, so that velocity gradients are weaker and the increase in $\varepsilon_{l,m}$ is modest.

Comparing the profiles of the three configurations in Fig. 7 shows that the reversed arrays significantly enhance micro-mixing and droplet breakup since they present the highest local energy dissipation rates. In this configuration, $\varepsilon_{l,m}$ is about 50% higher than in the aligned arrays and about 29% higher than the alternating arrays.

3.4. Turbulence kinetic energy and meso-mixing

Meso-mixing is the mixing process due to the large eddy scales of the inertial-convective domain. Meso-mixing is directly related to the velocity fluctuations of the eddies and can hence be characterized by the RMS of velocity fluctuations or TKE:

$$k_l = \frac{\sum_{i=1}^{i=3} \overline{u_i u_i}}{2} \tag{3}$$

To compare the meso-mixing efficiency in the geometries studied, local values of the TKE averaged on the tube cross-section can be computed as:

$$k_{l,k} = \frac{\sum_{k=1}^{n} k_{l,k}}{n} \tag{4}$$

The longitudinal evolution of the cross-section mean TKE ($k_{l,m}$) values is shown in Fig. 8: an oscillatory-like flow with the periodicity of the tabs is observed. The highest values of $k_{l,m}$ are located near the tab tips, where the shear layer is shed from the tab; these values decrease downstream of the tab due to the decrease in flow momentum.

A zoom view of the curves in the 6th array provides some hints about the fundamental mechanism in the TKE behavior. In the aligned and alternating arrays, the TKE increase as the fluid is advected through the tab array and reaches its maximum at the tab tip where the hairpin vortices are generated. Similar results were observed by Dong and Meng [6] and Yang et al. [25], suggesting that these transient structures carry most of the TKE downstream of the trapezoidal tabs. In the reversed arrays, on the other hand, the TKE values continuously decrease from a tab array until the new CVPs are generated by the next tabs, thus increasing TKE values. No significant effect of the necklace vortex is observed on the TKE behavior here.

From global analysis it can be concluded that the "reversed arrays" seem to exhibit the best performance in meso-mixing, since it presents the highest values of $k_{l,m}$. In this configuration the $k_{l,m}$ is about 25% higher than the classical HEV geometry (aligned arrays) and about 16% higher than the alternating tabs arrays.

3.5. Residence time distribution and macro-mixing

Numerical RTDs were obtained by injecting about 600 inert particles uniformly distributed in the cross-sectional plane of the reactor inlet. From knowledge of the velocities along the flow trajectories, the residence time of each particle is computed using a fourth-order Runge–Kutta method to evaluate the time necessary to cover their path in the flow.

As shown in Fig. 9, the RTDs for two different Reynolds numbers (a) Re = 7500 and (b) Re = 15,000 present bimodal behavior in all cases, which is typical of a bypass flow, except for the aligned arrays at Re = 15,000 which is modeled by a plug flow with axial dispersion having a Péclet number $Pe = 112$. For the aligned geometry, the bimodal behavior observed for Re = 7500 in Fig. 9(a) is vanished for Re = 15,000 due to the reduction of the recirculation flow behind the tabs.

In Fig. 9(b), two different classes of fluid particles can be identified:

1. High-momentum fluid particles, denoted *A*, that rapidly reach the heat-exchanger–reactor outlet ($\theta \approx 0.65$ in alternating and reversed arrays). In fact, in the alternating arrays, the number of particles reaching rapidly the reactor outlet ($E(\theta) \approx 25\%$) is larger than in the reversed arrays ($E(\theta) \approx 15\%$).
2. Low-momentum fluid particles, denoted *B*, that exit the system outlet after a longer time ($\theta \approx 1$ in the alternating arrays, and $0.8 < \theta < 1.2$ in the reversed arrays).

Both low- and high-momentum fluid particles have almost the same densities in the reversed arrays ($E(\theta) \approx 15\%$). However, the RTD in region *B* for the reversed arrays is much more spread than the two other reactors, resulting in less homogeneity in mixing different fluids. It should be noted that the particle density in the alternating arrays in region *B* ($E(\theta) \approx 8\%$) is much lower than in region *A* ($E(\theta) \approx 25\%$).

The axial mean velocity distributions in the three configurations are shown in Fig. 10, providing a qualitative interpretation for the bimodal behavior of the RTD. The two regions *A* and *B* identified in Fig. 9(a) and (b) are due to (i) high-momentum particles in the reactor bulk region that are rapidly convected and (ii) low-momentum fluid in the wake of the tabs that reach the reactor outlet later. In the alternating arrays the high axial velocity region takes up more space in the reactor volume, resulting in the high peak in the particle density shown in Fig. 9(a) and (b). This is due to the reduction in the flow cross-section (as shown in Fig. 2) which leads to an increase in the streamwise velocity.

3.6. Power consumption

Fig. 11 assesses the power consumption in the three geometries by comparing the normalized friction factor *Z* of different commercial static mixers, adapted from Thakur et al. [2], on which are superposed the present HEV configurations. The empirical correlations for the three reactors studied here, obtained by curve fitting of the numerical results, are shown in Fig. 11.

In fact, the HEV mixer (aligned arrays here) is known to have the lowest energy consumption among the commercial mixers [9,22]. This fact is also verified by the present results. Compared to the classical HEV geometry, the pressure drop is about 124% higher in the alternating arrays and 143% higher in the reversed arrays. However, the pressure drop in these new configurations is still below that in other commercial static mixers. In fact, greater pressure drop is necessary to achieve better mixing efficiency. However, the additional power consumption caused by the pressure losses in static mixers is much below that required to achieve the same mixing efficiency in agitated vessels, or in turbine vessels where mechanical agitators

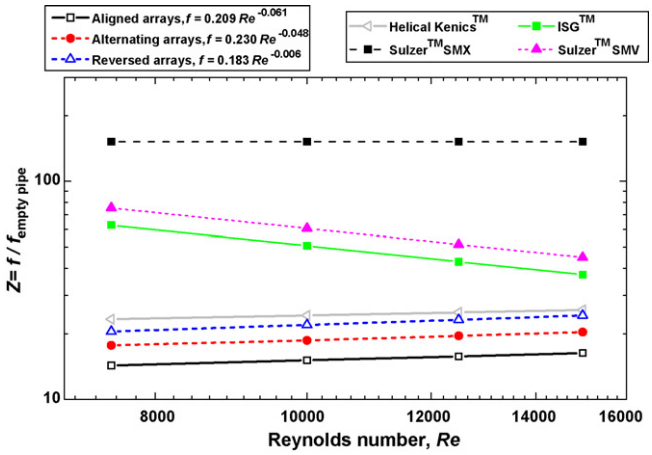

Fig. 11. Normalized friction factors for different commercial reactors and HEV geometries.
Data adapted from Thakur et al. [2].

are used [2]. This figure shows that the Sulzer^{TM} static mixers have the highest pressure drop of the mixers presented; this is caused by the presence of many corrugated plates in SMV and SMX [38].

4. Conclusions

In this study, new configurations of high-efficiency vortex mixers (HEV) in the turbulent regime are studied by CFD simulation. The aim is to identify the tab arrangements that best organize the flow structure for mixing intensification in the heat exchanger/reactors built based on the HEV concept.

The numerical procedure and turbulence model were validated by laser Doppler anemometry measurement of the local turbulent velocity field. The mixing process was characterized by macro-, meso- and micro-mixing, each related to different turbulent flow scales. Local turbulent field properties were used to assess the effects of geometry variation on mixing at different scales: turbulence energy dissipation was used to quantify micro-mixing, turbulence kinetic energy was used to evaluate meso-mixing, and the residence time distribution was used to assess macro-mixing.

Three tab arrangements were studied: classical aligned tab arrays (conventional HEV), alternating tab arrays and reverse tab arrays. We show that the reversed tab arrays give better efficiency in meso- and micro-mixing than the aligned and alternating arrays, but the pressure drop is about 1.4 times higher. The global pressure drop is directly proportional to the turbulence energy dissipation rate, showing that the micro-mixing enhancement is generally accompanied by increased pressure loss.

The computed residence time distribution showed bimodal behavior, suggesting a bypass flow in the three geometries studied. This flow type is due to the simultaneous presence of distinct low- and high-velocity regions: thus there are dead zones behind each tab and a high-velocity flow in the tube center and between the tabs of the same array.

Acknowledgements

C. Habchi would like to acknowledge fruitful discussions with E. Gadoin and H. Mohand Kaci, and also the technical support of J. Delmas for experiments. This work was partially supported by ADEME (Agence de l'Environnement et de la Maîtrise de l'Énergie). Dr. C. Garnier is kindly acknowledged for monitoring this grant.

Appendix A. Nomenclature

D	pipe inside diameter (m)
$E(\theta)$	density (Hz)
f	friction coefficient
$f_{\text{empty pipe}}$	empty pipe friction coefficient
k	turbulence kinetic energy (m^2/s^2)
L	mixer length (m)
l	mesh dimension
Re	Reynolds number
t	residence time (s)
u	fluctuating velocity (m/s)
W	axial mean velocity (m/s)
y^+	distance in wall coordinates
Z	normalized friction factor accession ($=f/f_{\text{empty pipe}}$)

Greek letters

ε	energy dissipation rate (m^2/s^3)
υ	kinematic viscosity
θ	reduced time ($=t/t_m$)

Subscripts

m	mean value
l	local value
i, j	Cartesian directions

References

[1] M. Fiebig, Vortices, generators and heat transfer, Chem. Eng. Res. Des. 76 (1998) 108–123.
[2] R.K. Thakur, C. Vial, K.D.P. Nigam, E.B. Nauman, G. Djelveh, Static mixers in the process industries – a review, Chem. Eng. Res. Des. 81 (2003) 787–826.
[3] S. Ferrouillat, P. Tochon, D. Della Valle, H. Peerhossaini, Open-loop thermal control of exothermal chemical reactions in multifunctional heat exchangers, Int. J. Heat Mass Transf. 49 (2006) 2479–2490.
[4] Z. Anxionnaz, M. Cabassud, C. Gourdon, P. Tochon, Heat exchanger/reactors (HEX reactors): concepts, technologies: state-of-the-art, Chem. Eng. Proc. 47 (2008) 2029–2050.
[5] W.J. Gretta, C.R. Smith, The flow structure and statistics of a passive mixing tab, J. Fluids Eng. 115 (1993) 255–263.
[6] D. Dong, H. Meng, Flow past a trapezoidal tab, J. Fluid Mech. 510 (2004) 219–242.
[7] C. Habchi, T. Lemenand, D. Della Valle, H. Peerhossaini, Alternating mixing tabs in multifunctional heat exchanger–reactor, Chem. Eng. Process. (2009), doi:10.1016/j.cep.2009.07.003.
[8] D Rauline, J.M. Le Blévec, J. Bousquet, P.A. Tanguy, A comparative assessment of the performance of the Kenics and SMX static mixers, Chem. Eng. Res. Des. 78 (2000) 289–296.
[9] T. Lemenand, D. Della Valle, Y. Zellouf, H. Peerhossaini, Droplets formation in turbulent mixing of two immiscible fluids, Int. J. Multiphase Flow 29 (2003) 813–840.
[10] R. Wadley, M.K. Dawson, LIF measurements of blending in static mixers in the turbulent and transitional flow regimes, Chem. Eng. Sci. 60 (2005) 2469–2478.
[11] S. Ferrouillat, P. Tochon, C. Garnier, H. Peerhossaini, Intensification of heat-transfer and mixing in multifunctional heat exchangers by artificially generated streamwise vorticity, Appl. Therm. Eng. 26 (2006) 1820–1829.
[12] S. Ferrouillat, P. Tochon, H. Peerhossaini, Micro-mixing enhancement by turbulence: application to multifunctional heat exchangers, Chem. Eng. Proc. 45 (2006) 633–640.
[13] R.K. Rahmani, T.G. Keith, A. Ayasoufi, Numerical study of the heat transfer rate in a helical static mixer, J. Heat Transf. 128 (2006) 769–783.
[14] A.M. Al Taweel, C. Li, H.G. Goma, P. Yuet, Intensifying mass transfer between immiscible liquids using screen-type static mixers, Chem. Eng. Res. Des. 85 (2007) 760–765.
[15] A. Mokrani, C. Castelain, H. Peerhossaini, Experimental study of the influence of the rows of vortex generators on turbulence structure in a tube, Chem. Eng. Proc. 48 (2009) 659–671.
[16] S. Hirschberg, R. Koubek, F. Moser, J. Schöck, An improvement of the Sulzer SMX™ static mixer significantly reducing the pressure drop, Chem. Eng. Res. Des. 87 (2009) 524–532.
[17] H. Mohand Kaci, T. Lemenand, D. Della Valle, H. Peerhossaini, Enhancement of turbulent mixing by embedded longitudinal vorticity: a numerical study and experimental comparison, in: Proceedings of ASME FEDSM, Miami, Florida, 2006.
[18] J. Baldyga, J.R. Bourne, Turbulent Mixing and Chemical Reactions, Wiley, Chichester, 1999.
[19] J.O. Hinze, Fundamentals of the hydrodynamic mechanism of splitting in dispersion processes, AIChE J. 1 (1955) 289–295.
[20] F.A. Streiff, P. Mathys, T.U. Fischer, New fundamentals for liquid–liquid dispersion using static mixers, Réc. Prog. Gén. Proc. 11 (1997) 307–314.
[21] T. Lemenand, P. Dupont, D. Della Valle, H. Peerhossaini, Turbulent mixing of two immiscible fluids, J. Fluids Eng. 127 (2005) 1132–1139.
[22] Chemineer, Kenics: Static Mixing Technology, Chemineer Inc., 1998, Bulletin 800 (commercial documentation).
[23] H. Mohand Kaci, T. Lemenand, D. Della Valle, H. Peerhossaini, Effects of embedded streamwise vorticity on turbulent mixing, Chem. Eng. Proc. 48 (2009) 1459–1476.
[24] R. Elavarasan, H. Meng, Flow visualization study of role of coherent structures in a tab wake, Fluid Dyn. Res. 27 (2000) 183–197.
[25] W. Yang, H. Meng, J. Sheng, Dynamics of hairpin vortices generated by a mixing tab in a channel flow, Exp. Fluids 30 (2001) 705–722.
[26] FLUENT Inc., FLUENT 6. 3 User's Guide, 2006.
[27] J.T. Barth, D. Jespersen, The design and application of upwind schemes on unstructured meshes, in: Proceedings AIAA 27th Aerospace Sciences Meeting, Reno, Nevada, 1989.
[28] R.F. Warming, R.M. Beam, Upwind second-order difference schemes and applications in unsteady aerodynamic flows, in: Proceedings AIAA 2nd Computational Fluid Dynamics Conference, Hartford, CT, 1975.
[29] S.V. Patankar, D.B. Spalding, A calculation procedure for heat mass and momentum transfer in three-dimensional parabolic flows, Int. J. Heat Mass Transf. 15 (1972) 1787–1806.
[30] B.E. Launder, D.B. Spalding, Lectures in Mathematical Models of Turbulence, Academic Press, London, 1972.
[31] M.M. Gibson, B.E. Launder, Ground effects on pressure fluctuations in the atmospheric boundary layer, J. Fluid Mech. 86 (1978) 491–511.
[32] B.E. Launder, G.J. Reece, W. Rodi, Progress in the development of a Reynolds stress turbulence closure, J. Fluid Mech. 68 (1975) 537–566.
[33] B.E. Launder, Second-moment closure: present. . . and future? Int. J. Heat Fluid Flow 10 (1989) 282–300.
[34] M. Wolfstein, The velocity and temperature distribution of one-dimensional flow with turbulence augmentation and pressure gradient, Int. J. Heat Mass Transf. 12 (1969) 301–318.
[35] H.C. Chen, V.C. Patel, Near-wall turbulence models for complex flows including separation, AIAA J. 26 (1988) 641–648.
[36] J.O. Hinze, Turbulence, 2nd ed., McGraw-Hill, New York, 1975, pp. 223–225.
[37] M.A. Elyyan, D.K. Tafti, A novel split-dimple interrupted fin configuration for heat transfer augmentation, Int. J. Heat Mass Transf. 52 (2009) 1561–1572.
[38] J.E. Visser, P.F. Rozendal, H.W. Hoogstraten, A.A.C.M. Beenackers, Three-dimensional numerical simulation of flow and heat transfer in the Sulzer SMX static mixer, Chem. Eng. J. 54 (1999) 2491–2500.

CORPUS DES ARTICLES

6. Flow structure and heat transfer induced by embedded vorticity

H. Mohand Kaci, **C. Habchi**, T. Lemenand, D. Della Valle, H. Peerhossaini

International Journal of Heat and Mass Transfer 53 (2010) 3575-3584.

International Journal of Heat and Mass Transfer 53 (2010) 3575–3584

Contents lists available at ScienceDirect

International Journal of Heat and Mass Transfer

journal homepage: www.elsevier.com/locate/ijhmt

Flow structure and heat transfer induced by embedded vorticity

Hakim Mohand Kaci [a], Charbel Habchi [a,b], Thierry Lemenand [a], Dominique Della Valle [a], Hassan Peerhossaini [a,*]

[a] Thermofluids, Complex Flows and Energy Research Group, LTN, CNRS UMR 6607, École Polytechnique, University of Nantes, rue Christian Pauc, B.P. 50609, 44306 Nantes, France
[b] Agence de l'Environnement et de la Maîtrise de l'Énergie (ADEME), 20 avenue du Grésillé, B.P. 90406, 49004 Angers, France

ARTICLE INFO

Article history:
Received 16 October 2009
Received in revised form 18 February 2010
Accepted 15 April 2010

Keywords:
Streamwise vortices
Transverse vortices
Heat-transfer intensification
Multifunctional heat exchangers
Three-dimensional numerical simulations

ABSTRACT

Several vortex generator shapes are used to increase heat and mass transfer in open and internal flows. Here we report a three-dimensional numerical study investigating the effects of longitudinal and transverse vortices on the heat and mass transfer mechanisms generated by rows of trapezoidal vortex generators. The turbulent macrostructures of these streamwise vortices appear greatly to enhance radial convective transfer. Due to Kelvin–Helmholtz instability, the shear layer shed from the tab's edge becomes unstable and generates periodic transverse vortices that enhance fluid mixing and heat transfer. A global performance analysis of the high-efficiency vortex (HEV) heat exchanger designed to exploit these embedded vortices, shows that the HEV is very competitive with other multifunctional heat exchangers/reactors, especially due to its very low energy consumption.

1. Introduction

Pressure-driven vortices and flow structures induced by shear instabilities play a crucial role in convective transport phenomena. Two types of vortices can be distinguished in these flows: transverse vortices and longitudinal vortices [1]. Transverse vortices are two-dimensional flows with axes perpendicular to the flow direction, while longitudinal vortices have their axes in the streamwise direction, implying a three-dimensional swirling flow. It has been shown that longitudinal vortices are more efficient in heat-transfer enhancement than transverse vortices because they combine the main mechanisms of heat-transfer enhancement [2]: the development of highly turbulent boundary or shear layers, the reduction of the laminar sublayer thickness near the wall, and the swirl movement of the streamwise vortex that enhances convective transfer.

Such vortices can be readily generated by flow separation behind vortex generators or turbulence promoters (such as transient structures caused by Kelvin–Helmholtz instabilities and counter- or co-rotating vortices caused by pressure differences across the tabs) [1–4], by surface curvature where the centrifugal force produces streamwise vortices (such as Dean and Görtler instabilities) [5–7], and by turbulent or laminar jets (such as ring vortices) [8,9].

In the domain of multifunctional heat exchanger–reactors, baffles and vortex generators can be easily incorporated inside compact channels or into empty pipes to enhance the convective transfer between low- and high-momentum fluids [10–13]. In addition to the vortical structures generated by the vortex generators, shear layers are also formed at the leading and trailing edges, giving raise to Reynolds-averaged energy transport that increases local and global heat transfer. High-velocity fluctuations caused by these shear layers, which can be characterized by the turbulence kinetic energy (TKE), entrain high-temperature fluctuations and can form a self-sustained oscillatory flow when they become unstable. This is the case for instance in the trapezoidal vortex generator, which has been widely studied due to its ability to enhance turbulent mixing and mass transfer with low energy consumption relative to triangular and rectangular wings [14]. When these tabs are fixed at an angle of inclination to channel or tube wall, a pressure difference is generated between the front and back sides of the tab because of the velocity gradient between the low-momentum fluid in the tab wake and the high-momentum fluid in the bulk region, which initiates in its turn a streamwise swirling motion in the form of two longitudinal counter-rotating vortices. Moreover, owing to the Kelvin–Helmholtz instability, the shear layer generated at the tab edges becomes unstable further downstream from the tabs and gives raise to periodic hairpin vortices convecting downstream and riding on the counter-rotating vortex pair (CVP) [4], as shown in Fig. 1a.

To the best of our knowledge, however, there is no data in the open literature concerning the effects of the flow structure downstream of the trapezoidal mixing tabs on the convective heat transfer and temperature distributions. In this paper we report on a numerical study to analyze the effects of the different flow structures on the thermal behavior downstream of several tab arrays

* Corresponding author. Tel.: +33 2 40 68 31 24; fax: +33 2 40 68 31 41.
E-mail address: hassan.peerhossaini@univ-nantes.fr (H. Peerhossaini).

0017-9310/$ - see front matter © 2010 Elsevier Ltd. All rights reserved.
doi:10.1016/j.ijheatmasstransfer.2010.04.029

Nomenclature

D	exchanger diameter (m)
f	friction factor
h	heat-transfer coefficient (W/m^2 K)
I	turbulence intensity
j	colburn factor
k	turbulent kinetic energy (m^2/s^2)
L	exchanger length (m)
Nu	Nusselt number
Pr	Prandtl number
r	radial coordinate (m)
R	tube cross-section radius (m)
Re	Reynolds number
T	temperature (K)
u	local fluctuating velocity (m/s)
U_m	mean flow velocity (m/s)
z	axial coordinate (m)
Greek symbols	
ε	turbulent energy dissipation rate (m^2/s^3)
ΔP	pressure drop (Pa)
ν	kinematic viscosity (m^2/s)
μ	dynamic viscosity (Pa s)
ρ	fluid density (kg/m)
ϕ	heat flux density (W/m)
Subscripts	
m	mean
Exp	experimental
Num	numerical
w	wall

in a circular pipe. The HEV mixer, a static mixer designed to exploit the above vortex structure and manufactured by Chemineer Inc. [15], is composed of several tab arrays inserted in a circular pipe as shown in Fig. 1b. Each array consists of four diametrically opposed trapezoidal vortex generators inclined with respect to the tube wall. The HEV static mixer has shown high efficiency in turbulent mixing and mass transfer with lower energy consumption than other industrial static mixers [15–17].

In the present numerical study (Section 2), the CFD software Fluent 6.3 [18], with a standard $k-\varepsilon$ model [19] associated with a two-layer model, is used to compute the flow in the near-wall region and the three-dimensional flow pattern; we then investigate the effects of these flows on the heat-transfer mechanism downstream of rows of trapezoidal vortex generators in a tube at constant wall temperature. The same numerical method and turbulence model were recently used to study the heat transfer in different complex geometries, and it was shown that the numerical results are in good agreement with experimental ones, even in non-isotropic turbulent flows [20–22]. Hydrodynamic numerical results for the present flow were validated by laser Doppler velocimetry (LDV) and pressure-drop measurements by Mohand Kaci et al. [23]. In Section 3 we show that a counter-rotating vortex pair (CVP) is responsible for convective transfer between the tab wake and the flow core region, while the statistical path of the hairpin-like structures coincides with inflection points in the temperature radial profiles; this suggests that these transient hairpin vortices attenuate the temperature decay from the wall towards the flow core, thus further enhancing the heat-transfer mechanisms.

This paper is organized as follows: in Section 2 the problem description is presented. Results are reported in Section 3 and in Section 4 we draw some conclusions.

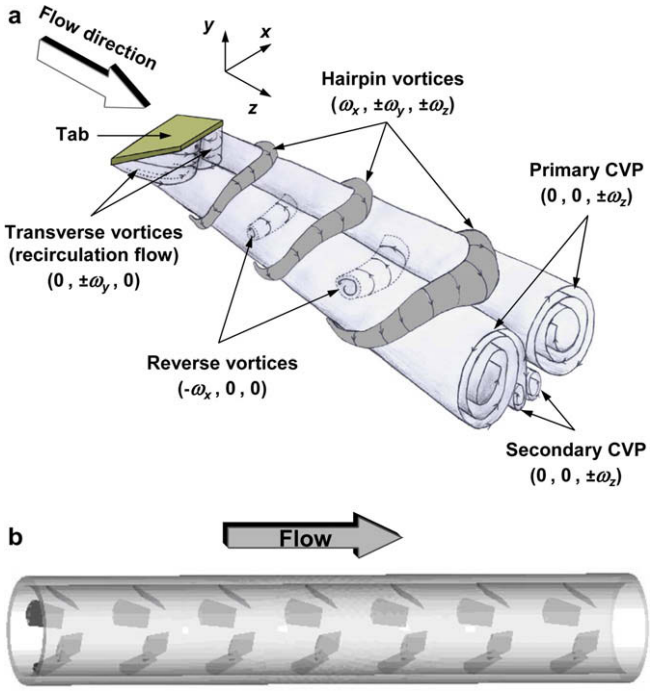

Fig. 1. (a) Different vortices generated behind a tab; and (b) global view of HEV static mixer as vorticity generator.

2. Problem description

2.1. Geometry

The mixer representing the flow geometry is made of a circular tube of 20 mm inner diameter in which seven tab arrays are fixed. Each array is composed of four trapezoidal tabs rotated 90° with respect to one another. The tabs are inclined at 30° relative to the tube wall in the flow direction. The tube is 140 mm long and the distance between two successive tabs rows is 20 mm. More details on the vortex generator dimensions are given in [16,23].

2.2. Governing equations and numerical procedure

The governing equations are the conservation of mass (Eq. (1)) and momentum (Eq. (2)), and the energy equation (Eq. (3)). These equations are solved for a turbulent, incompressible flow of Newtonian fluids, through the Reynolds-averaged Navier–Stokes equations (RANS). The Reynolds stress tensor $\tau_{ij} = -\rho\overline{u_i u_j}$, resulting from the averaging procedure on the non-linear convective terms in the momentum equations, are computed by the Prandtl closure hypothesis with the $k-\varepsilon$ standard model given in Versteeg and Malalasekera [19]. The equations for the turbulence kinetic energy (k) and its dissipation rate (ε) are given in Eqs. (4) and (5), respectively.

$$\frac{\partial \rho}{\partial t} + \frac{\partial}{\partial x_i}(\rho U_i) = 0, \tag{1}$$

$$\frac{\partial(\rho U_i)}{\partial t} + \frac{\partial}{\partial x_i}(\rho U_i U_j) = -\frac{\partial P}{\partial x_i} + \frac{\partial}{\partial x_j}\left[\mu\left(\frac{\partial U_i}{\partial x_j} + \frac{\partial U_j}{\partial x_i} - \delta_{ij}\frac{\partial U_j}{\partial x_i}\right)\right] + \frac{\partial}{\partial x_j}\left(\overline{-\rho u_i u_j}\right), \tag{2}$$

Table 1
Experimental ΔP_{exp} [23] and numerical ΔP_{num} pressure drop.

Reynolds number	ΔP_{num} (Pa)	ΔP_{exp} (Pa)	$\Delta P_{deviation}$ (%)
7500	301.5	287	5.1
10,000	498.4	466	7.0
12,500	766.6	710	8.0
15,000	1086.5	983	10.5

$$\frac{\partial(\rho E)}{\partial t}+\frac{\partial}{\partial x_i}[U_i(\rho E+P)]=\frac{\partial}{\partial x_j}\left(K_{eff}\frac{\upsilon_t}{\sigma_k}\frac{\partial T}{\partial x_j}+\tau_{ij,eff}u_i\right)+S_h, \quad (3)$$

$$\frac{\partial k}{\partial t}+U_i\frac{\partial k}{\partial x_i}=\upsilon_t\left(\frac{\partial U_i}{\partial x_j}+\frac{\partial U_j}{\partial x_i}\right)\frac{\partial U_i}{\partial x_j}+\frac{\partial}{\partial x_i}\left(\frac{\upsilon_t}{\sigma_k}\frac{\partial k}{\partial x_i}\right)-\varepsilon, \quad (4)$$

$$\frac{\partial \varepsilon}{\partial t}+U_i\frac{\partial \varepsilon}{\partial x_i}=C_{\varepsilon 1}\frac{\varepsilon}{k}\upsilon_t\left(\frac{\partial U_i}{\partial x_j}+\frac{\partial U_j}{\partial x_i}\right)\frac{\partial U_i}{\partial x_j}+\frac{\partial}{\partial x_i}\left(\frac{\upsilon_t}{\sigma_\varepsilon}\frac{\partial \varepsilon}{\partial x_i}\right)-C_{\varepsilon 2}\frac{\varepsilon^2}{k}. \quad (5)$$

Water is the working fluid, with physical properties assumed independent of temperature. Flow and heat-transfer simulations were carried out in a steady turbulent flow for Reynolds numbers 7500, 10,000, 12,500 and 15,000 and for constant wall temperature T_w = 360 K.

The solver used for the flow computation is the CFD code Fluent 6.3, which is based on an Eulerian approach to solving the Cauchy equations. The computational mesh is a cell-centered finite volume discretization. The solver options used in the calculations are segregated solver, second-order upwind discretization scheme [24,25], steady, implicit linearization, symmetric space and absolute velocity formulation. Pressure–velocity coupling is achieved by the SIMPLE algorithm. In the segregated approach, the governing equations (for mass, momentum, energy, and additional scalars) are solved sequentially, i.e. separately or segregated. The update is based on the current or initialized solution depending on the iteration run.

To determine an adequate convergence criterion, a series of flow simulations were carried out for stop-criteria values ranging from 10^{-3} to 10^{-9}. Beyond the value 10^{-6}, no significant changes are observed in the velocity field and turbulence quantities, and the value 10^{-6} is retained as the convergence criterion for complete simulations.

The mixer section studied is reduced to a 1/8 sector by symmetry. A non-uniform unstructured mesh is constructed and refined at all solid boundaries (using the software Gambit®), the volume of which grows gradually with distance from the wall. Mesh size is controlled by adjusting the number of the nodes in the radial direction, on the periphery of the element, and on the axial element length.

The solver is run for several mesh densities: the mesh density is increased until no effect on result quality is detected. The criterion for grid sensitivity is based on velocity profiles, turbulence dissipation rate, and friction factor 1.5 mm downstream from the 7th tab. The mesh with lowest node density yielding high-quality results was used to generate and simulate the entire geometry. The appropriate meshing contains 724,174 cells. More details on mesh density validation can be found in [23].

Mohand Kaci et al. [23] have carried out numerical simulations for various turbulence models, coupled standard wall functions (SWF) and two-layer model (TL). Comparison between numerical and experimental results showed clearly that the $k-\varepsilon$ standard turbulence model associated with the TL model wall approach is as accurate, for the HEV flow as more sophisticated and time-consuming models. We thus use the $k-\varepsilon$ standard turbulence model and TL wall approach to simulate the heat transfer

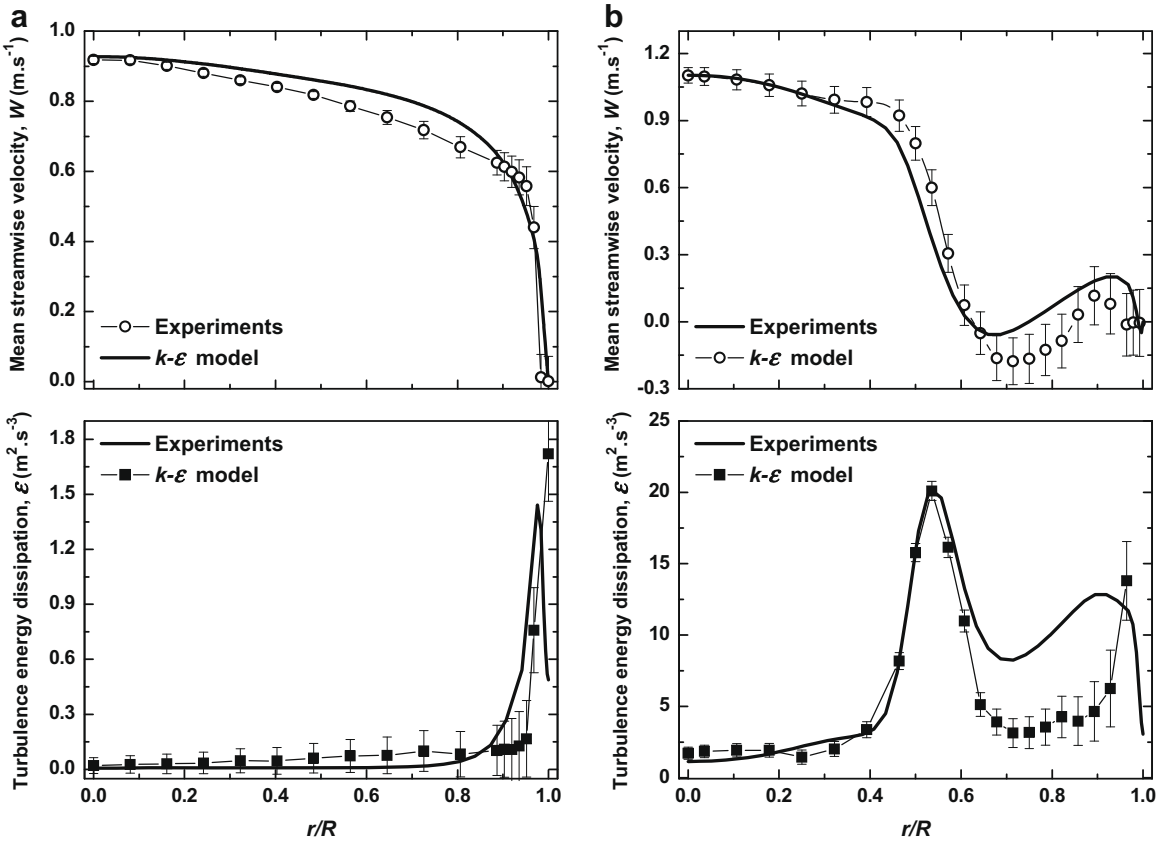

Fig. 2. Radial profiles of axial mean velocity and turbulence energy dissipation rate: (a) at the mixer inlet; and (b) 3 mm downstream from 7th tab, *Re* = 15,000. (Experiments are adapted from Mohand Kaci et al. [23].)

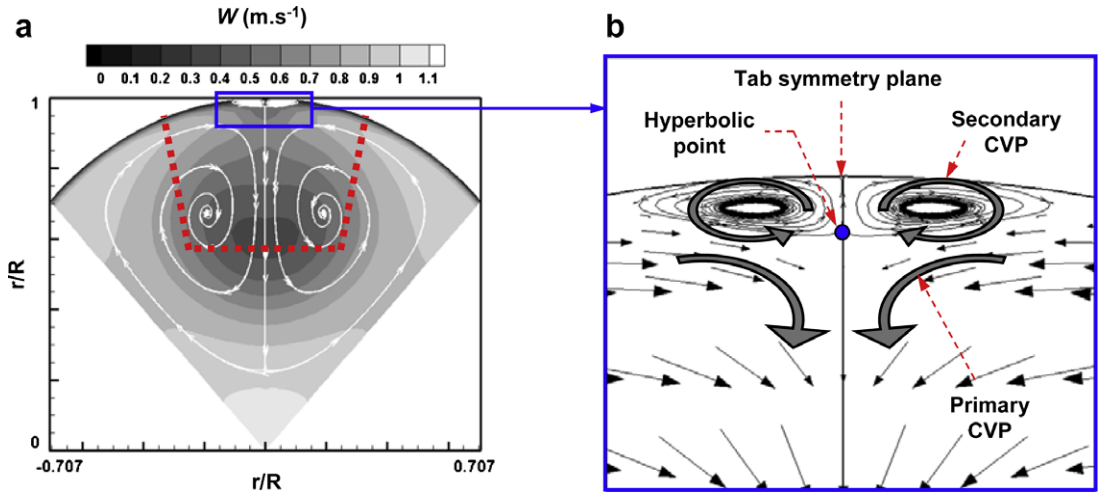

Fig. 3. Streamwise velocity distribution (a) and streamlines (b) in tube cross-section 9 mm downstream from the 4th tabs' tip (Re = 15,000).

in the HEV geometry. The same numerical procedure and turbulence model were used by Ismail et al. [20], Eldrainy et al. [21] and Naphon et al. [22] and numerical results showed good agreement with experimental ones.

The flow in the near-wall region is described by the "two-layer model", where the Navier–Stokes equations are solved in the viscous sublayer. The limit of the viscous boundary layer is determined by the value of the wall Reynolds number:

$$Re_w = \frac{\rho y \sqrt{k}}{\mu}. \tag{6}$$

When $Re_w < 200$, only the transport of the turbulence kinetic energy is computed, and the turbulent dissipation rate is related to the turbulence kinetic energy by the empirical formula [18]:

$$\varepsilon = \frac{k^{3/2}}{\ell_\varepsilon}, \tag{7}$$

where $\ell_\varepsilon = y c_\ell (1 - e^{-Re_w/A_\varepsilon})$, with A_ϵ and c_ℓ constants [18]. No-slip boundary conditions are applied on the tab surfaces and the pipe wall. The temperature is fixed at 360 K on the pipe and tabs walls for all simulations.

The velocity profile for fully turbulent developed pipe flow is used at the HEV inlet. The turbulence kinetic energy and the dissipation rate are given by the turbulence intensity I derived from the empty-tube equilibrium state [26]. The fluid temperature at the inlet is set at 293 K.

3. Results and discussion

3.1. Experimental validation

Since no experimental data are available for the HEV used as heat exchanger, our simulation results are compared to those obtained from LDV isothermal studies of Mohand Kaci et al. [23].

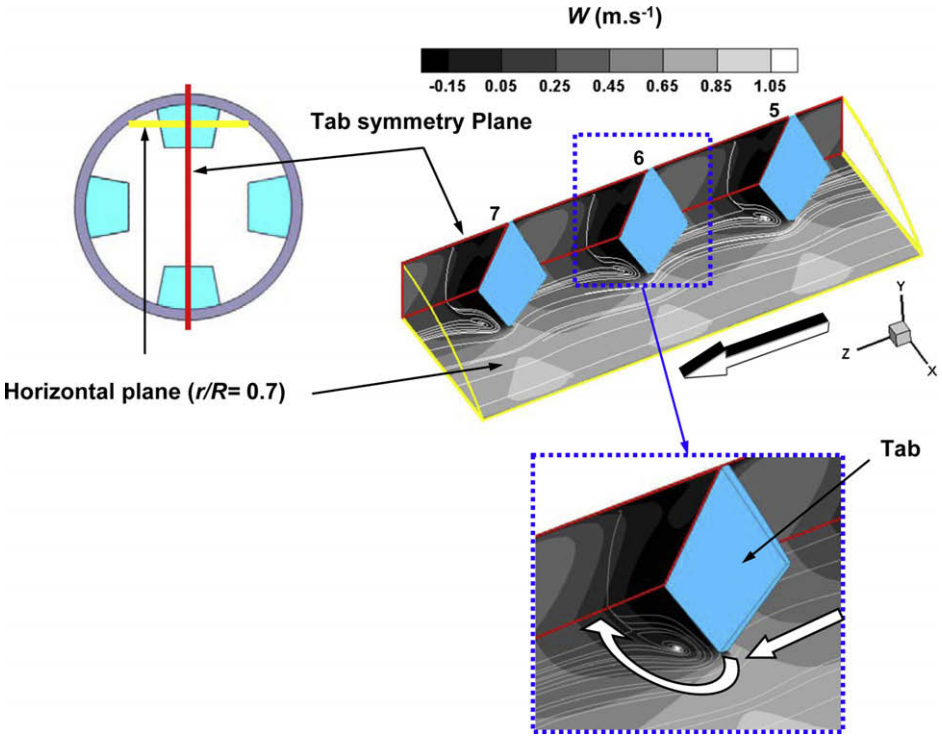

Fig. 4. Streamwise velocity distribution in tab symmetry plane and on horizontal plane located at r/R = 0.7 (Re = 15,000).

The computed pressure drop is also compared to the experimental measurements by a differential manometer in Table 1.

Fig. 2 shows fair agreement between experiments and CFD numerical simulations for the mean velocity and turbulence energy dissipation rate, especially in the bulk region. In the near-wall region, differences arise that can be explained by the difficulty of performing accurate LDV measurement in the wall region, where measurement noise is high [23]. In fact, the turbulence energy dissipation rate was calculated from autocorrelation functions obtained from LDV measurements by using the Taylor hypothesis of frozen turbulence. This hypothesis is not suitable for non-isotropic turbulent flows and hence produces inaccurate values for the turbulence energy dissipation rate. However, fair agreement is shown between experimental and numerical mean velocity profiles. As the temperature distribution and the convective heat-transfer mechanism are controlled by the flow velocity distribution, there will be no significant effect of the disagreement between the experimental and numerical values of ε.

Experimental and numerical values for the pressure drop are compared in Table 1. The deviation between experimental and CFD results ranges between 5% and 10%. The good agreement between numerical and experimental results suggests that the simulations quite fairly describe the hydrodynamics in the HEV static mixer.

3.2. Mean flow structure

Fig. 3, of the mean streamwise velocity distribution, shows that the axial velocity above the tab is greater than that in the wake region; the low-pressure region thus created above the tab initiates a swirling motion that produces two large symmetric counter-rotating vortices. This large motion entrains fluid particle transfer between the low-momentum region in the tab wake and the high-momentum fluid in the core region, thus enhancing convective transfer downstream of the vortex generators. This counter-rotating vortex pair (CVP) is convected downstream with the main flow until it encounters the downstream tab where new CVPs are generated.

Secondary counter-rotating vortices are also observed on both sides of the tab symmetry plane, as shown in Fig. 3. These vortices are caused by the interaction of the high-radial-velocity flow induced by the principal CVP with the stagnant fluid between the wall and the CVP. A hyperbolic point is thus generated at the splitting point of these four vortices. The secondary CVP is convected downstream with the main CVP until the flow encounters the next tab array.

Fig. 4 shows the axial mean velocity distribution on the tab symmetry plane and on a horizontal plane passing thought the tabs at radial position $r/R = 0.7$. From the streamlines here show pressure-driven transverse vortices in the wake of the tabs. Owing to the pressure difference across the tab, the flow detours around the tab edges towards the symmetry plan, creating a stationary transverse vortex-the recirculation flow (see also Fig. 1a).

3.3. Turbulence energy and temperature distribution

Fig. 5a shows the turbulence kinetic energy (TKE) distribution in the tube cross-section 9 mm downstream from the tip of the 4th tab. The maximum TKE values occur in the shear layer shed from the tab tip edge. In fact, high-velocity fluctuations are created in this region due to the velocity gradient between the core flow above the shear layer and the wake region beneath. It has been demonstrated in both experimental PIV [3] and DNS studies [4] that, owing to Kelvin–Helmholtz instability, this shear layer becomes more unstable and generates periodic hairpin-like structures convected downstream with the main CVP, as shown

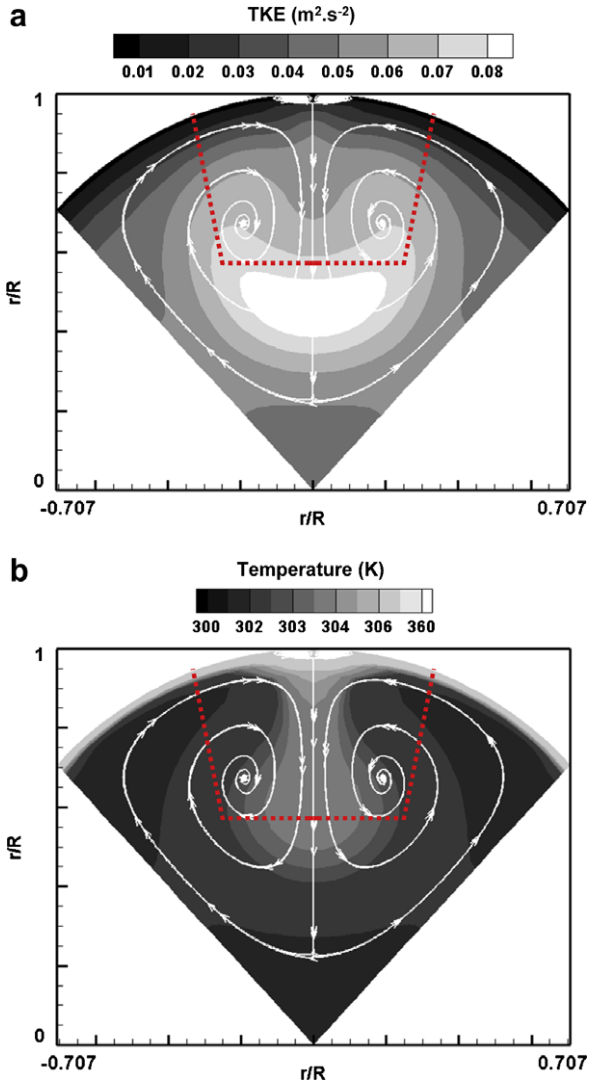

Fig. 5. (a) Turbulence kinetic energy and (b) temperature distribution in tube cross-section 9 mm downstream from 4th tab tip (T_w = 360 K, T_e = 298 K, Re = 15,000).

schematically in Fig. 1a. Since the present work uses steady RANS equations to investigate the effects of the trapezoidal vortex generators on the flow dynamics and heat transfer, the temporal effects of these time-periodic vortices cannot be captured here. However, the averaged effects of these instabilities are detected as inflection points in the axial mean velocity profiles ($\partial^2 W/\partial r^2 = 0$). Meanwhile, it has been shown [3,4] that the hairpin vortex heads coincide with the higher TKE values; this fact can be clearly seen in Fig. 5a, where the higher TKE values form an arc shape at the tip of the vortex generator, confirming that the TKE is carried by the heads of these unsteady transverse vortices.

Fig. 5b represents the temperature contours in a tube-cross section at 9 mm downstream from the 4th tab array. The pair of counter-rotating vortices spirals the flow around its axis and redistributes the heat in the tube cross-section. The common flow in the tab symmetry plane transfers heat from the near-wall hot region to the cold zone at the tube centerline, thus further enhancing the radial heat transfer.

Yang et al. [3] showed that the statistical path of the hairpin heads, which is in the region of high TKE, coincides with the inflection points on the streamwise mean velocity profiles ($\partial^2 W/\partial r^2 = 0$). The distance of the inflection point from the wall is equal to the tab height and increases with distance from the tab trailing edge.

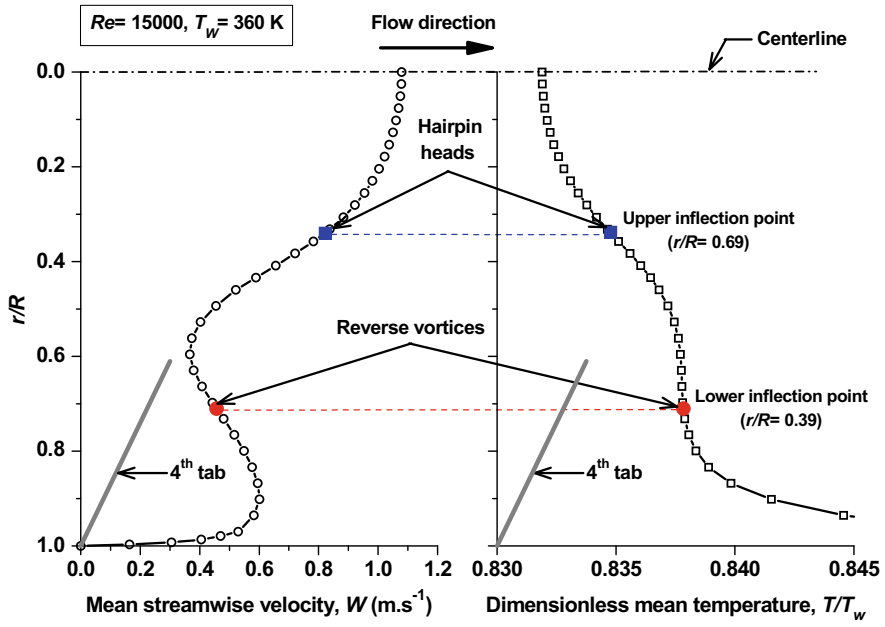

Fig. 6. Effects of primary and secondary vortices on radial profiles of mean axial velocity and mean temperature distribution on radial profiles at 9 mm downstream from the 4th tab tip (T_w = 360 K, T_e = 298 K, Re = 15,000).

Using the same argument, it was determined [3] that the lower inflection points in the axial mean velocity profiles coincide with the statistical path of the *reverse vortices* present in the tab wake. These reverse vortices are due to the interaction between the decelerated flow beneath the hairpin heads and the faster stream further underneath, as interpreted by Yang et al. [3] and Dong and Meng [4] and shown schematically in Fig. 1a.

Hence, by fitting the velocity profile from the present study in Fig. 6 with a high-order polynomial and calculating $\partial^2 W/\partial r^2 = 0$ on the radial velocity profile 9 mm downstream from the tab trailing edge, it was possible to obtain the radial position of the two inflection points and to determine the statistical path of the hairpin heads and reverse vortices. Fig. 6 shows that the inflection points ($\partial^2 W/\partial r^2 = 0$) can also be obtained from the temperature profile ($\partial^2 T/\partial r^2 = 0$). Hence, the averaged effect of the unsteady transverse vortices on the temperature distribution is to attenuate the temperature decay when moving away from the wall by adding high-velocity fluctuations (or TKE), and thus to enhance the convective heat-transfer mechanism.

The effect of the vortex generators on the longitudinal evolution of the TKE and flow temperature is shown in Fig. 7 in the tab symmetry plane. In this figure the turbulent boundary layer developed on the tab front face and then released into the core flow is visible. Once released, this boundary layer is integrated in the free shear layer on the tab tip and enhances mixing, which is carried out by the large-scale eddies of the convective inertial domain of the turbulence energy spectrum. Fig. 7a shows high-TKE values where the flow is detached from the tabs' trailing edge due to the shear layer developed, as in the flow cross-section plane in Fig. 5a. High-TKE values are further pushed to the pipe centerline to increase the mixing process over that in empty pipe turbulent flow.

Fig. 7b is a visualization of the thermal boundary layer (TBL) development. The growth of the TBL is closely linked to the hydrodynamics, and it is clear in the present case that it is controlled by the succession of vortex generators. Each tab row destabilizes the flow and renews the thermal boundary layer, superimposing it on the previous ones. Overheated regions can be observed beneath each tab where the recirculation zones are present, as shown in Fig. 4. In these regions heat is trapped in the stationary transverse

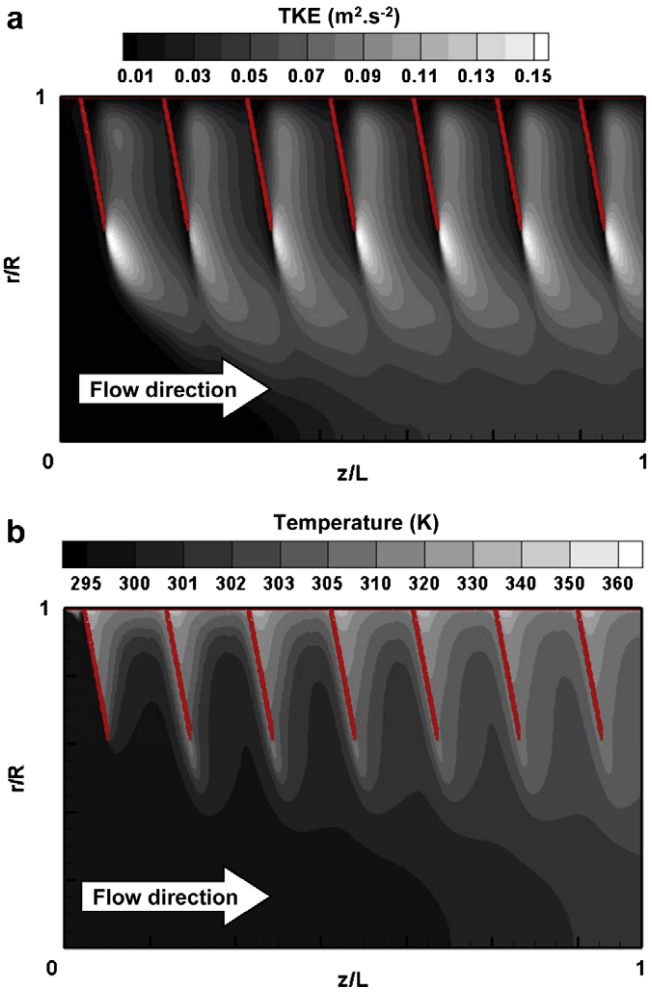

Fig. 7. (a) Turbulence kinetic energy and (b) temperature distribution in tab symmetry plane (T_w = 360 K, T_e = 298 K, Re = 15,000).

vortices (recirculation flow) and can be transported to the surrounding fluid only by diffusion. These overheated regions are undesirable for safety reasons when this device is used for exothermal chemical reactions.

Two longitudinal temperature profiles are presented in Fig. 8, one at a radial distance equal to the tabs' edge ($r/R = 0.61$), the other on the tube axis ($r/R = 0$). Since from here on we study the HEV mixer as a heat exchanger, the tube will henceforth be referred to as a heat exchanger. At the centerline, the overall temperature grows but without reaching the wall temperature. For the first three rows, the temperature on the heat exchanger axis does not vary because the arrival of hot particles in the core is delayed by the radial convection time. Beyond the third tab, however, the temperature starts a steady increase. On the other hand, in the shear region ($r/R = 0.61$) the temperature varies in a periodic way, a signature of the effect of the streamwise vortices. The highest temperature is reached at the top of the tabs, since the tabs are in fact an extension of the tube wall.

3.4. Heat-transfer coefficient

Fig. 9 shows the longitudinal evolution of the heat-transfer coefficient averaged on the cross-sections of the heat exchanger for different Reynolds numbers. The heat-transfer coefficient h is computed from the basic definition:

$$h = \frac{\varphi}{(T_w - T_m)}, \tag{8}$$

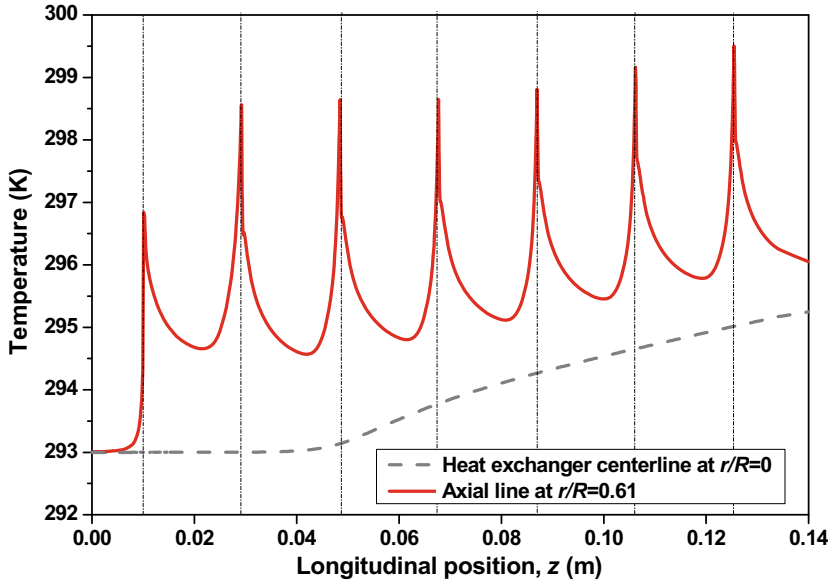

Fig. 8. Axial profile of mean temperature on the heat exchanger centerline ($r/R = 0$) and on an axial line at $r/R = 0.61$, ($T_w = 360$ K, $T_e = 298$ K, $Re = 15{,}000$) (vertical dash-dotted lines show locations of mixing tabs).

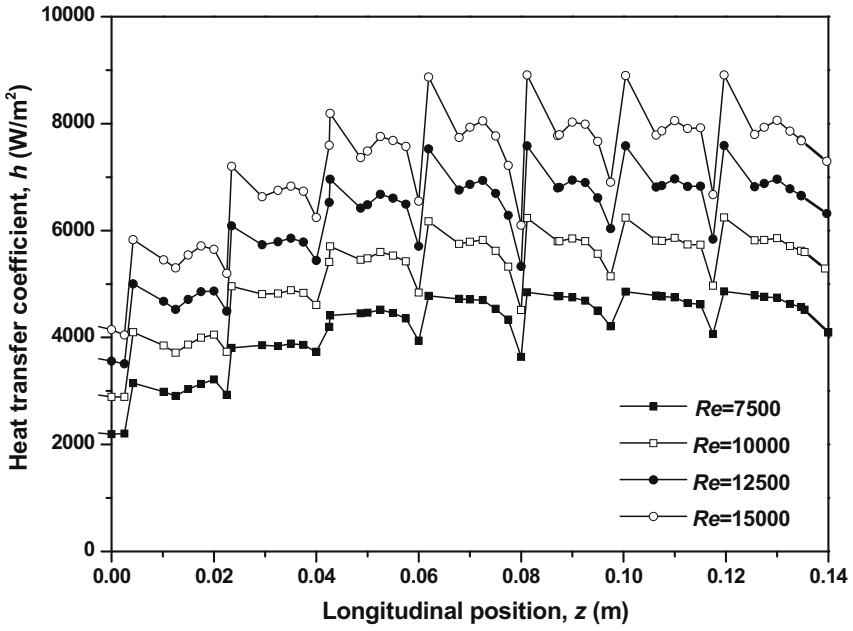

Fig. 9. Axial variation of heat-transfer coefficient in HEV-heat exchanger for different Reynolds numbers ($T_w = 360$ K, $T_e = 298$ K).

where φ is the heat flux and T_m is the mean temperature in the cross-section. This figure shows that h increases by steps at each tab array until the 4th tab, where it stabilizes and has the same variation for the different tabs. Meanwhile, an increase in Re enhances the global h values and yields better convective transfer.

To investigate the effect of the vortex generators and Reynolds number on the evolution of the heat-transfer coefficient, a zoom view of the sixth and 7th tabs arrays is shown in Fig. 10. Maximum h is observed in the near tab's wake, where the recirculation zone (transverse vortex) overheats the fluid. In fact, as h is averaged on the pipe cross-section, the mean temperature is very close to the wall temperature in the overheated zone, leading to a small temperature difference $(T_w - T_m)$ and consequent high h values. Further downstream, h increases due to the presence of the CVP, which enhances radial heat transfer.

3.5. Global analysis and thermal performance

The thermal performance for a heat exchanger is generally modeled by the Nusselt number, which represents the ratio of convective to conductive transfer and is defined as:

$$Nu_D = \frac{hD}{K}, \tag{9}$$

where h is the heat-transfer coefficient and K the thermal conductivity of the working fluid (water in the present study).

The Nusselt number is generally a function of Reynolds and Prandtl numbers through the expression

$$Nu = C\,Re^m\,Pr^n, \tag{10}$$

where C, m and n are constants to be determined in each geometry.

In the present simulations, the temperature dependence of the working fluid is not investigated, but correlations in the literature [27] show that the constant n is usually equal to 0.4 for turbulent flows. Then the plot of $Nu/Pr^{0.4}$ versus Re gives the trend curve for the Nusselt number in HEV-heat exchanger is fitted by:

$$Nu_D = 0.044\ Re^{0.823}\ Pr^{0.4}. \tag{11}$$

Kakac et al. [28] examined a large number of correlations for fully developed turbulent flow in a circular tube and concluded that the Gnielinski [29] equation below (Eq. (12)) describes the available data better than any other over a range of Prandtl number from 0.5 to 200 and Reynolds number from 2300 to 5×10^{-6}:

$$Nu_D = \frac{(f/8)(Re - 1000)Pr}{1 + 12.7(f/8)^{1/2}(Pr^{2/3} - 1)}, \tag{12}$$

where f is the friction factor in empty pipe flow [28]:

$$f = 0.079\,Re^{-0.25}. \tag{13}$$

The pressure drop, or friction factor, determines the energy consumption in the heat exchanger. From the static pressure loss between the entrance and exit of the HEV-heat exchanger, the friction factor can be correlated to the Reynolds number (Table 1) by:

$$f = 0.049\,Re^{-0.147}. \tag{14}$$

The friction factors for the HEV-heat exchanger and other types of heat exchangers (empty pipe of the same length and diameter, Sulzer SMX, Sulzer SMV, V-nozzle turbulators, Helical Kenics and helical coiled tube) are plotted in Fig. 11a. It appears that the pressure losses in the HEV are less than in all other heat exchangers, confirming that this device has the lowest power loss of the industrial heat exchangers.

The Colburn factor j quantifies grossly the ratio of thermal power transferred to the mechanical power consumed, and provides a global ranking criterion for comparing different heat exchangers; i.e., a higher Colburn factor indicates better heat transfer for a given energy consumption:

$$J = \frac{Nu}{Re\,Pr^{1/3}}. \tag{15}$$

Fig. 11b plots the Colburn factor j against Reynolds number for the same set of heat exchangers. The helical Kenics mixer has the best global performance and the HEV mixer is quite near. This figure shows that the HEV-heat exchanger enhances the Nusselt number by 500% over that in a turbulent circular tube flow.

4. Conclusions

Time-averaged turbulent Navier–Stokes and energy equations are solved in a circular tube equipped with trapezoidal tabs

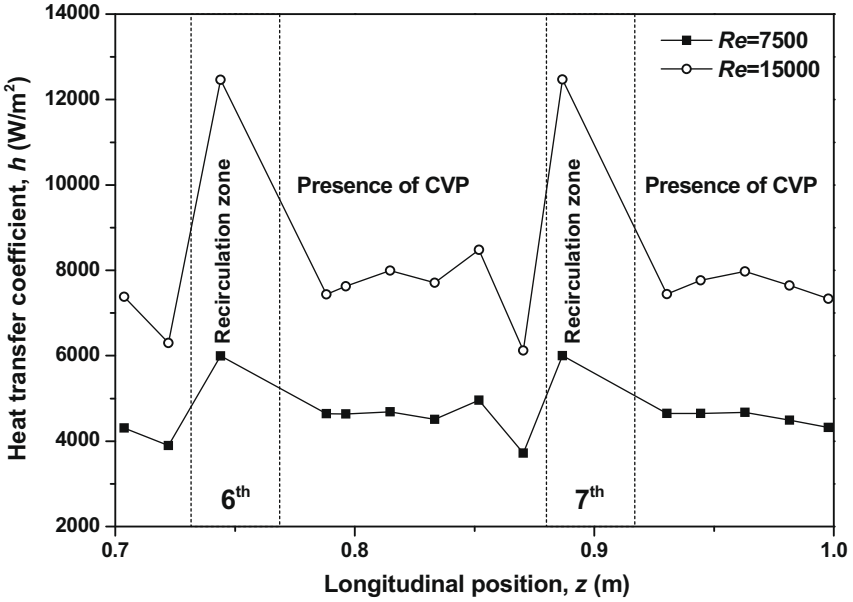

Fig. 10. Longitudinal distribution of heat-transfer coefficient in the sixth and 7th tab arrays for Reynolds numbers 7500 and 15,000 (T_w = 360 K, T_e = 298 K).

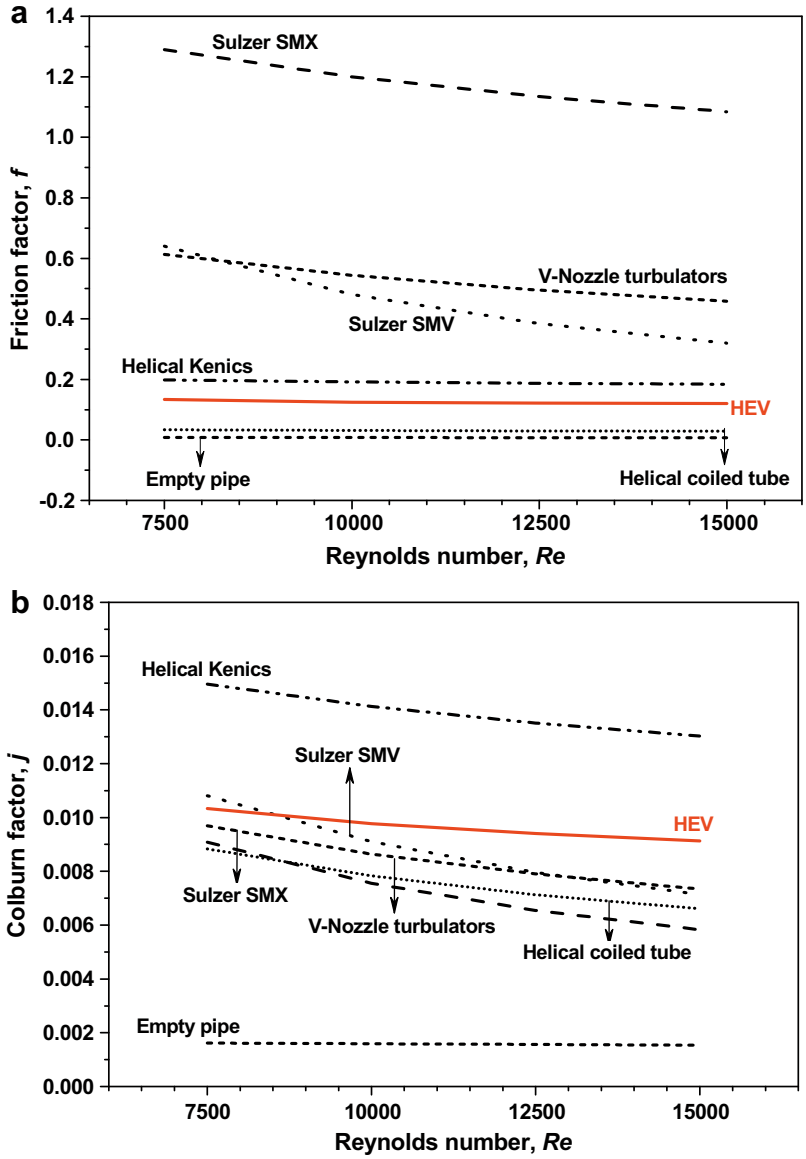

Fig. 11. (a) Friction factor and (b) Colburn factor for commercial heat exchangers in turbulent regime. *Source:* partially adapted from Thakhur et al. (2003).

designed to generate longitudinal and transverse vortices. It is shown that in such a geometry three types of vortices are generated that provide longitudinal and transverse vorticity (ω_z) in the flow: counter-rotating vortex pairs (CVP), which provide longitudinal vorticity in the flow, hairpin vortices produced by Kelvin–Helmholtz instability on the tip of the vortex generator, which introduce mainly a transverse vorticity parallel to the wall (ω_x), and flow recirculation behind the tabs, inducing transverse vorticity normal to the wall (ω_y). The aim of this work is to study the global effects of these vortices on the heat transfer from a tube wall maintained at a constant temperature. From the application point of view, the geometry examined here is also particularly interesting for use as a multifunctional heat exchanger, called here a HEV-heat exchanger.

The numerical study performed here lets us analyze the intensification mechanisms from knowledge of the flow pattern and evaluate the thermal performance of the HEV-heat exchanger. The heat-transfer intensification is attributed mainly to the counter-rotating longitudinal vortex pairs, which transport heat in the radial direction while being convected downstream.

The free shear-layer detached from the tip of the vortex generators (tabs) is the site of high-turbulence kinetic energy production. Kelvin–Helmholtz instability in this layer generates hairpin vortices whose statistical path coincides with the high-TKE concentration zone. The signature of this zone appears as an inflection point in both the mean streamwise velocity and mean temperature profiles. The averaged effects of the hairpin vortices are to produce a more uniform temperature distribution in the tube cross-section and also to intensify heat transfer from the tube wall to the core flow. In the streamwise direction, the fluid temperature at the height of the tab tips oscillates spatially; it is maximal in the transverse vortex zone behind the tabs. Since the temperature of the tab tip is in fact very close to the wall temperature, this injects heat in the core flow.

The overall heat-transfer enhancement, as described in the expression for the Nusselt number, shows faster growth with Reynolds number and 500% heat-transfer intensification than in turbulent empty pipe flow.

The Colburn factor for the HEV-heat exchanger has been shown to be higher than that for most of the commercial devices.

Compared to an empty tube of the same length and the same diameter, to Sulzer SMX, Sulzer SMV, V-nozzle turbulators and the helical coiled tube, the HEV-heat exchanger provides better heat-transfer performance for moderate turbulence. The HEV-heat exchanger appears to be slightly less efficient than the helical Kenics in the Reynolds number range studied. However, an important advantage of the HEV-heat exchanger is that its simple geometry does not require complicated manufacturing processes. The HEV-heat exchanger can hence be described as an "intensified geometry". With its ability to enhance heat transfer substantially, to reduce film buildup, to provide a more uniform temperature distribution in the flow field, and to prevent local heating or cooling, the HEV-heat exchanger can be considered a competitive heat exchanger.

Some aspects of the HEV-heat exchanger are not yet fully developed, such as its macro and micro mixing properties. Future experimental work will aim to characterize its potential as a reactor for fast chemical reactions, so that it can qualify as a multifunctional heat exchanger [30–32]. Also the knowledge of the heat and momentum transfer mechanisms in similar situations such as wall bounded flows should help the understanding transfer phenomena in HEV [33–35].

References

[1] M. Fiebig, Embedded vortices in internal flow: heat transfer and pressure loss enhancement, Int. J. Heat Fluid Flow 16 (1995) 376–388.
[2] M. Fiebig, Vortices, generators and heat transfer, IChemE 76 (A) (1998) 108–123.
[3] W. Yang, H. Meng, J. Sheng, Dynamics of hairpin vortices generated by a mixing tab in a channel flow, Exp. Fluids 30 (2001) 705–722.
[4] D. Dong, H. Meng, Flow past a trapezoidal tab, J. Fluid Mech. 510 (2004) 219–242.
[5] C. Habchi, T. Lemenand, D. Della Valle, H. Peerhossaini, Liquid/liquid dispersion in a chaotic advection flow, Int. J. Multiphase Flow 35 (2009) 485–497.
[6] L. Momayez, P. Dupont, H. Peerhossaini, Some unexpected effects of wavelength and perturbation strength on heat transfer enhancement by Görtler instability, Int. J. Heat Mass Transfer 47 (2004) 3783–3795.
[7] L. Momayez, P. Dupont, G. Delacourt, O. Lottin, H. Peerhossaini, Genetic algorithm based correlations for heat transfer calculation on concave surfaces, Appl. Therm. Eng. 29 (2009) 3476–3481.
[8] T.H. New, K.M.K. Lim, H.M. Tsai, Vortical structures in a laminar V-notched indeterminate-origin jet, Phys. Fluids 17 (2005) 054108. can '054108' be right?.
[9] R. Schwarze, J. Klostermann, C. Brücker, Experimental and numerical investigations of a turbulent round jet into a cavity, Int. J. Heat Fluid Flow 29 (2008) 1258–1267.
[10] A.M. Jacobi, R.K. Shah, Heat transfer surface enhancement through the use of longitudinal vortices: a review of recent progress, Exp. Therm. Fluid Sci. 11 (1995) 295–309.
[11] R.K. Rahmani, T.G. Keith, A. Ayasoufi, Numerical simulation of turbulent flow in an industrial helical static mixer, Int. J. Numer. Methods Heat Fluid Flow 18 (2008) 675–696.
[12] M.H. Nasiruddin, S. Kamran, Heat transfer augmentation in a heat exchanger tube using a baffle, Int. J. Heat Fluid Flow 28 (2007) 318–328.
[13] H. Hemida, F. Spehr, S. Krajnovic, Local heat transfer enhancement around a matrix of wall-mounted cubes using passive flow control: large-eddy simulations, Int. J. Heat Fluid Flow 29 (2008) 1258–1267.
[14] W.J. Gretta, C.R. Smith, The flow structure and statistics of a passive mixing tab, J. Fluid Eng. 115 (1993) 255–263.
[15] Chemineer, Kenics: Static Mixing Technology, Chemineer Inc., Bulletin 800 (commercial documentation), 1998.
[16] C. Habchi, T. Lemenand, D. Della Valle, H. Peerhossaini, Alternating mixing tabs in multifunctional heat exchanger–reactor, Chem. Eng. Process., in press, doi:10.1016/j.cep.2009.07.003.
[17] T. Lemenand, D. Della Valle, Y. Zellouf, H. Peerhossaini, Droplets formation in turbulent mixing of two immiscible fluids, Int. J. Multiphase Flow 29 (2003) 813–840.
[18] FLUENT, Inc., FLUENT 6.3 User's Guide, 2006.
[19] H.K. Versteeg, W. Malalasekera, An Introduction to Computational Fluid Dynamics: The Finite Volume Method, Prentice Hall, New York, 1995.
[20] S.L. Ismail, C. Ranganayakul, R.K. Shah, Numerical study of flow patterns of compact plate-fin heat exchangers and generation of design data for offset and wavy fins, Int. J. Heat Mass Transfer 52 (2009) 3972–3983.
[21] Y.A. Eldrainy, K.M. Saqr, H.S. Aly, M.N. Mohd Jaafar, CFD insight of the flow dynamics in a novel swirler for gas turbine combustors, Int. Commun. Heat Mass Transfer 36 (9) (2009) 936–941.
[22] P. Naphon, S. Ratchaneekorn, J. Kurujareon, Heat transfer and flow characteristics in the hard disk drive tester, Int. Commun. Heat Mass Transfer 36 (8) (2009) 820–826.
[23] H. Mohand Kaci, T. Lemenand, D. Della Valle, H. Peerhossaini, Effects of embedded streamwise vorticity on turbulent mixing, Chem. Eng. Process. 48 (2009) 1457–1474.
[24] R.F. Warming, R.M. Beam, Upwind second-order difference schemes and applications in unsteady aerodynamic flows, in: Proceedings of the AIAA 2nd Computational Fluid Dynamics Conference, Hartford, CT, 1975.
[25] J.T. Barth, D. Jespersen, The design and application of upwind schemes on unstructured meshes, in: AIAA 27th Aerospace Sciences Meeting, Reno, Nevada, Technical Report AIAA-89-0366, 1989.
[26] J.O. Hinze, Turbulence, second ed., McGraw-Hill, New York, 1975.
[27] R.K. Thakur, C. Vial, K.D.P. Nigam, E.B. Nauman, G. Djelveh, Static mixers in the process industries – a review, Trans. IChemE 81 (2003) 787–826.
[28] S. Kakac, R.K. Shah, W. Aung, Handbook of Single-Phase Convective Heat Transfer, John Wiley and Sons, New York, 1987.
[29] V. Gnielinski, New equations for heat and mass transfer in turbulent pipe and channel flow, Int. Chem. Eng. 16 (1976) 359–368.
[30] S. Ferrouillat, P. Tochon, D. Della Valle, H. Peerhossaini, Open-loop thermal control of exothermal chemical reactions in multifunctional heat exchangers, Int. J. Heat Mass Transfer 49 (2006) 2479–2490.
[31] S. Ferrouillat, P. Tochon, C. Garnier, H. Peerhossaini, Intensification of heat transfer and mixing in multifunctional heat exchangers by artificially generated stream-wise vorticity, Appl. Therm. Eng. 26 (2006) 1820–1829.
[32] S. Ferrouillat, P. Tochon, H. Peerhossaini, Micro-mixing enhancement by turbulence: application to multifunctional heat exchangers, Chem. Eng. Process. 45 (2006) 633–640.
[33] R. Toé, A. Ajakh, H. Peerhossaini, Heat transfer enhancement by Görtler instability, Int. J. Heat Fluid Flow 23 (2002) 194–204.
[34] A. Ajakh, M.D. Kestoras, R. Toé, H. Peerhossaini, Influence of forced perturbations in the stagnation region on Görtler instability, AIAA J. 37 (1999) 1572–1577.
[35] H. Peerhossaini, F. Bahri, On the spectral distribution of the modes in non-linear Görtler instability, Exp. Therm. Fluid Sci. 16 (1998) 195–208.

CORPUS DES ARTICLES

7. Entropy production and synergy field principle in turbulent vortical flows

C. Habchi, T. Lemenand, D. Della Valle, H. Peerhossaini

International Journal of Thermal Science, Submitted (THESCI-D-10-00581), 2010f

SUBMITTED TO

International Journal of Thermal Science
THESCI-D-10-00581

Entropy production and synergy field principle in turbulent vortical flows

Charbel Habchi[1,2], Thierry Lemenand[1], Dominique Della Valle[1,3] and Hassan Peerhossaini[1,*]

[1] *Thermofluids, Complex Flows and Energy Research Group, LTN, CNRS UMR 6607, École Polytechnique – University of Nantes, rue Christian Pauc, B.P. 50609, 44306 Nantes, France*

[2] *Agence de l'Environnement et de la Maîtrise de l'Énergie (ADEME), 20 avenue du Grésillé, B.P. 90406, 49004 Angers, France*

[3] *ONIRIS Géraudière, BP 82225, 44322 Nantes, France*

ABSTRACT

The heat transfer in turbulent vortical flows is investigated by three different physical approaches. Vortical structures are generated by inclined baffles in a turbulent pipe flow, of three different configurations. In the first, the vortex generators are aligned and inclined in the flow direction (called the *reference geometry*); in the second, a periodic 45° rotation is applied to the tab arrays (*alternating geometry*); the third is the reference geometry used in the direction opposite to the flow (*reversed geometry*). The effect of the flow structure on the temperature distribution in these different configurations is analyzed. The conventional approach based on heat-transfer analysis using the Nusselt number and the enhancement factor is used to determine the efficiency of these geometries relative to other heat exchangers in the literature.

The effect of vorticity on the Nusselt number is clearly demonstrated, and so as to highlight the respective roles of the coherent structures and the turbulence, a new parameter is defined as the ratio of the *vortex circulation* to the *turbulent viscosity*. The relative contribution of the radial convection to heat transfer appears to increase with Reynolds number. The effect of mixing performance on the temperature distribution is investigated by the *synergy field* method. A global parameter, namely the intersection angle between the velocity and temperature gradient, is defined in order to compare performances. Finally, an analysis of energetic efficiency by entropy production, involving both heat transfer and pressure losses, is carried out to determine the overall performance of the heat exchangers.

All these approaches lead to the same conclusion: that the reversed geometry presents the best heat transfer coefficient and the best energetic efficiency. The reference geometry shows the worst performance, and the alternating array has intermediate performance.

Keywords: streamwise vorticity; synergy field; entropy production; turbulence; multifunctional heat exchanger/reactor; vortex circulation; convective heat transfer.

* Corresponding author: H. Peerhossaini
Phone: + (33)-2-40683124, Fax: + (33)-2-40683141
E-mail address: hassan.peerhossaini@univ-nantes.fr

1. Introduction

Forced heat transfer in the turbulent regime is generally controlled by the convective motion of large-scale eddies that appear essentially as transverse and longitudinal vorticity (Fiebig, 1995; Jacobi and Shah, 1995). These embedded flow structures, which can be generated by shear instabilities or pressure gradients, play a crucial role in the heat- and mass-transfer mechanisms. The pattern of these vortices in the flow has a decisive impact on the hydrodynamic and thermal performance of thermal devices used in industrial applications (Peerhossaini and Bahri, 1998; Ajakh *et al.*, 1999; Toe *et al.*, 2002; Ferrouillat *et al.*, 2006; Aider *et al.*, 2010; Habchi *et al.*, 2009a, 2009b; Lögdberg *et al.*, 2010; Lemenand *et al.*, 2010). A physical understanding of this impact is a fundamental issue in optimizing the energetic efficiency of multifunctional heat exchangers-reactors (MHER) for Green Process Engineering (Anxionnaz *et al.*, 2008).

Several approaches have been used to investigate the heat-transfer mechanisms in the presence of longitudinal vortices in turbulent flow: global approaches using the Nusselt number and an enhancement factor, and also more advanced approaches involving i) the vortex circulation, ii) the synergy field principle, iii) entropy production, as described below. In the present work, vortices are produced by using three different vortex generator positions in a turbulent pipe flow: the vortex generators are aligned, alternating, or reversed. The global approach is based on the determination of the Nusselt number, which characterizes the convective heat transfer in the flow, and the friction factor, which determines pressure losses. The enhancement factor is defined as the ratio of the convective heat transfer coefficient of the straight-pipe flow over that of the current geometry (Promvonge and Thianpong, 2008; Rahimi *et al.*, 2009). This parameter allows comparison of the efficiency of different heat exchangers for the same power consumption.

The intensity of the secondary flow produced by the vortex generators, especially the streamwise vorticity (Fiebig, 1995), has a direct impact on the heat-transfer process. It is now well established that the circulation of the streamwise vortices is significantly correlated with the Nusselt number (Sohankar, 2007; Chang *et al.*, 2009; Tian *et al.*, 2009). However, the vortex circulation characterizes only the convective contribution of the longitudinal vortices and does not account for the fine-grained turbulent structures in the flow. These turbulent structures, which can be characterized by the turbulence kinetic energy (TKE), also play an important role in the heat-transfer mechanism (Elyan *et al.*, 2009). Hence, a new parameter is defined here to assess the relative effect of the vortex circulation and the turbulent viscosity.

Recently, Guo *et al.* (1998) proposed a new concept for analyzing the convective heat-transfer mechanism based on the combined effects of the temperature gradients and velocity vector and is therefore called the "*synergy field principle*". It was shown by Guo *et al.* (1998, 2005) and Tao *et al.* (2002a, 2002b) that heat-transfer enhancement is related to the angles between the streamlines and the isotherms and to the fullness of the dimensionless velocity and temperature profiles. This concept is similar to the alignment of scalar gradients with strain eigenvectors proposed by Lapeyre *et al.* (1999), which can be used to study two- dimensional flows, as in the alignment dynamics of the temperature gradient in Bénard-Von Kármán vortex flow behind a cylinder (Garcia *et al.*, 2005). The synergy field principle can be used for three-dimensional flows, especially in the design and optimization of MHER (Tao *et al.*, 2002a, 2002b; Wu and Tao, 2008a, 2008b). The convective heat-transfer intensification seems to increase with reduction of the intersection angle between the velocity and temperature gradient, and this configuration is the most favorable to produce uniform velocity and temperature profiles in the flow cross sections. This feature is confirmed in this study; a global parameter defined as "the average value of the intersection angle" in the cross section is useful in classifying the thermal efficiency of the different geometries.

The analysis of the entropy production (Bejan, 1996; Kock and Herwing, 2004, 2005), characterizing the amount of the available work in the flow characterizes the overall performance of a MHER by accounting for the heat transfers and pressure losses. Minimizing entropy production

provides greater heat-transfer rates and smaller friction factors (Jacobi and Shah, 1995), since less available work is lost in the thermal device. This approach appears to be pertinent in assessing heat-transfer enhancement in different MHER (Kock and Herwig, 2005; Herpe *et al.*, 2009). In the present study, the entropy production is determined by the model equations developed by Kock and Herwig (2004, 2005).

The present study investigates the influence of the vorticity rearrangement on heat transfer by using the approaches described above in the three flow configurations presented in section 2. The procedure for the numerical simulations, performed using the CFD code Fluent® 6.3, is detailed in section 3. The numerical results are validated and discussed in section 4, followed by a description of the different approaches. The main conclusions are stated in section 5.

2. Flow configurations

The three geometries are based on an empty straight pipe equipped with trapezoidal vortex generators, namely a HEV (High Efficiency Vortex) mixer (Chemineer, 2008). The HEV static mixer, studied previously as a mixer and heat exchanger (Lemenand *et al.*, 2003, 2005, 2010; Habchi *et al.*, 2009b; Mohand Kaci *et al.*, 2010), shows high efficiency compared to other geometries, especially due to its low energy consumption. In the present work the inner pipe diameter is 20 mm and seven tab arrays, each composed of four vortex generators diametrically opposed and inclined to the wall at a 30° angle, are placed along the 140 mm of the mixer length. More details on the tab geometry are given in Mohand Kaci *et al.* (2009). The three different configurations of the static mixer are shown in Fig. 1. In configuration (a), the tabs are fixed to the wall and inclined at 30° in the flow direction (*reference geometry*). In configuration (b), the arrays in the reference geometry are alternately shifted by 45° (*alternating geometry*). Configuration (c) is similar to configuration (a) but the flow direction is reversed compared to the reference configuration (*reversed geometry*).

Downstream from each vortex generator, a counter-rotating vortex pair (CVP) is generated due to the pressure difference between the two sides of the tab surfaces (Gretta and Smith, 1993; Dong and Meng, 2004). The CVP generated in the aligned arrays (Fig. 1 (a)) and in the alternating arrays (Fig. 1 (b)) produce a common outflow in the tab symmetry plane, from the wall towards the centerline, but the reversed arrays (Fig. 1 (c)) generate a common inflow from the centerline towards the wall (Habchi *et al.*, 2009b, 2010).

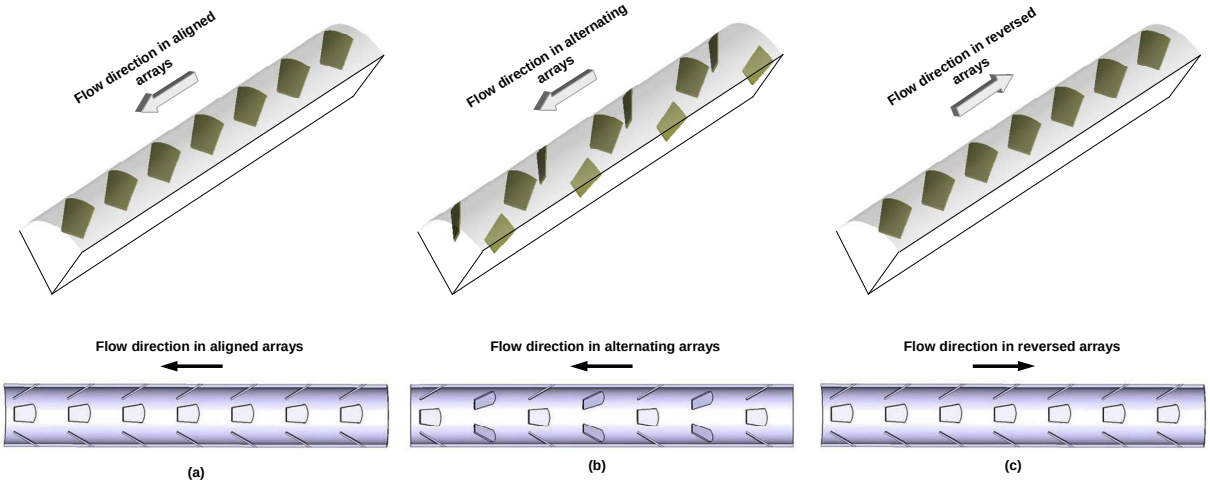

Fig. 1. 3D views and longitudinal sections of the geometries studied: (a) aligned, (b) alternating arrays, (c) reversed arrays

3. Numerical procedure

3.1. Solver and turbulence models

The numerical simulations are carried out using the CFD code Fluent® 6.3. The continuity equations for mass and momentum and the energy equation are solved sequentially with double precision (Barth and Jespersen, 1989), segregated and with second-order accuracy (Warming and Beam, 1975). Pressure-velocity coupling is performed by finite volumes with the SIMPLE algorithm (Patankar and Spalding, 1972).

Mohand Kaci *et al.* (2009) tested five different turbulence models for the flow dynamics in the HEV mixer with aligned arrays, and concluded that the standard $k-\varepsilon$ (Launder and Spalding, 1974; Versteeg and Malalasekera, 1995) and the RSM models (Launder *et al.*, 1975; Gibson and Launder, 1978; Launder, 1989), associated with a two-layer model to compute the wall region, give a satisfactory description of the flow pattern.

The two-layer model involves solving, in the viscous sublayer $\left(y^+ < 5\right)$, the one-equation model of Wolfstein (1969), namely the turbulent kinetic energy transport equation where the turbulent viscosity and energy dissipation are computed from empirical correlations based on length scales (Chen and Patel, 1988). The two-layer model avoids the use of empirical wall standard functions, which are not valid for three-dimensional complex flows. In the present study, the RSM model is used concomitantly with the $k-\varepsilon$ model to simulate the hydrodynamics and heat transfer in the three geometries.

The viscosity and thermal conductivity of the water are assumed piecewise linear functions of temperature, as proposed by Rahmani *et al.* (2006) using data from Lienhard IV and Lienhard V (2008). The specific heat and density, nearly constant for the temperature range, are set respectively at 4182 J kg^{-1} K^{-1} and 998 kg/m^3. The thermal conductivity of the tab is taken as constant (100 W m^{-1} K^{-1}).

3.2. Boundary and operating conditions

No-slip boundary conditions are applied at the solid surface of the tabs and at the pipe wall. Most of the simulations are done with a Dirichlet condition for the temperature at the wall $T_w = 360$ K. Heat conduction in the tab thickness is accounted for by the coupled option of the two-sided wall model, while the tabs are in contact on each side with the fluid.

At the computational domain inlet, a fully developed turbulent flow velocity profile is imposed; the TKE and the turbulence energy dissipation rate are fixed by the turbulence intensity I of the equilibrium turbulent tube flow (Hinze, 1975). The fluid temperature at the inlet is 298.15 K. Flow and heat-transfer simulations are carried out in a steady turbulent flow for Reynolds numbers in the range [7500, 15000].

3.3. Meshing and accuracy of the numerical solution

All three geometries are reduced to a 1/8 sector by axial symmetry. A non-uniform unstructured three-dimensional mesh with hexahedral volumes is built and refined at all solid boundaries using the software Gambit®. Mesh size is controlled by adjusting the number of nodes in the radial direction, on the tube periphery and the vortex generators, and on their axial length.

In each of the three geometries, the mesh density is increased until no effect on the quality of the result is detected, i.e., until the relative difference between the numerical results for two consecutive mesh densities does not exceed 1%. The criterion for grid sensitivity is based on velocity profiles, turbulence dissipation rate, and temperature profile in a location defined by the tab symmetry plane at the outlet. The mesh with the lowest density yielding high-quality results is used to generate and simulate the entire geometry. More details on the meshing can be found in Mohand

Kaci *et al.* (2009). The final mesh size is 695,178 for the aligned arrays, 724,174 for alternating arrays and 723,778 for reversed arrays.

The maximum value of the size of the wall cell y_c^+ is less than 2.2 in the three geometries, complying with the condition $y^+ < 4$, so that the viscous sublayer is properly modeled. Moreover, the more restrictive criterion of Defraeye *et al.* (2010) suggesting that the dimensionless wall normal distance y^* must be in the range 30-500 is also fulfilled, since the maximum value of y^* is found in the aligned arrays to be $y^*_{max} = 18.92$, for the alternating arrays $y^*_{max} = 18.48$ and for reversed arrays $y^*_{max} = 16.99$. Here the dimensionless wall distances y^+ and y^* are respectively obtained from $y^+ = u_* y / \upsilon$ and $y^* = C_\mu^{1/4} \kappa^{1/2} y / \upsilon$, where u_* is the friction velocity, y the distance to the nearest wall, υ the kinematic viscosity, $C_\mu = 0.09$ a constant used in the $k-\varepsilon$ model and $\kappa = 0.42$ the von Karman constant.

Series of simulations are carried out with stop-criteria values ranging from 10^{-3} to 10^{-9}. It is found that beyond the convergence criterion 10^{-6}, no significant changes are observed in the temperature field and turbulence quantities, and this 10^{-6} value is retained for the simulations.

To check the numerical accuracy, the global turbulence energy dissipation rate $\bar{\varepsilon}$, averaged on the whole volume of each geometry, is compared to that obtained from pressure drop expression:

$$\bar{\varepsilon} = \frac{W_m \Delta P}{\rho L} \tag{1}$$

with W_m the mean flow velocity, ΔP the pressure drop between the inlet and the outlet, ρ the fluid density and L the test section length. Results are in good agreement with a relative difference that does not exceed 10^{-4} for the three geometries.

3.4. Hydrodynamics validation

The numerical simulations of the hydrodynamic field with the $k-\varepsilon$ and the RSM models are compared with the experimental results of Habchi *et al.* (2010) using laser Doppler anemometry (LDA). Velocity profiles at the outlet in the tab symmetry plane for the three geometries are presented in Fig. 2 (a). The two turbulent models are in good agreement, and they model the experimental data quite well. Fig. 2 (b) presents the turbulence kinetic energy dissipation rate in the three geometries for the same cross section. It is observed that both turbulence models reproduce the experimental results well, especially in the flow core $(0 < r/R < 0.4)$ and in the shear region $(0.4 < r/R < 0.7)$. In the wake region, near the wall, the numerical results move slightly away from the experiments. This can be partly attributed to the relative inaccuracy of the experimental values in this region: the mean axial velocity is close to zero (recirculation flow), which enhances the noise in the LDV measurements, as reported in Habchi *et al.* (2010). On the other hand, the low convective velocity weakens the validity of the Taylor hypothesis of "frozen turbulence" necessary to compute ε.

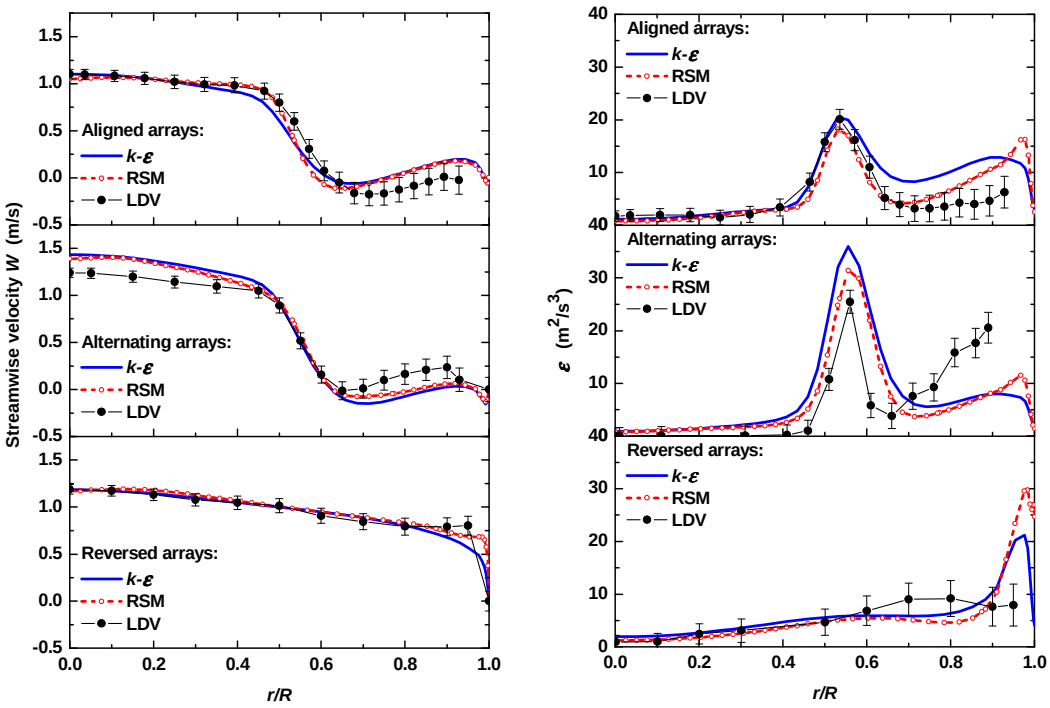

(a) (b)

Fig. 2. Numerical and experimental radial profiles at the outlet for the three geometries in the tab symmetry plane of (a) streamwise velocity and (b) turbulence energy dissipation rate for *Re*= 15000 (experiments adapted from Habchi *et al.* (2010))

4. Results and discussion

4.1. Flow pattern and temperature field description

Here the flow structures induced by the vortex generators and their effects on the temperature distribution are discussed. Flow charts and contours are shown for Reynolds number 15000. The temperature distribution combined with the velocity vector field and the flow streamlines are presented in Fig. 3 on a cross section at the outlet of the three geometries. The network of streamlines clearly indicates the presence of primary and secondary longitudinal vortices (inside the red squares), namely CVPs, that have been fully described in Habchi *et al.* (2010) and Le and Papavassiliou (2009). In Fig. 3 (a) and 3 (b), it can be observed that the CVPs rotate in the same direction in both aligned and alternating arrays since the vortex generators have the same inclination. The common outflow, in the tab symmetry plan, ejects hot fluid from the near-wall region towards the flow core, forming high-temperature ??strikes?? that contribute to the heat transfer by convective transport of the CVPs. The secondary CVPs have opposite vorticity and then a common inflow that reduces the heat pumping from the wall. In the reversed arrays in Fig 3 (c), the pressure gradient generating the primary CVP is reversed and so is the sense of rotation of the CVPs. In this case, the vortex generators induce a common outflow in the tab symmetry plane, from the flow core towards the wall. The primary CVP centers in the reversed arrays are more diverted from one another than in the aligned and alternating arrays, where the CVP centers stay within the limit of the tab. The secondary CVPs are located on the sides and generate a common inflow that reduces the convective transport of the common outflow, as in the aligned and alternating arrays.

The effect of the common out- and inflows on momentum transfer can be quantified by the convective term T_C in the transport equation for the TKE:

$$T_C = -\vec{U}.\vec{\nabla}k \tag{2}$$

with $\vec{U}$ the velocity vector and k the turbulence kinetic energy.

The radial component of T_C is computed in the tab symmetry plane at the outlet of the channels and corresponds to the common out- and inflows. It is observed that the average magnitude of T_C in the alternating array $\left(T_{C,alt} \approx 1.35\times10^{-2}\ \text{m}^2\text{s}^{-3}\right)$ is much greater than that in the aligned arrays $\left(T_{C,alg} \approx 6.34\times10^{-4}\ \text{m}^2\text{s}^{-3}\right)$, leading thus to an estimate of improved radial convective transport in the alternating configuration than the aligned geometry. The intensity of convective transport for the common out- and inflows in reversed arrays is greater than in the two other geometries $\left(T_{C,rev} \approx 3.24\times10^{-2}\ \text{m}^2\text{s}^{-3}\right)$, so the radial convective transport in the reversed configuration is much improved over the other two geometries.

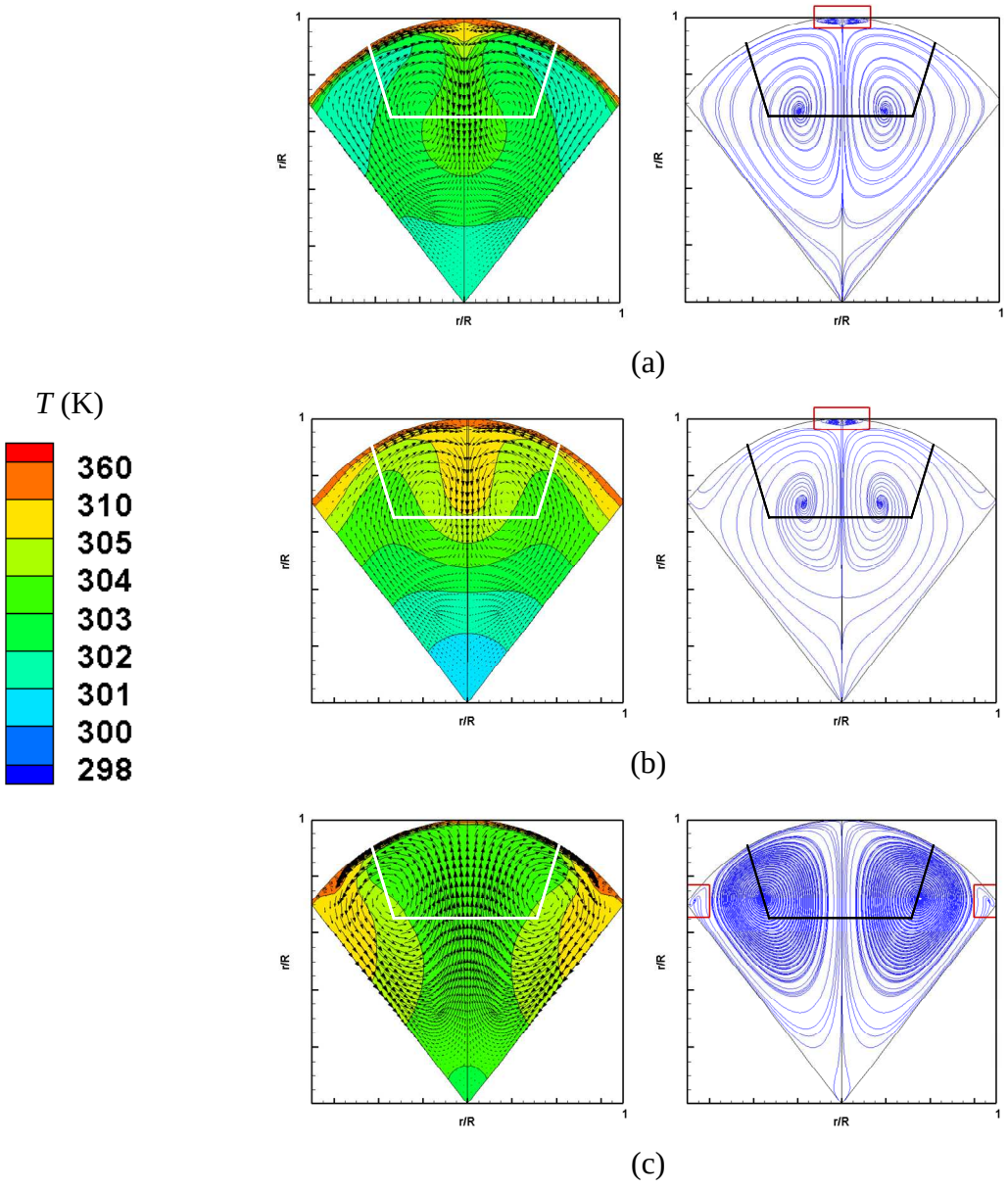

Fig. 3. Temperature distribution and velocity field (left) and streamlines (right) at the outlet cross section of the (a) aligned, (b) alternating, and (c) reversed arrays, *Re*= 15000

The side-view cross-section temperature contours in Fig. 4 (a) and (b) indicate that the temperature distribution is similar in the aligned and alternating arrays: the thermal boundary layer is renewed by each passage over a tab, and an overheated region is observed directly behind the tab in the wake region. This can be explained by the side view in Fig. 5 (a) and (b) at radial distance $r/R=0.8$, where the recirculation flow is observed directly behind the tabs. These transverse vortices are stagnant flows that trap heat and always have negative effects on performance. Fig. 4 (a) and (b) show clearly that, in the alternating geometry, the flow impacts the tab sharply and is instantaneously redirectd to the shear region where the streamlines are denser, while in aligned arrays, the flow is smoothly oriented towards the shear region. This process increases the velocity gradients in the alternating arrays and generates more energetic shear layers characterized by higher TKE and dissipation rates relative to the aligned arrays (Habchi *et al.*, 2009b). This can be observed in Fig. 2 (b): the TKE dissipation rates in the alternating geometry in the shear region for $0.4<r/R<0.7$ are above that in the aligned configuration. The temperature distribution and flow pattern are strongly modified in the reversed array. As seen in Fig. 4 (c), the overheated regions behind the tabs do not form because of the absence of any recirculation flow behind the vortex generators (see Fig. 5 (c)), and moreover the temperature distribution is more homogeneous in this transverse plane. Fig. 4 (d) represents the temperature distribution in the diametral symmetry plan corresponding to the common outflow in the reversed array, illustrating the effect of the efficient renewal of the thermal boundary layer.

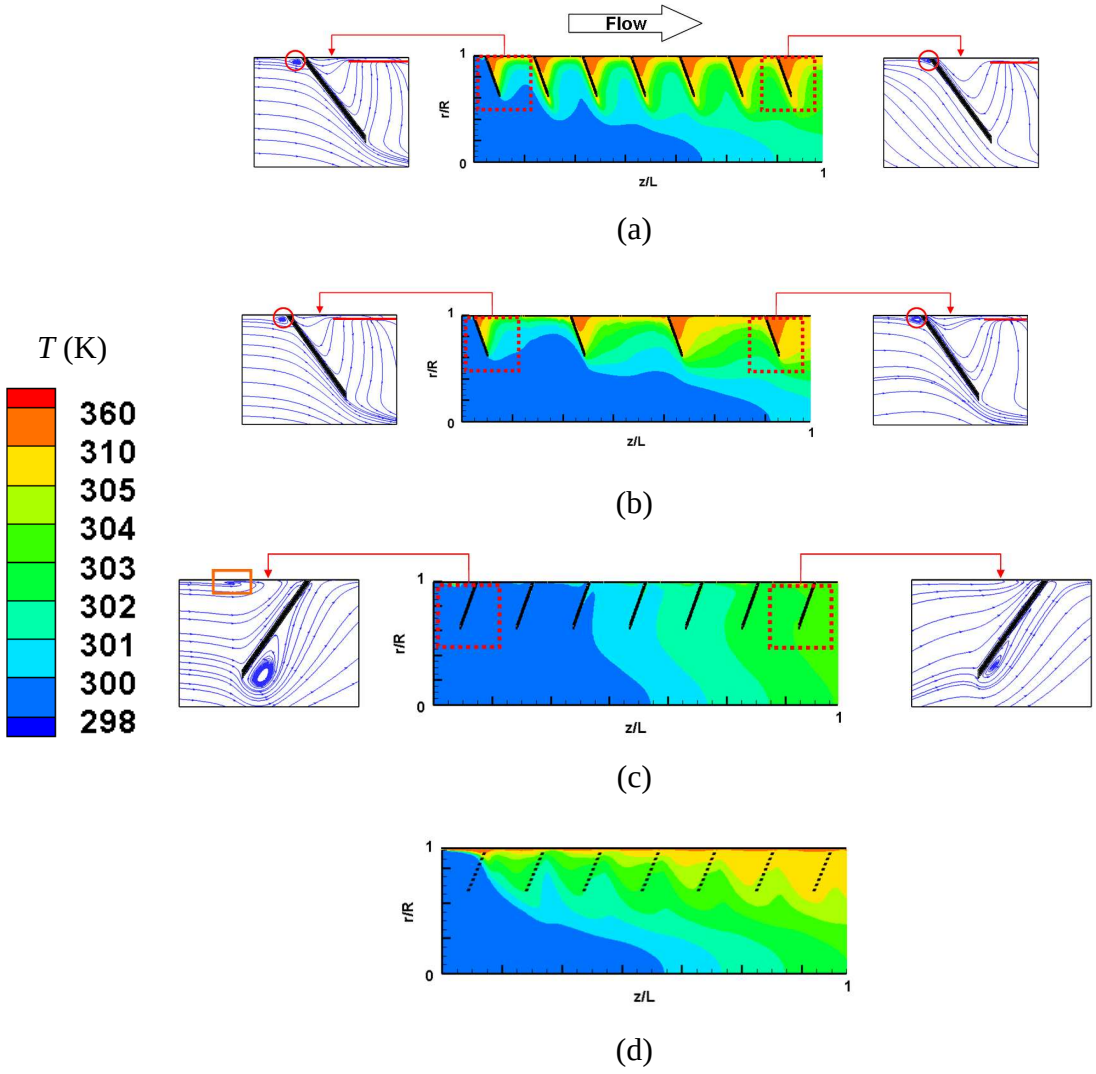

Fig. 4 Flow structure and temperature distribution in tab symmetry plane of (a) aligned, (b) alternating, (c) reversed arrays, and (d) in the axial section between two tabs of reversed array, for Re= 15000

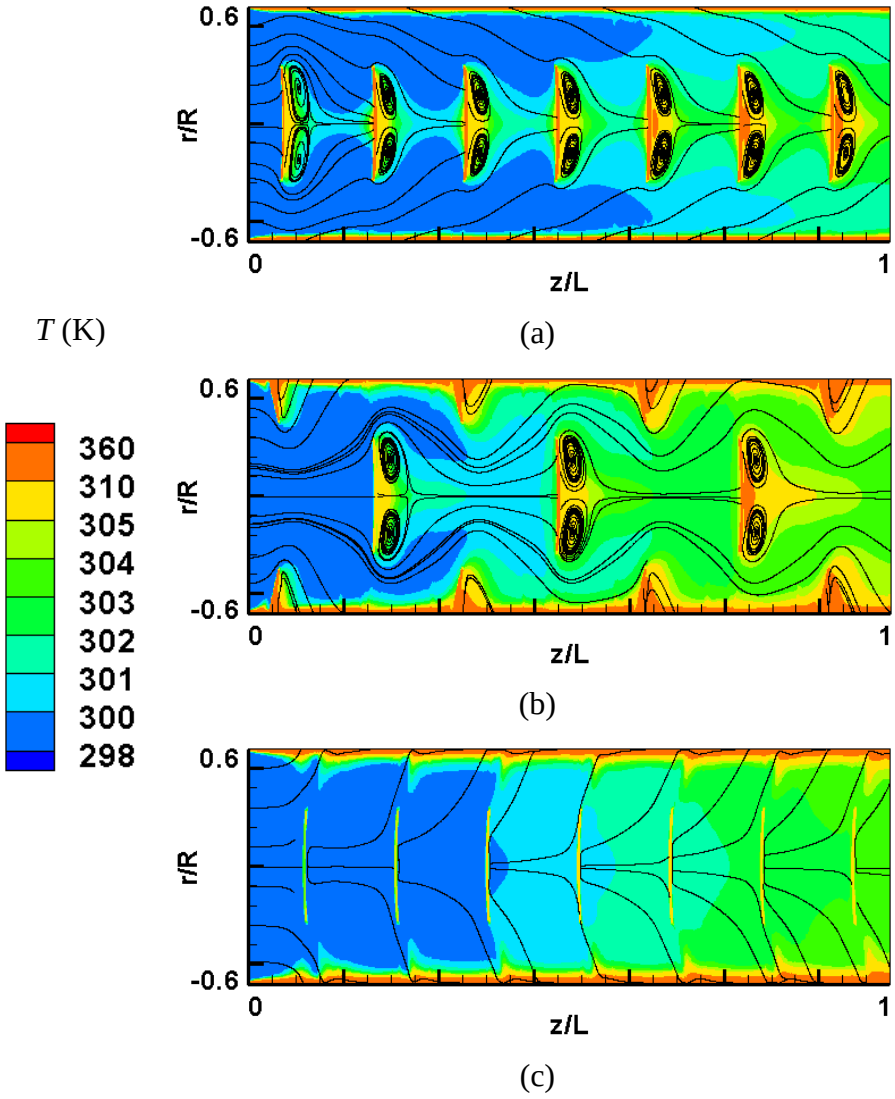

Fig. 5. Flow pattern and temperature field in a cross section at $r/R = 0.8$ for (a) aligned, (b) alternating and (c) reversed arrays, $Re = 15000$

4.2. Heat transfer efficiency

The Nusselt number Nu is computed by a user-defined function (UDF) along the flow direction as:

$$Nu = \frac{h\,D}{\lambda} = \frac{\varphi\,D}{\lambda\left(T_w - T_{b,z}\right)} \tag{3}$$

where h is the local convective heat transfer coefficient, λ the thermal conductivity of the working fluid (water here) and φ the heat flux density computed from the heat balance:

$$\varphi = \frac{\dot{m}\,c_p}{\pi\,D}\left(\frac{dT_{b,z}}{dz}\right) \tag{4}$$

with $\dot{m}$ the mass flow rate and $T_{b,z}$ the bulk temperatures on the cross sections of axial coordinate z.

This local Nusselt number is normalized by the corresponding Nusselt number for a straight turbulent pipe flow Nu_0. Kakac *et al.* (1987) examined a large number of correlations for fully developed turbulent flow in a circular tube and concluded that the Gnielinski (1976) equation (Eq. (5)) agrees with the available data better than any other expression over a range of Prandtl numbers from 0.5 to 200 and Reynolds numbers from 2300 to 5×10^6:

$$Nu_0 = \frac{(f_0/8)}{1+12.7(f_0/8)^{1/2}} \frac{Pr}{\left(Pr^{2/3}-1\right)} (Re-1000) \tag{5}$$

where f_0 is the friction factor in straight-pipe flow following the Blasius formula:

$$f_0 = 0.079\, Re^{-0.25} \tag{6}$$

It can be seen in Fig. 6 that the longitudinal evolution of the normalized Nusselt number Nu/Nu_0 in the three geometries is spatially periodic due to the tab arrays intervals. When the three configurations are classified by Nusselt number, the reversed-arrays configuration appears to be thermally most efficient: $Nu_{rev} > Nu_{alt} > Nu_{alg}$. The intensification is about tenfold with respect to the straight-pipe flow. In all flow configurations, the Nusselt number starts to increase from the leading edge of the tab, due to the generation of the secondary flow, and continues to decrease.

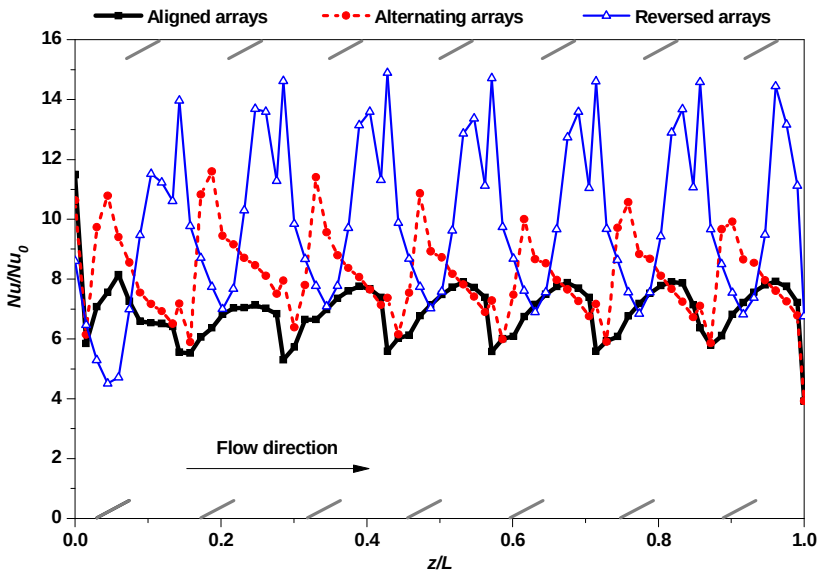

Fig. 6. Longitudinal evolution of normalized Nusselt number in the three geometries, $Re = 15000$. The positions of the vortex generators are shown on the x-axis for aligned and alternating configurations and on the top for the reversed configuration

The global friction factor in the three geometries is obtained by computing:

$$f = \frac{2}{L/D} \frac{\Delta P}{\rho W_m^2} \tag{7}$$

where ΔP is the pressure drop between the two ends of the test section.

Correlations expressing the friction factor of the three geometries are given in Table 1. The reversed arrays have the highest friction factor of the three flow configurations and the aligned arrays show the smaller pressure drop. The variation of f with Reynolds number in the three geometries is almost constant relative to that in the straight pipe flow.

The global Nusselt number can be obtained from the following equation:

$$Nu = \frac{\dot{m} c_p}{\pi L \lambda} \frac{T_{b,outlet} - T_{b,inlet}}{T_w - T_{mean}} \tag{8}$$

where $T_{mean} = \left(T_{b,inlet} + T_{b,outlet}\right)/2$.

Fig. 7 plots the global Nusselt numbers obtained from Eq. (8) for the three configurations compared to that in a straight pipe flow (Eq. (5)) for Reynolds numbers between 7500 and 15000: it is observed that the global Nusselt number in the reversed arrays is greater than that in the two other geometries. The trend slope of Nu versus Reynolds number is the same for the three configurations. The correlations for the global Nusselt number of the three geometries are presented in Table 1, after fixing the evolution of the Prandtl number at $Pr^{0.4}$ so as to obtain the same slope $Re^{2/3}$ in the three configurations.

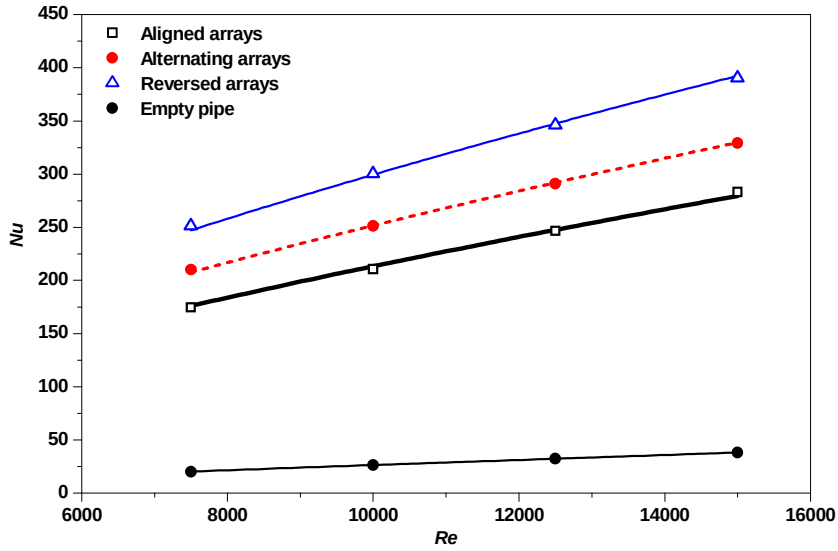

Fig. 7. Nusselt number versus Reynolds number for the three geometries and for the empty pipe

Empty pipe	Aligned arrays
$f_0 = 0.079\,Re^{-0.25}$	$f_{alg} = 0.858\,Re^{-0.057}$
$Nu_0 = \dfrac{(f_0/8)}{1+12.7(f_0/8)^{1/2}} \dfrac{Pr}{(Pr^{2/3}-1)}(Re-1000)$	$Nu_{alg} = 0.232\,Re^{2/3}\,Pr^{0.4}$
$\chi_0 = 0$	$\chi_{alg} = 63.2\,Re^{1/3}$

Alternating arrays	Reversed arrays
$f_{alt} = 0.948\,Re^{-0.047}$	$f_{rev} = 0.761\,Re^{-0.004}$
$Nu_{alt} = 0.274\,Re^{2/3}\,Pr^{0.4}$	$Nu_{rev} = 0.326\,Re^{2/3}\,Pr^{0.4}$
$\chi_{alt} = 68.5\,Re^{1/3}$	$\chi_{rev} = 88.5\,Re^{1/3}$

Table 1: Correlations of the friction factor, Nusselt number and parameter χ in the three geometries

To compare the efficiency of these three configurations for constant pumping power, a thermal enhancement factor η is used: it is the ratio of the convective heat transfer h to that in a straight pipe flow h_0, defined as (Promvonge and Thianpong, 2008; Rahimi *et al.*, 2009)

$$\eta = \left(\frac{Nu}{Nu_0}\right)\left(\frac{f}{f_0}\right)^{-1/3} \tag{9}$$

It is observed in Fig. 8 that η is always greater than unity, between 1.8 and 2.8 for these operating conditions. The enhancement factor tends to decrease with Reynolds number, meaning that the vortex generators play a larger role in the thermal enhancement for small Reynolds numbers. The enhancement factor η for the reversed arrays is 27% higher than for the aligned arrays and 12% higher than for the alternating arrays. The present values of η are much higher than the other data in the literature, which range between 0.5 and 1.5 (Promvonge and Thianpong, 2008; Rahimi *et al.*, 2009).

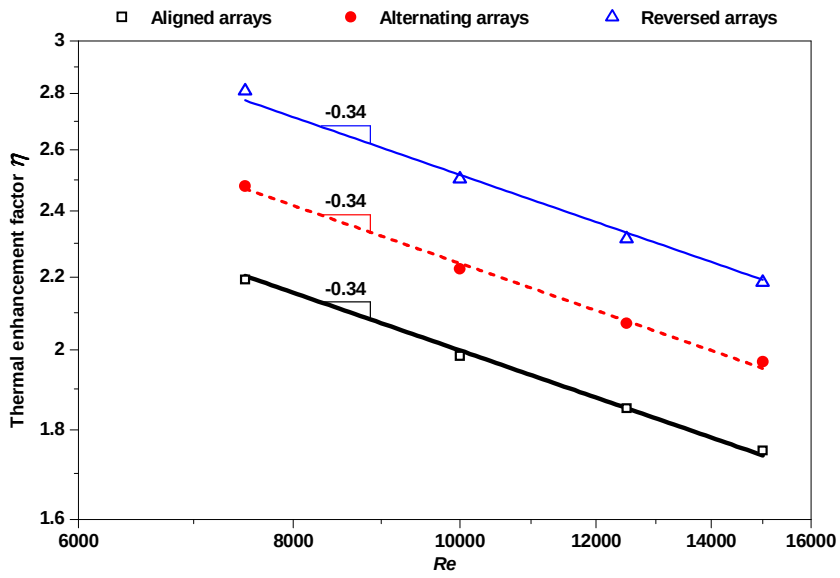

Fig. 8. Thermal enhancement factor versus Reynolds number

The Nusselt number is plotted in Fig. 9 versus the power dissipation and compared to some mixer-heat exchange geometries commonly used in the industry for the same Reynolds number interval, $7500 < Re < 15000$. The straight-pipe flow presents the lowest Nusselt number and power dissipation, since there are no inserts in the flow volume. The Helical Kenics^{TM} has almost the same performance as the aligned configuration. The intensification is improved in the alternating arrays configuration, and even more in the reversed arrays configuration, with negligible increase in power consumption. The other eight geometries exhibit a lower Nusselt number with power dissipation which varies over two orders of magnitude.

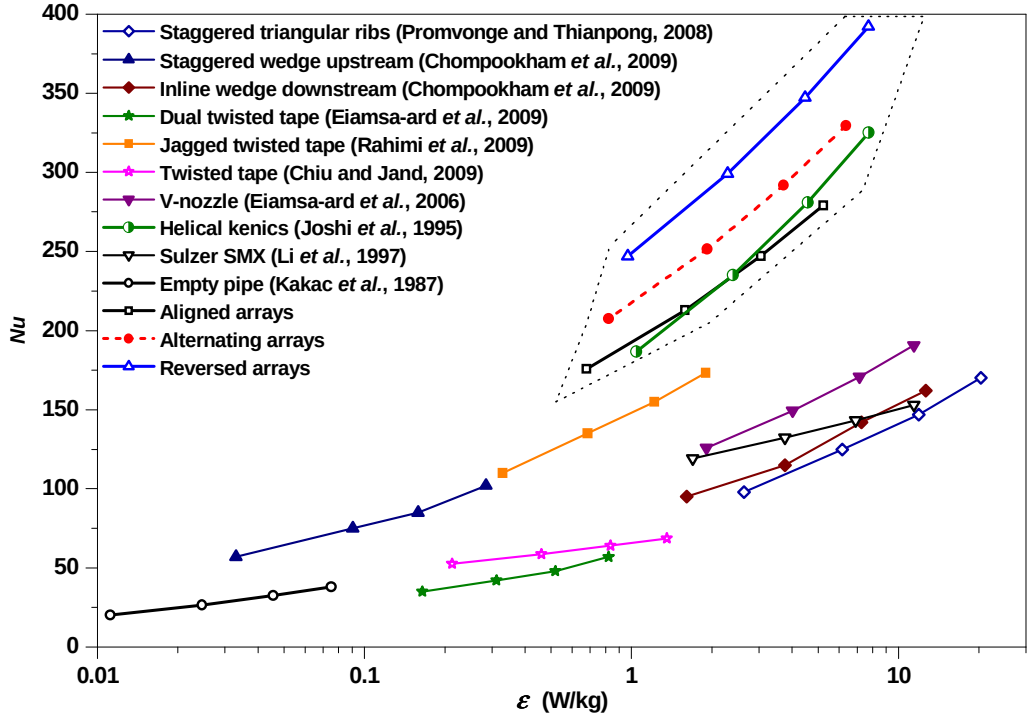

Fig. 9. Nusselt number versus power dissipation per mass unit of different heat exchangers for Reynolds number range [7500, 15000]

4.3. The vortex circulation approach

In this approach, the streamwise circulation, defined in Eq. (10), is the parameter illustrating the convective intensity of the secondary flow in the pipe cross section (Sohankar, 2007; Chang *et al.*, 2009; Tian *et al.*, 2009):

$$\Gamma_{\omega_z} = \iint_S |\omega_z| \, dx \, dy \tag{10}$$

where ω_z is the streamwise vorticity and S the surface area of the pipe cross section.

The average Nusselt number is plotted against the circulation of the primary CVP in Fig. 10 (a). It is observed that the slope for the aligned and alternating arrays geometries is almost the same, but for the same circulation, the heat-transfer coefficient is higher for the latter. For a given Reynolds number, the reversed arrays geometry shows both higher values of circulation and higher Nusselt number than the other two geometries. The slopes of the curves are quite constant with streamwise circulation. Given the linear relation between circulation and Reynolds number, these curves confirm the power law dependence of Nusselt number on Reynolds number with power 2/3.

In turbulent flow, the effect of large scale vertical motion on heat transfer enhancement compared to the turbulent diffusion of heat can be examined by estimating the relative effect of the

turbulent thermal diffusivity α_t, which is the ratio of the eddy viscosity υ_t to the turbulent Schmidt number, traditionally set to 1 (therefore, $\alpha_t = \upsilon_t$). Estimating the eddy viscosity with the $k-\varepsilon$ model leads to:

$$\alpha_t = \upsilon_t = C_\mu \frac{k^2}{\varepsilon} \tag{11}$$

where the coefficient C_μ = 0.09 (Launder and Spalding, 1974; Versteeg and Malalasekera, 1995).

Let us define a new parameter χ, which is the ratio of the convective motion of the large-scale vortices (represented by circulation) to the turbulent thermal diffusivity represented by eddy viscosity; the physical meaning of χ is similar to that of a Nusselt number:

$$\chi = \frac{\Gamma_{\omega_z}}{\upsilon_t} \tag{12}$$

The evolution of χ as a function of Reynolds number (Fig. 10 (b)) indicates that the relative importance of the convective cells increases with turbulence. In Table 1, the fitting functions for χ versus the Reynolds number show a power law relation with power 1/3 in the three configurations; with the highest values for the reversed array and the lowest for the aligned array, just as for the Nusselt number and the thermal enhancement factor.

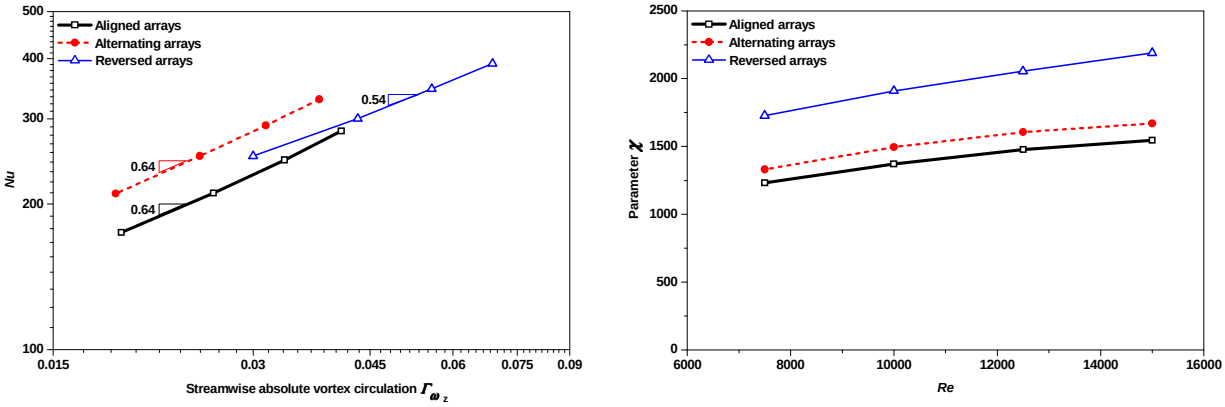

(a) (b)

Fig. 10. (a) Nusselt number versus CVP circulation, (b) the parameter χ versus the Reynolds number

4.4. The synergy field approach

In the synergy field approach, the basic assertion is that the intersection angle between velocity and temperature gradients is directly responsible for the heat transfer (Guo *et al.*, 1998; Tao *et al.*, 2002a). This can be briefly demonstrated starting from the stationary scalar transport equation

$$\rho c_p \vec{U} \cdot \vec{\nabla} T = \lambda \nabla^2 T \tag{13}$$

where $\vec{U}$ and T are respectively the local velocity and the temperature in Cartesian coordinates. By using Gauss's theorem to integrate Eq. (13) over the domain and neglecting axial conduction in the

fluid (since the Péclet number is greater than 100 (Kays and Crawford, 1980)), the energy equation can be written as:

$$\rho c_p \iiint_{Vol} \left(\vec{U} \cdot \vec{\nabla} T\right) dx\, dy\, dz = \Phi \propto Nu \tag{14}$$

with Φ the total wall heat flux, which is proportional to the Nusselt number (see He *et al.* (2005) for more details).

The Nu depends on the dot product $\vec{U} \cdot \vec{\nabla} T = \left|\vec{U}\right|\left|\vec{\nabla} T\right| \cos(\theta)$, where θ is the angle of intersection between the velocity vector and the temperature gradient. Hence, for fixed velocity and temperature gradient, the smaller the intersection angle θ, the larger the convective heat transfer rate.

The local θ can be obtained from the present numerical simulations by the expression

$$\theta = \arccos\left(\frac{U\frac{\partial T}{\partial x} + V\frac{\partial T}{\partial y} + W\frac{\partial T}{\partial z}}{\sqrt{U^2+V^2+W^2}\sqrt{\left(\frac{\partial T}{\partial x}\right)^2 + \left(\frac{\partial T}{\partial y}\right)^2 + \left(\frac{\partial T}{\partial z}\right)^2}} \right) \tag{15}$$

The volume-averaged intersection angle θ_{Vol} is retained as the characteristic parameter. It can be noted that, since the intersection angle varies between 0° and 180°, two ideal synergy cases exist: for $\theta = 0° \Rightarrow \cos(\theta) = 1$ and $\theta = 180° \Rightarrow \cos(\theta) = -1$. The non-synergy case is $\theta = 90° \Rightarrow \cos(\theta) = 0$, as in channel and straight-pipe flows where this angle is maximal (≈ 90°) since the flow streamlines are perpendicular to the temperature gradient. Moreover, regarding Eq. (14), the global heat transfer depends on the sign of the local synergy values. For heated fluid, the flow configuration must be designed so as to attain the highest values of positive $\cos(\theta)$; for cooled fluid, the flow configuration must be designed so as to make θ as close as possible to 180°.

The distribution of the synergy field $\vec{U}_{xy} \cdot \vec{\nabla}_{xy} T$ in the cross section of the three geometries is shown in Fig. 11. The index xy denotes the velocity and temperature gradient in the (x, y) reference frame, in order to observe the effect of the streamwise vortices on the synergy field. It can be seen from Fig. 11 (a) and (b) that the synergy is almost negative in the region of the common outflow in the reference and alternating arrays. Fig. 3 (a) and (b) show, in fact, that the velocity vectors of the common outflow are opposite to the temperature gradient, leading to a negative angle of intersection θ_{xy}. The same result is observed in the common outflow region of the reversed arrays. Moreover, in the center of the CVP (indicated by two circles in Fig. 11) in all geometries, the synergy $\vec{U}_{xy} \cdot \vec{\nabla}_{xy} T = 0$ because the velocity vector is $\vec{U}_{xy} = 0$. The case when $\vec{U}_{xy} \cdot \vec{\nabla}_{xy} T = 0$ is also observed in regions where the velocity vector is perpendicular to the temperature gradient. The highest values of positive $\vec{U}_{xy} \cdot \vec{\nabla}_{xy} T$ are observed in the regions where the velocity and the temperature gradient are aligned.

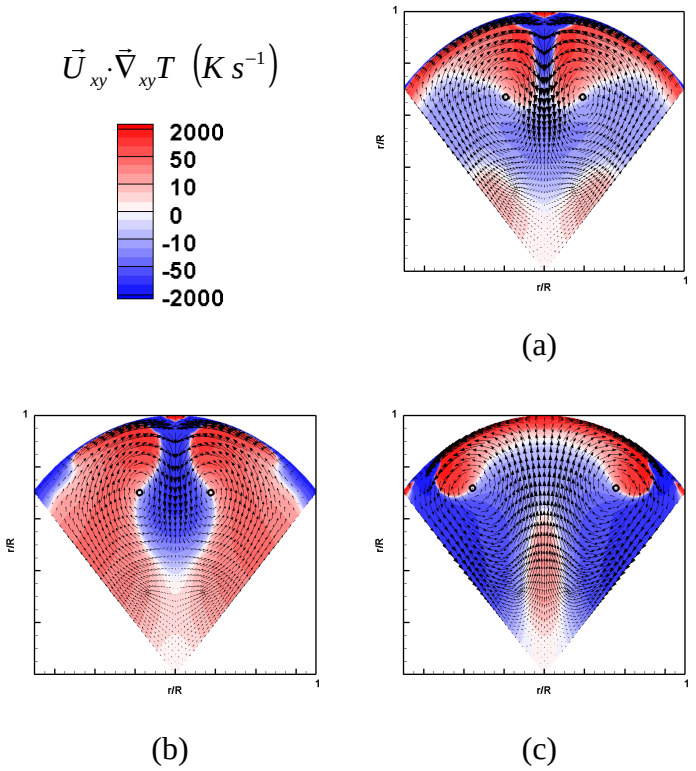

Fig. 11. Distribution of the synergy field in the tube cross section for (a) aligned, (b) alternating and (c) reversed arrays, $Re = 15000$

The global intersection angle θ_{Vol} provides a criterion for comparing the different geometries; as proposed in Fig. 12 (a) where this parameter is plotted versus Reynolds number. This figure shows that θ_{Vol} remains constant with Reynolds number and that the highest θ_{Vol} are obtained in the reference arrays, which leads to the lowest heat-transfer efficiency; the lowest θ_{Vol} is obtained for the reversed arrays, which are found to have the best heat-transfer performances, as established previously. Fig. 12 (b), plotting the Nusselt function versus θ_{Vol}, suggests that θ_{Vol} is a good representative parameter for the heat-transfer performance of the different geometries, since the lower the global intersection angle, the higher the Nusselt number.

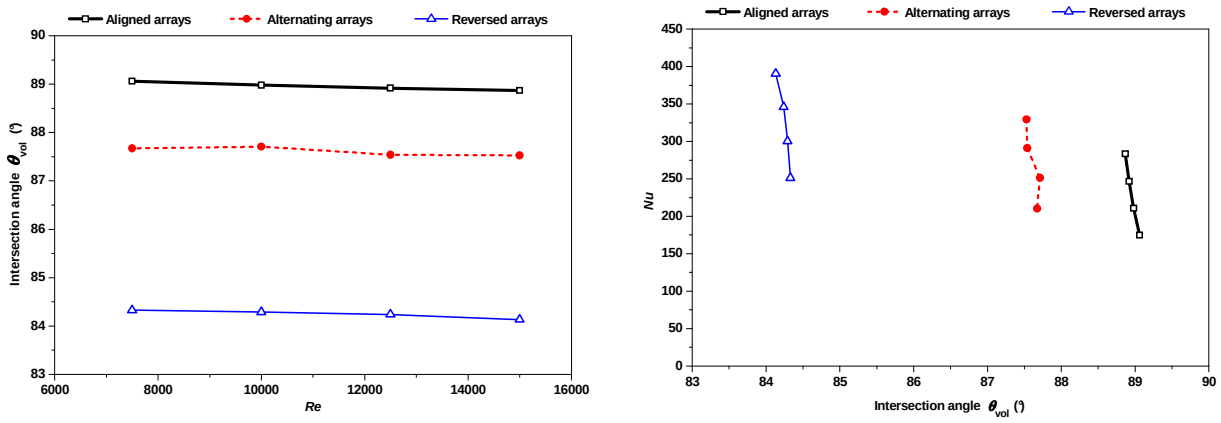

Fig. 12. (a) Intersection angle θ_{vol} and (b) Nusselt number as function of θ_{vol}

4.5. The entropy production approach

Entropy production involves both heat transfer and pressure losses and thus allows characterization of the overall performance of a MHER. Entropy production is computed for the three flow configurations by using the model of Kock and Herwig (2004, 2005), who identified four entropy production mechanisms in the entropy transport equation:

- the rate of entropy production by direct (viscous) dissipation with mean velocity gradients:

$$\dot{S}_{\bar{V}} = \frac{\mu}{T}\left\{2\left[\left(\frac{\partial U}{\partial x}\right)^2+\left(\frac{\partial V}{\partial y}\right)^2+\left(\frac{\partial W}{\partial z}\right)^2\right]+\left(\frac{\partial U}{\partial y}+\frac{\partial V}{\partial x}\right)^2+\left(\frac{\partial U}{\partial z}+\frac{\partial W}{\partial x}\right)^2+\left(\frac{\partial V}{\partial z}+\frac{\partial W}{\partial y}\right)^2\right\} \tag{16}$$

- the rate of entropy production by turbulent dissipation with fluctuating velocity gradients:

$$\dot{S}_{V'} = \frac{\rho\,\varepsilon}{T} \tag{17}$$

- the rate of entropy production by heat transfer with mean temperature gradients:

$$\dot{S}_{\bar{T}} = \frac{\lambda}{T^2}\left[\left(\frac{\partial T}{\partial x}\right)^2+\left(\frac{\partial T}{\partial y}\right)^2+\left(\frac{\partial T}{\partial z}\right)^2\right] \tag{18}$$

- the rate of entropy production by heat transfer with fluctuating temperature gradients:

$$\dot{S}_{T'} = \frac{\alpha_t}{\alpha}\frac{\lambda}{T^2}\left[\left(\frac{\partial T}{\partial x}\right)^2+\left(\frac{\partial T}{\partial y}\right)^2+\left(\frac{\partial T}{\partial z}\right)^2\right] = \frac{\alpha_t}{\alpha}\dot{S}_{\bar{T}} \tag{19}$$

The total entropy production is the sum of these four terms:

$$\dot{S} = \underbrace{\dot{S}_{\bar{V}}+\dot{S}_{V'}}_{\dot{S}_{viscous}} + \underbrace{\dot{S}_{\bar{T}}+\dot{S}_{T'}}_{\dot{S}_{thermal}} \tag{20}$$

where the first two terms on the right-hand side are due to viscous (laminar and turbulent) dissipation $\dot{S}_{viscous}$ and the second two terms are due to thermal dissipation $\dot{S}_{thermal}$.

Eqs. (16) to (19) are implemented in the post-processing of the CFD to obtain the local $\dot{S}$ and the global $\dot{S}_{pro}$ entropy production, the latter being the sum over the whole volume:

$$\dot{S}_{pro} = \iiint_V \dot{S}\,dx\,dy\,dz \tag{21}$$

According to Hesselgreaves (2000), the entropy production number $N_{\dot{S}_{pro}}$ is defined as:

$$N_{\dot{S}_{pro}} = \frac{\dot{S}_{pro}\,T_w}{Q_w} \tag{22}$$

where Q_w and T_w are respectively the wall heat flux and the wall temperature.

The parameter $N_{\dot{S}_{pro}}$ can be used to determine the thermal efficiency of MHER as shown in Fig. 13 (a), which plots $N_{\dot{S}_{pro}}$ versus Reynolds number. It can be observed, for the three geometries, an increase of $N_{\dot{S}_{pro}}$ with *Re*: the higher the Reynolds number, the less efficient the thermal transfer. The evolution of the entropy production number with Reynolds number is sharper for the reference arrays than the other geometries, and the increase in $N_{\dot{S}_{pro}}$ for the reversed arrays is the slowest, with a 0.1 trend slope. As $N_{\dot{S}_{pro},rev} > N_{\dot{S}_{pro},alt} > N_{\dot{S}_{pro},alg}$, the ordering among the three geometries is consistent with the previous results. Another representation of the thermal enhancement factor η in Fig. 13 (b) versus $N_{\dot{S}_{pro}}$ is also of interest by highlighting the fact that the decrease of the entropy production number is always accompanied by heat-transfer enhancement. Moreover, the slopes of the three curves are consistent with the previous results since they show that, in the reversed arrays, a smaller decrease in $N_{\dot{S}_{pro}}$ is needed to increase thermal enhancement, relative to the reference and alternating arrays (reflecting the fact that this geometry is more efficient for heat transfer than the other two configurations).

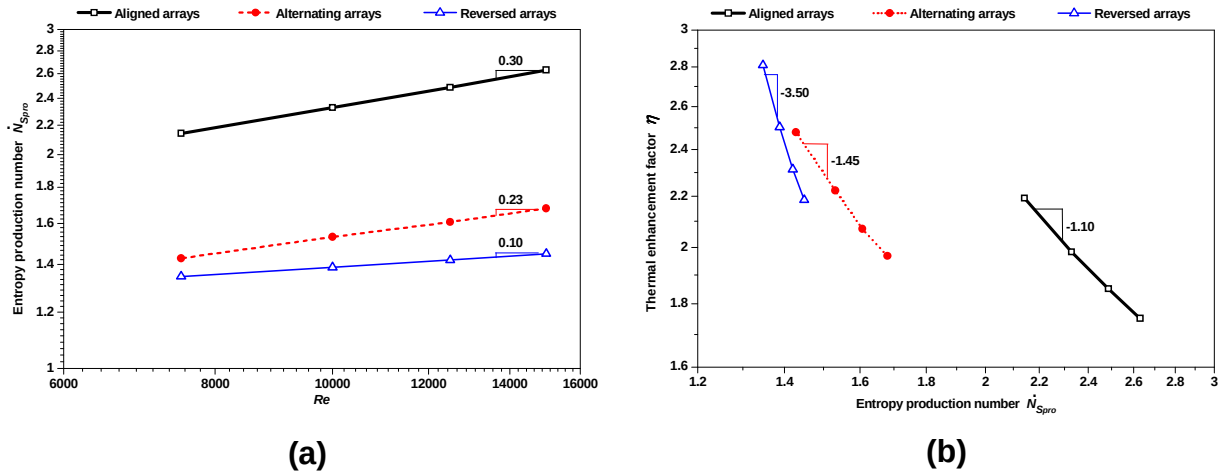

Fig. 13. (a) Entropy production number versus Reynolds number, (b) thermal enhancement factor versus entropy production number

5. Conclusions

In the present work, numerical simulations are performed to investigate the influence of flow structure on the heat transfer by using different physical approaches. The numerical procedure and turbulence model are validated by previous experimental results obtained by laser Doppler anemometry (Habchi *et al.*, 2010). Transverse and streamwise vorticity are produced by using different positions of vortex generators in a static mixer: aligned (the reference geometry), 45° tangential periodical shift (alternating geometry), and the reference geometry with an opposite flow direction (reversed geometry).

The global heat transfer appears to be highly correlated with the circulation of the streamwise vortices induced by the vortex generators. A new parameter, defined as the ratio of the vortex circulation (which characterizes the convective motion of large-scale vortices) and the turbulent viscosity, indicates that the role of these vortices is enhanced by increasing the Reynolds number.

The synergy field (Guo *et al.*, 1998; Tao *et al.*, 2002a) is characterized by an average intersection angle between the velocity and temperature gradient. This parameter, independent of the Reynolds number, is the signature of the global Nusselt number.

The entropy production (Bejan, 1996; Kock and Herwing, 2004, 2005) allows determining the overall performance of the heat exchangers. It is verified in the tested geometries that the minimum entropy production is concomitant with the maximum thermal efficiency and can thus be used as a design criterion for optimizing geometries aimed at intensified heat exchangers.

These complementary approaches converge to classify the three geometries in order of increasing efficiency: the reversed arrays geometry appears to be the most efficient and the reference geometry the least. That they lead in the present case to the same conclusion strongly suggests that each method can bring useful information for understanding and designing novel flow geometries.

Acknowledgments

C. Habchi would like to acknowledge fruitful discussions with Dr. M. Gonzalez, Dr. A. Ould El Moctar and Dr. M. Khaled. This work was supported in part by ADEME (Agence de l'Environnement et de la Maîtrise de l'Énergie). Dr. C. Garnier is gratefully acknowledged for monitoring this grant.

References

Aider, J.L., Beaudoin, J.F., Wesfreid, J.E., 2010. Drag and lift reduction of a 3D bluff-body using active vortex generators. Exp. Fluids. 48, 771-789.

Ajakh, A., Kestoras, M.D., Toe, R., Peerhossaini, H., 1999. Influence of forced perturbations in the stagnation region on Görtler instability. AIAA J. 37, 1572-1577.

Anxionnaz, Z., Cabassud, M., Gourdon, C., Tochon, P., 2008. Heat exchanger/reactors (HEX reactors): Concepts, technologies: State-of-the-art. Chem. Eng. Process. 47, 2029-2050.

Barth, J.T., Jespersen, D., 1989. The design and application of upwind schemes on unstructured meshes. Proceedings AIAA 27th Aerospace Sciences Meeting, Reno, Nevada.

Bejan, A., 1996. Entropy generating minimization, CRC Press.

Chang, L.M., Wang, L.B., Song, K.W., Sun, D.L., Fan, J.F., 2009. Numerical study of the relationship between heat transfer enhancement and absolute vorticity flux along main flow direction in a channel formed by a flat tube bank fin with vortex generators. Int. J. Heat Mass Transfer 52, 1794-1801.

Chattopadhyay, H., 2007. Augmentation of heat transfer in a channel using a triangular prism. Int. J. Therm. Sci. 46, 501-505.

Chemineer Inc., 2008. Kenics: Static Mixing Technology, Product Bulletin 800, USA.

Chen, H.C., Patel, V.C., 1988. Near-wall turbulence models for complex flows including separation. AIAA J. 26, 641-648.

Chiu, Y.W., Jang, J.Y., 2009. 3D numerical and experimental analysis for thermal–hydraulic characteristics of air flow inside a circular tube with different tube inserts. Appl. Therm. Eng. 29, 250-258.

Defraeye, T., Blocken, B., Carmeliet, J., 2010. CFD analysis of convective heat transfer at the surfaces of a cube immersed in a turbulent boundary layer. Int. J. Heat Mass Transfer 53, 297-308.

Dong, D., Meng, H., 2004. Flow past a trapezoidal tab. J. Fluid Mech. 510, 219-242.

Eiamsa-ard, S., Promvonge, P., 2006. Experimental investigation of heat transfer and friction characteristics in a circular tube fitted with V-nozzle turbulators. Int. Comm. Heat Mass Transfer 33, 591-600.

Eiamsa-ard, S., Thianpong, C., Eiamsa-ard, P., Promvonge, P., 2010. Thermal characteristics in a heat exchanger tube fitted with dual twisted tape elements in tandem. Int. Comm. Heat Mass Transfer 37, 39-46.

Elyyan, M.A., Tafti, D.K., 2009. A novel split-dimple interrupted fin configuration for heat transfer augmentation. Int. J. Heat Mass Transfer 52, 1561-1572.

Ferrouillat, S., Tochon, P., Garnier, C., Peerhossaini, H., 2006. Intensification of heat transfer and mixing in multifunctional heat exchangers by artificially generated stream-wise vorticity. Appl. Therm. Eng. 26, 1820-1829.

Fiebig, M., 1995. Embedded vortices in internal flow: heat transfer and pressure loss enhancement. Int. J. Heat Fluid Flow 16, 376-388.

Fluent Inc., 2006. Fluent 6.3 User's Guide.

Garcia, A., Gonzalez, M., Paranthoën, P., 2005. On the alignment dynamics of a passive scalar gradient in a two-dimensional flow. Phys. Fluids 17, 117102.

Gibson, M.M., Launder, B.E., 1978. Ground effects on pressure fluctuations in the atmospheric boundary layer. J. Fluid Mech. 86, 491-511.

Gnielinski, V., 1976. New equations for heat and mass transfer in turbulent pipe and channel flow. Int. Chem. Eng. 16, 359-368.

Gretta, W.J., Smith, C.R., 1993. The flow structure and statistics of a passive mixing tab. J. Fluid Eng. 115, 255-263.

Guo, Z.Y., Li, D.Y., Wang, B.X., 1998. A novel concept for convective heat transfer enhancement. Int. J. Heat Mass Transfer 41, 2221-2225.

Guo, Z.Y., Tao, W.Q., Shah, R.K., 2005. The field synergy (coordination) principle and its applications in enhancing single phase convective heat transfer. Int. J. Heat Mass Transfer 48, 1797-1807.

Habchi, C., Lemenand, T., Della Valle, D., Peerhossaini, H., 2009a. Liquid/liquid advection in a chaotic advection flow. Int. J. Multiphase Flow 35, 485-497.

Habchi, C., Lemenand, T., Della Valle, D., Peerhossaini, H., 2009b. Alternating mixing tabs in multifunctional heat exchanger-reactor. Chem. Eng. Process. (in press), doi:10.1016/j.cep.2009.07.003

Habchi, C., Lemenand, T., Della Valle, D., Peerhossaini, H., 2010. Turbulent mixing and residence time distribution in novel multifunctional heat exchangers-reactors. Chem. Eng. Process., (submitted).

He, Y.L., Tao, W.Q., Song, F.Q., Zhang, W., 2005. Three-dimensional numerical study of heat transfer characteristics of plain plate fin-and-tube heat exchangers from viewpoint of field synergy principle. Int. J. Heat Fluid Flow 26, 459-473.

Herpe, J., Bougeard, D., Russeil, S., Stanciu, M., 2009. Numerical investigation of local entropy production rate of a finned oval tube with vortex generators. Int. J. Therm. Sci. 48, 922-935.

Hesselgreaves, J.E., 2000. Rationalisation of second law analysis of heat exchangers, Int. J. Heat Mass Transfer 43, 4189-4204.

Hinze, J.O., 1975. Turbulence, second ed., McGraw-Hill, New York.

Jacobi, A.M., Shah, R.K., 1995. Heat transfer surface enhancement through the use of longitudinal vortices: a review of recent progress. Exp. Therm. Fluid Sci. 11, 295-309.

Joshi, P., Nigam, K.D.P., Bruce Nauman, E., 1995. The Kenics static mixer: new data and proposed correlations. The Chem. Eng. J. 59, 265-271.

Kakac, S., Shah, R.K., Aung, W., 1987. Handbook of Single-Phase Convective Heat Transfer, John Wiley and Sons, New York.

Kays, W.M., Crawford, M.E., 1980. Convective Heat and Mass Transfer. McGraw-Hill Book Company, New York, pp. 107, 246.

Kock, F., Herwig, H., 2004. Local entropy production in turbulent shear flows: a high-Reynolds-number model with wall functions. Int. J. Heat Mass Transfer 47, 2205-2215.

Kock, F., Herwig, H., 2005. Entropy production calculation for turbulent shear flows and their implementation in CFD codes. Int. J. Heat Fluid Flow 26, 672-680.

Lapeyre, G., Klein, P., Hua, B.L., 1999. Does the tracer gradient vector align with the strain eigenvectors in 2D turbulence? Phys. Fluids 11, 3729-3737.

Launder, B.E., Spalding, D.B., 1974. The numerical computation of turbulent flows. Comp. Meth. Appl. Mech. Eng. 3, 269-289.

Launder, B.E., Reece, G.J., Rodi, W., 1975. Progress in the development of a Reynolds stress turbulence closure. J. Fluid Mech. 68, 537-566.

Launder, B.E., 1989. Second-moment closure: present… and future? Int. J. Heat Fluid Flow 10, 282-300.

Le P.M., Papavassiliou D.V., 2009. A physical picture of the mechanism of turbulent heat transfer from the wall. Int. J. Heat Mass Transfer 52, 4873-4882.

Lemenand, T., Della Valle, D., Zellouf, Y., Peerhossaini, H., 2003. Droplets formation in turbulent mixing of two immiscible fluids. Int. J. Multiphase Flow 29, 813-840.

Lemenand, T., Dupont, P., Della Valle, D., Peerhossaini, H., 2005. Turbulent mixing of two immiscible fluids. J. Fluid Eng. 127, 1132-1139.

Lemenand, T., Durandal, C., Della Valle, D., Peerhossaini, H., 2010. Turbulent direct-contact heat transfer between two immiscible fluids. Int. J. Therm. Sci., in press.

Li, H.Z., Fasol, C., Choplin, L., 1996. Pressure drop of Newtonian and non-Newtonian fluids across a Sulzer SMX static mixer. Chem. Eng. Res. Des. 75, 792-796

Lienhard IV, J.H., Lienhard V, J.H., 2008. A heat transfer textbook, third ed., Phlogiston Press, Cambridge, Massachusetts, 691-724.

Lögdberg, O., Angele, K., Alfredsson, P.H., 2010. On the robustness of separation control by streamwise vortices, Eur. J. Mech. B/Fluids. 29, 9-17.

Mohand Kaci, H., Lemenand, T., Della Valle, D., Peerhossaini, H., 2009. Effects of embedded streamwise vorticity on turbulent mixing. Chem. Eng. Process. 48, 1457-1474.

Mohand Kaci, H., Habchi, C., Lemenand, T., Della Valle, D., Peerhossaini, H., 2010. Flow structure and heat transfer induced by embedded vorticity. Int. J. Heat Mass Transfer 53, 3575-3584.

Patankar, S.V., Spalding, D.B., 1972. A calculation procedure for heat mass and momentum transfer in three-dimensional parabolic flows. Int. J. Heat Mass Transfer. 15, 1787-1806.

Peerhossaini, H., Bahri, F., 1998. On the spectral distribution of the modes in nonlinear Görtler instability. Exp. Therm. Fluid Sci. 16, 195-208.

Promvonge, P., Thianpong, C., 2008. Thermal performance assessment of turbulent channel flows over different shaped ribs. Int. Comm. Heat Mass Transfer 35, 1327-1334.

Rahimi, M., Shabanian, S.R., Alsairafi, A.A., 2009. Experimental and CFD studies on heat transfer and friction factor characteristics of a tube equipped with modified twisted tape inserts. Chem. Eng. Process. 48, 762-770.

Rahmani, R.K., Keith, T.G., Ayasoufi, A., 2006. Numerical study of the heat transfer rate in a helical static mixer. J. Heat Transfer 128, 769-783.

Sohankar, A., 2007. Heat transfer augmentation in a rectangular channel with a vee-shaped vortex generator. Int. J. Heat Fluid Flow 28, 306-317.

Tao, W.Q., Guo, Z.Y., Wang, B.X., 2002a. Field synergy principle for enhancing convective heat transfer-its extension and numerical verifications. Int. J. Heat Mass Transfer 45, 3849-3856.

Tao, W.Q., He, Y.L., Wang, Q.W., Qu, Z.G., Song, F.Q., 2002b. A unified analysis on enhancing single phase convective heat transfer with field synergy principle. Int. J. Heat Mass Transfer 45, 4871-4879.

Tian, L.T., He, Y.L., Lei, Y.G., Tao, W.Q., 2009. Numerical study of fluid flow and heat transfer in a flat-plate channel with longitudinal vortex generators by applying field synergy principle analysis. Int. Comm. Heat Mass Transfer 36, 111-120.

Toé, R., Ajakh, A., Peerhossaini, H., 2002. Heat transfer enhancement by Görtler instability. Int. J. Heat Fluid Flow 23, 194-204.

Versteeg, H.K., Malalasekera, W., 1995. An introduction to computational fluid dynamics, the finite volume method. Prentice Hall, New York, 62-146.

Warming, R.F., Beam, R.M., 1975. Upwind second-order difference schemes and applications in unsteady aerodynamic flows. Proceedings AIAA 2nd Computational Fluid Dynamics Conference, Hartford, CT.

Wu, J.M., Tao, W.Q., 2008a, Numerical study on laminar convection heat transfer in a rectangular channel with longitudinal vortex generator, Part A: Verification of field synergy principle. Int. J. Heat Mass Transfer 51, 1179-1191.

Wu, J.M., Tao, W.Q., 2008a. Numerical study on laminar convection heat transfer in a rectangular channel with longitudinal vortex generator, Part B: Parametric study of major influence factors. Int. J. Heat Mass Transfer 51, 3683-3692.

Wolfstein, M., 1969. The velocity and temperature distribution of one-dimensional flow with turbulence augmentation and pressure gradient. Int. J. Heat Mass Transfer. 12, 301-318.

CORPUS DES ARTICLES

8. Liquid/liquid dispersion in a chaotic advection flow

C. Habchi, T. Lemenand, D. Della Valle, H. Peerhossaini

International Journal of Multiphase Flow 35 (2009a) 485-497.

International Journal of Multiphase Flow 35 (2009) 485–497

Contents lists available at ScienceDirect

International Journal of Multiphase Flow

journal homepage: www.elsevier.com/locate/ijmulflow

Liquid/liquid dispersion in a chaotic advection flow

Charbel Habchi [a,b], Thierry Lemenand [a], Dominique Della Valle [a], Hassan Peerhossaini [a,*]

[a] Thermofluids, Complex Flows and Energy Research Group, Laboratoire de Thermocinétique de Nantes, CNRS UMR 6607, École Polytechnique – Université de Nantes, rue Christian Pauc, B.P. 50609, 44306 Nantes, France
[b] Agence de l'Environnement et de la Maîtrise de l'Énergie (ADEME), 20 avenue du Grésillé, B.P. 90406, 49004 Angers, France

ARTICLE INFO

Article history:
Received 12 September 2008
Received in revised form 10 February 2009
Accepted 22 February 2009
Available online 12 March 2009

Keywords:
Chaotic advection
Liquid/liquid dispersion
Drop size distribution
Multifunctional heat exchanger

ABSTRACT

Mixing by chaotic advection in a twisted-pipe flow is used here to investigate the efficiency of this flow in the liquid/liquid dispersion process. This study focuses on water/oil dispersions produced by continuous water injection into a main oil flow, for small Dean numbers. The drop sizes obtained with the chaotic-advection twisted-pipe flow are compared with those in a straight pipe and a helically coiled flow for the same conditions. It is found that the resulting dispersions are finer and more mono-dispersed in the chaotic advection flow. These results are compared with the theoretical maximum diameter d_{max} determined by the Grace theory in which the viscous stress controls the breakup phenomena. For this purpose, the kinematic field is computed from the theoretical formulae for Dean flow. The strain rate fields in the pipe cross-section are then analytically computed and used to predict the maximum drop diameter. The theoretical values are identical for the three configurations (straight, helically coiled, and twisted pipe) up to a critical Dean number, where the secondary flow becomes significant. Beyond this value, the shear stress is enhanced in the twisted-pipe flow compared with the straight-pipe flow, and the predicted drop diameters are smaller. An interpretation of the higher dispersive performance of the chaotic flow is provided by the Lagrangian trajectories of the particles.

1. Introduction

The advantages offered by a chaotic-advection twisted pipe-flow used as a mixer and/or heat exchanger have been established in previous studies (Aref, 1984; Jones et al., 1989; Acharya et al., 1992; Peerhossaini et al., 1993; Castelain et al., 1997; Mokrani et al., 1998a,b; Le Guer et al., 2001; Lemenand and Peerhossaini, 2002) when compared with a straight pipe or helically coiled pipe. The geometric perturbation of the twisted-pipe configuration generates three-dimensional chaotic trajectories in the secondary Dean flow induced by curvature effects. The Dean number characterizes the ratio between the viscous forces and the centrifugal forces, and is defined as

$$De = \frac{W^2 a^3}{R\nu^2} \tag{1}$$

where a is the tube inner radius and R the bend curvature radius.

Chaotic advection in such geometries produces efficient macro-mixing and heat transfer in the laminar regime. The heat transfer is enhanced in a particular range of the Dean number [60–1000], without significant increase in the pressure drop (Mokrani et al., 1998a,b).

This flow finds applications in the pharmaceutical industry or food industry to process highly viscous fluids or fluids with stress-sensitive long molecular chains. The purpose of this study is to investigate the capacity of chaotic advection to generate liquid/liquid dispersion.

An experimental study was undertaken in order to observe the effect of chaotic advection on the dispersion of water in a laminar oil flow, and also to obtain experimental data for validation of the results of a theoretical approach to the water–oil dispersion in this flow. The theoretical approach is based on the determination of drop equilibrium under the joint action of viscous stresses generated by chaotic advection flow and interface tension.

In a curved pipe, the centrifugal force induces a secondary flow in the form of counter-rotating cells called Dean roll-cells that are superimposed on the axial flow and play the role of internal agitators of the flow. Analytical solutions for Dean flow have been proposed by Jones et al. (1989) and Le Guer and Peerhossaini (1991).

In the present work, the theoretical determination of the equilibrium drop size is based on Taylor's analysis (Taylor, 1953) as extended by Grace (1982). From this it is possible to compute the Eulerian distribution of the strain rates in the pipe cross-section, and to propose a model for the maximum shear and elongation rates introduced in Grace's work (1982) to calculate the theoretical maximum diameters with no fitting constant. The additional forces introduced by Dean flow above a certain Dean number generate stresses due to stretching and folding that are over and above the basic strain rates in the straight pipe, and these stresses enhance the breakup of water drops injected into the main oil flow.

* Corresponding author. Tel.: +33 2 40 68 31 24; fax: +33 2 40 68 31 41.
E-mail address: hassan.peerhossaini@univ-nantes.fr (H. Peerhossaini).

0301-9322/$ - see front matter © 2009 Elsevier Ltd. All rights reserved.
doi:10.1016/j.ijmultiphaseflow.2009.02.019

From this point of view, there is no theoretical difference between the helically coiled and twisted-pipe chaotic advection configurations. The drop diameters predicted by the theoretical approach are then compared with the experimental values for the three configurations (straight, helically coiled, and twisted-pipe flows).

A Lagrangian analysis of the flow was undertaken to explain the finer drop size observed experimentally in the chaotic advection flow. A comparison of the trajectories and of the Poincaré section of the fluid particles after 25 bends, for helically coiled and chaotic advection flows, qualitatively confirms that the latter configuration provides better macro-mixing. This feature is clear in the residence time distribution (RTD) for the two configurations and helps to explain the better dispersive performance of the chaotic advection flow. An illustration for $De = 100$ shows the improved homogenizing properties of the chaotic advection configuration.

This paper is organized as follows. In Section 2 the experimental setup and experimental results for the water–oil dispersion are presented. Section 3 is devoted to the theoretical prediction of droplet diameters by an Eulerian approach. The mechanical history of droplets in the flow determined by Lagrangian approach is given in Section 4, as is a presentation of the resident time distribution of fluid particles. Conclusions are drawn in Section 5.

2. Experimental setup and methods

2.1. Experimental setup

As shown in Fig. 1, the test section is composed of a succession of 90° bends with a given curvature radius. It can be arranged in both the helically coiled pipe and the twisted-pipe configurations where each bend is rotated in the orthogonal plane with respect to the preceding one, as seen in Fig. 2. Both geometries have 25 bends of 8 mm inside diameter D, the same unfolded length ($L = 2$ m) and the same bend curvature radius ($R = 44$ mm). The straight pipe has also an inside diameter of $D = 8$ mm and unfolded length $L = 2$ m. The dimensions of the test section are given in Table 1.

A schematic diagram of the hydraulic loop used here is shown in Fig. 3a. It has four main elements:

- oil admission circuit;
- water injection system;
- test section;
- flow visualization device at the test section exit.

The tank contains 100 L of a vegetable oil, allowing experimentation for 1 h at a Reynolds number of $Re = 50$ and 5 min at $Re = 600$. The flow rates are measured by rotameters with 5% accuracy (Sart Von Rohr SAS™ for water and Krohne Dusburg™ for oil).

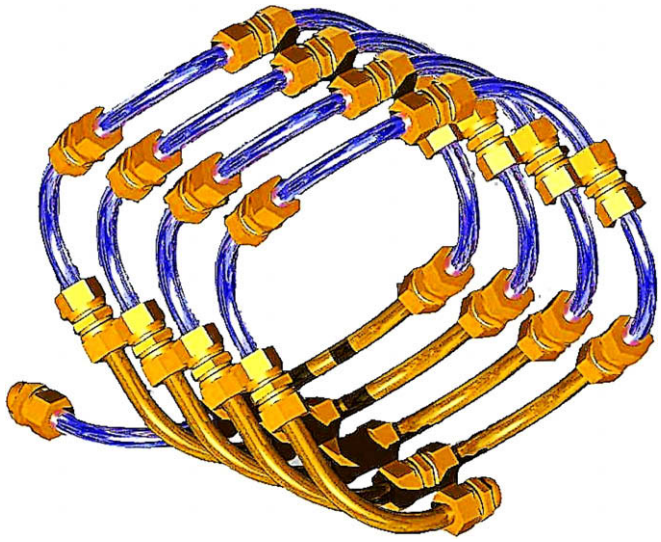

Fig. 2. Twisted pipe test section.

Table 1
Test section dimensions.

Diameter of circular duct	8 mm
Bend curvature radius	44 mm
Curvature angle in bend plane	$\frac{\pi}{2}$ rad
Number of bends	25
Total curved length	1.8 m
Straight length between bends	0.2 m
Total length	2 m

The oil is pumped by a centrifugal pump, while the water is supplied by a constant-level feed tank connected to the water supply network. The flow rate is monitored by a back-pressure valve. Water is injected at the twisted pipe inlet by an injection needle of inside diameter 2 mm, designed so that the velocity ratio (injection/main flow) does not exceed 1.5 for the most extreme conditions (water volume fraction of 10%). The current volume fractions are much lower, so that perturbations at the injection might not induce an additional breakup of the water droplets.

2.2. Drop size measurement

The flow visualization system (Fig. 3b) is a rectangular Plexiglas™ window positioned on top of a parallelepipedic box,

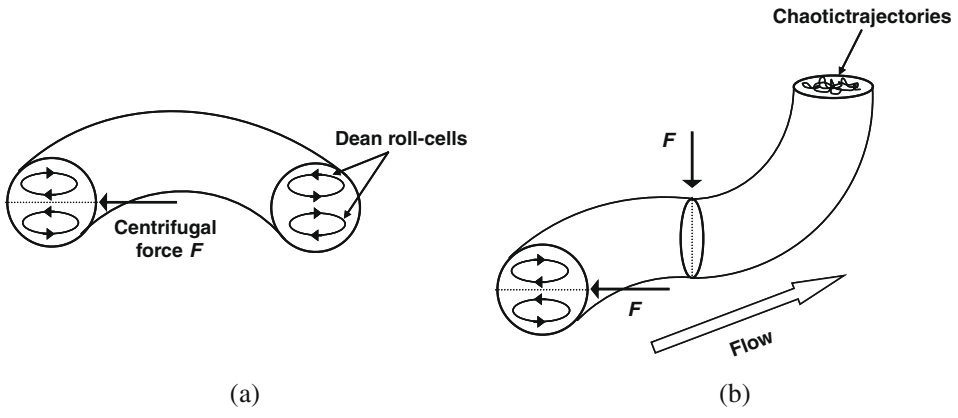

Fig. 1. Generation of spatially chaotic particle paths in laminar, steady, and three-dimensional flow: (a) regular Dean flow; and (b) twisted pipe Dean flow.

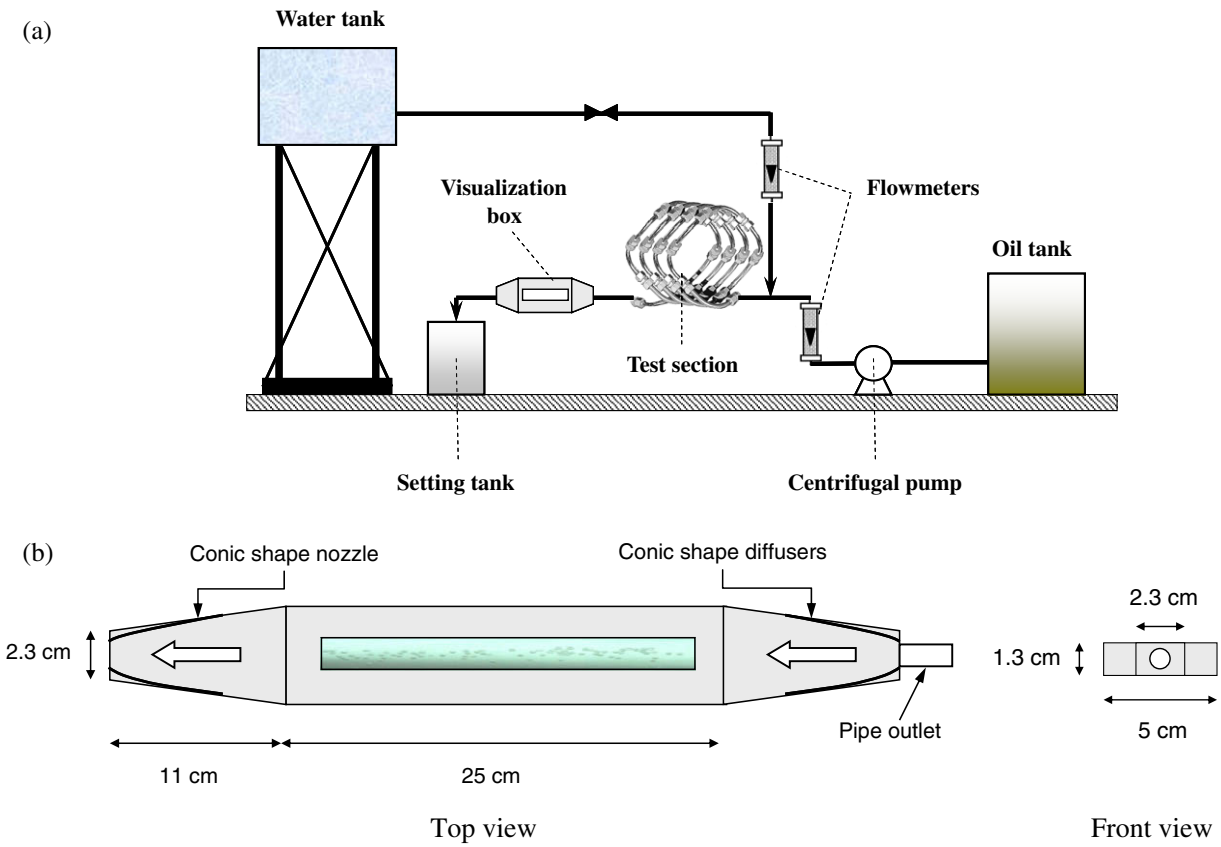

Fig. 3. (a) Schematic diagram of experimental setup. (b) Flow visualization system.

with conic/rectangular connections at each end. At the entrance, directly at the exit of the test section, the diffuser, is designed to minimize flow disturbances by maintaining (as much as possible) the shear stresses at the same level as in the test section, and, with a 7° angle, to avoid recirculations at low flow rates and thus to prevent drop coalescence at the pipe exit. Moreover, the box depth is small enough (depth is 13 mm, equals to 1.625 D) to prevent drops overlapping. In fact overlapping did not occur for the range of flow rates in this experiment, but may occur for higher flow rates.

Pictures of the emulsion are taken with a high-frequency digital Canon™ camera placed vertically above the visualization window with its optical axis perpendicular to the window's plane. The emulsion flow in the visualization box is lit from below by an intense diffuse white light. For given operating conditions, a sequence of independent images is selected and recorded; this sequence, an example of which is shown in Fig. 4, constitutes our statistical sample of the drops. Drop diameters are measured from the recorded images using IMAQ Vision Builder 6 software. At the end of the analysis, a table of diameters of at least 400 drops for each run is obtained. The experimental size distributions are fitted with a log-normal law. By taking 99% of the cumulative volume curve, a representative value for the maximum diameter can be determined. The standard deviation factor is also of interest for the quality of the emulsification process in further applications. If k is the log-standard deviation, the linear deviation β can be deduced from

$$\beta = \sinh(k) \tag{2}$$

Measurements were carried out for the three configurations: straight pipes, helically coiled pipes, and twisted pipes. By the log-normal law, the maximum drop diameter is found by reading 99% from the frequency of the cumulative diameter values on the fitted log-normal curve, as shown in Fig. 5 for a straight tube.

2.3. Working fluids

The continuous phase is commercial food-grade vegetable oil, and tap water is injected as the dispersed phase. The kinematic viscosity of the oil was measured using a Mettler™ RM180 rheometer. To measure the surface tension of the working fluid we used the Wilhelmy method: a metallic blade suspended from a balance by a stem is plunged into the liquid; the balance measures the vertical

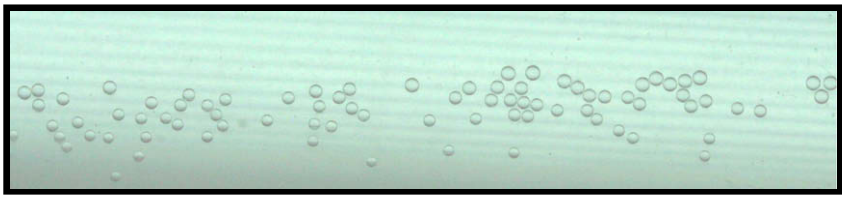

Fig. 4. Image of droplets taken by fast digital camera (chaotic advection configuration – oil flow rate $Q = 50\,\mathrm{l\,h^{-1}}$).

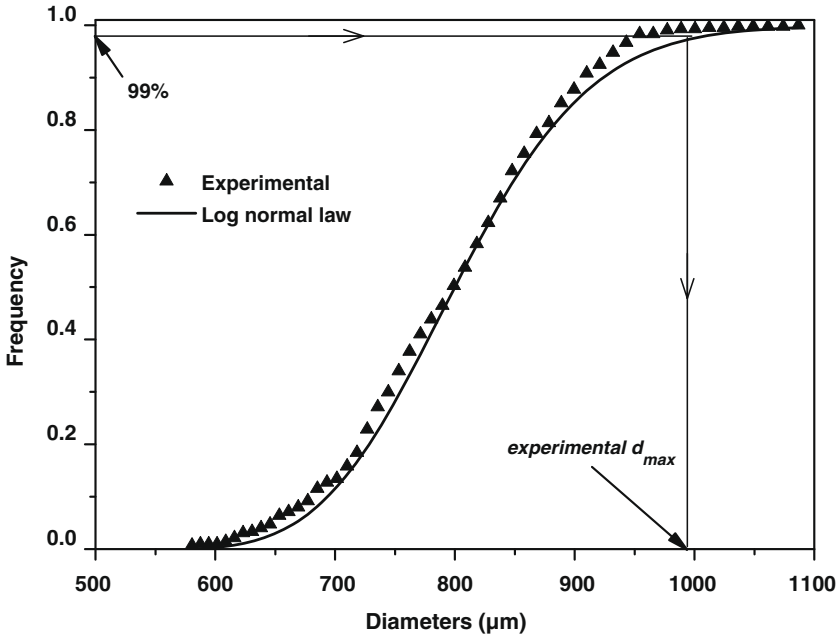

Fig. 5. Experimental droplet diameter distribution fitted by log-normal curve (straight pipe with oil flow rate $Q = 80\ \mathrm{l\ h^{-1}}$).

force F exerted on the stem by withdrawing the blade from the liquid. The surface tension σ is calculated by:

$$F = \sigma \zeta \cos\theta \tag{3}$$

where ζ is the wet perimeter. The platinum blade is previously passed through a flame to obtain perfect adhesion to the liquid surface. The ideal contact angle is $\theta = 0°$, for which the term $\cos\theta$ in Eq. (2) tends to 1. Therefore the value of the surface tension σ can be deduced from the geometric characteristics of the blade.

As the oil viscosity μ_c is very sensitive to temperature and has significant consequences on the dispersion through the viscous stress, the oil temperature T was controlled by a Chromel/Alumel (type K) thermocouple in the oil admission circuit. For modelling purposes, oil viscosity was measured with an AR1000 TA Instr™ rheometer and fitted by Arrhenius' law:

$$\mu_c = \mu_{c_0} \exp\left(\frac{E}{RT} - \frac{E}{RT_0}\right) \tag{4}$$

where $E = 29$ kJ, $R = 8.314\ \mathrm{J\ K^{-1}\ mol^{-1}}$ and μ_{c_0} is the oil viscosity for a given temperature T_0. The physical properties of the two fluids are given in Table 2.

2.4. Reproducibility

Runs were repeated three times on different days to check the effect of a new operator and a new trial on the measured characteristics of the final emulsion in the test section. Nominal operating conditions at Dean number $De = 70$; the resulting size distributions of the three runs were compared, leading to a maximum error of ±6% in the maximum drop diameter.

Table 2
Characteristics of working fluids used in experiments.

Interfacial tension	0.0192 N m^{-1}
Oil density	910 kg m^{-3}
Water density	1000 kg m^{-3}
Water dynamic viscosity	0.001 Pa s
Oil dynamic viscosity at 25 °C	0.052 Pa s
Viscosity ratio	0.0192

2.5. Experimental results for drop diameters

Drop size distributions were measured for the three configurations: straight, helically coiled and twisted pipes. A summary of the results is given in Table 3.

The maximum drop diameters are plotted versus the oil flow rate in Fig. 6. As expected, the drop diameters decrease with increasing flow rate, since the viscous stresses increase with yield velocity and velocity gradients. The water (dispersed phase) flow rate is not taken into account as an operating parameter unless it increases the global (two-phase) flow rate. This approximation is reasonable as long as we work with the lowest injection rate (about 5% volume fraction) to minimize flow disturbance at the injection point and to prevent drop coalescence: at this level, the dispersed phase volume fraction does not influence the drop breakup. The drop diameters obtained in the chaotic flow are smaller than those in the helically coiled flow, the latter being smaller than that in the straight tube.

For an oil flow rate of about $100\ \mathrm{l\ h^{-1}}$, a transition can be observed on the drops diameters in the twisted pipe chaotic flow. In fact, at this stage, which corresponds to a Dean number of about 60, the chaotic advection becomes significant. These results confirm the idea that the chaotic advection flow improves the liquid/liquid dispersion.

For the same runs, the standard deviation of the drop size distribution, shown in Fig. 7, is about 20% less for the twisted pipe than for the helically coiled pipe. This trend appears more clearly

Table 3
Measured maximum droplet diameters.

Flow rate (l h^{-1})	Straight pipe (mm)	Helically coiled pipe (mm)	Chaotic twisted pipe (mm)
40	1.58	1.39	1.28
50	1.56	1.24	1.11
60	1.20	1.12	1.01
70	1.19	1.08	0.94
80	0.98	0.92	0.84
90	0.96	0.89	0.79
100	0.84	0.79	0.57

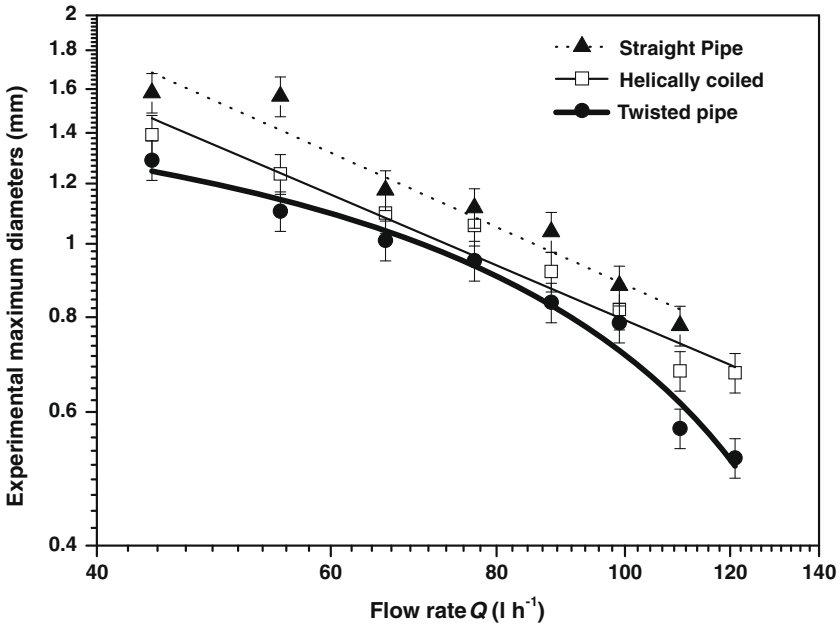

Fig. 6. Experimental d_{max} versus oil flow rate.

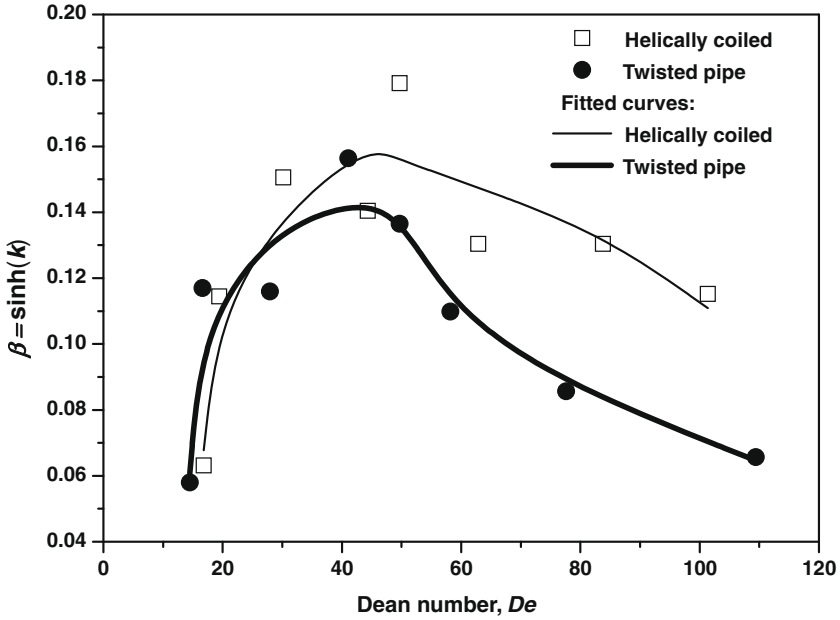

Fig. 7. Droplet diameter dispersion factor for helically coiled and chaotic twisted pipe – curves fitted using Savitzky–Golay method.

for Dean numbers higher than 50, where the chaotic behaviour begins to induce strains of the same magnitude as the shear flow. The standard deviation seems minimal at low Dean numbers where the mixing process is globally homogeneous over the whole test section but has the lowest mixing efficiency. Increasing the Dean number increases the standard deviation; i.e. the non-homogeneity of the observed emulsion is increased because of the poor radial distribution of the fluid in the mixer cross-section until an effective Dean number is achieved at which the homogeneity and mixing efficiency are intensified.

The Sauter mean diameter d_{32} is a statistical parameter that can be used to characterize the drop size distribution in the flow. This diameter, given in Eq. (5), represents the mean surface diameter:

$$d_{32} = \frac{\int \ell^3 f(\ell)\, d\ell}{\int \ell^2 f(\ell)\, d\ell} \tag{5}$$

where $f(\ell)$ is the distribution function representing the proportion of drops having a given diameter ℓ in the observed emulsion.

The proportionality between the Sauter mean diameter d_{32}, and the maximum drop diameter d_{max} is represented in Fig. 8. The experimental results show that the d_{32} and d_{max} diameters are linearly correlated in the limit of validity, here $10 < De < 110$. When the slope of the fitted line is equal to one it implies that the Sauter mean diameter is equal to the maximum drop diameter, and therefore that the drop fragmentation is uniformly distributed over the whole observed emulsion. The more this coefficient is close to 1,

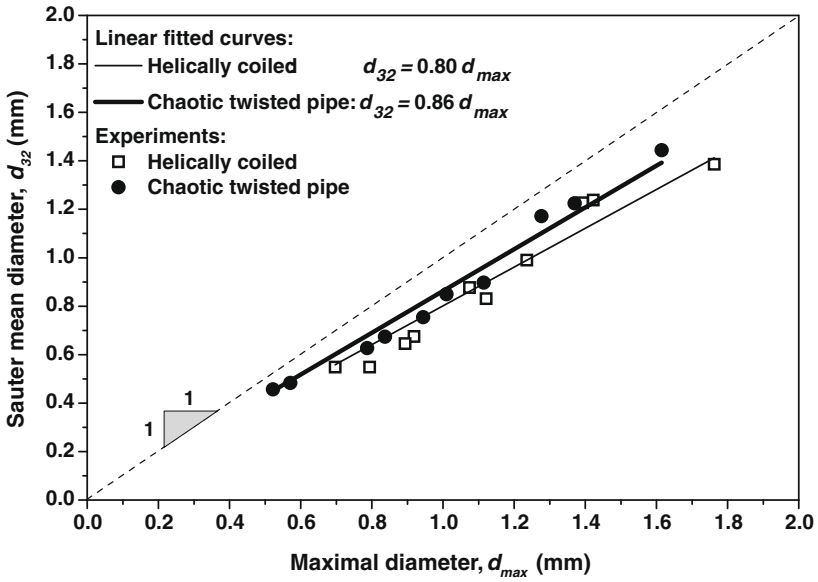

Fig. 8. Sauter mean diameter versus maximal diameter of droplets in helical coiled and chaotic advection twisted pipes.

the sharper is the distribution. It was found by Zhou and Kresta (1998) that the slope value for agitated tanks and bent tubes equipped with a static mixer is between 0.38 and 0.7; these values are much smaller than that in the present work, meaning a much less homogeneous droplet size distribution.

To investigate the efficiency of helically coiled and chaotic twisted pipe flows, the energy cost is compared in Fig. 9 with that of existing inline mixers reported by previous investigators (Haas, 1987; Streiff et al., 1997; Lemenand et al., 2003, 2005).

The interfacial contact area A is given by the Sauter diameter:

$$A = \frac{6\Phi}{d_{32}} \tag{6}$$

where Φ is the mass fraction of the dispersed phase.

The energy consumption E is calculated from the pressure drop ΔP:

$$E = \frac{\Delta P}{\rho} \tag{7}$$

The pressure drop ΔP is obtained from the theoretical correlation of Ito (1969) for laminar flow in curved pipes.

From Fig. 9, the helically coiled and chaotic twisted pipe flows are located in the small-energy consumption zone (between 1 and 12 J kg^{-1}) with a good interfacial area (between 300 and 1100 m^2 m^{-3}). The Sulzer mixer seems to have the highest interfacial area but in the range of high energy consumption. The HEV has the same behavior as the geometries studied in the present work, which are both better than Kenics static mixer.

The very low energy consumption and the relatively good interfacial contact show that helically coiled and chaotic twisted pipe flows can have good impacts in the industrial applications, especially when mixing fluids that cannot tolerate high shear rates.

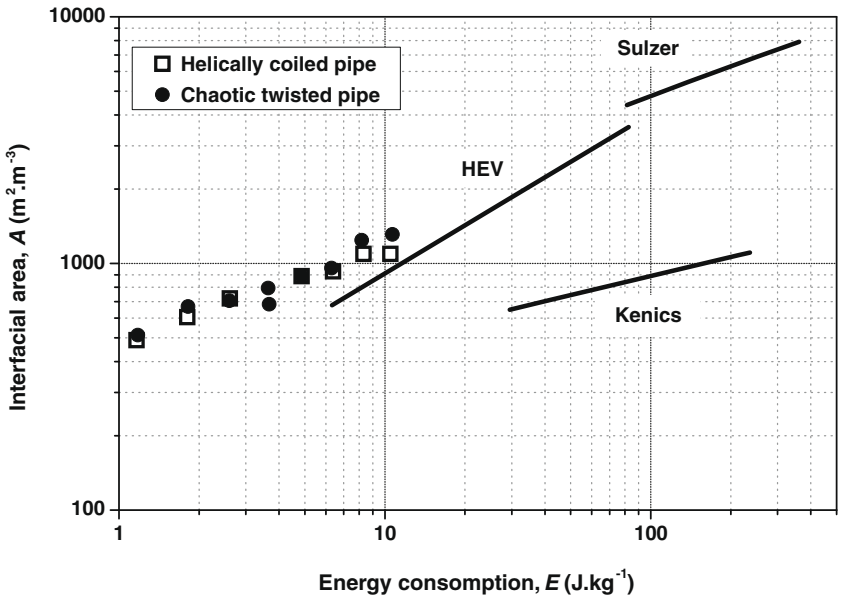

Fig. 9. Comparison of the energy consumption of the helically coiled and chaotic twisted pipes with classical static mixers (data from Thakur et al., 2003).

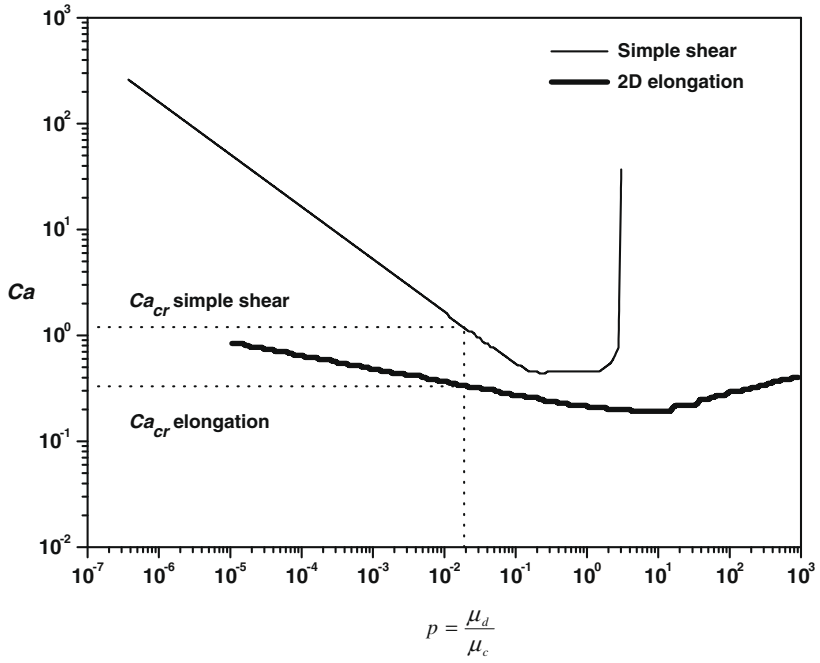

Fig. 10. Critical capillary number for shear and elongation rates; curves adapted from Grace (1982).

3. Theoretical prediction of drop diameters

3.1. Breakup theory for laminar flows

The Taylor theory for drop breakup is based on a balance among the following forces acting on a single drop of an immiscible fluid in a continuous fluid flow:

- The external viscous flow forces that tend to deform the drop; for example, in a shear flow the viscous flow force can be written as:

$$\tau = \mu_c \dot{\gamma} \tag{8}$$

  where $\dot{\gamma}$ is the shear rate.
- The interfacial or capillary forces that tend to preserve the spherical shape of a drop of diameter d_{drop}; the pressure difference at the interface balances the interfacial tension σ as expressed by the Laplace formula

$$P_{int} - P_{ext} = \frac{4\sigma}{d_{drop}} \tag{9}$$

  (P_{int} and P_{ext}) are the interior and the exterior pressures, respectively.
- The internal viscous forces that resist deformation.

In order to characterize the relative effect of the different forces, a dimensionless parameter *Ca* (the capillary number) is defined:

$$Ca = \frac{\text{Viscous forces}}{\text{Capillary forces}} = \frac{d_{drop}\tau}{2\sigma} \tag{10}$$

Grace (1982) considered that drop breakup occurs when the capillary number exceeds a critical value that depends upon the viscosity ratio (the dispersed-phase viscosity by the continuous-phase viscosity) as the manifestation of the drop's internal viscous resistance.

The dimensional values of the maximum diameter that can withstand an existing stress τ can hence be expressed by the equation

$$d_{max} = \frac{2\sigma}{\tau} Ca_{cr} \tag{11}$$

The critical capillary numbers are given by the Grace experimental curves (Fig. 10) for simple shear flows ($Ca_{cr,shear}$) and elongational flows ($Ca_{cr,elongation}$). The effective capillary number in laminar dispersion phenomena depends on the critical capillary number, Ca_{cr}, of both simple shear and elongation, and on the ratio of these deformation rates $\Gamma = \dot{\varepsilon}_{max}/\dot{\gamma}_{max}$.

By making simple linear interpolation we can find Ca_{cr} from the following expression:

$$Ca_{cr} = (1-\Gamma)Ca_{cr,shear} + \Gamma Ca_{cr,elongation} \tag{12}$$

Knowing the viscous stresses, we obtain the Γ value, and by substituting Eqs. (8) and (12) in Eq. (11), we can predict the maximum equilibrium diameter of the drop size distribution.

3.2. Determination of the strain rates in Dean flow

The analytical expressions for the velocity field in Dean flow in a curved channel were obtained from Dean's asymptotic solution (Dean, 1928). In the present work, the analytical solution was calculated from the stream function given by Jones et al. (1989) expressed in a local frame of reference, as shown in Fig. 11. All computations were carried out with MATLAB™. Table 4 presents the dimensionless variables involved in the analysis.

As in all the previous work, the parabolic axial velocity profile is assumed

$$w = 2\frac{R}{a}(1-r^2) \tag{13}$$

The potential stream function in the cross-section is given by

$$\psi = \frac{R}{Wa^2}\frac{vDe}{72}(4-r^2)(1-r^2)^2 y \tag{14}$$

where $r^2 = x^2 + y^2$ is the radial coordinate in the tube cross-section, v the effective kinematic viscosity, and W the flow mean velocity.

In the local coordinate system (x, y, z), the secondary velocity u and v can be written as

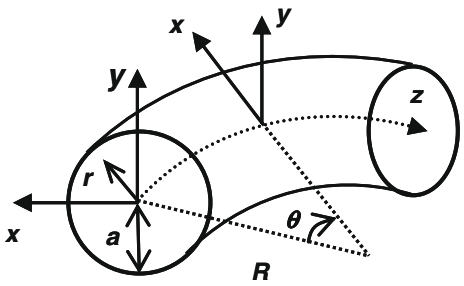

Fig. 11. Toroidal coordinates.

Table 4
Flow variables.

	Dimensionless variable	Dimensional variable
Radial distance	r	$r' = ar$
Time	t	$t' = \frac{R}{W}t$
Coordinate	x	$x' = ax$
Coordinate	y	$y' = ay$
Axial coordinate	z	$z' = az$
Velocity component	u	$u' = a\frac{W}{R}u$
Velocity component	v	$v' = a\frac{W}{R}v$
Axial velocity	w	$w' = a\frac{W}{R}w$
Shear rate	$\dot{\gamma}$	$\dot{\gamma}' = \frac{W}{R}\dot{\gamma}$
Elongation rate	$\dot{\varepsilon}$	$\dot{\varepsilon}' = \frac{W}{R}\dot{\varepsilon}$
Stream function	$\psi = \frac{R}{Wa^2}\frac{\nu De}{72}(4-r^2)(1-r^2)^2 y$	$\psi' = \frac{Wa^2}{R}\psi$
Reynolds number	$Re = 2\frac{Wa}{\nu}$	
Dean number	$De = \frac{a}{4R}Re^2$	

$$u = \frac{\partial\psi}{\partial y} \qquad v = -\frac{\partial\psi}{\partial x} \tag{15}$$

which leads to the following two equations:

$$\begin{aligned} u &= \alpha(1-r^2)[6y^2(3-r^2) - (4-r^2)(1-r^2)] \\ v &= -6\alpha xy(1-r^2)(3-r^2) \end{aligned} \tag{16}$$

where $\alpha = \frac{Re}{144}$.

For the fully developed flow, the velocity field in the pipe cross-section appears to be independent of z. The effect of the radius of curvature is not explicit in this system because of the dimensionless scaling of the coordinates.

The generalized shear rate $\dot{\gamma}$ and elongation rate $\dot{\varepsilon}$ given by Eq. (17), and calculated from the analytical derivatives of the velocity components, are given in Germain (1962) and also in Bird (2007), and are defined, respectively, as the second invariant of the deformation rate tensor and the extension along the axis carried by the first eigenvector of the deformation rate tensor. These expressions are also used by Khakhar and Ottino (1986).

$$\begin{cases} \dot{\gamma} = \left(2\left(\frac{\partial u}{\partial x}\right)^2 + 2\left(\frac{\partial v}{\partial y}\right)^2 + 2\left(\frac{\partial w}{\partial z}\right)^2 + \left(\frac{\partial u}{\partial y} + \frac{\partial v}{\partial x}\right)^2 \right. \\ \qquad \left. + \left(\frac{\partial u}{\partial z} + \frac{\partial w}{\partial x}\right)^2 + \left(\frac{\partial v}{\partial z} + \frac{\partial w}{\partial y}\right)^2\right)^{1/2} \\ \dot{\varepsilon} = \frac{u^2\left(\frac{\partial u}{\partial x}\right) + v^2\left(\frac{\partial v}{\partial y}\right) + w^2\left(\frac{\partial w}{\partial z}\right) + uv\left(\frac{\partial u}{\partial y} + \frac{\partial v}{\partial x}\right) + uw\left(\frac{\partial u}{\partial z} + \frac{\partial w}{\partial x}\right) + vw\left(\frac{\partial v}{\partial z} + \frac{\partial w}{\partial y}\right)}{u^2 + v^2 + w^2} \end{cases} \tag{17}$$

In a flow, it is the maximal value of the shear and elongation rates, $\dot{\gamma}_{\text{max helic}}$ and $\dot{\varepsilon}_{\text{max helic}}$, that determine the droplets' maximum diameter. These values are obtained from Eq. (17) and are expressed as:

$$\begin{cases} \dot{\gamma}_{\text{max helic}} = 4\frac{R}{a}\left[1 + \frac{1}{150}\frac{a}{R}De\right]^{0.5} \\ \dot{\varepsilon}_{\text{max helic}} = 1.1\frac{R}{a}\left[1 + 2\times 10^{-7}\frac{a}{R}De^3\right]^{0.7} \end{cases} \tag{18}$$

The classical dimensionless maximal shear rate for the straight pipe is given by

$$\dot{\gamma}_{\text{max straight tube}} = 4\frac{R}{a} \tag{19}$$

For the range of Dean numbers studied here, the maximum shear and elongation rates in the flow cross-section fitted with trend curves (Eqs. (18) and (19)) are presented in Fig. 12 for use in the dispersion model. It can be noted that, following the analytical solution, the helical-pipe flow shear rate begins to deviate from that of the straight pipe flow at an estimated Dean number around $De = 55$. On the other hand, for a Dean number of about 600, the elongation rate begins to dominate the shear rate and governs the dispersion process. This would lead to a decrease of 1/3 in the diameter and would enhance the eventual benefits of the chaotic advection flow. This range of Dean number, however, cannot be achieved in the present experimental setup and will not be discussed further.

The theoretical maximum diameters of the drops can be calculated by using Eq. (11) coupled with the above maximum shear rates (Eqs. (18) and (19)). Theoretical and experimental maximum diameters are compared in Fig. 13. The theoretical curve is unique for the twisted-pipe flow (chaotic advection) and the helically coiled pipe flow, since the Eulerian velocity fields are the same in both cases.

The experimental maximum diameters of the drops are also shown in Fig. 13. At least a part of the discrepancy between experimental and theoretical results can be explained by the numerous hypotheses of the theoretical models, both the Taylor–Grace model (based on an assumed dynamic equilibrium situation) and the Dean–Jones equations (which give an approximate solution for the velocity field). Nevertheless, the maximum global difference with experimental results does not exceed 10%, showing that the present theoretical approach captures the basic physics underlying the problem.

It can be noticed in Fig. 13 that the maximum drop diameters measured in the chaotic flow are smaller than in the helically coiled pipe flow, suggesting that, in addition to the deformation rates responsible for drop breakup in the helically coiled pipe flow, there exists another mechanism that leads to better drop fragmentation in the chaotic advection flow. It is shown in the next section through a Lagrangian analysis that this mechanism is, in fact, the way in which droplets are randomly passed to zones of higher shear and strain rates in the chaotic advection flow compared to the helically coiled flow.

4. Lagrangian analysis of the flow

4.1. Mechanical history

This Lagrangian study is based on following a fluid particle trajectory from its initial location at the inlet up to the outlet, as well as on tracking the shear and elongations to which it is submitted, i.e. its "mechanical history". The Lagrangian equations for the passive advection of a fluid particle in a three-dimensional space are given by the following dynamical system:

$$\begin{cases} \dot{x} = u(x,y,z,t) \\ \dot{y} = v(x,y,z,t) \\ \dot{z} = w(x,y,z,t) \end{cases} \tag{20}$$

The equations are the same for helically coiled and twisted pipe flows. For the helically coiled pipe, there is no change of the frame reference axes while passing from one elbow to another. For the twisted pipe flow, the frame reference axes are rotated of ±90° as follows: at the end of each elbow of even number, a rotation of

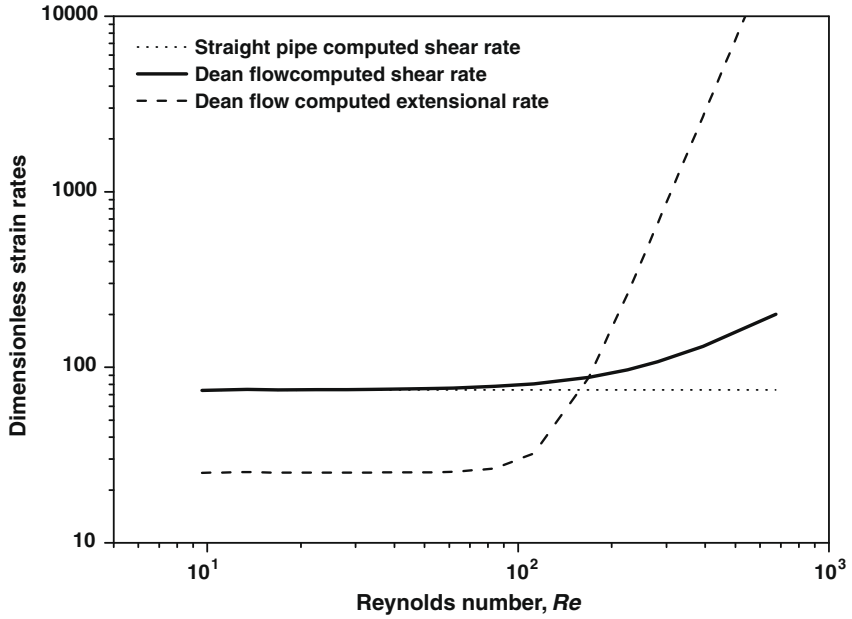

Fig. 12. Computed strain rates in straight pipe and helically coiled pipe – maximum values in pipe cross-section.

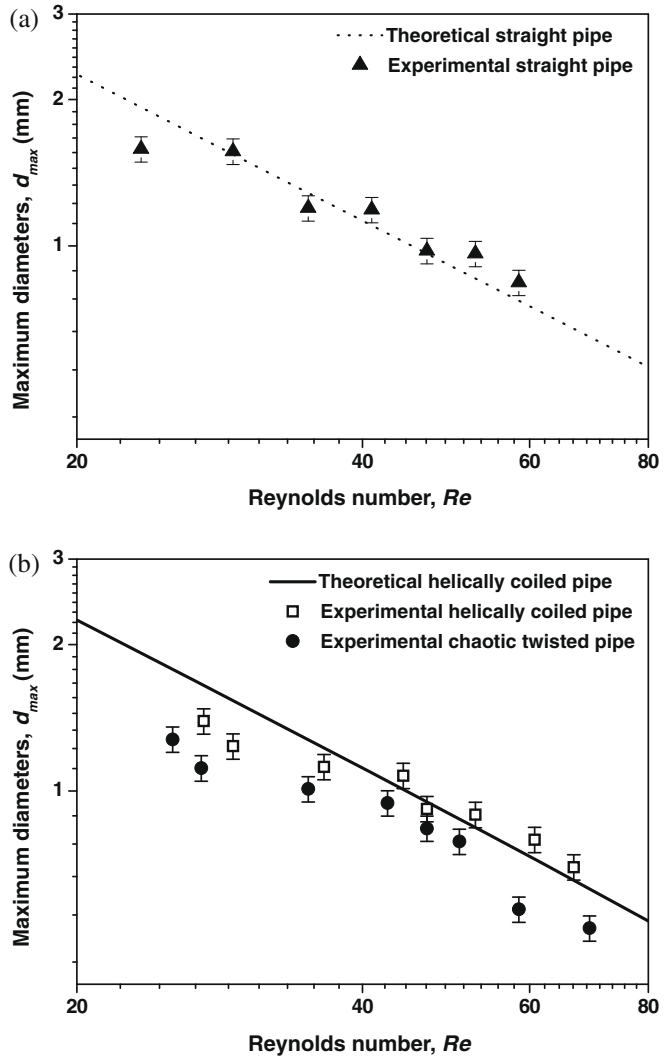

Fig. 13. Droplet diameters – experiments compared with theoretical values: (a) straight pipe, and (b) helically coiled and chaotic twisted pipes.

90° is applied to the reference axes (i.e. we replace x by y, and y by $-x$ in the velocity equations), otherwise, at the end of each elbow of odd number, a rotation of −90° is applied.

Integration along the trajectory is carried out in the numerical procedure by a fourth-order Runge–Kutta scheme. The passage of a particle from the outlet of one bend to the inlet of the next must be calculated very accurately; the convergence is realized by a Newton–Raphson iterative process.

The sensitivity of the trajectory to the time step dt was computed by studying the time step at which the solution converges to a constant value for different Dean numbers and the final position of the particle becomes independent of the maximal dt value given in

$$dt = \frac{\left(\frac{\pi}{2}\frac{R}{a}\right)}{W} \cdot 10^{-4} \tag{21}$$

Results for Dean number 150 are illustrated in Fig. 14, where the trajectories of a passive fluid particle in the helically coiled pipe flow are compared with those of a twisted-pipe flow along 25 bends and for two initial positions. In the chaotic flow, the particle sweeps all the cross-section of the pipe, while in helically coiled flow the particles remain on the same trajectory, depending on their initial positions. It can even be noted that in the helically coiled flow, for injection location $x_0 = 0$, $y_0 = 0.43$, the particle leaves the last bend at exactly the same cross-sectional position at which it entered the pipe; this point is the centre of the Dean roll-cell at which $u = v = 0$ and therefore there is no radial velocity.

Fig. 15 shows the Poincaré sections for the two configurations, helically coiled and chaotic, and for an initial position of a disk of diameter equal to 5% of the pipe cross-sectional diameter, made up of 5000 neighbouring points. It is observed again that in the helically coiled configuration, the particles remain in the Dean roll-cell, while in the chaotic advection case the particles spread over the whole tube cross-section. This has a direct consequence for the mechanical history of the fluid particle. In fact, along its chaotic trajectories the particle visits the zones of maximum shear and elongational rates. Figs. 16 and 17 show the particle's mechanical history, that is, the dimensionless shear and elongation rates that a fluid particle undergoes at each moment along 25 bends,

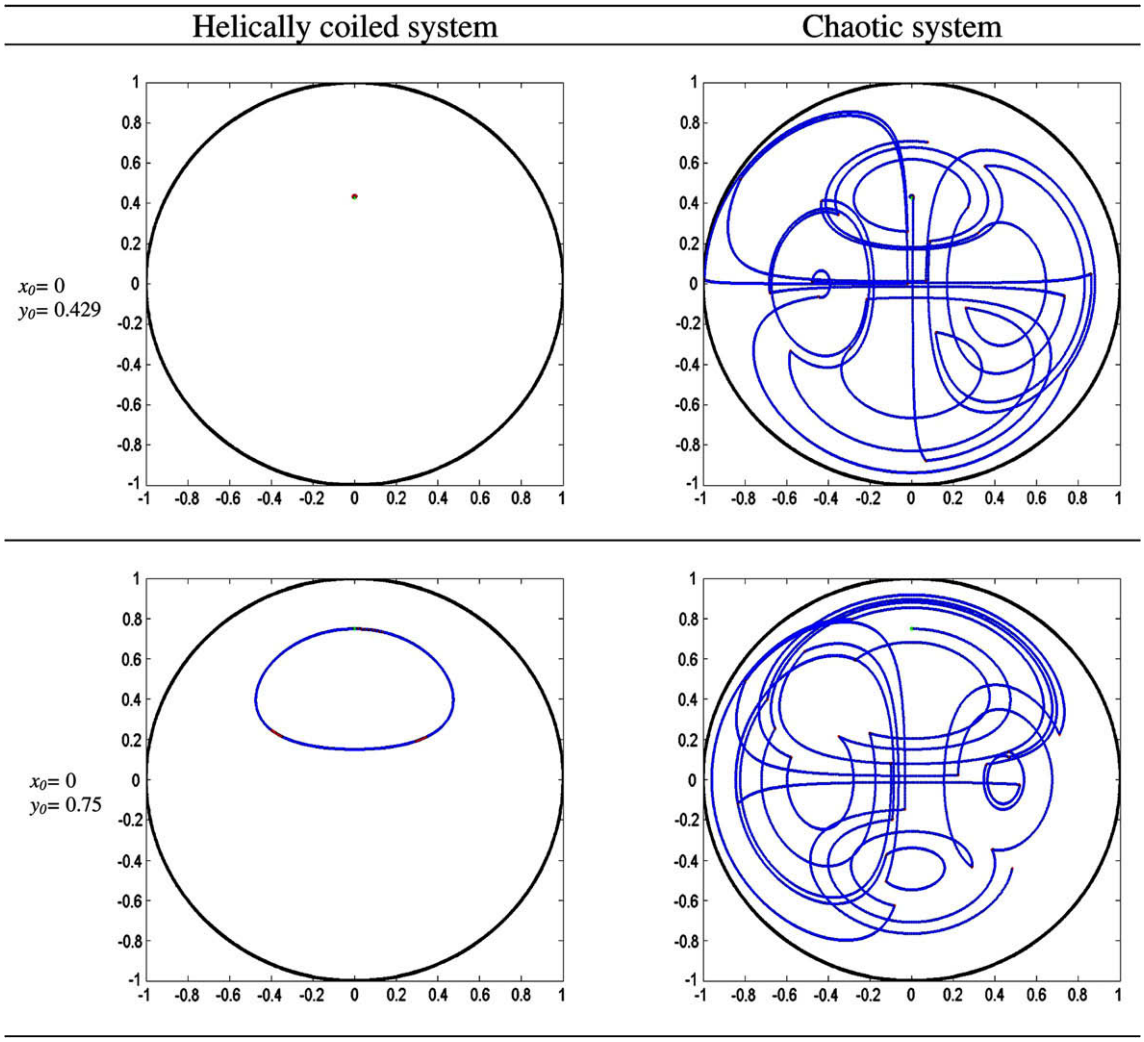

Fig. 14. Trajectories of passive tracer ($De = 150$, $Re = 81$, $Nc = 25$).

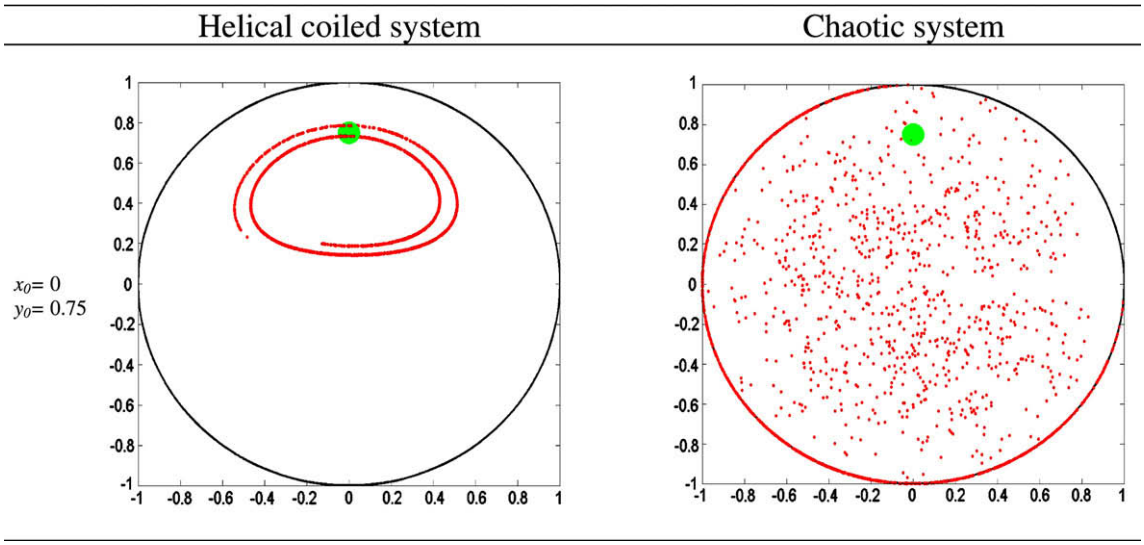

Fig. 15. Poincaré sections ($De = 150$, $Re = 81$, $Nc = 25$).

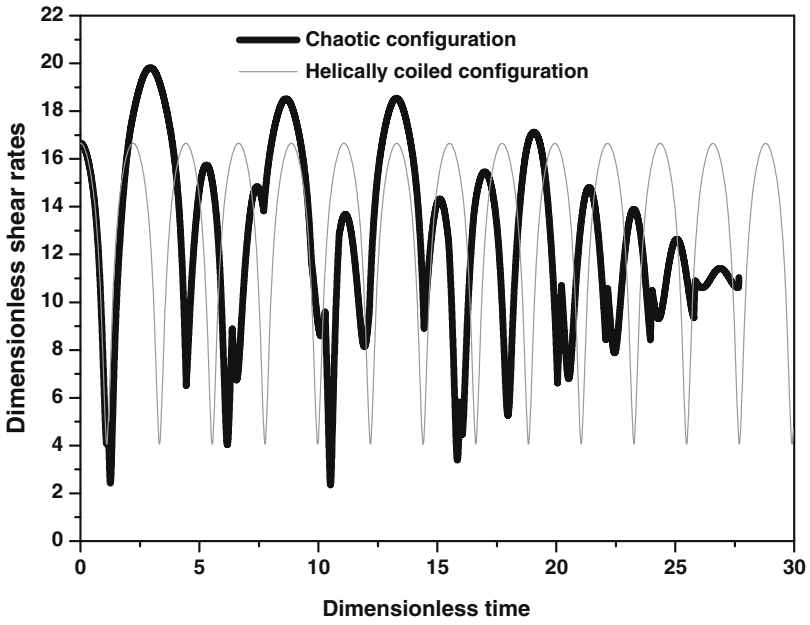

Fig. 16. Mechanical history of shear rates ($x_0 = 0$, $y_0 = 0.75$, $De = 100$).

for $De = 100$ and initial position $x_0 = 0$, $y_0 = 0.75$. In the helically coiled configuration, the particle has a periodic trajectory and remains caged between two limiting (maximum and minimum) values of the viscous stress. On the other hand, in a chaotic flow the particle randomly undergoes all levels of strain rates, especially the maximum values that are more efficient for drop breakup.

4.2. Residence time distribution (RTD)

The residence time distribution can be established by computing the trajectories for a sufficiently large number of particles (about 6000), which are uniformly distributed in the inlet plane section. Fig. 18 presents the RTD as a function of dimensionless residence time defined in Table 4 for helically coiled pipe flow and twisted-pipe chaotic advection flow. In this figure are also superposed the RTD for a straight pipe flow and an axial dispersed plug flow as expressed in Eqs. (22) and (23), respectively:

$$f(t) = \frac{1}{2}\left(\frac{Pe_L}{\pi\Theta}\right)^{\frac{1}{2}} \exp\left(-\frac{Pe_L(1-\Theta)^2}{4\Theta}\right) \tag{22}$$

$$f(t) = \frac{1}{2t\Theta^2} H\left(t - \frac{tm}{2}\right) \tag{23}$$

where t is the residence time, $t_m = \frac{L}{W}$ the mean residence time and $\Theta = \frac{t}{t_m}$ the reduced time.

It can be seen from Fig. 17 that even for a small Dean number of 100, while the helically coiled pipe flow presents a RTD profile similar to that of straight pipe, the RTD profile of the chaotic advection

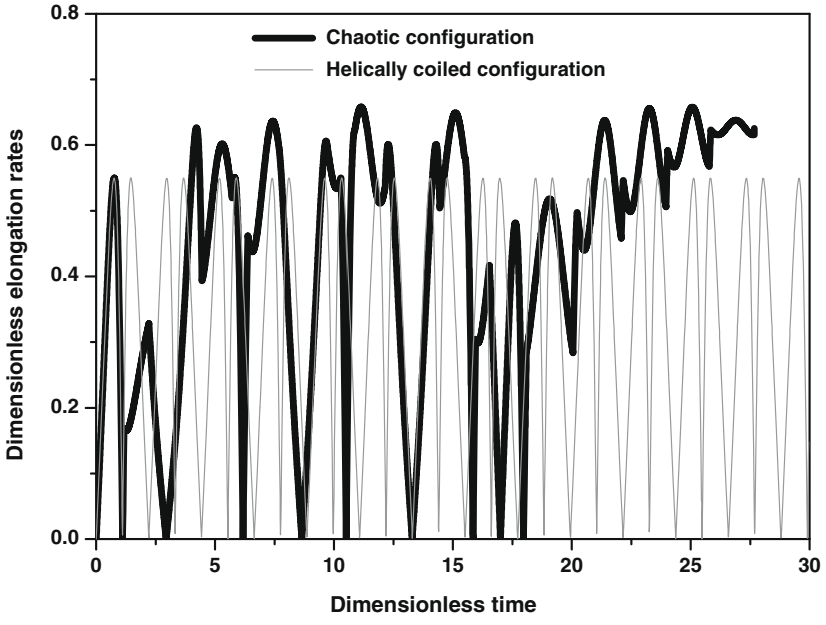

Fig. 17. Mechanical history of absolute elongation rates ($x_0 = 0$, $y_0 = 0.75$, $De = 100$).

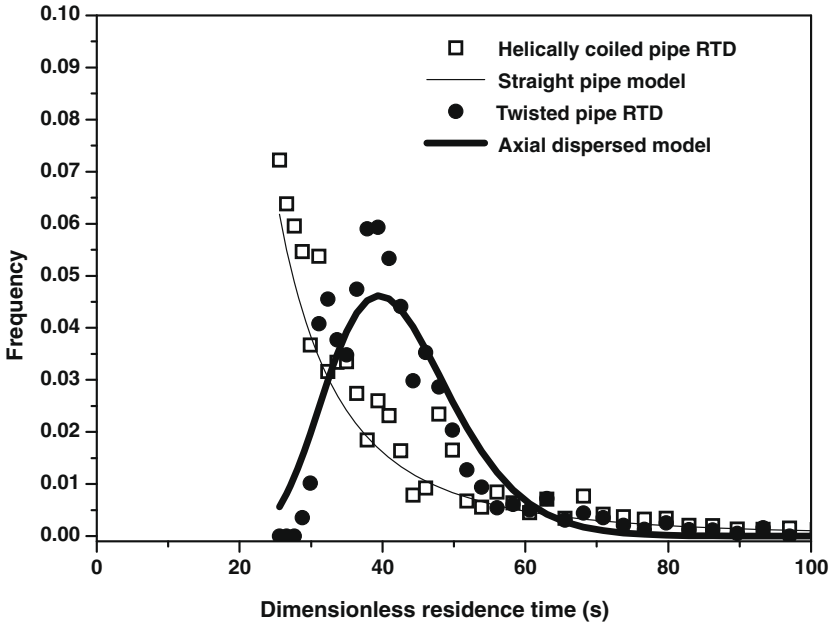

Fig. 18. Dimensionless residence time distribution: 25 bends for $De = 100$.

twisted pipe can be modeled by an axial dispersed plug flow. In this situation, the Péclet number based on the pipe length L, $Pe_L = \frac{WL}{D_{ax}}$, is about 43, where, D_{ax} is the axial diffusion coefficient.

In agreement with the trajectories presented in Fig. 13, the residence time dispersion is narrower in the chaotic advection configuration, accounting for the radial transfer enhancement. This result was also found by Castelain et al. (1997) in studying the RTD in chaotic twisted pipe and helically coiled pipe flows.

5. Conclusions

Careful experiments were carried out on liquid/liquid dispersion in oil/water flows to assess the effects of chaotic advection on droplet breakup, in terms of both the mean diameter and the size homogeneity. Both properties have strategic implications in many technological processes in the pharmaceutical and cosmetics industries, as well as in new biological renewable-energy processes. These experiments showed that the chaotic advection flow generated in the twisted pipe clearly increases the efficiency of contactors and mixers by providing smaller and more homogeneously dispersed droplets. The energy expenditure to obtain this dispersion remains similar to that of the rival technology, the helically coiled mixer.

To clarify the physical mechanism underlying this high dispersion efficiency of the chaotic advection flow compared to similar laminar flows, and also for the future design and optimization of multifunctional heat exchangers and reactors, a mechanistic modelling of this flow was undertaken. Both Eulerian and Lagrangian approaches were applied to three flow geometries in the laminar regime: straight, helically coiled and twisted pipes. While in most fluid dynamics problems the ultimate aim is to obtain the velocity field in the flow, in the chaotic advection problem the velocity field is the starting point. To this end, we used the analytical expression of the stream function in a curved pipe obtained by Dean (1927) as the building block of the model. Shear and elongation rates were then calculated and were used in conjunction with Taylor–Grace theory to study droplet breakup.

It was shown that the Eulerian approach cannot explain the higher dispersion efficiency of the chaotic advection flow. On the contrary, the Lagrangian approach allows calculation of the fluid particle trajectories and especially the "mechanical history" of a fluid particle. From this we showed that chaotic advection causes fluid particles to make random visits to zones of high shear and elongation rates and therefore contributes further to droplet breakup.

The model also allowed calculation of the RTD of fluid particles in helically coiled and twisted-pipe flows. The RTD analysis revealed that even for very small Dean number laminar flows, the chaotic advection flow shows a RTD distribution as narrow as an axially dispersed plug flow, while the helically coiled tube flow has a residence time distribution similar to a straight tube flow. Thus in liquid/liquid dispersion the chaotic advection flow has two principal advantages over its counterpart helically coiled pipe flow: first, generation of smaller droplets, second, a more homogenous droplet diameter distribution.

The mechanistic model developed in this work provides a solid basis for obtaining physical insight into dispersion phenomena by laminar flows and offers a powerful design and optimization tool to designers of future innovative devices. Future work will focus on gas/liquid dispersion by chaotic advection.

Acknowledgements

The authors gratefully acknowledge Dr. P. Carrière of LMFA (Laboratoire de Mécanique des Fluides et d'Acoustique) of École Centrale de Lyon (France), for fruitful and enlightening discussions.

References

Acharya, N., Sen, M., Chang, H.C., 1992. Heat transfer enhancement in coiled tubes by chaotic advection. Int. J. Heat Mass Transfer 35, 2475–2489.
Aref, H., 1984. Stirring by chaotic advection. J. Fluid Mech. 143, 1–21.
Bird, R.B., 2007. Transport Phenomena. Wiley, New York.
Castelain, C., Mokrani, A., Legentilhomme, P., Peerhossaini, H., 1997. Residence time distribution in twisted pipe flows: helically coiled system and chaotic system. Exp. Fluids 22, 359–368.
Dean, W.R., 1927. Note on the motion of fluid in curved pipe. Philos. Mag. 4, 208–227.
Dean, W.R., 1928. The streamline motion of fluid in curved pipe. Philos. Mag. 5, 673–695.
Germain, P., 1962. Mécanique des milieux continues. Ed. Masson.

Grace, H.P., 1982. Dispersion phenomena in high viscosity immiscible fluid systems and application of static mixers as dispersion devices in such systems. Chem. Eng. Commun. 14, 225–277.
Haas, P.A., 1987. Turbulent dispersion of aqueous drops in organic liquids. AIChE J. 33, 987–995.
Ito, H., 1969. Laminar flow in curved pipes. Z. Angew. Math. Mech. 11, 653–663.
Jones, S.W., Thomas, O.M., Aref, H., 1989. Chaotic advection by laminar flow in a twisted pipe. J. Fluid Mech. 209, 335–357.
Khakhar, D.V., Ottino, J.M., 1986. Deformation and breakup of slender drops in linear flows. J. Fluid Mech. 166, 265–285.
Le Guer, Y., Peerhossaini, H., 1991. Order breaking in Dean-flow. Phys. Fluids A 3, 1029–1032.
Le Guer, Y., Castelain, C., Peerhossaini, H., 2001. Experimental study of chaotic advection regime in a twisted duct flow. Eur. J. Mech. B 20, 205–232.
Lemenand, T., Peerhossaini, H., 2002. A thermal model for prediction of the Nusselt number in a pipe with chaotic flow. Appl. Therm. Eng. 22, 1717–1730.
Lemenand, T., Della Valle, D., Zellouf, Y., Peerhossaini, H., 2003. Droplet formation in turbulent mixing of two immiscible fluids in a new type of static mixer. Int. J. Multiphase Flow 29, 813–840.
Lemenand, T., Dupont, P., Della Valle, D., Peerhossaini, H., 2005. Turbulent mixing of two immiscible fluids. J. Fluids Eng. 127, 1132–1139.
Mokrani, A., Castelain, C., Peerhossaini, H., 1998a. Mesure du chaos dans les systèmes conservatifs en vue de l'étude des transferts dans les systèmes ouverts. Rev. General. Therm. 37, 459–474.
Mokrani, A., Castelain, C., Peerhossaini, H., 1998b. The effect of chaotic advection on heat transfer. Int. J. Heat Mass Transfer 40, 3089–3104.
Peerhossaini, H., Castelain, C., Le Guer, Y., 1993. Heat exchanger design based on chaotic advection. Exp. Therm. Fluid Sci. 7, 333–344.
Streiff, F.A., Mathys, P., Fischer, T.U., 1997. New fundamentals for liquid–liquid dispersion using static mixers. In: Recents Progrés en Genie des Procedés 11 (51, Mixing 97: Recent Advances in Mixing), pp. 307–314.
Taylor, G., 1953. Dispersion of soluble matter flowing slowly through a tube. Proc. Roy. Soc. Lond. A 219, 186–203.
Thakur, R.K., Vial, C., Nigam, K.D.P., Nauman, E.B., Djelveh, G., 2003. Static mixers in the process industries – a review. Inst. Chem. Eng. 81, 787–826.
Zhou, G., Kresta, S.M., 1998. Correlation of mean drop size and minimum drop size with the turbulence energy dissipation and the flow in an agitated tank. Chem. Eng. Sci. 53, 2063–2079.

REFERENCES BIBLIOGRAPHIQUES

ADEME, *Maîtrise de l'énergie et énergie renouvelable - Chiffres clé*, Publication, 2008.

Alben S., Simulating the dynamics of flexible bodies and vortex sheets, *J. Computational Physics* 228 (2009) 2587-2603.

Al Taweel A.M., Chen C., A novel static mixer for the effective dispersion of immiscible liquids, *Trans. IChmE* 74 (1996) 445-450.

Anxionnaz Z., Cabassud M., Gourdon C., Tochon P., Heat exchanger/reactors (HEX reactors): Concepts, technologies: State-of-the-art, *Chem. Eng. Process.* 47 (2008) 2029-2050.

Anxionnaz Z., *Étude de l'influence de la géométrie des canaux sur les performances d'un échangeur/réacteur*, Thèse, Université de Toulouse, 2009, France.

Aref H., Stirring by chaotic advection, *J. Fluid Mech.* 143 (1984) 1-21.

Aubin J., Ferrando M., Jiricny V., Current methods for characterising mixing and flow in microchannels, *Chem. Eng. Sci.* (2010) doi:10.1016/j.ces.2009.12.001

Baldyga J., Bourne J.R., Principles of micro-mixing, Encyclopedia Fluid Mech., Gulf Publishing, Houston, TX, 1986.

Baldyga J., Bourne J.R., Simplification of micro-mixing calculations. I. Derivation and application of a new model, *Chem. Eng. J.* 42 (1989) 83-92.

Baldyga J., Bourne J.R., Comparison of the engulfment and the interaction by exchange with the mean micro-mixing models, *The Chem. Eng. J.* 45 (1990) 25-31.

Baldyga J., Bourne J.R., *Turbulent mixing and chemical reaction*, Wiley, Chichester, England, 1999.

Baldyga J., Bourne J.R., B. Dubuis, A.W. Etchells, R.V. Gholap, B. Zimmermann, Jet reactor scale-up for mixing controlled reactions, *Chem. Eng. Res. Des.* 75 (1995) 497-502.

Baldyga J., Bourne J.R., Hearn S.J., Interaction between chemical reactions and mixing on various scales, *Chem. Eng. Sci.* 52 (1997) 457-466.

Baldyga J., Bourne J.R., Yang Y., Influence of feed pipe diameter on meso-mixing in stirred tank reactors, *Chem. Eng. Sci.* 48 (1993) 3383-3390.

Baldyga J., Pohorecki R., Turbulent micromixing in chemical reactors – A review, *The Chem. Eng. J.* 58 (1995) 183-195.

Batdyga J., Roieli A., Mostert F., A model of laminar micromixing with application to parallel chemical reactions, *Chem. Eng. J.* 69 (1998) 7-20.

Batchelor G.K., *The Theory of homogeneous turbulence*, Cambridge University Press, Cambridge, England, 1953.

Bejan, A., *Entropy generating minimization*, CRC Press, 1996.

Boomsma K., Poulikakos D., Zwick F., Metal foams as compact high performance heat exchangers, Mech. Materials 35 (2003) 1161-1176.

Bourne J.R., Kut O.M., Lenzner J., An improved reaction system to investigate micromixing in high-intensity mixers, *Ind. Eng. Chem. Res.* 31 (1992) 949-958.

Bourne J.R., Mixing and the selectivity of chemical reactions, *Org. Proc. Res. Dev.* 7 (2003) 471-508.

Bourne J.R., Comments on the iodide/iodate method for characterising micro-mixing, *Chem. Eng. J.* 140 (2008) 638-641.

Branebjerg J., Fabius B., Gravesen B., *Application of miniature analysers: from microfluidic compnents to mTAS*, Van den Berg A., Bergfeld P. (Eds.), Micro Total Analysis Systems, Kluwer, Dordrecht, pp.141-151, 1995.

Breysse J., Mathieu C., Fine chemical processes: diagnosis and performance optimisation, *Oil & Gas Sci. Technology – Rev. IFP* 55 (2000) 227-229.

Brundtland H., *Notre avenir à tous*, Commission mondiale sur l'environnement et le développement, Assemblée nationale des Nations Unies, 1986.

Carrière P., On a three-dimensional implementation of the baker's transformation, *Phys. Fluids* 19 (2007) 118110.

Castelain C., Mokrani A., Legentilhomme P., Peerhossaini H., Residence time distribution in twisted pipe flows: helically coiled system and chaotic system, *Exp. Fluids* 22 (1997) 359-368.

Cazan R., Aiduna C.K., Experimental investigation of the swirling flow and the helical vortices induced by a twisted tape inside a circular pipe, *Phys. Fluids* 21 (2009) 037102.

Chemineer Inc., *Kenics: Static Mixing Technology*, Product Bulletin 800, USA, 2008.

Colloque Énergie CNRS, *Programme interdisciplinaire énergie du CNRS*, 7ème Colloque énergie, Polytech, Université de Nantes, 2009.

Corrsin S., The isotropic turbulent mixer: Part II. Arbitrary Schmidt number, AIChE J. 10 (1964) 870-877.

Dean W.R., Note on the motion of fluid in curved pipe, *Philos. Mag.* 4 (1927) 208-227.

Dean W.R., The streamline motion of fluid in curved pipe, *Philos. Mag.* 5 (1928) 673-695.

Della Valle D., Peerhossaini H., Lemenand T., Mohand Kaci H., Mise à l'échelle industrielle des réacteur-échangeur multifonctionnels pour l'amélioration de l'efficacité énergétique des procédés chimiques, 7ème Colloque énergie, Polytech, Université de Nantes, pp. 20, 2009.

Doligalski T.L., Smith C.R., Walker J.D.A, Vortex interactions with walls, *Annu. Rev. Fluid Mech.* 26 (1994) 573-616.

Dong D., Meng H., Flow past a trapezoidal tab, *J. Fluid Mech.* 510 (2004) 219-242.

Durandal C., *Étude du micromélange dans les réacteurs chimiques en écoulement turbulent : évaluation des modèles de micromélange pour l'interprétation des données de la sonde chimique*, Thèse, Université de Nantes, France, 2007.

Dushman S., The rate of the reaction between iodic and hydriodic acids, *J. Phys. Chem.* 8 (1904) 453.

Elavarasan R., Meng H., Flow visualization study of role of coherent structures in a tab wake, *Fluid Dyn. Res.* 27 (2000) 183-197.

Eiamsa-ard S., Wongcharee K., Eiamsa-ard P., Thianpong C., Heat transfer enhancement in a tube using delta-winglet twisted tape inserts, *App. Thermal Eng.* 30 (2010) 310-318.

Falk L., Commenge J.M., Performance comparison of micro-mixers, Chem. Eng. Sci. 65 (2010) 405-411.

Fernando H.J.S., Zajic D., Di Sabatino S., Dimitrova R., Hedquist B., Dallman A., Flow, turbulence, and pollutant dispersion in urban atmospheres, *Phys. Fluids* 22 (2010) 051301.

Ferrouillat S., *Étude du micro-mélange pour la caractérisation des performances d'échangeur-réacteur compacts multifonctionnels*, Thèse, Université de Nantes, France, 2004.

Ferrouillat S., Tochon P., Della Valle D., Peerhossaini H., Open loop thermal control of exothermal chemical reactions in multifunctional heat exchangers, *Int. J. Het Mass Transfer* 49 (2006a) 2479-2490.

Ferrouillat S., Tochon P., Garnier C., Peerhossaini H., Intensification of heat transfer and mixing in multifunctional heat exchangers by artificially generated streamwise vorticity, App. Therm. Eng., 26 (2006b) 1820-1829.

Ferrouillat S., Tochon P., Peerhossaini H., Micromixing enhancement by turbulence: Application to multifunctional heat exchangers, *Chem. Eng. Proc.* 45 (2006c) 633-640.

Fiebig M., Vortices, generators and heat transfer, *Trans. IChem.* 76 (1998) 108-123.

Fournier M.C., Falk L., Villermaux J., A new parallel competing reaction system for assessing micro-mixing efficiency - determination of micromixing time by simple mixing model, *Chem. Eng. Sci.* 51 (1996a) 5053-5064.

Fournier M.C., Falk L., Villermaux J., A new parallel competing reaction system for assessing micro-mixing efficiency - experimental approach, *Chem. Eng. Sci.* 51 (1996b) 5053-5064.

GIEC, *Bilan 2007 des changements climatiques : rapport de synthèse*, GIEC, Genève, Suisse, 103 pages, 2008.

Gibson M.M., Launder B.E., Ground effects on pressure fluctuations in the atmospheric boundary layer, *J. Fluid Mech.* 86 (1978) 491-511.

Grace H.P., Dispersion phenomena in high viscosity immiscible fluid systems and application of static mixers as dispersion devices in such systems, Chem. Eng. Commun. 14 (1982) 225-277.

Gretta W.J., Smith C.R., The flow structure and statistics of a passive mixing tab*, J. Fluid Eng.* 115 (1993) 255-263.

Guichardon P., Falk L., Characterisation of micro-mixing efficiency by the iodide-iodate reaction system. Part I: experimental procedure, *Chem. Eng. Sci.* 55 (2000) 4233-4243.

Guichardon P., Falk L., Villermaux J., Characterisation of micro-mixing efficiency by the iodide-iodate reaction system. Part II: kinetic study, *Chem. Eng. Sci.* 55 (2000) 4245-4253.

Gnielinski V., New equations for heat and mass transfer in turbulent pipe and channel flow, *Int. Chem. Eng.* 16 (1976) 359-368.

Guo Z.Y., Li D.Y., Wang B.X., A novel concept for convective heat transfer enhancement, *Int. J. Heat Mass Transfer* 41 (1998) 2221-2225.

Habchi C., Lemenand T., Della Valle D., Peerhossaini H., Liquid/liquid dispersion in a chaotic advection flow, *Int. J. Multiphase Flow* 35 (2009a) 485-497.

Habchi C., Ouarets S., Lemenand T., Della Valle D., Bellettre J., Peerhossaini H., Influence of viscosity ratio on droplets formation in a chaotic advection flow, *Int. J. Chem. Reactor Eng.* 7 (2009b) A50.

Habchi C., Lemenand T., Della Valle D., Peerhossaini H., Assessment of micro-mixing in turbulent flows by chemical probe, *Chem. Eng. J.*, Submitted, 2010a.

Habchi C., Lemenand T., Della Valle D., Anxionnaz Z., Tochon P., Cabassud M., Gourdon C., Peerhossaini H., A new adaptive procedure for using chemical probes to characterize mixing, *Chem. Eng. Sci.*, Submitted, 2010b

Habchi C., Lemenand T., Della Valle D., Peerhossaini H., Turbulence behavior of artificially generated vorticity, *J. Turbulence*, 11 N°36 (2010c) 1-28.

Habchi C., Lemenand T., Della Valle D., Peerhossaini H., Alternating mixing tabs in multifunctional heat exchanger-reactor, *Chem. Eng. Process.* 49 (2010d) 653-661.

Habchi C., Lemenand T., Della Valle D., Peerhossaini H., Turbulent mixing and residence time distribution in novel configurations of multifunctional exchanger-reactor, *Chem. Eng. Process.* 49 (2010e) 1066-1075.

Habchi C., Lemenand T., Della Valle D., Peerhossaini H., Convective heat transfer in turbulent vortical flows, *Int. J. Thermal Sci.*, Submitted, 2010f.

Habchi C., Lemenand T., Della Valle D., Peerhossaini H., *Nouvelles géométries pour l'intensification de l'efficacité énergétique d'un échangeur/réacteur multifonctionnel: Rangées alternées-Rangées décalées*. Enveloppes SOLEAU n° 356995 (2009d).

Habchi C., Lemenand T., Della Valle D., Peerhossaini H., *Intensifying the turbulent kinetic energy dissipation rate by redistributing the streamwise vorticity*, GPE-EPIC, Venise, Italy, 2009e.

Habchi C., Khaled M., Lemenand T., Della Valle D., Peerhossaini H., *The temperature distribution in Dean flow: an analytical approach*, ICTEA, Abu Dhabi, UAE, 2009f.

Habchi C., Ouarets S., Lemenand T., Della Valle D., Bellettre J., Peerhossaini H., *Viscosity effects on liquid-liquid dispersion in laminar flows*, ICHMT, Hamamat, Tunisia, 2009g.

Habchi C., Lemenand T., Della Valle D., Peerhossaini H., *Turbulent mixing and residence time distribution in novel multifunctional heat exchangers-reactors*, SFGP, Marseille, France, 2009h.

Habchi C., Lemenand T., Della Valle D., Peerhossaini H., *Effets des rangées de perturbateurs pariétaux sur les transferts de chaleur*, Proceedings SFT, Vannes, France, 2009i.

Habchi C., Lemenand T., Della Valle D., Peerhossaini H., *On the correlation between vorticity flux and heat transfer coefficient*, IHTC-ASME, Washington, USA, 2010h.

Habchi C., Lemenand T., Della Valle D., Peerhossaini H., *On the synergy field between velocity vector and temperature gradient in turbulent vortical flows*, ThETA 3, Cairo, Egypt, 2010i.

Harion J.L., Peerhossaini H., Habchi C., Lemenand T., Della Valle D., *Échangeurs-réacteurs multifonctionnels continus: amélioration des performances par une modification passive dynamique du fonctionnement*. Enveloppes SOLEAU n° 348694 (2009).

Hessel V., Hardt S., Löwe H., Schönfeld F., Laminar mixing in different interdigital micromixers: I.Experimental characterization, *AIChE J.* 49 (2003) 566-577.

Hesselgreaves J.E., Rationalisation of second law analysis of heat exchangers, *Int. J. Heat Mass Transfer* 43 (2000) 4189-4204.

Hinze J.O., *Turbulence*, second ed., McGraw-Hill, New York, 1975.

IEA, *Key world energy statistics 2006*, Atelier de cartographie de sciences PO, Documentation Française, 2006.

Jacobi A.M., Shah R.K., Heat transfer surface enhancement through the use of longitudinal vortices: a review of recent progress, *Exp. Therm. Fluid Sci.* 11 (1995) 295-309.

Jones S.W., Thomas O.M., Aref H., Chaotic advection by laminar flow in a twisted pipe, *J. Fluid Mech.* 209 (1989) 335-357.

Kakac S., Shah R.K., Aung W., *Handbook of Single-Phase Convective Heat Transfer*, John Wiley and Sons, New York, 1987.

Kock F., Herwig H., Local entropy production in turbulent shear flows: a high-Reynolds number model with wall functions. *Int. J. Heat Mass Transfer* 47 (2004) 2205-2215.

Kock F., Herwig H., Entropy production calculation for turbulent shear flows and their implementation in cfd codes. *Int. J. Heat Fluid Flow* 26 (2005) 672-680.

Kockmann N., Kiefer T., Engler M., Woias P., Silicon microstructures for high throughput mixing devices, *Microfluid Nanofluid* 2 (2006) 327-335.

Kölbl A., Further comments on the iodide iodate reaction method for characterising micro-mixing, *Chem. Eng. J.*, 145 (2008) 176-177.

Launder B.E., Spalding D.B., The numerical computation of turbulent flows, Comp. *Meth. Appl. Mech. Eng.* 3 (1974) 269-289.

Launder B.E., Reece G.J., Rodi W., Progress in the development of a Reynolds stress turbulence closure, *J. Fluid Mech.* 68 (1975) 537-566.

Launder B.E., Second-moment closure: present… and future?, *Int. J. Heat Fluid Flow* 10 (1989) 282-300.

Le Guer Y., Peerhossaini H., Order breaking in Dean flow, *Phys. Fluids A* 3 (1991) 1029.

Lemenand T., *Étude expérimentale de l'intensification des transferts dans un échangeur-réacteur statique : Mélange de deux fluides non miscibles*, Thèse, Université de Nantes, France, 2002.

Lemenand T., Della Valle D., Zellouf Y., Peerhossaini H., Droplets formation in turbulent mixing of two immiscible fluids, *Int. J. Multiphase Flow* 29 (2003) 813-840.

Lemenand T., Dupont P., Della Valle D., Peerhossaini H., Turbulent mixing of two immiscible fluids, *J. Fluids Eng.* 127 (2005) 1132-1139.

Lightnin Inc., *Lightnin Inliner Mixers Series 45 - High-Efficiency Mixers for a Broad Range of Applications*, Product Bulletin 2008.

Lögdberg O., Fransson J.H.M., Alfredsson P.H., Streamwise evolution of longitudinal vortices in a turbulent boundary layer, *J. Fluid Mech.* 623 (2009) 27-58.

Mao W.B., Xu J.L., Micromixing enhanced by pulsating flows, *Int. J. Heat Mass Transfer* 52 (2009) 5258-5261.

Mohand Kaci H., *Caractérisation des capacités de micromélange des échangeurs/réacteurs multifonctionnels par sonde chimique - Application au HEV*, Thèse, Université de Nantes, France, 2007.

Mohand Kaci H., Habchi C., Lemenand T., Della Valle D., Peerhossaini H., Flow structure and heat transfer induced by embedded vorticity, *Int. J. Heat Mass Transfer* 53 (2010) 3575-3584.

Mokrani A., *Analyse expérimentale et numérique de deux procédés complémentaires de mélange et de transfert thermique en écoulement tridimensionnel ouvert: advection chaotique laminaire et écoulement turbulent Eulérien*, Thèse, Université de Nantes, France, 1997.

Mokrani A., Castelain C., Peerhossaini H., Experimental study of the influence of the rows of vortex generators on turbulence structure in a tube, *Chem. Eng. Proc.* 48 (2009) 659-671.

Moulijn J.A., Stankiewicz A., Grievink J., Gòrak A., Process intensification and process systems engineering: A friendly symbiosis, *Comp. Chem. Eng.* 32 (2008) 3-11.

Muzzio F.J., Meneveau C., Swanson P.D., Ottino J.M., Scaling and multifractal properties of mixing in chaotic flows, *Phys. Fluids A* 4 (1992) 1439.

Palmer D.A., Ramette R.W., Mesmer R.E., Triodide ion formation equilibrium and activity coefficients in aqueous solution, *J. Solution Chem.* 13 (1984) 673.

Paul E.L., Atiemo-Obeng V., Kresta S.M. (Eds.), *Handbook of Industrial Mixing*, Wiley, Hoboken, NJ, 2004.

Pfaudler Inc., DIN Reactors CE, http://www.pfaudler.de/images/stories/File/116-2_des.pdf, Documentation commercial.

Projet VORFLEX, *Projet Exploratoire du PIE CNRS, Concept innovant d'échangeurs-réacteurs de haute efficacité par contrôle dynamique passif avec des générateurs de vorticité flexibles*, Collaboration entre le LTN CNRS UMR 6607 et le DEI Ecole des Mines de Douai, coordinateur T. Lemenand (LTN) obtenu en 2010.

Promvonge P., Thianpong C., Thermal performance assessment of turbulent channel flows over different shaped ribs. *Int. Comm. Heat Mass Transfer* 35 (2008) 1327-1334.

Rahimi M., Shabanian S.R., Alsairafi A.A., Experimental and CFD studies on heat transfer and friction factor characteristics of a tube equipped with modified twisted tape inserts, *Chem. Eng. Process.* 48 (2009) 762-770.

Saulnier J.B., *Les enjeux en énergie et le programme du CNRS*, SFT 2009, Vannes, France.

Stamixo, *GV Static Mixer Product Bulletin*, Product Bulletin GV-2.2, 2006.

Stankiewicz A.I., Moulijn J.A., Process intensification: transforming chemical engineering, *Chem. Eng. Prog.* 1 (2000) 22-34.

Sulzer, Sulzer Chemtech, *Mixing and Reaction Technology, Pace-setting technology worldwide*, Product Bulletin 23.27.06.40-III.09-50, Switzerland, 2009.

Tao W.Q., Guo Z.Y. Wang B.X., Field synergy principle for enhancing convective heat transfer-its extension and numerical verifications, *Int. J. Heat Mass Transfer* 45 (2002) 3849-3856.

Taylor G.I., Statistical theory of turbulence, *Proc. R. Soc. London, Ser. A* 151 (1935) 421-444.

Timité B., Jarrahi M., Castelain C., Peerhossaini H., Pulsating flow for mixing intensification in a twisted curved pipe, *J. Fluids Eng.* 131 (2009) 121104.

Trambouze P., Euzen J.P., *Les réacteurs chimiques de la conception à la mise en œuvre*, Éditions Technique, Paris, 2002.

Versteeg H.K., Malalasekera W., *An introduction to computational fluid dynamics, the finite volume method*, Prentice Hall, New York, 1995, pp. 62-146.

Villermaux J., *Génie de la réaction chimique. Conception et fonctionnement des réacteurs*, Éditions Technique et Documentation, Lavoisier, Paris, 1984.

Wallace J.M., Twenty years of experimental and direct numerical simulation access to the velocity gradient tensor: What have we learned about turbulence, *Phys. Fluids* 21 (2009) 021301.

Wiggins S., Ottino J.M., Foundations of chaotic mixing, *Phil. Trans. R. Soc. Lond. A* 362 (2004) 937-970.

Yang W., Meng H., Sheng J., Dynamics of hairpin vortices generated by a mixing tab in a channel flow, *Exp. Fluids* 30 (2001) 705-722.

ANNEXES

Annexe A : Types de mélangeurs statiques et leurs applications

Plusieurs types d'ERM existent dans l'industrie, utilisés pour diverses applications industrielles (industries pharmaceutique, chimique et agroalimentaire) (voir Figure A-1).

(a) Helical Kenics KM™ (Chemineer Inc., 2008)
Mélange de fluides visqueux - Homogénéisation thermique

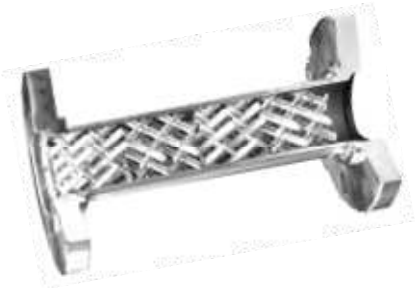

(b) Kenics KMX™ (Chemineer Inc., 2008)
Mélange de fluides très visqueux - Dispersion gaz-liquide

(c) Corrugated Plate GV™ (Stamixo, 2006)
Dispersion de fluide immiscible ayant faible viscosité

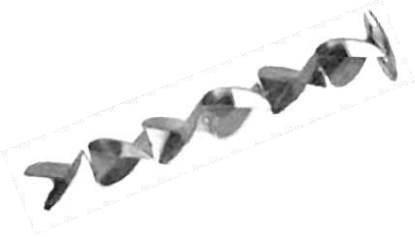

(d) Inliner series 45 (Lightnin Inc., 2008)
Réactions chimiques rapides - Mélange de fluides visqueux

(e) SMX™ (Sulzer, 2009)
Homogénéisation et dispersion de liquides très visqueux et ayant des différences de viscosité

(f) HEV™ (Chemineer Inc., 2008)
Mélange de liquides non miscibles, échangeur thermique, meilleure efficacité pour de grands nombres de Reynolds

Figure A-1 : Types de mélangeurs statiques utilisés dans l'industrie et leurs principales applications

Il existe essentiellement des ERM conçus avec des inserts hélicoïdaux pour la séparation et la recombinaison du fluide (Figure A-1 (a)). Ce type d'ERM peut être adapté pour créer des trajectoires chaotiques améliorant ainsi la qualité du mélange et l'homogénéité. D'autre ERM sont conçus avec des lames entrecroisées pour achever rapidement un bon mélange dans la section de l'ERM (Figure A-1 (b-e)). De plus, il existe des ERM qui utilisent des générateurs de vorticité pour améliorer les transferts radiaux de masse et de chaleur, et créer des couches de cisaillement dans le but d'améliorer le mésomélange.

Lemenand *et al.* (2005) ont étudié les mécanismes de dispersion liquide-liquide dans le mélangeur statique HEV. La Figure A-2 compare la consommation énergétique et la surface de contact A, définie comme $A = 6\Phi / d_{32}$, obtenue dans le mélangeur HEV par rapport à d'autres mélangeurs statiques industriels. Φ est la fraction de la phase dispersée (de l'huile dans ce cas) et d_{32} est le diamètre de Sauter. D'après la Figure A-2, le domaine de travail du mélangeur HEV se situe dans de faibles intervalles de consommation énergétique, entre 0.1 et 1 Jkg^{-1}, et pour des surfaces interfaciales typiques de 300 à 3000 m^2m^{-3}. La faible consommation énergétique et les surfaces de contacts relativement élevées montrent le bon potentiel des mélangeurs statiques HEV pour des applications industrielles.

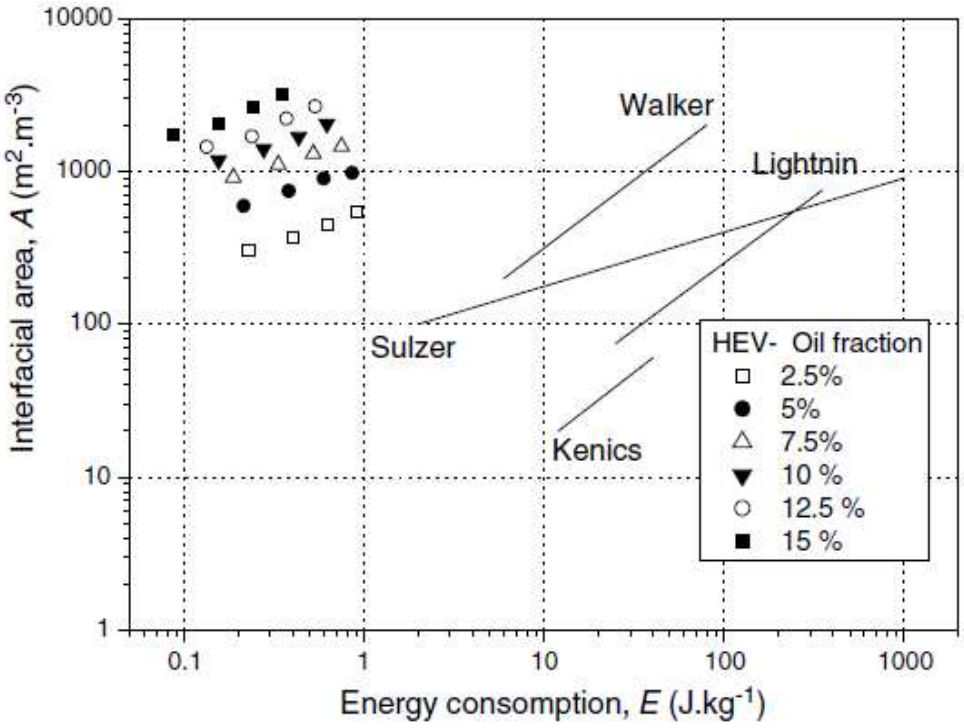

Figure A-2 : Comparaison des performances de dispersion du mélangeur statique HEV avec des mélangeurs statiques industriels (Lemenand et al., 2005)

Annexe B : Générateur de tourbillon trapézoïdal

Dong et Meng (2004) ont utilisé la simulation numérique directe (DNS) pour étudier la structure de l'écoulement généré par un perturbateur trapézoïdal. La Figure B-1 montre la structure de l'écoulement en représentant des iso-surfaces de la vorticité et de pression instantanée. Un tourbillon quasi-stable de forme « collier », ou « necklace vortex », noté (i) dans la Figure B-1 (a) et (vii) dans la Figure B-1 (b) se forme parce que l'écoulement impactant le perturbateur rencontre un fort gradient axial de pression dans le sens inverse à l'écoulement. Ceci, couplé avec le gradient de pression perpendiculaire à l'écoulement génère une courbure dans l'écoulement autour de l'ailette et conduit à une concentration de vorticité (Doligalski *et al.*, 1994).

La couche de cisaillement (iii) est due au gradient de vitesse entre l'écoulement accéléré au-dessus de l'ailette et le fluide décéléré dans la zone de sillage derrière l'ailette. Due à une instabilité de type Kelvin-Helmholtz, cette couche de cisaillement devient instable et génère une séquence périodique de structures « fer à cheval », ou bien « hairpin » vortices, notées (iv) et (v) dans les Figure B-1 (a) et (b).

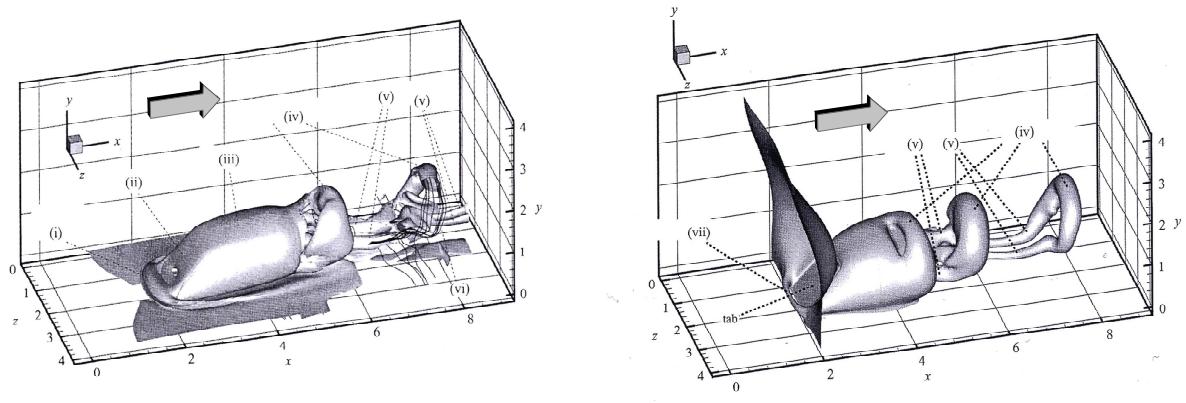

(a) (b)

Figure B-1 : Iso-surfaces représentant la structure de l'écoulement généré par un perturbateur trapézoïdal : (a) grandeur de la vorticité adimensionnelle instantanée $|\omega| = 3.5$ *et (b) pression adimensionnelle instantanée* $P = -0.16$ *(Dong and Meng, 2004)*

La Figure B-2, montre que des zones de vorticité positive $\omega_z > 0$ existent dans le sillage de l'ailette au dessous des têtes des hairpins. Ces structures secondaires, nommées « tourbillons inversés », ou bien « reversed vortices », sont dues à une couche de cisaillement inversée formée par l'interaction du fluide décéléré au dessous des têtes des hairpins, et du fluide plus rapide au dessous (Yang *et al.*, 2001 ; Dong et Meng, 2004).

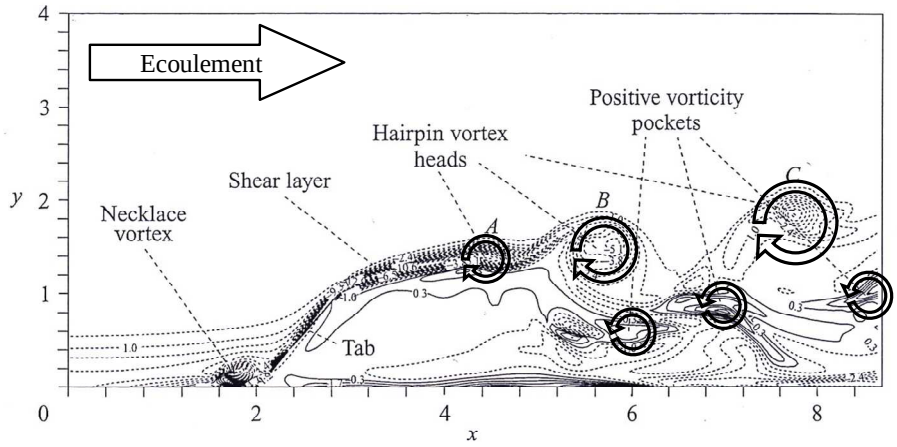

Figure B-2 : Contour de la vorticité instantanée ω_z dans le plan de symétrie de l'ailette (Dong and Meng, 2004)

Annexe C : Les différentes configurations du HEV

Le mélangeur statique HEV est composé d'un tube droit circulaire dans lequel sept rangées de perturbateurs sont insérées aux parois comme le montre la Figure C- 1 (a). Chaque rangée de perturbateur est composée de quatre perturbateurs trapézoïdaux, diamétralement opposés et inclinés de 30° par rapport à la paroi. Cet ERM est largement étudié au sein du LTN due à sa bonne capacité en mélange turbulent et sa moindre consommation énergétique par rapport à d'autres ERM de l'industrie (Lemenand *et al.*, 2003 ; Mokrani *et al.*, 2009 ; Mohand Kaci *et al.*, 2009) (voir l'Annexe A).

Dans le but d'améliorer l'efficacité énergétique du mélangeur statique HEV, nous proposons deux modifications géométriques dans le but de mieux redistribuer les champs de vorticité et de turbulence dans le volume du réacteur. La première modification consiste à inverser le sens de l'écoulement relativement à la géométrie classique du HEV comme représenté dans la Figure C- 1 : (c). La deuxième géométrie consiste à alterner périodiquement les rangées de perturbateurs, l'une par rapport à l'autre, d'une manière tangentielle et d'un angle de 45° comme le montre la Figure C- 1 : (b).

Le tube contenant les rangées de perturbateurs, de 20 mm de diamètre intérieur, est fabriqué en plexiglas pour avoir un accès optique satisfaisant. Toutes les rangées de perturbateurs sont séparées l'une de l'autre d'une distance de 20 mm. Les géométries étudiées sont placées à la zone de section test dans la boucle hydraulique (voir Figure 7).

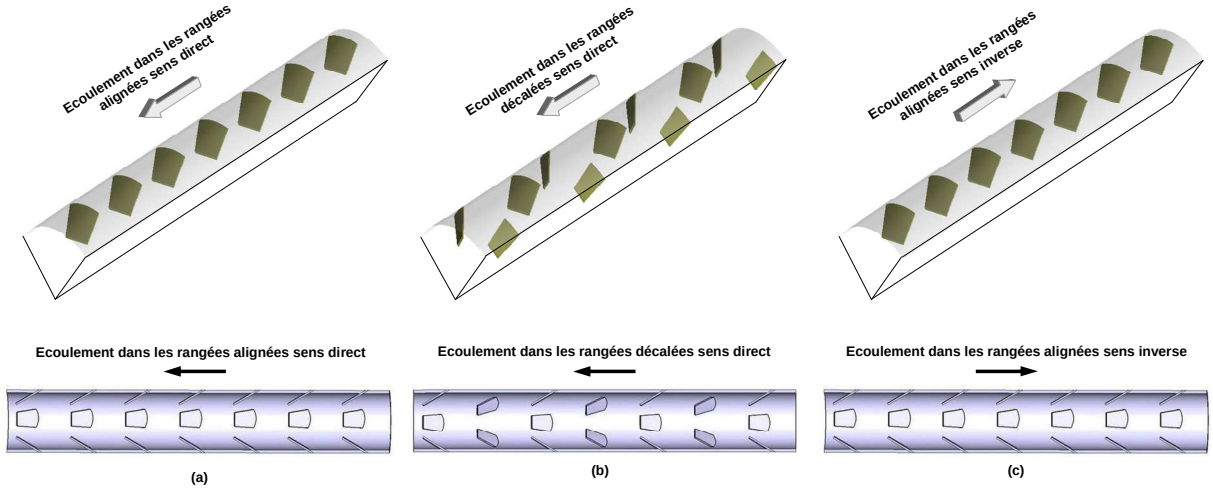

Figure C- 1 : Géométries étudiées (a) géométrie classique du HEV notée ASD (aligné sens direct), (b) HEV classique avec les rangées en alternance noté DSD (décalé sens direct), (c) HEV dans le sens inversé noté ASI (aligné sens inverse)

Les générateurs de tourbillon sont de forme trapézoïdale comme le détaille la Figure C- 2. Chaque générateur de tourbillon est fixé à la paroi par sa grande base avec une inclinaison de 30°. En effet la dynamique de l'écoulement de ce type de perturbateur a été largement étudiée dans la littérature due à sa capacité de générer un écoulement complexe, topologiquement proche d'une turbulence naturelle aux zones proches de la paroi (Gretta et Smith, 1993 ; Elavarasan et Dong, 2000 ; Yang *et al.*, 2001 ; Dong et Meng 20004) (voir l'Annexe B).

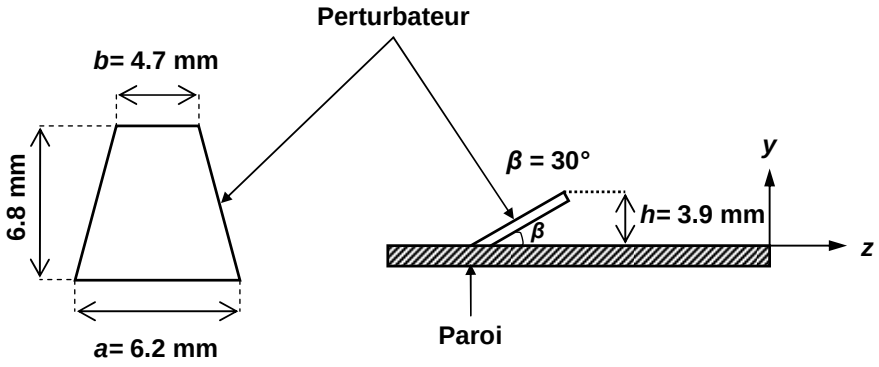

Figure C- 2 : Dimensions du générateur de tourbillons dans les géométries étudiées

Les outils utilisés pour cette étude sont la LDA (laser Doppler velocimetry) et les simulations numériques en utilisant le modèle de turbulence $k-\varepsilon$ standard (Launder et Spalding, 1974 ; Versteeg et Malalasekera, 1995) et le modèle RSM (Launder *et al.*, 1975 ; Gibson et Launder, 1978 ; Launder, 1989). Le développement des tourbillons longitudinaux et l'évolution de leurs intensités sont étudiés en utilisant un modèle pseudo-visqueux développé par Lögdberg *et al.* (2009). Un récapitulatif des méthodes utilisées pour cette étude est donné dans le Tableau C- 1.

Nombre de Reynolds *Re*	Une seule rangée (isotherme)	Rangées alignées sens direct ASD	Rangées décalées sens direct DSD	Rangées alignées sens inverse ASI
7500	--	$k-\varepsilon$ standard	$k-\varepsilon$ standard mesures LDA	$k-\varepsilon$ standard mesures LDA
10000	--	$k-\varepsilon$ standard	$k-\varepsilon$ standard mesures LDA	$k-\varepsilon$ standard mesures LDA
12500	--	$k-\varepsilon$ standard	$k-\varepsilon$ standard mesures LDA	$k-\varepsilon$ standard mesures LDA
15000	RSM mesures LDA	$k-\varepsilon$ standard RSM	$k-\varepsilon$ standard RSM mesures LDA	$k-\varepsilon$ standard RSM mesures LDA

Tableau C- 1 : Récapitulatif des méthodes utilisées pour l'étude du champ hydro-thermique dans les trois géométries. Les deux simulations numériques pour chaque modèle $k-\varepsilon$ et RSM correspondent à des parois adiabatiques et à des parois à une température imposée $T_w = 360$ K

Annexe D : Production scientifique de C. Habchi par ordre chronologique

Revues à comités de lecture

[1] C. Habchi, T. Lemenand, D. Della Valle, H. Peerhossaini.
Liquid-liquid dispersion in a chaotic advection flow.
International Journal of Multiphase Flow, 35 (2009) 485-497.

[2] C. Habchi, S. Ouarets, T. Lemenand, D. Della Valle, J. Bellettre, H. Peerhossaini.
Influence of viscosity ratio on droplets formation in a chaotic advection flow.
International Journal of Chemical Reactor Engineering, 7 (2009) A50.

[3] C. Habchi, T. Lemenand, D. Della Valle, H. Peerhossaini.
Alternating mixing tabs in multifunctional heat exchanger-reactor.
Chemical Engineering and Processing 49 (2010) 653-661.

[4] H. Mohand Kaci, C. Habchi, T. Lemenand, D. Della Valle, H. Peerhossaini.
Flow structure and heat transfer induced by embedded vorticity.
International Journal of Heat and Mass Transfer, 53 (2010) 3575-3584.

[5] C. Habchi, T. Lemenand, D. Della Valle, H. Peerhossaini.
Turbulence behavior of artificially generated vorticity.
Journal of Turbulence, 11 N°36 (2010) 1-28.

[6] C. Habchi, T. Lemenand, D. Della Valle, H. Peerhossaini.
Turbulent mixing and residence time distribution in novel multifunctional heat exchangers-reactors.
Chemical Engineering and Processing, 49 (2010) 1066-1075.

[7] C. Habchi, M. Khaled, T. Lemenand, D. Della Valle, H. Peerhossaini.
A Semi-Analytical Approach for Temperature Distribution in Dean Flow.
Journal of Heat Transfer ASME, Submitted for Publication (2010).

[8] C. Habchi, T. Lemenand, D. Della Valle, Z. Anxionnaz, P. Tochon, M. Cabassud, C. Gourdon, H. Peerhossaini.
A new adaptive procedure for using chemical probes to characterize mixing.
Chemical Engineering Science, Submitted for Publication (2010).

[9] C. Habchi, T. Lemenand, D. Della Valle, H. Peerhossaini.
Assessment of micro-mixing in turbulent flows by chemical probe.
Chemical Engineering Journal, Submitted for Publication (2010).

[10] C. Habchi, T. Lemenand, D. Della Valle, H. Peerhossaini.
Entropy production and synergy field principle in turbulent vortical flows.
Intentional Journal of Thermal Science, Submitted for Publication (2010).

Enveloppes SOLEAU

[1] C. Habchi, T. Lemenand, D. Della Valle, H. Peerhossaini.
Nouvelles géométries pour l'intensification de l'efficacité énergétique d'un échangeur/réacteur multifonctionnel: Rangées alternées-Rangées décalées.
Enveloppes SOLEAU N° 356995 du 22/07/2009.

[2] J.L. Harion, H. Peerhossaini, C. Habchi, T. Lemenand, D. Della Valle.
Échangeurs-réacteurs multifonctionnels continus: amélioration des performances par une modification passive dynamique du fonctionnement.
Enveloppes SOLEAU n° 348694 du 17/04/2009.

Conférences avec actes

[1] C. Habchi, T. Lemenand, D. Della Valle, H. Peerhossaini.
Intensifying the turbulent kinetic energy dissipation rate by redistributing the streamwise vorticity.
GPE-EPIC, Venise, Italy, 2009.

[2] C. Habchi, M. Khaled, T. Lemenand, D. Della Valle, H. Peerhossaini.
The temperature distribution in Dean flow: an analytical approach.
ICTEA, Abu Dhabi, UAE, 2009.

[3] C. Habchi, S. Ouarets, T. Lemenand, D. Della Valle, J. Bellettre, H. Peerhossaini.
Viscosity effects on liquid-liquid dispersion in laminar flows.
ICHMT, Hamamat, Tunisia, 2009.

[4] C. Habchi, T. Lemenand, D. Della Valle, H. Peerhossaini.
Turbulent mixing and residence time distribution in novel multifunctional heat exchangers-reactors.
SFGP, Marseille, France, 2009.

[5] C. Habchi, T. Lemenand, D. Della Valle, H. Peerhossaini.
Effets des rangées de perturbateurs pariétaux sur les transferts de chaleur.
SFT, Vannes, France, 2009.

[6] C. Habchi, T. Lemenand, D. Della Valle, H. Peerhossaini.
On the correlation between vorticity flux and heat transfer coefficient.
IHTC-ASME, Washington, USA, 2010.

[7] C. Habchi, T. Lemenand, D. Della Valle, H. Peerhossaini.
On the synergy field between velocity vector and temperature gradient in turbulent vortical flows.
ThETA 3, Cairo, Egypt, 2010.

Étude expérimentale et numérique des phénomènes de mélange turbulent et de transfert thermique en présence de vorticité

Cette étude porte sur les phénomènes de mélange turbulent et de transfert thermique dans des *échangeurs/réacteurs multifonctionnels* (ERM) à *générateurs de vorticité*. La géométrie des ERM conditionne leur efficacité énergétique en déterminant la structure de l'écoulement. Ainsi, la compréhension fine des mécanismes du mélange turbulent et des transferts convectifs constitue un enjeu fondamental pour l'amélioration de l'efficacité énergétique des ERM. La démarche scientifique est décomposée en deux parties :

Tout d'abord, nous étudions l'utilisation de la *sonde chimique* dans le but de caractériser le micromélange dans des écoulements turbulents continus homogènes. Nous proposons une *procédure expérimentale adaptative* permettant d'adapter les cinétiques chimiques aux conditions locales de turbulence. De plus, nous définissons un *domaine de validité*, dépendant des conditions hydrodynamiques au point de mesure, en s'appuyant sur la modélisation physique de l'interaction entre les différentes échelles du mélange.

Ensuite, nous étudions le *mélange* et les *transferts thermiques* dans trois géométries d'écoulements turbulents en présence de vorticité générée par des perturbateurs insérés dans un tube droit circulaire. Cette étude repose sur des mesures par LDA (laser Doppler anemometry) et de la simulation numérique CFD. Différentes approches physiques sont utilisées : statistique de turbulence, intensité de la vorticité, production d'entropie et synergie des champs. La complémentarité de ces approches permet de proposer une méthodologie afin d'évaluer les performances d'un ERM en régime turbulent.

Mots-clés : Mélange turbulent / Echangeurs-réacteurs multifonctionnels / Micromélange / Méthode de sonde chimique / Générateur de vortex / Advection chaotique / Interaction écoulement-structure

Experimental and numerical study of turbulent mixing and heat transfer phenomena in presence of vorticity

The aim of the present doctoral thesis is the study of turbulent mixing and heat transfer in *multifunctional heat exchangers/reactors* (MHER) of *vortex generator type*. The geometry of the MHER strongly influences its energetic efficiency by controlling the flow structure. Thus, understanding of the mechanisms of turbulent mixing and convective heat transfer is a key issue for improving the energetic efficiency of these devices.

This work is composed of two main parts:

First, we investigate the *chemical probe* methods, based on a system of parallel-competitive chemical reactions, which are then used to characterize the micromixing in continuous flows. Here, we propose an *adaptive experimental procedure* to adapt the kinetics of the chemical reactions to the local turbulence. In addition, based on physical modeling of the interaction between the different turbulent mixing scales, we define a *domain of validity* for this method depending on the hydrodynamic conditions at the probe measurement point.

The second part is devoted to the study of the turbulent *mixing* and *heat transfer* phenomena in three different turbulent flows in the presence of artificially generated vorticity in a straight circular tube. The tools used in this investigation are the laser Doppler anemometry (LDA) and CFD simulation. Several physical approaches are used to characterize the different mechanisms of turbulent mixing and heat transfer aimed at determining the best configuration of vorticity generation.

Keywords: Turbulent mixing / Multifunctional heat exchangers-reactors / Micro-mixing / Chemical probe method / Vorticity generator / Chaotic advection / Flow-structure interaction

Discipline : Sciences pour l'Ingénieur N° ED 498-130